LASER WELDING OF TITANIUM AND TIN PLATE

by

JYOTIRMOY MAZUMDER, B.E.(MET.)

A thesis presented for the
Degree of Doctor of Philosophy of the
University of London

April 1978

John Percy Research Group in
Process Metallurgy,
Department of Metallurgy and
Materials Science,
Imperial College of Science and
Technology,
London SW7 2BP

ABSTRACT

Welding of titanium alloy (6Al-4V-Ti) and tin coated mild steel (tinplate for containers) has been studied using a 10.6 μ laser produced by a B.O.C. 2kW CW CO_2 laser as the energy source. The relationship between the main welding parameters such as laser power, welding speed, substrate thickness on fusion width, heat affected zone and weld properties are described.

The mechanical properties of the welds are evaluated together with their corrosion resistance.

Phase transformation and structural change of laser irradiated material and HAZ has been studied using optical scanning and transmission electron microscopy. The microstructures have been compared with mechanical properties.

The heat transfer mechanism of the process has been mathematically modelled using a finite difference method and classical heat conduction theory. The predicted temperature cycle and temperature distribution have been compared with structural variations as obtained experimentally for various welding parameters. Welding of these materials by means of a laser has been shown not only possible but one of the better methods.

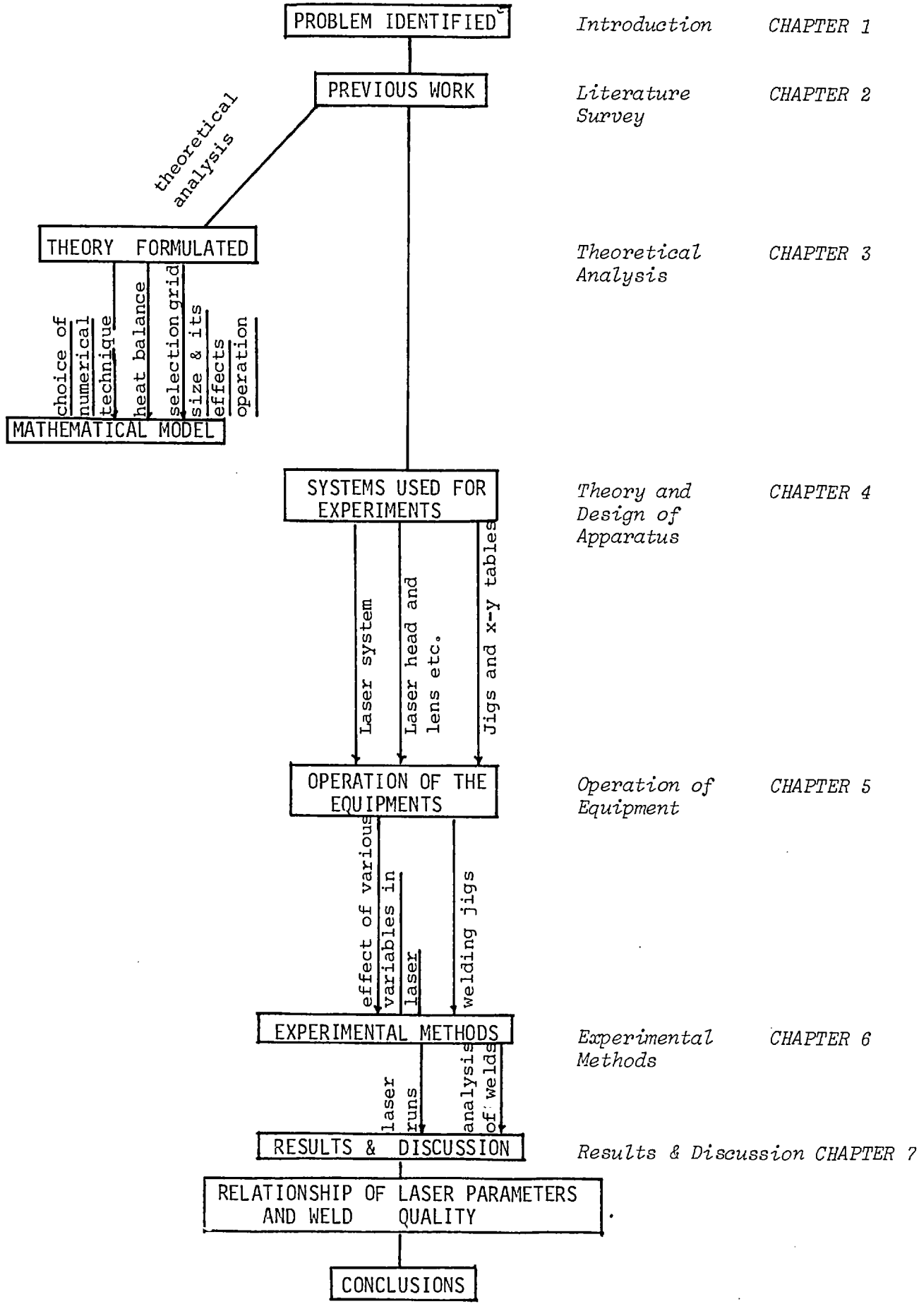
PROBLEM IDENTIFIED
Introduction
CHAPTER 1
PREVIOUS WORK
Literature Survey
CHAPTER 2
theoretical analysis
THEORY FORMULATED
Theoretical Analysis
CHAPTER 3
choice of numerical technique
heat balance
selection grid size & its effects
operation
MATHEMATICAL MODEL
SYSTEMS USED FOR EXPERIMENTS
Theory and Design of Apparatus
CHAPTER 4
Laser system
Laser head and lens etc.
Jigs and x-y tables
OPERATION OF THE EQUIPMENTS
Operation of Equipment
CHAPTER 5
effect of various variables in laser
welding jigs
EXPERIMENTAL METHODS
Experimental Methods
CHAPTER 6
laser runs
analysis of welds
RESULTS & DISCUSSION
Results & Discussion
CHAPTER 7
RELATIONSHIP OF LASER PARAMETERS AND WELD QUALITY
CONCLUSIONS

CONTENTS

CHAPTER 1

INTRODUCTION

1.1 Definition of the Process

1.1.1 Laser material interaction mechanism

The interaction of intense laser light with matter is a complex process. Firstly, there is the probability of extremely rapid heating. Depending on the power density heating rates could be as high as 10^{10} celsius degrees per second[1]. However, the interaction mechanisms can be divided into three broad groups by considering the power density of the laser beam.

i) Heating without phase change (power density $< 10^5$ W/cm^2)

With fluxes of magnitude less than 10^5 W/cm^2 the radiation is partly reflected and partly absorbed at the surface layer. This causes a temperature rise in the material but the magnitude and extent of this rise depends on the thermal constants of the material together with the time of exposure[16]. For example, insulators can be drilled at the power level of $\leq 10^5$ W/cm^2 but not the metals.

ii) Laser induced melting ($10^5 \leq$ power density $\leq 10^7$ W/cm^2)

Continued irradiation of a sample with $10^5 \leq F(t) \leq 10^7$ W/cm^2 will result in a temperature rise to the melting point, at which time a fusion front will then propagate into the material. When the surface temperature rises toward the boiling temperature an evaporation front begins to move into the material, reducing the thickness of the liquid layer[16]. Nevertheless, even when rapid evaporation is occurring, the evaporation surface will be preceeded by a thin liquid layer whose thickness has been estimated by Rykalin and Uglov[84]. As the hole generated by the evaporation front deepens, incident radiation will be more effectively trapped and the surface of the hole will be coated with a liquid layer.

Welding applications fall within the power range.

iii) Laser vaporisation and particle emission (Power density > 10^7 W/cm^2)

As incident laser intensity rises above 10^7 W/cm^2 a host of new interaction effects are observed such as particle emission. Prokhorov et al[240] have predicted that for a critical incident intenstiy of $10^7 < F(t) \leqslant 10^8$ W/cm^2 a transparency wave begins to propagate into the target. Passage of this wave converts liquid metal into liquid dielectric for a critical temperature of boiling front. However, this discussion is beyond our scope.

Duley[16] reports that evaporation regime typically begins at $F(t) \simeq 10^8$ W/cm^2

1.1.2 Laser welding

The scope for technically and commercially feasible laser welding applications has increased greatly since the development of multikilowatt CW CO_2 lasers around 1970[2-5]. The lasers capability for generating a power density greater than 10^6 watt/in^2[1,6-8] is a primary factor in establishing its potential for welding. A power density of this magnitude can only be duplicated with an electron beam. At these high power densities deep penetration welding is possible. The mechanism of deep penetration welding by a laser beam is very similar to that encountered with an electron beam i.e., energy transfer via keyhole[1,6,9]. This keyhole may be produced when a beam of such high power density on the substrate leads to vapourisation of the substrate and the pressure produced by the vapour in the crater causes displacement of the molten metal upwards along the walls of the hole. This hole acts as a blackbody and aids the absorption of the laser beam as well as distributing the heat deep in the material.

However, the deep penetration capability of EBW extends only a short distance outside a vacuum and for optimum efficiency electron beam welding needs to be done in a vacuum[6]. By contrast, CO_2 laser beams can be transmitted for appreciable distances through the atmosphere without serious attenuation or optical degradation. The

laser thus offers an easily manoeuvred, chemically clean, high intensity, atmospheric welding process producing deep penetration welds (aspect ratio greater than 1:1) with narrow HAZ and subsequent low distortion.

1.2 Outline of the Problem

a) Fundamental investigation of the influence of various welding parameters during the laser welding of the following materials:

i) Titanium alloy (6Al-4V-Ti)

ii) Tin coated mild steel and drum quality steel (Tin plate)

b) To study the quality of the weld obtained. This is to study the heat affected material after welding to find the nature of phase transformation and the heating cycle suffered due to laser welding and to correlate it with the mechanical properties.

c) To develop a mathematical model to simulate a laser weld in order to help to evaluate the thermal cycle undergone during the process. The classical heat transfer theory was used for this purpose which is argued, by Schawlow[1] and Duley[16], to hold good for the power density used here.

1.3 Possible Applications

a) Titanium Alloy

The purpose of using this material for the investigation lies in the wide applications of the material for aero-space industry and to some extent in chemical industries and power plants.

Due to the high oxygen affinity of titanium conventional atmospheric welding processes face difficulties in producing welds of a desired quality. At the moment electron beam welding is the main process used for the welding of the alloy. But the requirement of a vacuum for EB welding makes this process expensive.

Laser welding may have the following advantages:-

1) High quality welds

2) Welding at atmospheric pressure

3) High speed welding

4) Chemical clean welding

b) Tin coated mild steel and drum quality mild steel

Lasers are particularly effective on thin materials. One of the major application for thin material welding is in can making (Metal Box are the largest customers of B.S.C.) Hence the investigation on tin plate welding is considered. Commercially the main consideration is welding speed, however, the laser welds produced showed other advantages.

The material under investigation is largely used to manufacture different kinds of containers. The most common method of making a can is lock-seam and solder, but this poses the problems of the cost of solder and the health risk from lead in a food container, also the presence of solder is not very convenient for recycling. The alternative use of aluminium is currently being considered but the cost of aluminium will always be a problem

However, another process to fabricate cans called the "Soudronic" process has already been adopted for production. It has its own limitations[10,11]. With the co-operation of British Steel Corporation and Metal Box Limited, the laser welding work reported here was undertaken to try and establish the future application for the laser in this field.

CHAPTER 2

PREVIOUS WORK

2.1 General Welding Processes

As summerised by Houldcroft[12] every welding process must fulfil four requirements:-

1) A supply of energy to create union by fusion or pressure
2) A mechanism for removing superficial contamination from the joint faces
3) Avoidance of atmosphere contamination or its effects
4) Control of weld metallurgy.

Welding processes may be classified according to the way in which the first three basic requirements are satisfied. The energy for welding is almost always supplied as heat so that divisions can be made according to the methods by which heat is generated locally. These methods may be defined and grouped as follows[12]:-

a) Mechanical
Heat generated by impact or friction or liberated by the elastic or plastic deformation of the metal.

b) Thermo-Chemical
Exothermic reactions, flames and arc plasmas. According to Houldcroft[12] plasmas should be put in the same class as oxy-fuel gas flames. Although chemical reactions may not take place in a plasma the method of heat transfer to the work is the same as for processes employing an envelope of burning gas.

c) Electric Resistance
Heat generated by either the passage of a current introduced directly to the metal to be joined or by a current induced within the parent metal.

d) Electric Arc

Both a.c. and d.c. arcs with electrodes which melt and those which do not.

e) Radiation

This category is suggested to cover the new processes such as laser and electron beam welding and others which may yet be developed. The essential feature of a radiation process is that energy is focussed on the workpiece and heat is generated only where the focussed beam is intercepted.

As it is not possible to define all welding processes completely by the source, especially for different types of arc welding, Houldcroft[12] tried to complete the classification by reference to the way the process satisfies the condition of atmosphere control. All welding processes can be examined in the same way by placing the names of the processes within a grid formed by listing the sources of heat along one axis and methods of avoiding atmospheric contamination along the other axis as is explained in Table 2.1 by Houldcroft[12]. The table can now be divided up into areas enclosing processes with basic similarity. Seven such areas are readily identified corresponding to processes as follows:-

1) Solid-phase
2) Thermo-Chemical
3) Electric Resistance
4) Unshielded Arc
5) Flux Shielded Arc
6) Gas-Shielded Arc
7) Radiation

In Table 2.1 certain areas can be marked out as regions where welding processes could not exist - for example flames cannot be used in vacuum.

(a) after Houldcroft - Ref. 12

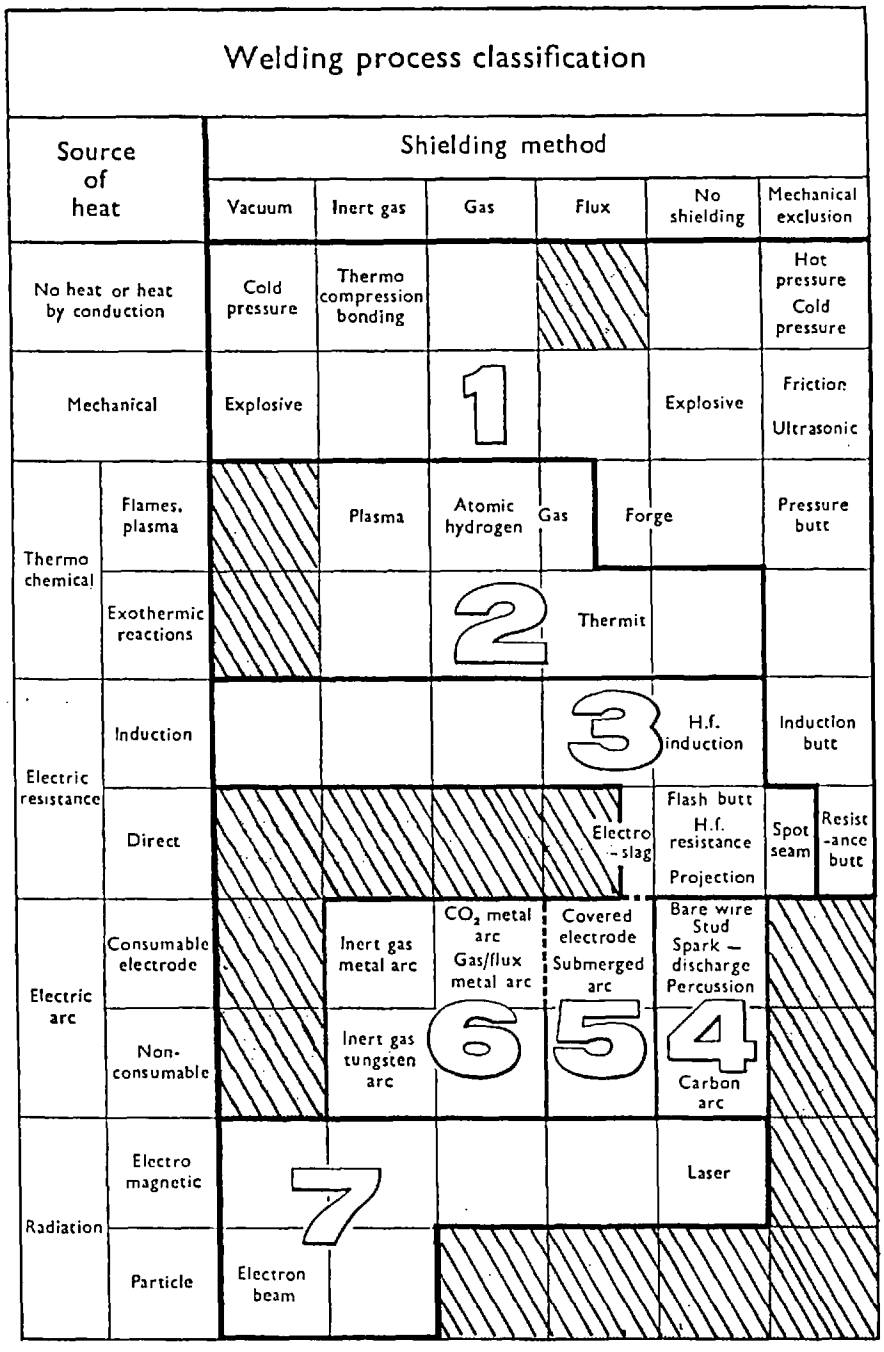

TABLE 2.1

Grouping of welding processes according to heat source and shielding method[a]

According to Houldcroft[12] this way of classifying welding processes is less rigid than the family tree method and makes it possible to account for certain anomalies. The resistance butt welding process, for example, while truly a solid-phase welding process, is normally included in the resistance welding category. In Table 2.1 the position of this process is clarified by drawing the boundary of the group (1) solid-phase processes to include resistance butt and to exclude the remaining resistance processes. Similarly, electro-slag welding and its derivatives can be placed correctly in the resistance heat source grid, but may be linked with the flux-shielded arc processes with which they have a great deal in common.

2.2 Radiation Welding Processes

The following processes employ energy for welding in the form of "Radiation"[12].

a) Optical or arc image

b) Electron Beam System

c) Laser

While an electron beam[6,12] is a stream of fast-moving particles, the other two processes employ energy as-electro-magnetic radiation.

Uniqueness of the radiation welding method lies in the fact that the energy for welding may be focussed on the object to be welded, heat being generated only where the focussed beam strikes the workpiece. Unlike arc or flame sources, therefore, the work is not brought in contact with any heated media, gas or metal vapour, and the processes may be carried out in vacuum or low pressure systems where the ultimate in cleanliness is achieved. Finally, in contrast to arc welding, the molten pool is subjected to only negligible pressure.

2.3 Previous Use of Laser as Heat Source

Very early in the history of Lasers, the beam from the laser was focussed by a simple lens on a piece of metal and holes were produced. The possibility of using a laser as a heat source was recognised at once. A larger number of papers[18-20, 44-160] and several books[13-16] have described and discussed several applications of laser as heat source. However, the following applications have attracted the interest of many a research worker.

(i) Isotope Separation[16, 18-43]

(ii) Forming Shaped Deposits[17, 44-46]

(iii) Micro-metalisation[17, 47,48]

(iv) Laser Deposition of Thin Films[14-17, 49-72]

(v) Surface hardening[73-79, 82-83]

(vi) Surface Alloying and Cladding[77, 80-81]

(vii) Drilling[14,16,17,20,85-100]

(viii) Cutting and Machining[14,16,82,101-122]

ix) Welding[14,16,122-160]

An excellent review of most of the above processes is available in W.M. Steen's Ph.D. thesis[17]. Many of the above activities are summarised in the papers by I.J. Spalding[18], Scott and Hodgett[19] and Cohen and Epperson[20]. However, certain important features of above processes are noted below.

2.3.1 (i) Isotope separation

Though the authors work involves thermo-mechanical material processing with lasers, mention of isotope separation process using laser is made in view of its immense scientific and economic possibility and to give an idea of complex behaviour of laser material interaction.

The process[16,18] is simply to excite selectively an energy level of an isotopic species in a gas or solid containing that species in the normal isotopic abundance. And according to Spalding[18] this

is based on the fact that the electronic energy levels of atoms are slightly shifted by interactions with nuclear spin, nuclear charge distribution and for lighter atoms and for molecules, by changes of reduced mass. If levels can be chosen in which the isotope shift permits strong light absorption by one isotopic species at a frequency at which all the other species are transparent, it should be possible to selectively excite that species with a sufficiently monochromatic (and tunable) laser.

Some basic methods by which isotopic separation may in principle be accomplished by laser excitation are:

a) Selective two step photoionisation[16,18,21-23]

b) Selective two step photodissociation[16,18,24,25]

c) Photopredissociation[16,18,22,26,30-35]

These processes are discussed in detail by Moore[22] and summarised by Duley[16] and Spalding[18]. Only a few data are available on the practical systems of above processes[21-30].

Recent results on the separation of isotopes by reactions catalysed with CO_2 laser radiation have been reported by Ambastzumian et al[36], Freund and Ritter[37] and Lyman and Rockwood[38] (Boron isotopes from BCl_3); Lyman and Rockwood[38] (^{13}C from CF_2Cl_3); Lyman and Rockwood[38] (^{29}Si from SiF_4); Ambastzumian et al[39] and Lyman et al[40] (^{34}S from SF_6). But the main interest of isotope separation is centered on separation of ^{235}U, but here, not unexpectedly, there is no published data. The problem associated with obtaining an economically feasible process is discussed by Farrer and Smith[41] and Altschuler[42]. Some information about separation of "Deuterium" (D_2O) from Formaldehyde using near-ultraviolet laser has been published recently by Vanderleeden[43].

2.3.2 Forming shaped deposits

Deposition of material in localised patterns by means of shaped heating elements is suggested by Powell et al[44]. A patent to this effect has been taken out by Toulmin[45] in which he proposes to have shaped heating elements on the back of a thin low conductivity substrate.

The general trend in chemical vapour deposition work has been to concentrate on "throwing power" or "covering power" producing uniform deposits over large areas. The subject is thoroughly reviewed in the book by Powell et al[44]. The direct production of a shaped deposit from the vapour was studied by Davies[46] who examined the deposit shape formed in a varying mass transfer field under an impinging jet.

Using Davies[46] mass transfer work as background Steen[17] studied the process of forming shaped deposits of cobalt oxide on glass using CO_2 laser. Both theoretical and experimental aspect of the process has been discussed by Steen[17].

2.3.3 Micrometalisation

Micrometalisation is another way of forming shaped deposits of metals using differential mass-transfer or concentration fields. A Young and W.M. Steen[17] studied the localised condensation of the laser induced plasma plume. According to Young and Steen[17] this technique produces fairly thick (1-2μ) traces having moderately neat edges in a few milliseconds. They used 1.06μ radiation from a YAG laser focussed through a glass slide or any transparent sheet on to a target material lying directly beneath the transparent sheet. Then if the beam has adequate power a plume of target material bursts away from the hot spot (≈5000 - 10,000°C[47]) and condenses on the transparent sheet some 0.1mm away. Traces of conducting copper and zinc have been prepared this way by Clarke[48].

2.3.4 Laser deposition of thin films

The evaporation of materials by a laser beam leads to the possibility of using laser for deposition of thin films[14-17, 49-72].

Since a laser beam can be directed into a high vacuum system through a window to heat a component inside the system, material to be deposited can be heated selectively without the necessity of heating the container to a corresponding temperature. Therefore, contamination of systame vacuum and the thin film substrate will be reduced to a great extent. Furthermore, the possibility of reactions between the deposition material and the crucible in which it is heated can be reduced. Again, laser evaporation can be made to occur at very high temperatures, deposition rates with laser heating are often larger than those attainable with conventional heating methods. However, evaporation at high temperature in general results in a different vapour composition and the tendency for the sample to eject relatively large particles of material. Anyway, an excellent discussion and review of the process is available in Duley's[16] book. As summerised by Duley[16] a list of some materials evaporated with pulsed or CW lasers and some properties of the thin films are produced in Table 2.2.

The initial work of Smith and Turner[50] showed that while Q-switched or normal pulse ruby lasers were suitable for depositing thin films of many materials, the tendency for liquid droplets or even small particles of solids to be ejected resulted in films that were often of poor quality. Though Schwarz et al[55] reports that the deposition rate could be as high as 10^5 - $10^6 A^o$/sec. but according to Duley[16] the thickness attainable with a single millisecond laser pulse is limited to a few thousand angstroms even at high pulse energies.

The deposition process can be made continuous by the use of either CW Nd or CO_2 lasers. As first shown by Groh[51], the CW CO_2 is well suited to the deposition of thin films of many nonmetallic materials. This is due in part to the high absorption of 10.6μm radiation in most insulators and semiconductors.

Zavitsanos et al[53] have made a careful comparison between the structure of Ge and GaAs thin films produced with pulsed ruby laser with those produced by conventional means. They[53] noted

Material	Refractive index	Laser	Comments	References
Sb_2S_3	2.7	Ruby, 10^6-10^8 W/cm^2	100-3000 Å thick film per laser pulse	Smith and Turner (Ref. 50)
As_2S_3	2.4			
Fuchsine	--			
Se	2.4			
Ni-dimethyl gloxime	--			
ZnTe	2.7			
Te	5.0			
MoO_3	2.0			
$PbCl_2$	1.8		Carbon coating required	
PbTe	5.0			
Ge	3.8			
SiO		cw CO_2, 25W	Rate: 4000 Å/min	Groh (Ref. 51)
ZnS			Rate: 4000 Å/min	
ZnSe			Rate: 4000 Å/min	
PbF_2			Rate: 4000 Å/min	
Na_3AlF_6			Rate: 3000 Å/min	
SiO_2			Rate: 2000 Å/min	
MgF_2			Rate: 1500 Å/min	
Si_3N_4			Rate: 200 Å/min	
$LaAlO_3$			Rate: 100 Å/min	
TiO_2			Rate: 35 Å/min	
Al_2O_3			Rate: 20 Å/min	
SiO	1.55-2.0	cw CO_2	Rate: 150 Å/sec	Hass and Ramsey (Ref. 54)
SiO_2	1.46		Rate: 400 Å/min	

(a) (After Duley, Ref. 16, p277).

TABLE 2.2 SUMMARY OF MATERIALS EVAPORATED WITH PULSED AND CW LASERS (a)

that the degrees of crystallinity obtained with laser-deposited films was attainable by conventional means only by heating the substrate to 200-400^{o}C. Moreover, electron diffraction patterns of GaAs films showed that GaAs was deposited without disproportionation[57]. Similar conclusion was reached by Schwarz et al[55] for Barium Titanate and Strontium Titanate films. It is still uncertain whether dissociation of the parent molecules occurs on laser impact but is followed by recombination on the target with the same stoichiometry as the parent material or whether individual molecules are transported intact from the source to the substrate. Evidence in favour of dissociation has been given by Mirkin[58-62]. Ban and Kramer[63] have found that congruent evaporation of compounds of group III-V occurs when a pulsed ruby laser is used, but not when low-power CW CO_2 laser is used, presumably the difference is due to the different power intensity rather than the wavelength.

Difference in chemical composition during evaporation using high power laser was first examined quantitatively by Baldwin[64]. By collecting the vapour ejected from standard brass samples he[64] found that Zn/Cu ratio increases considerably and the enrichment of Zn in vapour was about 30%. But Kliwer[70] after performing similar kind of experiment found the composition of laser-excited brass vapour within a few percent of the source materials. Kilwer's result was further discussed and extended by Baldwin[65]. He demonstrated that the stoichiometry of a laser-deposited sample depends strikingly on the incident laser intensity and on geometrical factors such as the relative attitudes of the evaporating source and the collecting substrate.

CW lasers, yielding a lower evaporation temperature and little if any ejection of liquid phase would seem to be more suitable for the productions of films having compositions similar to that of the parent material.

In another application, the CO_2 laser has been used effectively in chemical vapour deposition[66,17]. Reaction between a vapour and a surface occurs only in the region heated to the prescribed temperature by the focussed laser beam.

Alekseevskii et al[68-69] has reported a novel method of preparing pure superconducting films of Ag, Au and Cu alloys with Germanium. Laser sampling has been used to investigate the chemical composition of irradiated uranium oxide fuel rods[71].

2.3.5 Surface Hardening

The basic objective of using laser for surface hardening is to selectively "transformation harden" materials, with minimal or no surface melting or distortion. The high reflectivity of metals at below their melting temperature necessitates the use of absorptive surface coatings to effect the required coupling of laser energy to the material[73-76]. The transformation hardening process depends solely on the interaction of the laser beam with the energy absorbing coating on the surface. The heat generated at this surface is then conducted into the base metal, raising the base metal to the austenitizing temperature, up to the desired depth. The rapid quenching rates achieved by heat conduction into the cold interior provide sufficient self quenching and therefore external liquid quenching is not normally required. The surface temperature and hardened case depth are controlled by the laser power, laser beam size and dwell time.

Maximum process flexibility for laser heat-treatment calls for an ability to independently adjust beam width and length. Seaman and Gnanamuthu[77] report that they have achieved that desired flexibility by rapidly oscillating the beam in a sweeping motion over the work surface. Their system can treat a path up to 18mm wide. Methods of beam handling for laser heat treatment are discussed at length by Engel[73] and Seaman et al[77].

Lock and Hella[82] and Schaffer[83] discussed and reviewed several heat treatment applications using 10kW CW CO_2 laser.

Seaman et al[77] reports that at 15kW a hardened case depth of 2.03mm may be obtained for carbon steel (AISI-1045) at the rate of 108 mm^2/s. Engel[73] reported the heat treatment data for grey

cast iron using a laser of power output 1500W. Wakefield[78] reports that cast iron piston ring grooves of 0.46cm width are hardened in 50 sec. using 10kW CO_2 laser. Courtney[79] has shown that high alloy steel like high speed tool steel can be hardened with little distortion.

However, it is of interest to mention that the mathematical model derived here gives good correlation with En8 steel heat treatment using a 2kW laser done by Courtney[241]. In his En8 steel he found that depth of hardening was linearly related to the parameter (Total Power / $\sqrt{\text{Beam diameter x velocity}}$) whereas surface melting was correlated to the parameter (Power/Beam diameter^2 x velocity).

2.3.6 Surface Alloying and Cladding

Surface alloying is a process whereby a thin layer at the surface of a metal is melted by a laser beam, with the simultaneous addition of the desired alloying element, thus changing the surface chemical composition of the metal. The alloying elements that are added to the melted surface diffuse in a thin layer of liquid metal which, on freezing, forms solid solutions and compounds. The modified surface thus processed can have superior chemical, physical or mechanical properties. The depth of the alloyed zone, which coincides with the diffusion depth of the alloying elements, can be controlled by the laser power and the total time of application of the laser beam.

The concentration of added element (Cr to steel) up to 50% is reported to be achieved by Seaman and Gnanamuthu[77]. Surface alloying characteristics of steels (AISI-1018 and AISI-4815) has also been published by them[77].

Cladding with hardfacing alloys, like those commercially available in cast rod or powder form, can be melted in a controlled manner by a laser beam to cover the surface of a given base material. Control of heat input is critical during cladding because excessive

heat can locally melt the base material and cause undesirable dilution of the cladding material.

Laser cladding is a highly localised and fast process. Thus this process will utilize only a fraction of the cladding material used by conventional techniques. Therefore, substantial savings on expensive cladding material can be realized. In addition both laser cladding and surface alloying is highly amenable to automation and therefore large areas could be processed at an economic rate.

Work done at AVCO[80] shows that a clad zone, of Haynes Stellite Alloy No.1, of 1.25mm thick, hardness Rc-58-63 could be achieved while HAZ and base metal are less than Rc 30. Fundamental study of cladding of Triballoy powder on Nimonic was carried out by Steen and Bennett[81].

It is also relevant to mention that the mathematical model developed here may predict the case depth and permissible beam traverse speed.

2.3.7 Drilling

Depending on the laser intensity the incident beam may interact in a variety of ways with a solid target. Continued irradiation of a sample with $10^5 < F < 10^7$ W/cm^2 (F = power density) will result in a temperature rise to the melting point, at which time a fusion front will then propagate into the material[16]. When the surface temperature rises towards the boiling temperature an evaporation front begins to move into the material, reducing the thickness of the liquid layer. Nevertheless, even when rapid evaporation is occurring, the evaporating surface will be preceded by a thin liquid layer whose thickness has been estimated by Rykalin and Uglov[84]. As the hole generated by the evaporation front deepens, incident radiation will be more effectively trapped and the surface of the whole will be coated with a liquid layer. The interaction between escaping vapour and this layer may result in a

"flushing" mechanism, whereby liquid is swept out of the hole[16] and prevented from falling to the base of the hole in the case of vertical drilling; thus a drilled hole will be formed. The material removal rate will depend on the power density and time and in case of pulsed laser on the temporal power profile.

The whole process is excellently reviewed by Ready[14] and Duley[16]. The Review of Cohen and Epperson[20] has been summarised by Steen[17] which describes the important physical aspects.

There have been a number of studies of the relation between hole depth, entrance diameter and shape, and the thermophysical parameters of materials using laser[14,16,85-89].

Akimov and Mirkin[86] reports that the depth of the hole is greater for metals of lower melting point whereas Klocke[87] also reports the same adding that the cross-section of the hole is also greater for lower melting point metal.

The measurements of Chun and Rose[88] show that the mass of material removed increases slowly with the duration of the laser pulse for first 100 μsec. or so and subsequently increases linearly with time. Spitz[90] found that the volume of the material removed by the laser could be fitted by the expression

$$V = V_0 \, [1 - \exp(-\beta S)] \qquad [2.1]$$

where V_0 = limiting volume removed by an infinite no. of shots,
S = no. of shots
β = a constant

Spitz[90] correlated this expression with a hole drilled in uranium using a pulsed CO_2 laser. Each "shot" consisted of a 1-sec burst of 245 pulses with each pulse lasting for 1 μsec when the beam was focussed just below the surface. He found that the theoretical prediction of hole shape is excellent close to the focal plane. He also reports that, for harder material, the volume removed by a laser is smaller.

Gagliano et al[91] reports that a valuable technique for reducing hole size in aperturing the laser beam. This reduces the effective beam divergence angle. According to Ready[14] (P-19) the radius of the focal area for a lens is given by the following expression

$$\gamma_s = 1.22\pi\lambda L/2\pi a = 1.22\lambda L/2a \qquad [2.2]$$

λ = wavelength
γ_s = radius of focal area
L = focal length of the lens
a = radius of the beam
1.22π = first minimum of Bessel function J_1

Gagliano et al[91] studied the effect of aperture size on hole diameter for holes produced in ceramic by a ruby laser and found that for aperture sizes between 0.05 and 0.15in, the hole size is a strong function of the aperture diameter.

To drill a fine hole of large aspect ratio in many insulating materials using conventional machine tool technology is very difficult. However, Cohen[92] reports that lasers on the other hand, produced a hole of aspect ratio of 25:1 in ceramics. One of the first industrial applications of high-power pulsed lasers was in drilling fine holes in diamonds[93]. Laser drilling of holes in alumina ceramic has been treated theoretically by Peak et al[94] and experimentally by Longfellow[95] and Nadka and Giles[96].

Drilling of fused quartz sheet with a CW CO_2 laser has been reported by Duley and Gonsalves[97,98] and Duley and Young[99]. Quartz is well suited for CO_2 laser since it strongly absorbs 10.6 μm radiation. An interesting study, both theoretical and experimental, on the rate of movement of vapourisation front is published by Duley[16] and Duley and Gonsalves[97-98].

A three-dimensional moving heat source model is reported by Bar-Isaac and Korn[100] to explain the effect of a focussed laser beam in laser drilling processes. Using Green's function technique

and assuming a plane disc approximation for the evaporation surface, general integral equations for the motion of this surface and equations for temperature profile are derived by Bar-Isaac et al[100].

2.3.8 Cutting and machining

Cutting and machining with a laser, as for drilling, necessitates the formation of a vapourisation front. There are three mechanisms for utilizing the high energy beam of a laser for cutting of metals. They are the following:

1) Vaporization - In this process the metal along the trajectory of the beam is heated through the boiling point and leaves the cut region as a vapour.

2) Gas-Jet Assistance - Sullivan and Houldcroft[101] were the first to suggest that addition of a gas jet assist could aid cutting, and drilling with CW lasers. Usually a concentric jet of gas is used.

As summarised by Duley[16] (P-254) the effects of a gas jet seem to be at least two-fold:

a) It assists in the removal of material from the focal area and reduces the amount of material ejected back toward the laser. This helps to prevent a cloud of attenuating material from building up in front of the workpiece. By removing material from focal area it ensures a cleaner cut.

b) It can either promote or inhibit reactions that may occur due to heating in air. Inert gas assists may be used in cutting flammable materials, while oxygen jet assist has been shown to enhance the burning of metals in air and hence to increase the maximum attainable cutting rate with a given laser power[102-104].

3) Arc Augmentation - Study of using arc in conjunction with gas assist laser beam in order to augment the cutting rate is under investigation by Clarke and Steen[105]. They find that although, requiring considerable skill and caution to lock the TiG arc and the laser beam there is a possibility of increasing the cutting rate to an appreciable extent.

However, at present, it seems that gas jet assisted cutting is the most popular method of laser cutting. There are several studies of gas jet assisted cutting with CW CO_2 which have been published[82,102-110, 112-113]. There are also several publications on gas jet assist cutting using different lasers[111,114-118]. An interesting review is available in Duley's book[14].

Some experimental data of CO_2 laser cutting without gas assist was published by Spalding[119] and Lock et al[120].

However, a compilation of experimental data for laser cutting for both metals and non-metals are furnished in Appendix 1.

An extremely important aspect of cutting studies, which is relevant to the present investigation, is the mathematical modelling of the complex heat transfer situation. The main features of this heat transfer has been described by Duley[16,102] and Babenko et al[104] using a modification of the moving point source theory. They studied the situation for both with and without reactive gas jet assist.

Babenko and Tychinskii[104] reported a modification of the moving point source model in which the heat source has a Gaussian distribution.

Dutta[117] developed a complex finite difference model, which includes mass transfer effects in the slag. A complex analytical approach of laser cutting, considering it as an intensely heated evaporating boundary, has been reported by Andrews and Atthey[122].

2.3.9 Welding

From the initial development, the laser has been hailed as a potentially useful welding tool for a variety of applications. Until the seventies, however, laser welding had been restricted to relatively thin materials and low speeds by the limited continuous power available.

As reviewed by Duley[4], by 1965, a variety of laser systems had already been developed for the production of micro-welds in the fabrication of electronic circuit boards, inside vacuum tubes, and in other specialised applications where conventional welding technology was unable to provide reliable joining.

As summarised by Spalding[119] the potential advantages of laser welding or machining are the following:-

1) Light is inertialess; hence high "tool" velocities with very rapid stopping and starting becomes possible.

2) Difficult materials (e.g. Titanium, quartz etc.) could be handled.

3) The workpiece need not be rigidly held.

4) No electrode or filler materials required.

5) Narrow kerfwidth; low wastage in case of cutting.

6) Very accurate cuts or welds are possible.

7) Welds with little or no contamination can be produced

8) Narrow heat affected zone adjacent to cut or weld.

9) Intricate shapes can be cut or welded at high speed, using automatically controlled light deflection techniques.

Reviews of laser welding studies have been published by Ready[14] and Duley[16]. The more important works are noted here.

The localised heating obtained with laser sources was soon realised to be an important advantage. Anderson and Jackson[123] reported an interesting comparison between heating effects produced with a conventional arc source and those occurring with a pulsed laser. Their result is shown in Fig. 2.1. They show that not only the heat affected zone is small but also the laser source is more efficient since it requires only 37.8 J/cm^2 to produce melting to the required depth, while the arc source must deliver 246J/cm^2 to the workpiece.

Pfluger and Maas[124] have discussed the problems associated with making wire-wire and wire-ribbon welds. Application of laser-formed wire-wire welds to the generation of a plated-wire magnetic memory device has been described by Cohen et al[125]. Laser welding of fine wires without the need of removing insulation are reported by Anderson and Jackson[126] and Lebeder and Granista[127]. Lebeder and Granista[127] report that the strength of lap welds of enamel-coated wires 0.1-0.2mm in diameter were found to be 70-90% that of the wire.

A quantitative study of the strength of laser spot welds in sheets made with a gap between the sheets is reported by Velichko et al[128] and he reports that gaps of 0.1mm before welding do not seem to affect the subsequent strength of the bond. In this case, however, the laser power and pulse duration must be tailored to produce optimum melt penetration.

Some specialized laser welding have been discussed by Miller and Nunnikhoven[129] and Miller[130]. One involved the welding of a bearing assembly made of type 321 stainless steel to a massive type 440C stainless bearing housing. GTAW, resistance spot welding, and EBW had previously been used without satisfactory results whereas a circumferential weld was made with a ruby laser by overlapping individual spot welds which satisfied all design requirements.

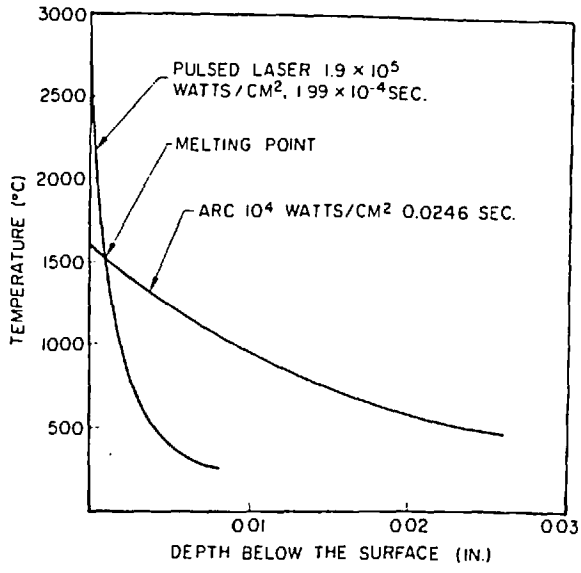

FIG. 2.1 Maximum temperature reached as a function of depth in iron for heating with a laser pulse and the pulse from a conventional arc source (Ref. 123)

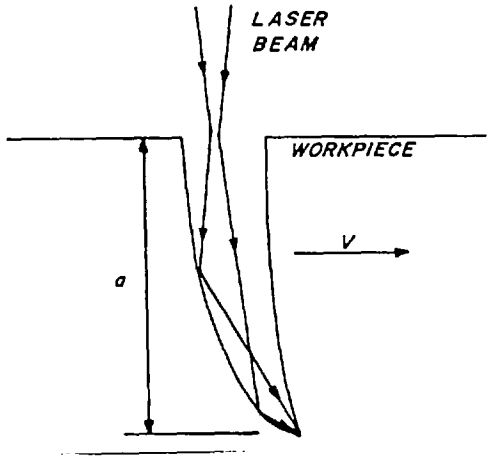

FIG. 2.2 Shape of "keyhole" during laser welding of quartz (Ref. 159)

Welding measurements on Rene 41, columbium D-36 and Molybdenum TZM materials have been reported by Earvolino and Kennedy[131].

An experimental approach for feasibility study for laser welding has been discussed by Schmidt et al[132].

Moorhead[133] reports some data on the welding of thermocouples to various metals with a ruby laser. Laser micro-welding studies are reviewed by Nichols[134].

Laser welds have been produced between a variety of dissimilar metals when other methods prove unsatisfactory. Possibly due to the more rapid rate of cooling and smaller HAZ there is an alteration of formation of phases allowing more pairs of dissimilar metals to be welded using laser. Miller and Nunnikoven[129] have described successful welds between a B-113 steel feed through and type 321 stainless steel casting in a thermistor enclosure.

Garashchuk and Molchan[135] have reported a metallographic analysis of laser welds between Nickel and copper, Nickel and Titanium, and Copper and Titanium. Garaschuk et al[135] reports that fusion region in the Nickel-Titanium weld showed a finely dispersed structure and an intermetallic phase at the boundary of the melt. But there was no comment on crack formation, whereas, Seretsky and Ryba[136] confirm the presence of intermetallics but reports that 75% of their welds were cracked. Garaschuk et al[135] also reports the welding of Tantalum-Molybdenum. Baranov et al[137-138] reports the laser welding of brass, mild steel, and stainless steel to copper.

Gagliano[145] reports welding between tungsten and aluminium using a ruby laser. There are several other useful publications[139-145] reporting laser welding of dissimilar metals. Some of these are listed in Appendix 2, (Table I).

Heat transfer situation for laser welding of dissimilar metal is discussed by Rykalin and Uglov[142] but there are other publications[9,134,146-150] dealing in general for laser welding. However, heat transfer problem for laser welding will be discussed in Chapter 3.

The possiblity of deep penetration welding was realised only after the development of CW CO_2 laser systems around 1970[2-5,7-9]. As the present study involves penetration welding using 2kW CW CO_2 laser, it is discussed separately in Section 2.4.

2.4 Previous work on CO_2 laser welding

The advent of high power CW lasers opens the door to metal working applications previously reserved for the more conventional high flux heat sources such as reacting gas jets, electric arcs, plasma arcs and electron beams. The limitations of current welding technology have stimulated much interest in deep penetration welding using CW CO_2 lasers.

The studies of penetration welding using CO_2 laser has been excellently reviewed by Duley[16](P241-8). However, some important works are noted here.

A series of studies, by Banas[8,151,157], Locke et al[82,152-3], Baardsen et al[154], Hoag et al[153] and Ball and Banas[156], have examined the parameters with CW CO_2 lasers and have noted the similarity of the process to that obtained with high power electron beams. In both cases, radiation trapping by formation of a keyhole permits the workpiece to absorb most of the incident laser radiation. Heat is then transferred from the surface of this keyhole to the bulk material. Swifthook and Gick[9] theoretically discussed the keyhole mechanism.

An interesting experiment on the mechanism of deep penetration welding with a CW CO_2 laser has been reported by Siekman and Morijn[158-9]. This experiment was performed on transparent fused quartz so that the

development of the weld in time could be directly followed photographically. The laser was seen first to drill a hole in the quartz, which was then translated through the material. However, they found that the profile of the hole varies as the welding speed increases. A schematic representation of this profile at high speed is shown in Fig. 2.2. The tip of the hole is seen to bend around toward the direction in which the workpiece is translated. This process is caused by the reflection of laser light from the leading edge of the hole. Material evaporated at this surface is effectively trapped by the cooler trailing edge. Thus, material is transported across the laser beam from the hot leading edge to the cooler trailing edge, without significant ejection of material back out toward the beam. For welding speeds in the range 10-45mm/min, the depth of penetration was found to be linearly related to welding speed. As expected, the penetration was least for the highest welding speed.

Lock et al[82] and Baardsen et al[154] report that penetration increases almost linearly with incident laser power which is evident from Figs. 2.3 and 2.4.

The correlation of penetration depth with laser welding speed is discussed by Duley[16] (P-241) and Lock et al[82] in comparison with that of electron beam welding. It is evident from Fig. 2.5 that the penetration in the laser weld is consistently less than that possible with an electron beam, but the difference between the two penetration depths diminishes as the welding speed increases. But Duley[16] (P241) found that this was somewhat surprising, since as pointed out by Baarsden et al[154] the time to form a void or "keyhole" may become comparable to the illumination time for a particular area on the surface of the workpiece as the welding speed increases. When this occurs, the average power dissipated in the sheet is expected to drop because the keyhole is no longer a completely effective trap for the incident laser radiation. For an electron beam, the absorptivity of the material is independent of the shape and extent of the keyhole and hence the total power dissipated in the workpiece will be less strongly dependent on the welding speed. However, Crafer[160] reports that keyhole

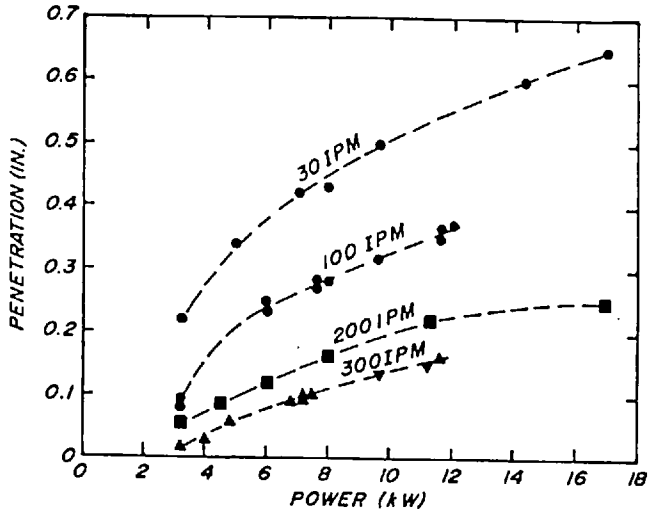

FIG. 2.3 Relation between penetration depth vs. laser power for welding with the AVCO CO_2 laser, (Ref. 82)

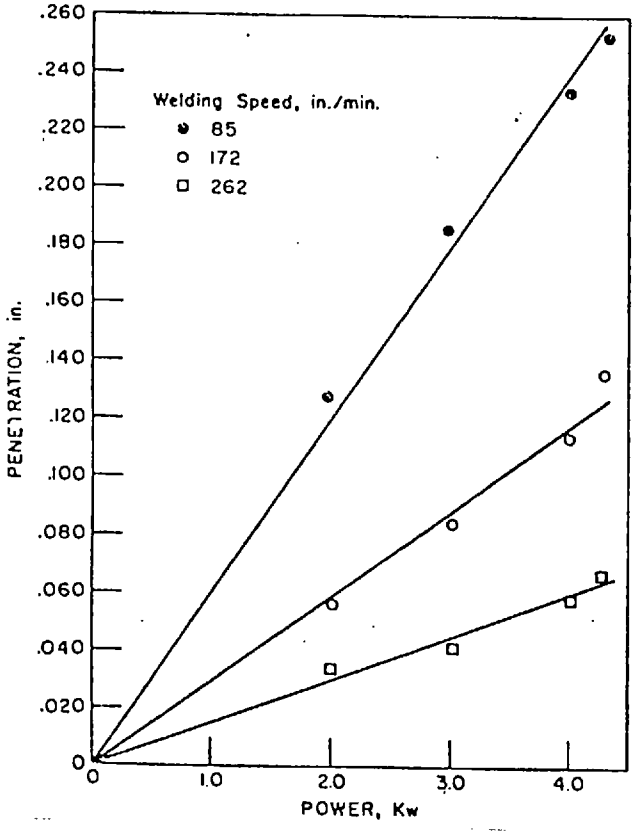

FIG. 2.4 Relation between penetration depth vs. laser power for welding with the United Technologies CO_2 laser (Ref. 154)

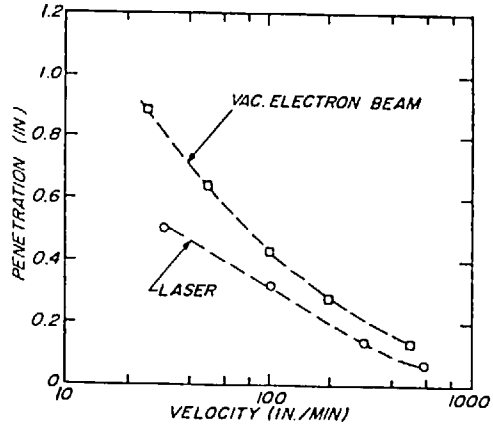

FIG. 2.5 Weld penetration vs. weld speed for type 304 stainless steel welded with a 10kW-CO_2 laser.

penetration threshold for laser or electron beam of radius 0.1mm incident on steel surface of thermal diffusivity ≈ 10mm^2/sec. is achieved in 1 milli sec which could be regarded as instantaneous. Again, for very low welding speeds, the penetration depth of laser welds becomes significantly less than that attainable with the electron beam. According to Lock et al[152-3] this has been attributed to the formation of a plasma cloud, which attenuates the incident beam, specially 10.6 μm.

Banas[157] and Lock et al[152-3] report that good penetration, efficient use of incident laser power (i.e. to overcome beam attentuation by plasma) necessitates the incorporation of "gas jet assit". Lock et al[152-3] reports that best results are obtained for a gas jet of helium or argon directed through the laser beam parallel to the workpiece surface. This produces a combination of good penetration and weld smoothness. Directing the gas jet toward the surface yields greater penetration but caution is needed to achieve good weld bead geometry. Banas[157] stresses that shield gas composition for laser welding must be selected on the basis of gas breakdown characteristics as well as on weld zone metallurgical requirements.

Lock and Hella[82] have investigated the effect of focussing on the depth of penetration for constant power and welding speed. They report that for focussing to a point within the workpiece, the weld is cone-shaped and the penetration is less than that obtained for focussing closer to the target surface. The highest penetration and best uniformity of the weld is obtained for focussing to a point just inside the sheet surface. As expected, focussing with a longer focal length optics is less critical than that for shorter focal length optics.

Swift-Hook and Gick[9] report that melting efficiency (i.e. ratio of the power transferred in the form of heat to the workpiece, to produce weld ingot to the total incident laser power) for laser welding can approach a theoretical maximum of 48%. But they did not consider latent heat of fusion for their calculation. However, a

summary of currently available data on deep penetration welding with CO_2 lasers is given in Table II, Appendix 2.

2.5 Previous Work on Titanium Alloy Welding

The usefulness of titanium and titanium alloys application depends to a large extent upon the successful monitoring of their welding. As summarised by Gurevitch et al[161], this is because of the fact that welding titanium involves a number of serious difficulties, caused by specific physical and chemical properties of this metal. The important difficulties encountered are as follows:

1) The high activity of Titanium and Titanium based alloys towards gases, such as oxygen, nitrogen, and hydrogen.

2) The introduced impurities - gases
   a) embrittle weld metal
   b) raise its tendency to cold cracking in welded joints
   c) cause porosity in cast metal and
   d) greatly influence the character of phase and structural transformations occurring under an effect of thermal cycle of welding.

3) Due to the great chemical activity of titanium, serious difficulties arise due to a considerable grain growth tendency when heating over α-β transformation temperature in the process of welding.

4) Grain growth problem during welding is aggravated by low thermal conductivity & volumetric heat capacity of this material.

5) Grain growth in the areas of heat-affected zone (HAZ) adjacent to fusion line, involves a decrease of
   a) ductility
   b) rupture strength and other characteristics of welded zone as a whole.

In view of the foregoing Gurevitch et al[161] stresses the following points when selecting a method for welding titanium and its alloys.

1) The liquid metal pool, cooling weld ingot and HAZ should be carefully protected from the atomsphere.

2) Titanium welding should be performed with as little heat as possible.

2.5.1 Different welding techniques used

There is a range of joining processes for titanium alloys that are established. But, the continuing need for ever-lighter aerospace structural assemblies has encouraged the introduction of more sophisticated joining techniques in high strength titanium alloys.

Some of the joining technqiues either already established or still under investigation are as follows:

1) Electron beam welding
2) Plasma arc welding
3) Gas Tungsten arc welding
4) Laser welding
5) Resistance welding
6) Diffusion bonding

2.5.2 Relative achievements

Any comparison between different welding processes is always somewhat artifical because each welding process has its own optimum range of metal thickness, power dissipations, joining rate etc. A meaningful approach to compare between the welding processes is reported by Crafer[160].

However, Miller[162], Wedge[163] and Banas[164] report the comparison between different joining techniques based on titanium

alloy (6Al-4V) studies.

Banas[164] after direct comparison of laser beam, electron beam and arc welding of Ti-6Al-4V alloy summarises his findings which are noted below.

1) Radiographically sound welds were formed in Ti-6Al-4V alloy by electron beam, laser beam and arc welding processes.

2) The tensile properties of laser, electron beam and arc welds are subjected to a post-weld stress relief of two hours at 538^{o}C exceeded base material levels in all but one specimen the latter, exhibited an ultimate tensile strength essentially equal to that of the base material.

3) The fracture toughness of all welds formed was lower than that of the base material. Plasma arc welds exhibited a toughness reduction of approximately 10% over that of the base material while the reduction for beam welds was of the order of 40%. But fracture toughness for beam welds could be improved by using higher stress-relieving temperature.

4) The weld energy per unit length for laser and electron beam welds was substantially lower than for arc welds. The lower specific energy input led to more rapid cooling in beam welds and therefore to a harder and finer-grained weld structure.

5) General overall correlation was obtained among results of metallographic, energy input, hardness and mechanical test observations. An apparent anomaly relative to hardness and specific energy comparisons in electron beam and laser welds was attributed to the influence of convective cooling on laser welds.

Wedge[163] reports successful resistance flash butt welding of Ti-6Al-4V. The weld shows consistant mechanical properties across the joint face. Though resistance welding is the only joining technique for titanium where shielding could be avoided but it is implicit that care must be taken with surface cleaning prior to welding. But to minimise the possibility of trapped air weld surface preparation needed is rather demanding. Besides there is no satisfactory nondestructive testing methods to test the quality of weld. And the basic nature of welding restricts its applications.

It has been reported by Wedge[163] that efforts have been made to exploit the significant advantage offered by diffusion bonding but at present all are proved to be economically disappointing. This is essentially due to the degree of precision required at the joint faces.

However, it was evident from previous discussion (Section 2.4, Ref. 8, 151-157) that laser beam welding is characteristically similar to electron beam welding. But as pointed out by Fielding[165] the following problems encountered during EBW gives laser welding an edge over EBW.

1) Lower speed for relatively thin sheets.

2) Porosity. Adler et al[166] also reports massive void formation due to hydrogen entrapment in Ti-6Al-4V.

3) Unsatisfactory surface contour, i.e. undercut in weld bead geometry. This leads to lower fatigue value due to stress concentration at undercut.

4) Requirement of vacuum chamber and alignment problem for job handling inside a vacuum chamber.

At higher thickness penetration for EBW is better than that for laser welding.

Problem of grain growth during gas tungsten arc welding (GTAW) of Titanium alloy is reported by Simpson[167].

The effect of micro-structure obtained during welding processes on mechanical properties is discussed in section 7.2.4.

2.6 Previous Work on Tinplate Joining

Tin plates (Mild steel - coated with tin or chromium oxide etc.) is mostly used for making various types of cans and containers. Tin cans have been traditionally made by the process of lock, seam and soldering (L.S.S.) and this is still today the joining technique by which most cans are made. But use of solder invites health hazards.

As the present study of laser welding of tin plate is largely aimed at the development of the welding technique for can making. Therefore, discussion on previous work on tinplate joining is restricted to the techniques used in can making.

2.6.1 Different joining techniques used

There are several techniques of can making still under trial and some of them are already in the production line in limited scale. A list of different processes of can making with relative advantages and disadvantages are furnished in Table III, Appendix 2, some of the processes do not need joining (e.g. Draw Wall Ironing Method). However, processes using joining techniques are as follows:

1) Lock seam solder
2) Resistance welding
3) Soudronic

2.6.2 Relative achievements

The lock seam solder process has the advantage of high speed (10m/min to 30m/min depending on the type of can) and reliability derived from years of experience. As mentioned before it is still the primary process for can making.

It has, however, three major weaknesses in that it uses tin/lead solders to make the seal.

1) Solders are costly.
2) They are potential health hazards.

A 1972 survey[168] revealed that the average lead content of canned beef (taken over 17 samples) was 1.2 mg/kg. The samples varied from 0.16 mg/kg to 5.5 mg/kg lead. While the FAO/WHO Committee[169] on food additives established a provisional tolerance weekly intake of 3 mg of lead per adult person, with a lower level for children.

3) Tin/lead solder prevents the possibility of recycling the cans by furnace melting since a brittle Sn/Fe intermetallic forms.Without the tin of solder trapped at the joint the tin of thin coating (0.007 - 0.076mm)[170] could be removed and recovered by fuming and a scrap product acceptable for many applications could be produced.

As a consequence of these problems there is an interest in producing a method of making cans avoiding the need to solder. Welding being natural alterative, at one stage, resistance welding was investigated by Williams[170]. But he found that electrode life is rather adversely affected in the process. Tin coated steels need higher electrode currents as well[170]. Brittle fracture is also not unfamiliar[170]. But relativily new processes using pulsed resistance welding named after its inventors "Soudronic" has been found quite feasible. It is already being used in a production line to make aerosol cans. A detailed investigation of this process is published by Williams, Thomas and Wood[10-11]. This process also produces can at a welding speed of 15m/min to 40m/min. But at higher speed limit achieving a continuous nugget is not easy[10-11] due to electrical reasonance in the can. However, acceptable weld quality suggested by Williams et al[10-11] are described as large weld nuggets separated by an acicular ferrite and coalesced carbide region but free of interfacial line or soldered joint.

The electrode problem is partially offset by using an elliptical copper wire in between the electrode and the workpiece. But Williams et al[10] reports that very few welds are free of porosity in this process. Their estimate of porosity or cavities is at least one per each nugget. They[11] also report that at higher welding speeds (30m/min) hardness of welding zone falls within a range of 350-370 HV which is 200-250 HV over the initial hardness. This can, however, be subsequently heat treated. However, to achieve an even better process laser welding possibility is investigated under present study.

CHAPTER 3

THEORETICAL ANALYSIS

3.1 Introduction

In the penetration welding of metals the important data from the metallurgical point of view are summarised by Borland and Jordan[171] which are as follows:

(i) The thermal cycle at each point in the weld zone and heat affected zone since this determines the type of extent of any phase change.

(ii) The peak temperature distribution since this can define the extent of the heat affected zone.

(iii) The cooling rate through certain cooling ranges because this indicates the likelihood of the formation for metastable products such as martensite in titanium or steel.

Important data, from the process point of view, in welding metals with a CW CO_2 laser would include some of the following physical aspects, reviewed by Steen[17], and these also should be considered.

(i) The problem of finding beam spot size

(ii) The significance of surface reflectivity and condition initiation power densities

(iii) Mode structure of laser beam

(iv) The obscure part played by the vaporisation plume. Ready[172] reports that it behaves as a black body while Sepole[173] has measured the absorption of plumes from low power interactions and found the plumes to be almost totally transparent.

(v) The problems in modelling the heat transfer due to
(a) the convective movement of a molten puddle, and the addition of latent heat effects due to both melting and vaporisation.
(b) Hydrodynamic effects which become significant when vaporisation occurs at the surface, particularly when sonic shock waves occur due to the emission of hot vapour as in the deflagration model of Pert[174] and Bobin[175]. These phenomena can be expected with energy intensities 10^8 W/cm^2[17].

(vi) Thermal stress and shock stress. Shock stress due to sudden heating generates a shock wave capable of reflection within the substrate resulting in the chipping of the surface, requires power intensities $\simeq$ 2000 W/cm^2 as a 10 ns pulse[17]. These effects are not expected in the present study which used continuous power.

(vii) Interaction of photon avalanches with matter (the inverse Bremsstrahlung effect - ejection of electrons by collision with photons) or the possibility of increasing material density by shock and thermal effects to stimulate atomic fusion. This requires power intensities greater than 10^{13} W/cm^2[14] which is well beyond the power range of the present study.

In this chapter a mathematical model for laser welding is drawn up with a view to calculating the necessary metallurgical data identified earlier. Assumptions are made on the important physical aspects of laser material interaction where necessary.

3.2 Physical Definition of the Process to be Modelled

In order to develop the mathematical model the process is physically defined as follows:-

An axi-symmetric laser beam having a defined power distribution strikes the surface of an opaque substrate having finite width and

thickness and infinite length moving in the positive x-direction (along the length) with a uniform velocity. Some of the incident radiation is reflected, the rest is absorved but the reflectivity is considered to be zero if the temperature exceeds the boiling point by $200^{o}K$ since it is assumed that a keyhole is produced by vaporisation which acts as a blackbody. Some of the absorbed energy is lost by radiation and convection from the surface while the rest is conducted into the substrate. The convective heat transfer is enhanced due to a concentric gas jet used for shielding .

The system is assumed to be in a quasi-steady state condition after the keyhole initiation period which for most practical purposes may be regarded as instantaneous[160] and will only occur at the beginning of a welding run.

3.3 Previous Solutions

A large number of investigations have been made with the object of obtaining data for heat transfer during welding processes as discussed in Section 3.1. It has been found that all these thermal factors are strongly influenced by the welding process, the welding variables, the thermal properties of the material and the geometry of the weldment[171]. Presumably, as a consequence attention has been concentrated on theoretical techniques for calculating the thermal history associated with welding rather than direct experimental measurement. There is a range of numerical and analytical methods which have been developed and are discussed in the following sections.

3.3.1 Analytical solutions

Different methods for solving the heat conduction equations for various conditions are elegantly and methodically described by Carslaw and Jaeger[177].

Myers, Uyehara and Borman[176] have reviewed a large number of investigations on the theoretical techniques for calculating the thermal history associated with welding. The analytical methods discussed here are summarised in Table 3.1.

Type of Mathematical Model	Particular Process Aimed	Eqn. No.	Reference
1) Moving point heat source for three dimensional heat flow	General welding processes	3.1	Rosenthal Ref: 171, 178, 179 Christensen Ref: 184
2) Moving line heat source for two dimensional heat flow	General Welding Processes	3.2	" "
3) Moving line source for two dimensional heat flow	Laser and Electron beam	3.5-3.16	Swifthook and Gick Ref: 9
4) Uniform and finite heat source for one dimensional heat flow	CO_2 laser welding	3.17-3.18	Alwang et al Ref: 183
5) Uniform band or rectangular heat source for steady state two dimensional heat flow	EBW and CW laser welding	--	Arata et al Ref: 150
6) Uniform circular heat source of a semi-infinite slab (i.e. for two dimensional heat flow calculating transient surface isotherms	Pulsed Laser	3.19	Guenot and Racinet Ref: 185
7) Stationary gaussian or uniform circular heat source for transient temperature distribution in thin film	Electron Beam Heating	3.20	Tung Po Lin Ref: 188

TABLE 3.1

Among numerous analytical methods reported, the most generally useful appears to be that involving the equations developed by Rosenthal[178.179] and Rykalin[180]. Although their equations do not give the most accurate results, according to Borland and Jordan[171], they do show clearly the type and magnitude of the thermal changes occurring in welding and the way they are affected by material and process variables.

Two specific welding situations are considered by Rosenthal[178-179]

(i) A point source of heat moving over the surface of an infinitely wide thick plate where the heat flow can be regarded as three dimensional.

(ii) A line source of heat moving through an infinitely wide thin plate where the heat flow may be regarded as two dimensional.

These two idealised situations correspond to the final passes in a multirun weld in thick plate and a single run full penetration in thin plate respectively. In the first instance Rosenthal [178-179] derived equations for the temperature distribution around the moving sources.

For the three-dimensional case:-

$$(T - T_o) = \frac{Q}{2\pi K} \cdot e^{-VX/2\alpha} \cdot \frac{e^{-VR/2\alpha}}{R} \qquad (3.1)$$

For the two-dimensional case:-

$$(T - T_o) = \frac{Q}{2\pi Kg} \cdot e^{-VX/2\alpha} \cdot K_o\left(\frac{VR}{2\alpha}\right) \qquad (3.2)$$

where:-

T = the temperature at a point (X, R) in ^{o}K
T_o = the original plate temperature in ^{o}K
Q = heat input per unit time in watts
g = plate thickness in metres
K = thermal conductivity in $Wm^{-1}\ K^{-1}$
K_o = Bessel function of second kind and zero order
α = thermal diffusivity in $m^2\ s^{-1}$
ρ = density in kg m^{-3}
C = specific heat in $J\ kg^{-1}\ K^{-1}$
V = welding speed in ms^{-1}
t = time in seconds
R = distance to heat source in metres
X = distance along weld centre line in metres
Y = distance from weld centre line in metres

From these Rosenthal then obtained expressions for the centre line cooling rate since this could be regarded as representative of the weld zone

For the three-dimensional case

$$\frac{dT}{dt} = 2\pi K \left(\frac{V}{Q}\right)(T - T_o)^2 \qquad (3.3)$$

For the two-dimensional case

$$\frac{dT}{dt} = 2\pi K\rho C \left(\frac{Vg}{Q}\right)^2 (T - T_o)^3 \qquad (3.4)$$

Subsequently, Adams et al[181,182] produced peak temperature equations for the same two situations and also provided means for generalising all the equations to a much wider range of practical conditions.

Christensen, Davies and Gjermundsen[184] used Rosenthal equation for point sources moving across the surface of a semi-infinite body (similar to Eqn. 3.1) to construct a temperature chart for the particular set of materials properties, heat input, and welding speed under consideration. They generalised the Rosenthal equation (Eqn. 3.1) by using dimensionless parameters. Then they produced a series of dimensionless temperature contours against different dimensionless welding parameters. This generalised chart in turn predicts temperature distribution for various welding conditions but it has the limitations due to the assumptions in the point source equation. They have also reported a method of calculating weldpool volume.

The Rosenthal equation for the three-dimensional case (Eqn. 3.1) when applied for present study of laser welding, produced unsatisfactory temperature profiles. This indicates that for laser welding heat source can not be assumed as point source. Temperature profile obtained for using Eqn. 3.1 is discussed in section 3.11.

Swifthook and Gick[9] also report that for deep penetration welds, a point source theoretical solution, is not appropriate. According to them[9] the beam (electron or laser) must produce some sort of "keyhole" through the material into which it deposits its energy. The molten pool around this keyhole will be in the form of a cylinder as shown in Fig. 3.1. The mathematical description of heat flow in the material will be two-dimensional to a good approximation and the appropriate mathematical solution is that for a line source. Swifthook and Gick[9] solved the moving line source model of Carslaw and Jaeger[177] for steady state heat diffusion ignoring the transients at the beginning and end of the process. They deduced the following equation which would give the isotherms.

$$\theta = \frac{q}{2\pi} [\exp(Ur \cos\phi)] \, K_0(Ur) \qquad (3.5)$$

where $q = P/a$, $\theta = KT$, $x = r\cos\phi$, $U = v/2\alpha$

a = penetration depth

P = power

v = velocity in positive x direction

K_0 = Bessel function of 2nd kind and zero order

K = thermal conductivity

α = thermal diffusivity

Now, writing the power per unit depth the above equation becomes

$$M = [2\pi/K_o(Ur)] \exp(-Ur \cos\phi) \qquad (3.6)$$

where $M = P/a\theta$

Swifthook and Gick[9] have shown that at the point where the melt has its greatest width the following condition is satisfied.

$$\frac{\delta M/\delta\phi}{\delta M/\delta r} = \frac{\delta y/\delta\phi}{\delta y/\delta r} \qquad (3.7)$$

where y = half width of the molten pool
$= r \sin\phi$

Then using Eqn. 3.6 in Eqn. 3.7 they have deduced the following relationships

$$\cos\phi = -K_o(Ur)/K_o'(Ur) \qquad (3.8)$$

The normalized maximum melt width

$$Y_{max} = vW/\alpha = 2UW = 4Ur\,[\,1 - K_o^2(Ur)/K_o'^2(Ur)]^{\frac{1}{2}} \qquad (3.9)$$

where W = total melt width = $2y$

Substituting $\cos\phi$ in Eq. 3.6 one gets

$$M = \frac{2\pi}{K_o(Ur)} \exp\left[\frac{Ur\ K_o(Ur)}{K_o'(Ur)}\right] \qquad (3.10)$$

The relation between absorbed power P and the melt width W can be found by eliminating Ur in Eqns. 3.9 and 3.10. Swifthook and Gick[9] discuss two limiting cases when this can be done analytically.

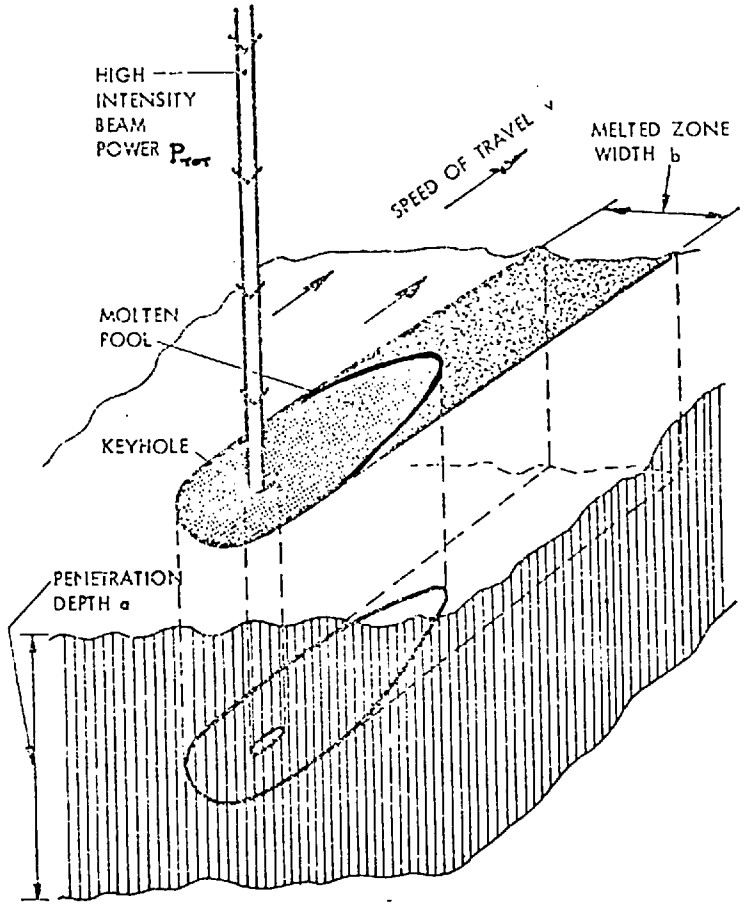

FIG. 3.1 Penetration weld geometry (Ref. 9)

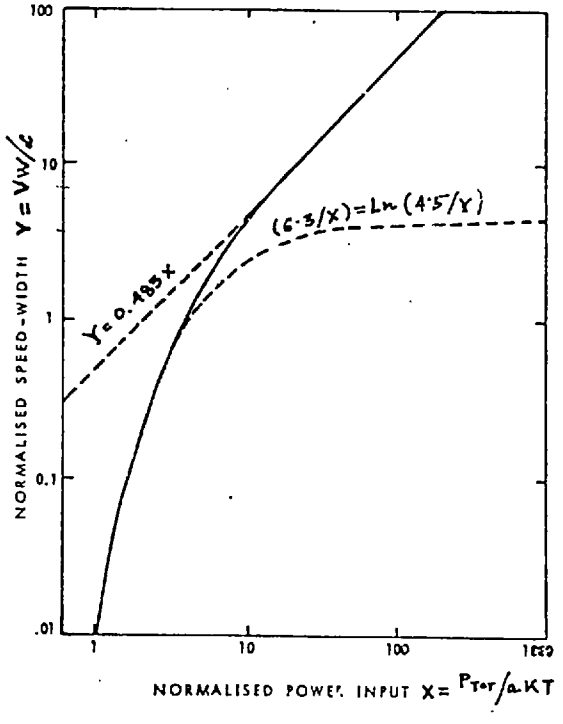

FIG. 3.2 Theoretical curve for penetration welds (Ref. 9)

In the high speed limit (Ur large), the Bessel functions can be expanded to give

$$M \simeq 8.26(Ur)^{\frac{1}{2}} \tag{3.11}$$

and

$$Y_{max} \simeq 4(Ur)^{\frac{1}{2}} \tag{3.12}$$

so that

$$Y_{max} \simeq 0.484M \quad \text{(Ur large)} \tag{3.13}$$

When the speed is low (Ur small)

$$M \simeq \frac{2\pi}{\ln(2e^{-\gamma}/Ur)} \tag{3.14}$$

and

$$Y_{max} \simeq 4Ur \tag{3.15}$$

so that

$$Y_{max} \simeq \exp(1.50 - 2\pi/M) \quad \text{(Ur small)} \tag{3.16}$$

where $\gamma = 0.577$ Euler's constant.

Figure 3.2 shows a plot of Y_{max} versus M constructed from these two limiting solutions with an interpolation in the intervening region where neither solution in strictly valid[9].

Alwang et al[183] reports a one-dimensional solution for heat transfer for CW CO_2 laser welding. In such a system they had to assume that the incident power density in the beam was uniform and thus independent of position and the temperature distribution and used Carslaw and Jaeger's[177] one-dimensional equation of linear heat flow for heat generation within the sample which is as follows.

$$\frac{\partial^2 T}{\partial z^2} - \frac{1}{\alpha}\frac{\delta T}{\delta t} = \frac{\varepsilon_a F(t)\, e^{\varepsilon_a z}}{K} \qquad (3.17)$$

T = Temperature
z = Depth into material
= Thermal diffusivity
t = Time
F(t) = Incident beam power density
ε_a = Optical absorption coefficient

According to Alwang et al[183] a solution for semi-infinite slab approximation of above equation assuming a constant flux i.e. $F(t)=F_o$ is as follows:

$$T(x,t) = \frac{2F_o\varepsilon_a(\alpha t)^{\frac{1}{2}}}{K}\ \text{ierfc}\left(\frac{z}{2(\alpha t)^{\frac{1}{2}}}\right) - (F_o/\varepsilon_a.K)\, e^{\varepsilon_o.z}$$

$$+ (F_o/2.\varepsilon_a.K)\exp(\varepsilon_a{}^2\alpha\, t - \varepsilon_a.z)\ \text{erfc}\left[\varepsilon_a(\alpha t)^{\frac{1}{2}}\right.$$

$$\left. - z/2(\alpha t)^{\frac{1}{2}}\right] + (F_o/2.\varepsilon_o.K)\exp(\varepsilon_a{}^2.\alpha.t + \varepsilon_a.z)$$

$$x\ \text{erfc}(\varepsilon_a.(\alpha t)^{\frac{1}{2}} + z/2(\alpha t)^{\frac{1}{2}} \qquad \ldots\ldots(3.18)$$

This equation is approximately true when the beam diameter is large compared to the thickness of the workpiece.

Arata and Miyamoto[150] report that a model using line heat source provides an infinite temperature at the location of the source and leads to a noticeable error in temperature estimation at points distant from the beam axis compared with the beam diameter. In a line source model the size of the beam spot can not be taken into account in calculating the temperature rise in spite of the fact that the weld depth is considerably affected by the beam diameter.

Therefore, Arata et al[150] introduced a band or rectangular plane heat source of uniform intensity which moves in the direction perpendicular to the source plane, and whose width corresponds to the hole diameter. They described the temperature and bead penetration depth by a set of non-dimensional variables in order to establish a universal relationship independent of parameters such as physical constants of material, welding speed, beam diameter, and beam power.

Arata et al[150] simplified the problem assuming that heat distributes two-dimensionally at steady state and neglected the variation of physical constants of material, radiation heat loss and convection in the molten pool.

Guenot and Racinet[185] proposed a new mathematical formulation for pulsed laser welding by means of which the transient isothermal surfaces can be calculated for any sheet material as a function of heating conditions at the surface. They assumed a circular heat source of uniform intensity on a semi-infinite solid (practically a thick plate) and used the theory of instantaneous heat sources[186,187] to obtain a convenient formulation for temperature distribution. It reads as follows

$$r \geq r_b, \bar{\Theta} = \Theta_i/\Theta_M = t^* \int_0^{\phi_0} \{\psi[\bar{R}_1/t^*] - \psi[\bar{R}_2/t^*]\}d\phi$$

$$r < r_b, \bar{\Theta} = \Theta_i/\Theta_M = t^* \int_0^{\pi} \{\psi[\bar{z}/t^*] - \psi[\bar{R}_2/t^*]\}d\phi \qquad \ldots.(3.19)$$

where $\bar{\Theta}$, t^*, R_i ($i = 1$ or 2) are dimensionless parameters

Θ_i = instantaneous temperature rise of the material

z = depth

r = radial distance

$\bar{\Theta} = \Theta_i/\Theta_M$ setting $\Theta_M = \dfrac{q_o \cdot r_b}{K}$

q_o = uniform intensity of circular heat source

$t^* = \sqrt{t/t_o}$ setting $t_o = r_b^2/4\alpha$

= dimensionless time

$\bar{R}_i = R_i/r_b$ setting $R_i^2 = l_i^2 + z^2$, (i = 1 or 2)

l_1, l_2 = functions of the polar angle ϕ defined as the roots of the quadratic equation.

$l^2 - 2\ell \cos\phi + r^2 - r_b^2 = 0$

ϕ_o = limiting value for the real roots,

ψ = integrated complementary error function (known as "iefc" in Carlsaw and Jaeger[177])

Their results are presented diagrammatically using dimensionless parameters such as dimensionless temperature and time, thus providing the best working conditions for any material of any thickness.

Tung-Po Lin[188] calculated the transient temperature rise of heating thin films with a stationary gaussian or uniform circular source when radiation loss from the surface is not neglected but thermal conductivity is assumed to be constant i.e. independent of temperature. For that purpose they solved the fundamental differential equation for heat conduction suggested by Carslaw and Jaeger[177]

$$\rho C(\delta T/\delta t) = K \nabla^2 T + Q - w \qquad (3.20)$$

where,

w = heat loss (sink) per unit time per unit volume

Q = heat supply (source) per unit time per unit volume at a particular point and time.

All the studies discussed above ignored latent heat associated with phase change, however, Andrews and Atthey[122] calculated penetration speeds for various power ranges for the steady state condition and variable thermal conductivity.

Andrew and Atthey[189] also studied the hydrodynamic limit to penetration of a material by a high power beam. For this purpose they considered a stationary beam and a semi-infinite molten pool. They discussed the shape and depth of the molten pool and concluded that surface tension reduces the depth of penetration. But for simplicity they assumed that all incident power is used to evaporate and totally neglected the heat conduction. Therefore, their work is not particularly relevant to the present study.

3.3.2 Numerical solutions

Numerical calculations remove many of the limitations that apply to the analytical method. Such as:

(1) The heat source does not have to be concentrated in a point line or plane

(2) The geometry of the workpiece may be taken into account

(3) Physical properties of the substrate may be considered temperature dependent without much difficulty.

(4) Truncation error from series expansion of different functions associated with analytical solutions is absent

(5) Difficulty of application of analytical solution of heat flow equation to real boundary conditions is eliminated.

But few numerical models for heat flow in welding have been developed partly due to the large computer time and storage required for the solution.

However, Westby[190], Arata & Inoue[121], and Paley & Hibbert[191] have reported numerical models for temperature distribution in welding processes. Steen[17,192] has presented a numerical solution of the thermal history of a stationary spot heated by a laser.

Arata and Inoue[121] report that a point or line heat source approximation frequently gives unsatisfactory results for the temperature surrounding the heat source. Therefore, they have presented a medium case between a point heat source approximation and line heat source approximation by introducing a dimensionless quantity "β" and they have calculated the temperature distribution numerically. In a nutshell they have numerically calculated the temperature distribution in the vicinity of the heat source for a moving line heat source of non-uniform input energy. They have suggested that the actual heat input situation in a welding process is as follows:

$$Q^*(Z^*) = (1 - Z^*)^{\beta} \qquad (3.21)$$

where β is the index of input energy distribution

$Z^* = Z/g$ = dimensionless quantity

q = plate thickness

$Q^*(Z^*)$ = dimensionless energy distribution function

Then the problem becomes the determination of "β" for a given value of V*; where V* = dimensionless velocity

$$V^* = \frac{v\ g}{2\alpha}$$

Then they integrated the above input energy distribution for a line source using Simpson's Rule.

Arata and Inoue[121] have presented their results in the term of dimensionless isothermal contours.

Rykalin[193] provided a numerical solution for the one and two-dimensional heat flow cases and Westby[190] tackled the problem using a large modern computer and developed a program for both constant and variable thermal properties.

Paley and Hibbert[197] based their computer program on Westby's[190] work and they have added several capabilities to the program. These include (a) the capability of analyzing non-rectangular cross sections such as single and double V and U grooves and (b) non-uniform mesh of finite difference scheme which allows a better approximation of the nonrectangular cross-section as well as permitting the placement of a finer grid size in regions of higher thermal gradients.

Paley and Hibbert's[191] program also permits the option of resuming the computation from the point left off in a previous run as well as the capability of intermediate print out in order to check the convergence of the results.

Three dimensional gaussian heat source has been used by Paley and Hibbert[191] and they have used the following assumptions to simplify their mathematical model.

1) The size of the workpiece is infinitely long.
2) Quasi-steady state conditions are required
3) Heat exchange with the surroundings are neglected
4) The path of the electrodes is on an axis of symmetry and is parallel to the length of the plate.

Paley and Hibbert[191] have presented their results of computations in graphical displays of isothermal contours at a given section perpendicular to one of the three co-ordinates. They report that there is a reasonable correlation when compared with macro-structure of the weld. They have also plotted different temperature cycles.

Steen[17,192] reports a numerical solution of the thermal history of a spot heated by a stationary gaussian laser beam source. He obtained the solution by finite difference method and incorporated both convective and radiant surface heat losses. The results were plotted in the form of dimensionless graphs. His work has particular relevance to the present study because his method of heat loss calculation is followed here.

By necessity a full simulation of a welding run would require one or more quasi-steady state boundaries separating two phase e.g. solid/liquid or liquid vapour.

In the moving source problem considered here, this would result in a temperature gradient discontinuity at the boundary. It would thus be necessary, for accuracy, to place the grid points on this boundary, if possible.

To find where the boundary lies would have to be done iteratively.

The inclusion of two phase boundaries would further introduce a latent heat term. However, the latent heat of fusion is only a tenth of that for evaporation[122]. Thus latent heat is not the predominant effect at melting (though it is certainly not negligible) The latent heat of evaporation, however, should not be ignored. Evaporation occurs at keyhole. Therefore, it could be allowed as plasma reflection or some such since vapour boundary is a very fine cylinder.

However, in view of the foregoing, moving boundary problem is not considered in the present study but it can only be tackled by numerical methods. For moving boundary conditions heat flow equations must be solved for both molten and solid regions. The conservation of the energy at the moving boundary gives the following condition.

$$K_2 \delta T_2/\delta x - K_1 \delta T_1/\delta x = L_f . \rho . dx(t)/dt \qquad (3.22)$$

where $x(t)$ = position of the boundary at time (t)

L_f = latent heat of fusion per unit mass

1&2 = refer to liquid and solid region respectively where K is thermal conductivity and T is temperature.

At the boundary, the temperature equals the melting temperature and at the surface the boundary condition is:-

$$-K\delta T/\delta x = F(t); \quad x=0 \qquad (3.23)$$

where F(t) = the absorbed laser flux.

Crank[194] solved this general problem by the finite difference method and Cohen[195] solved it by analog computer technique.

3.4 Choice of Numerical Techniques

A large number of numerical techniques have been reported[196-202] to solve partial differential equations. For the present study a finite difference method using "relaxation" technique has been chosen.

Finite difference equations can be solved mainly by two techniques[198], which are:

1) Method of iteration
2) Method of relaxation

Iteration and relaxation methods are compared by Scarborough[198] Some of the important points are noted below.

1) Both methods require that the bounded region be divided into a network of squares or other similar polygons

2) Both methods require that the boundary values be written down and that rough values of the function be computed, estimated or assumed for all interior points of the network.

3) In order to start a computation, the iteration method assumes that a functional value at any mesh points satisfies the given difference equation and thereby

derives the relation which must exist between the functional value and the adjacent functional values. The process of iteration is then applied until the required relation is satisfied.

4) The method of relaxation, on the other hand, recognises at the start that an assumed functional value at any mesh point will not satisfy the given difference equation, but that there will be a "residual" at that point. The residuals are computed for all points before the relaxation process is started.

5) The method of iteration proceeds to correct all net work values by means of the following formula (3.24, in case of Laplace's equation), using the latest computed values available.

$$u(x,y) = \frac{1}{4}\,[u(x + h,y) + u(x,y + h) + u(x - h,y) + u(x,y-h)] \qquad \ldots\ldots(3.24)$$

where h = the increment.

The process is carried out in a systematic and definite order, point by point until the end of the line.

6) The method of relaxation requires that the residuals at every interior netpoint be computed by the following formula (3.25 for Laplace equation).

$$\text{Residual} = u_1 + u_2 + u_3 + u_4 - 4u_0 \qquad (3.25)$$

where u_i is the point surrounding u_0 when i = 1,2,3,4

Then these residuals are liquidated or reduced to zero (or nearly so) as quickly as possible by altering (relaxing) the netpoint values at any extent that seems advisable,

always observing that the increment of the function must be of the same sign as the residual at that point. The revised values of the function should also be recorded at the time of alteration.

7) a) The iteration process is slow, sure and frequently long.

b) The relaxation process is more rapid, less certain, and usually reasonably short. Due to the scope of "over-relaxation"[198] residuals could be liquidated quickly.

8) The arithmetic operations are easier and shorter with the method of relaxation.

9) a) The greater drawback to the method of iteration is its length.

b) The greatest drawback to the method of relaxation is its requirement of great care to avoid mistakes. The recent fast computer and its uneasing vigilance helps to overcome this drawback.

Both the methods have same type of accuracy but the speed and convenience of programming lead us to choose the relaxation technique.

3.5 Derivation of the Mathematical Model

3.5.1 Assumptions

The mathematical model has to fit the physical definition given in section 3.2.

The following assumptions are made here.

1) The laser beam remains stationary relative to earth on an axis of symmetry and the workpiece flows in the

positive x-direction (along the length) with uniform velocity. The system is diagrammatically represented in Figure 3.3.

2) The workpiece is infinite in length (i.e. in x-direction) but has finite width and thickness.

3) Quasi-steady state is assumed..

4) The power distribution in the beam is gaussian

5) The thermal conductivity, density and specific heat are constant with temperature unless otherwise mentioned.

6) Latent heat of fusion is compensated by latent heat of solidification.

7) Reflectivity is considered to be zero when the temperature exceeds boiling point.

8) There is a radiation loss from both surfaces of the workpiece.

9) There is convective heat loss due to shielding gas flow.

3.5.2 Mathematical statement of the problem

The differential equation of heat flow for moving heat source for quasi-stationary state expressed in rectangular co-ordinates (x,y,z) which are referred to a fixed origin in the solid is given by Fourier's second law and has the well known form of Laplace's[176-7] equation with an additional source term due to the convection of material.

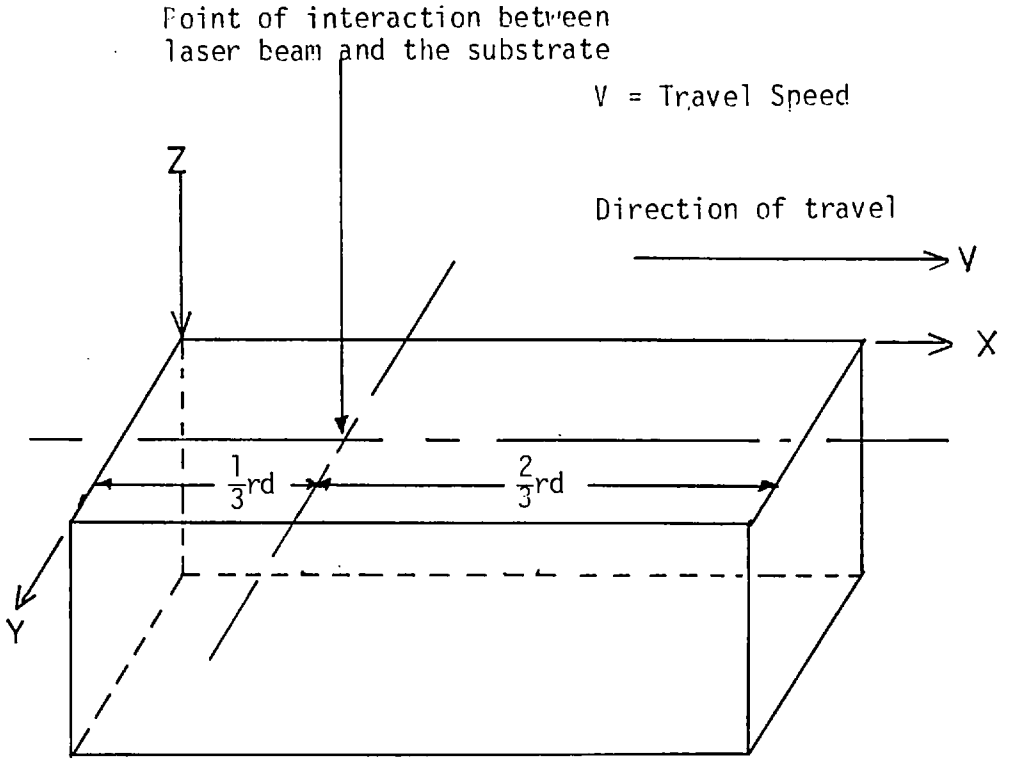

FIG. 3.3 Geometry of the workpiece with respect to the laser beam

Within the body of the substrate:

$$\frac{\delta T}{\delta t} = 0 = \frac{K}{C\rho}\left(\frac{\delta^2 T}{\delta x^2} + \frac{\delta^2 T}{\delta y^2} + \frac{\delta^2 T}{\delta z^2}\right) + u\left(\frac{\delta T}{\delta x}\right)$$

$$= \alpha\left(\frac{\delta^2 T}{\delta x^2} + \frac{\delta^2 T}{\delta y^2} + \frac{\delta^2 T}{\delta z^2}\right) + u\left(\frac{\delta T}{\delta x}\right) \qquad (3.25)$$

At the top surface

$$-K\left(\frac{\delta T}{\delta z}\right)_{x,y,1} = \frac{P_{tot} \cdot (1 - r_f)}{A} - h_{tot} \times \Delta T \qquad (3.26)$$

where $z = 1$

$h_{tot} = h_c + h_r$

At the bottom surface

$$-K\left(\frac{\delta T}{\delta z}\right)_{x,y,IZ} = -h_{tot} \cdot \Delta T \qquad (3.27)$$

where $z = IZ$

when IZ = last point on the z-axis i.e. bottom surface

At the eastern boundary

$$T_{1x+1,y,z} = TEMPA \qquad (3.28)$$

TEMPA = Ambient temperature

IX = last point in x-axis

At the western boundary

$$T_{o,y,z} = TEMPA \qquad (3.29)$$

At the Northern Boundary

$$T_{x,o,z} = TEMPA \tag{3.30}$$

At the Southern Boundary

$$T_{x,IY+1,z} = TEMPA \tag{3.31}$$

IY = last point in y-axis.

3.5.3 Calculation regimes

All the three sets of planes, (x,o,o), (o,y,o) and (o,o,z) of the calculation regimes for the workpiece were divided into matrix points which were arranged to expand exponentially as shown in Fig. 3.4.

The matrix size identified was 32 x 31 x 4. That means the x-y planes (o,o,z), had 32 and 31 grid points for x and y axis respectively. Whereas z-axis had 4 grid points.

The x-y plane was perpendicular to the incident laser beam and the centre of the beam was considered to be at (11, 16, 1) i.e. at the middle of the y-axis and $\frac{1}{3}$ of x-axis. The grid mesh of x-y plane was arranged to expand exponentially from the point (11, 16, z) in both x and y direction. Whereas, grid of x-z plane (o,y,o) expanded exponentially from the surface down-wards.

Different calculation regimes governed by different sets of equations and boundary conditions were identified with the respective planes as follows:

Region 1 - The Body

It is a rectangular parallelopiped bounded by the following planes:- (2,o,o) (31,o,o), (o,2,o), (o,30,o), (o,o,2) and (o,o,3)

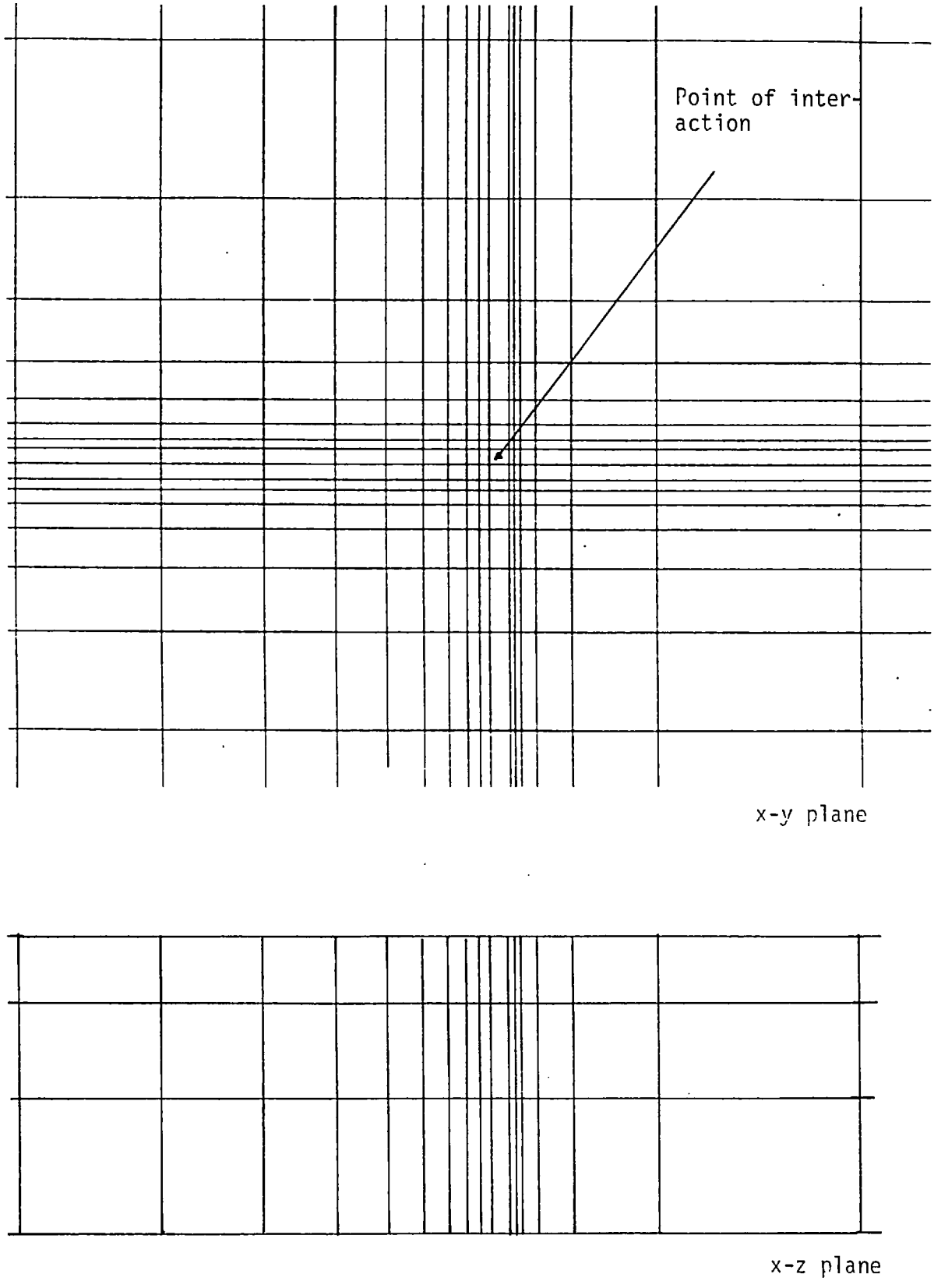

FIG. 3.4 Arrangement of grid division for mathematical model

Region 2 - The Top Surface (o,o,1) plane

Region 3 - The Bottom Surface (o,o,4) plane

Region 4 - The Eastern Boundary (32,o,o) plane

Region 5 - The Western Boundary (1,o,o) plane

Region 6 - The Northern Boundary (o,1,o) plane

Region 7 - The Southern Boundary (o,31,o) plane

3.5.4 Derivation of the Finite Difference Equations

3.5.4.1 Within the body of the substrate - Region 1

There are two basic approaches to draw up a finite difference equation describing the flow of heat within a lattice of points[17].

a) Solve the differential equation for the flow of heat across each point.

b) Solve the heat conservation equation about a finite rectangular block.

In the case of method (a) Fourier's Second Law as applied to the present problem expressed in Eqn. 3.25 has to be solved for each point. But it was reported by Steen[17] that this method was intrinsically unstable for exponentially expanding grids. Although he found it to be successful for uniform grids.

As an exponentially expanding grid has been used for the present study, the model has been based on the block conservation interpretation of method (b).

Any point 'P' inside the control volume, as shown in Fig. 3.5, was considered to be the lattic point. Then heat balance was calculated

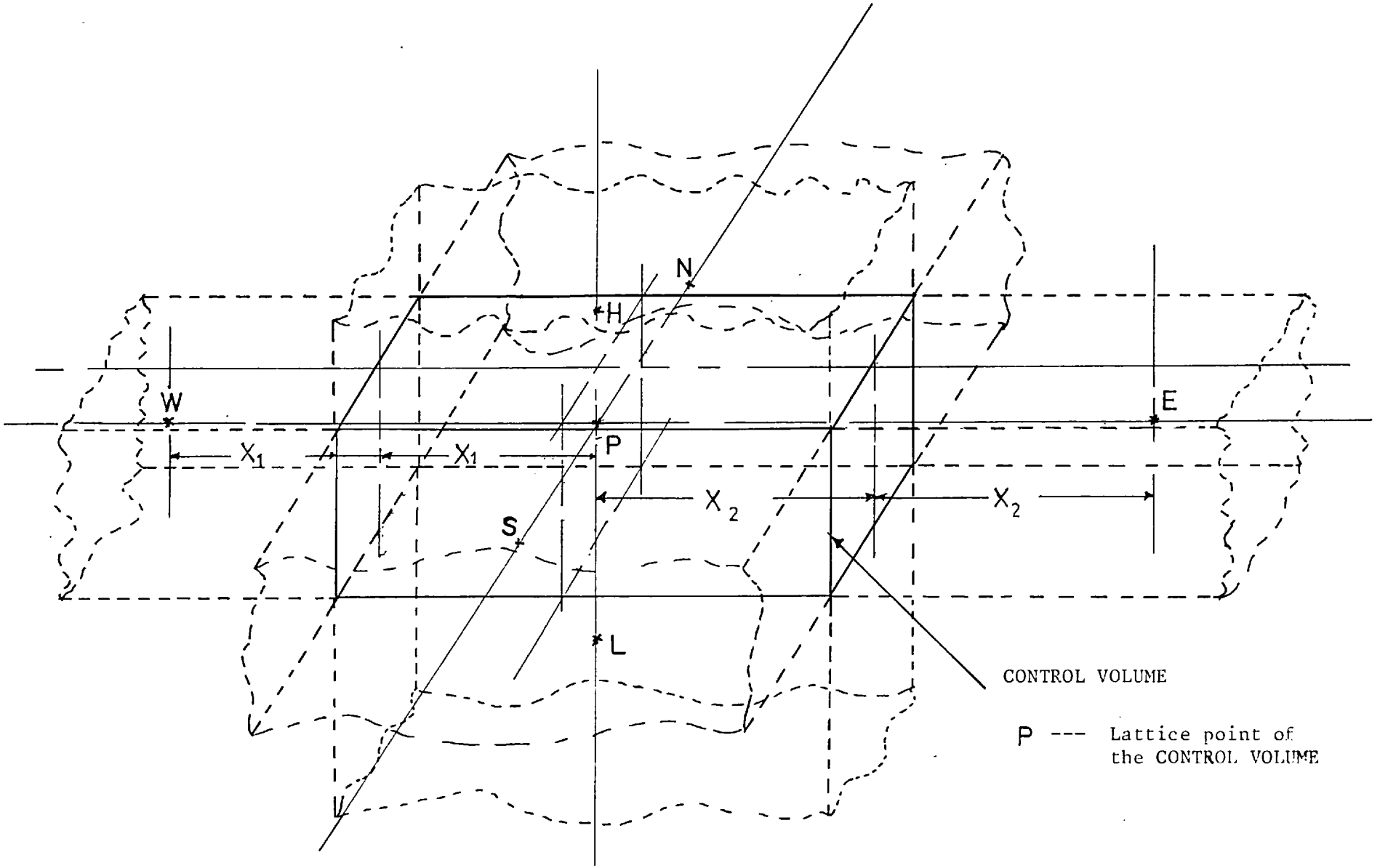

FIG. 3.5 Location of lattice points in control volumes

with respect to the six neighbouring points E, W, N,S, H, and L using Fourier's first law. The Fourier equation is as follows.

$$Q_x = - KA\frac{dT}{dx} \qquad (3.32)$$

where Q_x = heat conduction rate in x-direction
T = temperature
A = area perpendicular to the flow of heat
K = a proportionality constant known as thermal conductivity of conducting medium.
x = direction along which heat is flowing

Considering heat flow in positive x, y and z direction

Heat In

$$-K\delta z\delta y(\frac{\delta T}{\delta x})_{PW} - K\delta x \cdot \delta z(\frac{\delta T}{\delta y})_{PN} - K\delta x\delta y(\frac{\delta T}{\delta z})_{PH}$$

$$+\rho \cdot u \cdot Cp \cdot \delta y \cdot \delta z(\frac{T_W + T_P}{2})$$

i.e.
$$- K \frac{\delta z\delta y}{\delta x} (T_P - T_W) - K \frac{\delta x\delta z}{\delta y} (T_P - T_N) - K \frac{\delta x\delta y}{\delta z} (T_P - T_O)$$

$$+ \rho \cdot u \cdot C_p \cdot \delta y \cdot \delta z \, (\frac{T_W + T_P}{2})$$

Heat Out

$$-K\delta z\delta y(\frac{\delta T}{\delta x})_{EP} - K\delta x\delta z(\frac{\delta T}{\delta y})_{SP} - K\delta x\delta y(\frac{\delta T}{\delta z})_{LP}$$

$$+ \rho \cdot u \cdot C_p \cdot \delta z \cdot \delta y \, (\frac{T_P + T_E}{2})$$

i.e.
$$- K \frac{\delta z\delta y}{\delta x} (T_E - T_P) - K \frac{\delta x\delta z}{\delta y} (T_S - T_P)$$

$$- K \frac{\delta x\delta y}{\delta z} (T_L - T_P) + \rho \cdot u \cdot C_p \cdot \delta z \cdot \delta y \, (\frac{T_P + T_E}{2})$$

Heat Accumulated

Heat accumulated was assumed to be zero as we had postulated quasi-steady condition.

Heat Balance

Heat in = Heat out + Heat Accumulated

Therefore:-

$$-K\delta z\delta y\left(\frac{\delta T}{\delta x}\right)_{PW} - K\delta x\delta z\left(\frac{\delta T}{\delta y}\right)_{PN} - K\delta x\delta y\left(\frac{\delta T}{\delta z}\right)_{PH} + \rho . u . C_p . \delta y . \delta z\left(\frac{T_W + T_P}{2}\right)$$

$$= -K\delta z\delta y\left(\frac{\delta T}{\delta x}\right)_{EP} - K\delta x\delta z\left(\frac{\delta T}{\delta y}\right)_{SP} - K\delta x\delta y\left(\frac{\delta T}{\delta z}\right)_{LP} + \rho . u . C_p . \delta z . \delta y\left(\frac{T_P + T_E}{2}\right) \quad \ldots (3.33)$$

or

$$-K\delta y\delta z\left(\frac{\delta T}{\delta x}\right)_{PW} - K\delta x\delta z\left(\frac{\delta T}{\delta y}\right)_{PN} - K\delta x\delta y\left(\frac{\delta T}{\delta z}\right)_{PH} + \rho . u . C_p . \delta y . \delta z\left(\frac{T_W + T_P}{2}\right) + K\delta y\delta z\left(\frac{\delta T}{\delta x}\right)_{EP} + K\delta x\delta z\left(\frac{\delta T}{\delta y}\right)_{SP} + K\delta x\delta y\left(\frac{\delta T}{\delta z}\right)_{LP} - \rho . u . C_p . \delta z . \delta y\left(\frac{T_P + T_E}{2}\right) = 0 \quad \ldots (3.34)$$

Dividing eqn. 3.34 by $\rho \cdot C_p \cdot \delta x \cdot \delta y \cdot \delta z$ and putting $\alpha = K/(\rho \cdot C_p)$ we get:-

$$- \frac{\alpha}{\delta x}\left(\frac{\delta T}{\delta x}\right)_{PW} - \frac{\alpha}{\delta y}\left(\frac{\delta T}{\delta y}\right)_{PN} - \frac{\alpha}{\delta z}\left(\frac{\delta T}{\delta z}\right)_{PH}$$

$$+ \frac{u}{\delta x}\left(\frac{T_W + T_P}{2}\right) + \frac{\alpha}{\delta x}\left(\frac{\delta T}{\delta x}\right)_{EP} + \frac{\alpha}{\delta y}\left(\frac{\delta T}{\delta y}\right)_{SP}$$

$$+ \frac{\alpha}{\delta z}\left(\frac{\delta T}{\delta z}\right)_{LP} - \frac{u}{\delta x}\left(\frac{T_P + T_E}{2}\right) = 0 \qquad \ldots (3.35)$$

Expressed in finite difference form the heat balance as written in eqn. 3.35 becomes:-

$$- \frac{2\alpha}{(X_E - X_W)} \times \left(\frac{T_P - T_W}{X_P - X_W}\right) - \frac{2\alpha}{(Y_S - Y_N)} \times \left(\frac{T_P - T_N}{Y_P - Y_N}\right)$$

$$- \frac{2\alpha}{(Z_L - Z_H)} \times \left(\frac{T_P - T_H}{Z_P - Z_H}\right) + \frac{2u}{(X_E - X_W)} \times \left(\frac{T_P + T_W}{2}\right)$$

$$+ \frac{2\alpha}{(X_E - X_W)} \times \left(\frac{T_E - T_P}{X_E - X_P}\right) + \frac{2\alpha}{(Y_S - Y_N)} \times \left(\frac{T_S - T_P}{Y_S - Y_P}\right)$$

$$+ \frac{2\alpha}{(Z_L - Z_H)} \times \left(\frac{T_L - T_P}{Z_L - Z_P}\right) - \frac{2u}{(X_E - X_W)} \times \left(\frac{T_E + T_P}{2}\right)$$

$$= 0 \qquad (3.36)$$

The above finite difference equation was solved for each and every grid block of the main body of the matrix. The exponentially expanding matrix was generated by the subroutine "Matrix" of the

program "WMOD" which is given in Appendix 3. "WMOD" is the main program which solves the above eqn. 3.36 using Relaxation method.

3.5.4.2 The Top Surface - Region 2

3.5.4.2.1 General Equation - Region 2

Heat flow term in z-direction "$(\alpha/\delta z)(\delta T/\delta z)_{PH}$" in the general heat balance equation (eqn. 3.35) was changed for the top surface. Because heat input by the laser beam was done on this surface and from here heat had been conducted away to the rest of the substrate. Therefore, surface temperature gradient i.e. "$(\delta T/\delta z)$" was calculated from the surface heat flux keeping provision for heat loss due to reflection, convection and radiation.

Recalling the eqn. 3.26 and assuming the temperature beyond the substrate to be ambient temperature we could write:-

$$K\left(\frac{\delta T}{\delta z}\right)_{x,y,1} = \frac{P_{tot}(1 - r_f)}{A} - (h_c + h_r)\,(T_{surf} - TEMPA)$$

$$= \left[P_{x,y}(1 - r_f) - (h_c + h_r)(T_{surf} - TEMPA)\right] \qquad (3.37)$$

where $P_{x,y}$ is the power density at the point (x,y,1).

Therefore

$$\left(\frac{\delta T}{\delta z}\right)_{x,y,1} = \left[P_{x,y}(1 - r_f) - (h_c + h_r)(T_{surf} - TEMPA)\right]/K$$

$$= GRSURF(x,y) \qquad (3.38)$$

Using eqn. 3.38 we defined

$$\frac{\alpha}{\delta z}\left(\frac{\delta T}{\delta z}\right)_{PH} = \frac{\alpha}{z_L - z_{surf}}\, GRSURF(x,y) \qquad (3.39)$$

Therefore finite difference equation governing top surface points only is:-

$$-\frac{2\alpha}{(X_E - X_W)}\left(\frac{T_P - T_W}{X_P - X_W}\right) - \frac{2\alpha}{(Y_S - Y_N)}\left(\frac{T_P - T_N}{Y_P - Y_N}\right) - \frac{\alpha}{(Z_L - Z_{surf})}$$

$$\times \text{GRSURF}(x,y) + \frac{2u}{(X_E - X_W)}\left(\frac{T_P + T_W}{2}\right) + \frac{2\alpha}{(X_E - X_W)} \times \left(\frac{T_E - T_P}{X_E - X_P}\right)$$

$$+ \frac{2\alpha}{(Y_S - Y_N)} \times \left(\frac{T_S - T_P}{Y_S - Y_P}\right) + \frac{\alpha}{(Z_L - Z_{surf})} \times \left(\frac{T_L - T_P}{Z_L - Z_P}\right)$$

$$- \frac{2u}{(X_E - X_W)}\left(\frac{T_E + T_P}{2}\right) = 0 \qquad (3.40)$$

In order to calculate GRSURF(x,y) in eqn. 3.38 we had to calculate $P_{x,y}$, h_c and h_r. Mode of calculation of above terms are discussed below.

3.5.4.2.2 Laser power density distribution

Intensity distribution for laser output is defined by a Laguerre-Gaussian profile for *Circular* symmetry[14,17,203]. For lowest order mode TEM_{oo} the power density profile in either case is given as a Gaussian distribution of the form:

$$P_{x,y} = P(r) = P_o . \exp(-2r^2/r_b^2) \qquad (3.41)$$

where r = radial distance from centre and $r^2 = x^2 + y^2$

P_o = power density at the centre of the beam

r_b = Gaussian beam radius defined as the radial distance at which the power density has fallen to $1/e^2$ of centre value.

If r_b is gaussian beam radius at 1/e of the central value then power density distribution is given by

$$P(r) = P_o \exp(-r^2/r_b^2) \qquad (3.42)$$

Ready[14] reports that defining beam radius as 1/e simply amounts to introducing a factor of $\sqrt{2}$ but it often reduces the complexity. But using radius at 1/e gives negative power distribution for higher order mode. However, for TEM_{oo} it does not pose any problem as pointed out by Ready[14].

Total power can be obtained by integrating the power density distribution (eqn. 3.41 and 3.42). Therefore, for beam radius at $1/e^2$ of central value

$$P_{total} = \int_0^\infty P_o \exp(-2r^2/r_b^2) 2\pi r \, dr$$

$$= (P_o \pi r_b^2)/2$$

or

$$P_o = \frac{2 \times P_{Total}}{\pi r_b^2} \qquad (3.43)$$

Thus

$$P(r) = \frac{2 \times P_{Total}}{\pi r_b^2} \, e^{-(2r^2/r_b^2)} \qquad (3.44)$$

similarly for beam radius at 1/e of central value

$$P(r) = \frac{P_{Total}}{\pi r_b^2} \, e^{-(2r^2/r_b^2)} \qquad (3.45)$$

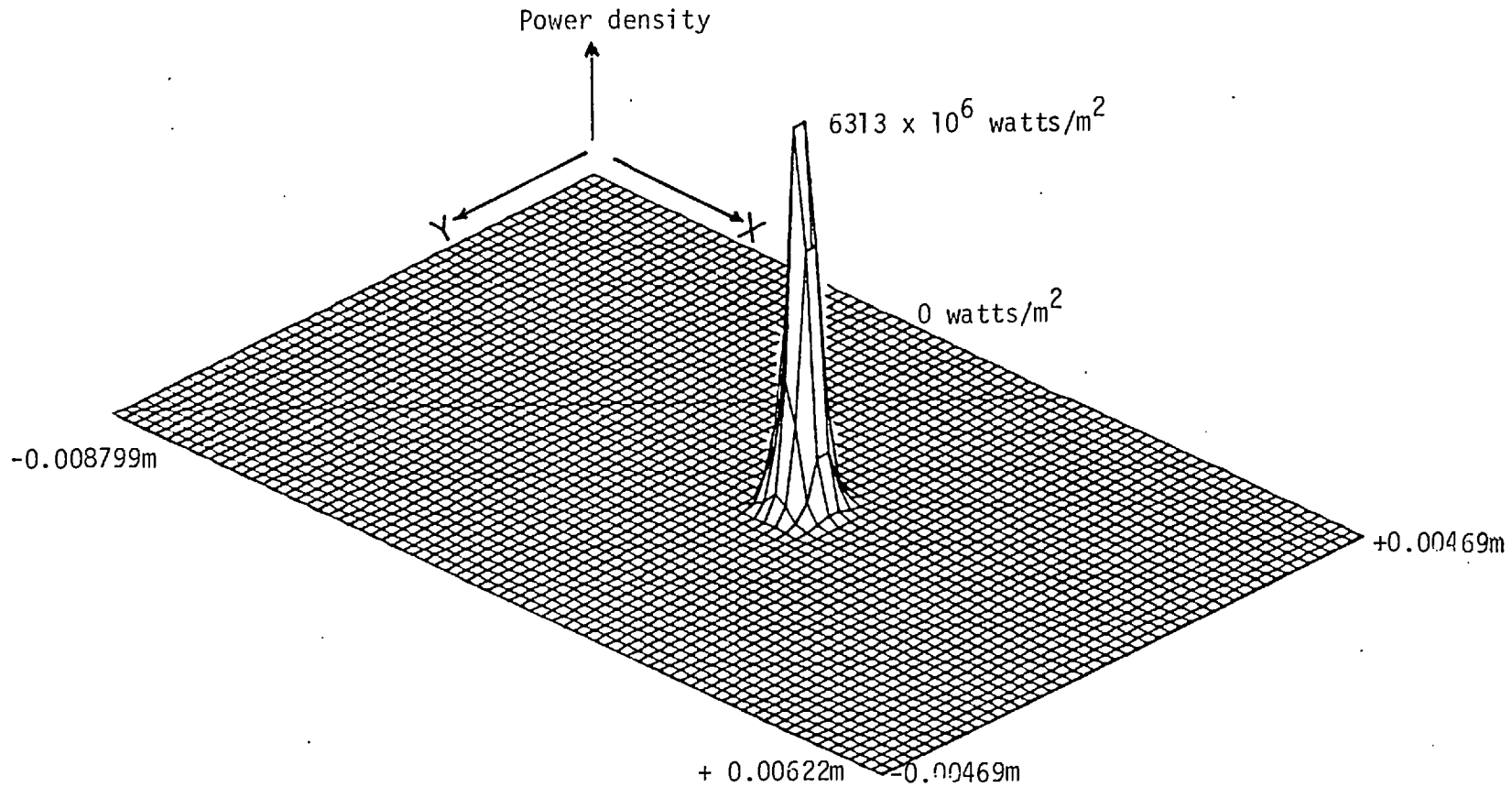

FIG. 3.6a Laser power distribution

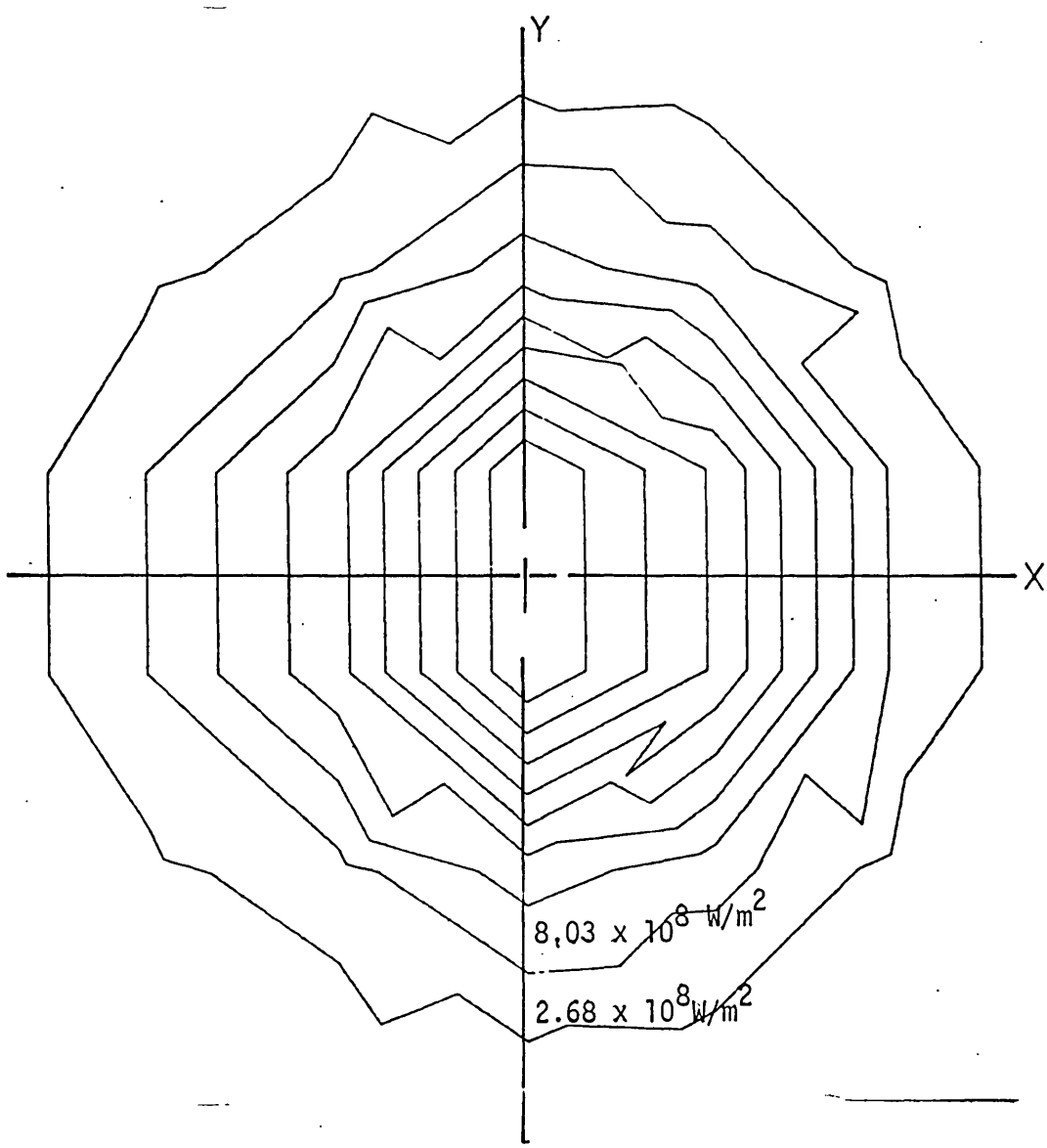

FIG. 3.6b Laser power distribution

Step for contours = 5.353×10^8 watts/m^2

N.B. Squarish appearance is due to transformation of power distribution term from cylindrical co-ordinate to cartesian co-ordinates

In order to best approximate the actual power distribution in the experiments the mode structure was assumed to be TEM_{oo} and the eqn. 3.45 was used to calculate the distribution. Power distribution computed and plotted as shown in Fig. 3.6.

3.5.4.2.3 Convective heat transfer coefficient at the top surface

Gordon and Cobonpue[204] report that at the stagnation point of a vertically impinging jet:-

$$Nu_o = 13 \cdot Re^{0.5} D_j/B \qquad (3.46)$$

using the correlations given by Polhausen[205], Steen[17] derived that:-

$$Nu_o = 13\ Re^{0.5}\left[D_j/B\right] \cdot Pr^{0.33} = h_c\ D_j/K_{gas}$$

or

$$h_c = 13\ Re^{0.5}\ Pr^{0.33} \cdot K_{gas}/B \qquad (3.47)$$

where K_{gas} = thermal conductivity of the boundary layer gas at the boundary layer film temperature

B = jet plate distance.

This correlation (eqn. 3.47) is unlikely to be perfectly correct. The constant multiplier may require refinement with variation of Reynold's number. BothReynold's number and Prandtl's number are susceptible to the change of physical properties of gas with temperature whereas average thermal properties of gas were used for the present calculation. Furthermore, the variation of the convective heat transfer coefficient with radial position relative to the jet axis was ignored.

Those above approximations were made in view of the relatively small convective heat loss term being calculated. Besides that, since the convective heat loss = h_c x ΔT and that Δt

for laser welding is only appreciable near the beam radius ΔT is small for bulk of the body and points removed from the shielding jet where h_c is uncertain have only a small ΔT making careful refinement of h_c in this region unnecessary. Therefore, the above correlation (eqn. 3.47) should be reasonable approximation without unnecessary complexity.

3.5.4.2.4 Radiative heat transfer coefficient

The heat transfer by radiation is computed from the Stefan-Boltzman equation which is as follows:-

$$q_{r.loss} = A\,\sigma(1 - r_f)(T_{surf}^4 - T_{sink}^4)$$

$$= A\,\sigma(1 - r_f)(T_{surf}^4 - TEMPA^4) \qquad (3.48)$$

where σ = Stefan Boltzman constant

A = area

T_{sink} = Temperature of sink = TEMPA

$q_{r.loss}$ = heat loss due to radiation

Again radiative heat transfer coefficient "h_r" is given by

$$q_{r.loss} = h_r\,A(T_{surf} - TEMPA) \qquad (3.49)$$

Now using eqn. 3.48 and eqn. 3.49 we find

$$h_r = \frac{q_{r.loss}}{A(T_{surf} - TEMPA)}$$

$$= \sigma(1 - r_f)(T_{surf}^2 + TEMPA^2)(T_{surf} + TEMPA) \qquad ...(3.50)$$

But here boundary layer bulk temperature is taken to be the ambient temperature "TEMPA" whereas to be more precise it would be some integral over the hemispherical solid angle of the temperature of all surfaces with a view of the spot. The difference is

considered negligible[17,206].

3.5.4.3 The bottom surface - Region 3

Heat out term in z-direction "$(\alpha/\delta z)(\delta T/\delta z)_{LP}$" in the general heat balance equation (eqn. 3.35) was changed for the bottom surface. Because in the bottom surface heat was received only by conduction like the main body but these were convective heat loss due to bottom shielding gas. Radiative heat loss was also taken into consideration.

Recalling the eqn. 3.27 we could write:-

$$K\left(\frac{\delta T}{\delta z}\right)_{x,y,IZ} = -(h_c + h_r)(T_{surf} - TEMPA)$$

$$\text{or, } \left(\frac{\delta T}{\delta z}\right)_{x,y,IZ} = -\left[(h_c + h_r)(T_{surf} - TEMPA)/K\right]$$

$$= GRSURFB(x,y) \qquad (3.51)$$

Therefore finite difference equation governing bottom surface points only is:-

$$-\frac{2\alpha}{(X_E - X_W)} \times \left(\frac{T_P - T_W}{X_P - X_W}\right) - \frac{2\alpha}{(Y_S - Y_N)} \times \left(\frac{T_P - T_N}{Y_P - Y_N}\right) - \frac{\alpha}{(Z_{surf} - Z_H)}$$

$$\times \left(\frac{T_P - T_H}{Z_P - Z_H}\right) + \frac{2u}{(X_E - X_W)} \times \left(\frac{T_P + T_W}{2}\right) + \frac{2\alpha}{(X_E - X_W)} \times \left(\frac{T_E - T_P}{X_E - X_P}\right)$$

$$+ \frac{2\alpha}{(Y_S - Y_N)} \times \left(\frac{T_S - T_P}{Y_S - Y_P}\right) + \frac{\alpha}{(Z_{surf} - Z_H)} \times GRSURFB(x,y)$$

$$- \frac{2u}{(X_E - X_W)} \times \left(\frac{T_E + T_P}{2}\right) \qquad \ldots\ldots (3.52)$$

Radiative heat transfer coefficient is same for both the surfaces. Method of calculation is shown in Section 3.5.4.2.4.

The bottom shielding gas was in the form of several jets impinging the bottom surface. Therefore, convective heat transfer coefficient used was the same as that for top surface, which is discussed in the section 3.5.4.2.3.

3.5.4.4 The eastern boundary - Region 4

Temperature beyond the eastern boundary was assumed to be ambient temperature as expressed in eqn. 3.28. Therefore, heat flow terms in x-direction "$(\alpha/\delta x)(\delta T/\delta x)_{EP}$" and "$(u/\delta x)(T_P+T_E/2)$" were changed.

After changing the above terms and using eqn. 3.36, the equation governing the eastern boundary becomes:-

$$-\frac{\alpha}{(X_P - X_W)}\left(\frac{T_P - T_W}{X_P - X_W}\right) - \frac{2\alpha}{(Y_S - Y_N)} \times \left(\frac{T_P - T_N}{Y_P - Y_N}\right) - \frac{2\alpha}{(Z_L - Z_H)} \times \left(\frac{T_P - T_H}{Z_P - Z_H}\right)$$

$$+\frac{u}{(X_P - X_W)}\left(\frac{T_P + T_W}{2}\right) + \left(\frac{\alpha}{X_P - X_W}\right) \times \left(\frac{TEMPA - T_P}{X_P - X_W}\right) + \left(\frac{2\alpha}{Y_S - Y_N}\right)\left(\frac{T_S - T_P}{Y_S - Y_P}\right)$$

$$+\frac{2\alpha}{(Z_L - Z_H)} \times \left(\frac{T_L - T_P}{Z_L - Z_P}\right) - \frac{u}{(X_P - X_W)}\left(\frac{TEMPA + T_P}{2}\right)$$

$$= 0 \qquad \ldots(3.53)$$

But for the matrix points in eastern boundary common to the boundary planes such as top surface and bottom surface heat balance equation should accommodate the characteristic heat flow terms for the other boundary plane as well as eastern boundary.

3.5.4.5 The western boundary - Region 5

Similarly to eastern boundary temperature beyond western boundary was also assumed to be ambient temperature as expressed in eqn. 3.29. Therefore, the heat flow term in x-direction at the boundary "$(\alpha/\delta x)(\delta T/\delta x)_{PW}$" and "$(u/\delta x)(T_P + T_W/2)$" were changed.

The finite difference term for the expression $(\alpha/\delta x)(\delta T/\delta x)_{PW}$ is:-

$$\frac{\alpha}{(X_E - X_P)} \times \left(\frac{T_P - TEMPA}{X_E - X_P}\right) = DXWF \qquad (3.54)$$

where $$DXWF = \frac{\alpha}{\delta x}\left(\frac{\delta T}{\delta x}\right)_{PW}$$

Similarly,

$$\frac{u}{\delta x}\left(\frac{T_P + T_W}{2}\right) = DXWC = \frac{u}{(X_E - X_P)} \times \left(\frac{T_P + TEMPA}{2}\right) \qquad (3.55)$$

using the expressions 3.54 and 3.55 in eqn. 3.36 we got the equation governing the western boundary. Relevant heat flow terms were changed for the matrix points common to other boundary planes as well as western boundary.

3.5.4.6 The northern boundary - Region 6

As expressed in eqn. 3.30 the temperature beyond northern boundary was assumed to be ambient temperature. Therefore, heat flow terms in y-direction was modified using the expressions

$$T_{N-1} = TEMPA$$

when we get

$$\frac{\alpha}{\delta y}\left(\frac{\delta T}{\delta y}\right)_{PN} = DYNF = \frac{\alpha}{(Y_S - Y_P)}\left(\frac{T_P - TEMPA}{Y_S - Y_P}\right) \qquad (3.56)$$

using the eqn. 3.36 and 3.56 and taking necessary considerations of points common to more than one boundary planes we derived the equation governing the northern boundary.

3.5.4.7 The southern boundary - Region 7

As discussed in previous sections in eastern, western and northern boundary the heat flow term modified was:

$$\frac{\alpha}{\delta y}\left(\frac{\delta T}{\delta y}\right)_{SP} = DYSF = \frac{\alpha}{(Y_P - Y_N)}\left(\frac{TEMPA - T_P}{Y_P - Y_N}\right) \qquad (3.57)$$

3.6 Calculation of the Temperature Profile

The calculation of the temperature distribution was started by setting temperature for each grid point to ambient temperature.

The equation for the conservation of heat at each grid point, as discussed in section 3.5.4, was solved and the residue was calculated. The biggest residue for the whole field was stored for the iteration step. If the biggest residue "RES" is greater than the convergency limit then calculation for next iteration step to solve heat balance equation was started by resetting the temperature as shown below. But a weighing factor "W" was used to damp the oscillation.

$$TEMP(K,I,L) = TEMP(K,I,L) + RES/W \qquad (3.58)$$

where TEMP (K,I,L) was the temperature at the location (K,I,L) calculated in the most recent iteration step. This iteration loop was carried on till the biggest residue was less than the convergency limit. The weighting factor or the relaxation factor "W" was varied with number of iteration loop to suit the situation for needed damping of oscillation.

The convergency limit was chosen depending on the accuracy and computing time needed.

The provision for keyholing is made by assuming that if any grid point temperature exceeds boiling point by 200^{o}K then the next grid point in z-direction receives the surface temperature gradient. This is shown in Appendix 3, line numbers - 4200, 4310, 5130, and 5240.

3.7 Substrate and Gas Properties used for Calculation of Temperature Profile

Physical properties of substrate materials and shielding gas used for calculation of temperature profile were obtained from different handbooks[231-235,242]. It was assumed that most of the physical properties remain constant during temperature change.

The physical properties of the substrate used for the present study are given in Table 3.2 and that for gas are given in Table 3.3.

3.8 Convergency and Operating Efficiency of the Program

3.8.1 Selection of grid size

For a substrate of particular dimension and a fixed number of grid points the grid size was determined by the number of points considered to be within the beam. As the matrix was divided logarithmically more points inside the beam means bigger grid sizes at the points further from the beam material interaction point. Therefore, the effect of the grid-size can be studied by varying the number of grid points inside the beam.

This arbitrary division, however, affects the computing time but needed to be checked to ensure that it did not also affect the answer. It was observed that the fewer the points inside the beam the faster the computing. Again above a certain number the program does not converge because the relatively fewer grid blocks of bigger sizes out side the beam could not smoothly damp the enormous temperature gradient near the beam. The analysis of the effect of grid size on the program is given in the Table 3.4.

The effect of the grid size on the temperature profile is shown in Fig. 3.7 and Fig. 3.8. It is observed from these figures that the grid size does not appreciably effect the temperature profile, though fewer points inside the beam give a slightly

Material	Properties	Reference No.	Value	Units
Ti-6Al-4V (AMS 4911)	Density	235	4420.0	Kg/m^3
	Thermal Conductivity	232	7.3269	W/m^oK
	Specific Heat	235	599.97	W/m^oK
	Electrical Resistivity	232	$170x10^{-8}$	ohm-metre
	Melting Point	242	1950	^oK
	Boiling Point	243	3500	^oK
Mild Steel	Density	242	7860	Kg/m^3
	Thermal Conductivity	242	63	$Wm^{-1}\ K^{-1}$
	Specific Heat	242	420	W/m^oK
	Electrical Resistivity	242	$15x10^{-8}$	ohm-metre
	Melting Point	242	1700	^oK
	Boiling Point	170	3333	^oK

TABLE 3.2

Material	Property	Reference No.	Value	Units (SI)
Helium (He_4)	Gas density at 1 atm. and 25°C	232	0.17850	Kg/m^3
	Gas velocity	232	198.5×10^{-7}	NS/m^2
	Specific heat	231	5191.632	J/Kg^oK
	Thermal conductivity	231	0.148	W/m^oK
Argon	Gas density	232	1.7838	Kg/m^3
	Gas viscosity	232	226.4×10^{-7}	NS/m^2
	Specific heat	231	523.35	J/Kg^oK
	Thermal conductivity	231	0.0175	W/m^oK

TABLE 3.3

smaller heat affected zone.

No of points inside the beam (ITP) for the matrix size 32 x 31 x 4	central processor time in seconds	Number of iteration	Approx. time/grid pt/iteration $x10^{-3}$	Accuracy of solution
7	824.859	272	0.76	Comparable to solution for ITP = 9
9	906.818	297	0.77	Good
11 (did not converge)	17.731	4	0.00117	Do not converge

TABLE 3.4

3.8.2 Selection of Overall Matrix Size

The chosen overall matrix size also determines the grid block sizes for a substrate of particular dimension. Therefore, it should have similar effects as described in the Section 3.8.1. Besides that, it should have a more pronounced effect on computing time and memory required; because the matrix size determines the number of points to be calculated per iteration loop and storage memory required for storing of input and output array. Greater the matrix size greater the computing time and memory required.

The present model being a three-dimensional one it naturally requires a greater memory than a two-dimensional model. For the Imperial College CDC 6500 and CYBER 174 computers the matrix size of 32 x 31 x 4 was found to be optimum. Above this size the memory requirement overflows the available memory. On the other hand if the matrix size is reduced for the same substrate overall dimensions then difficulty with convergence arises similar to that described in Section 3.8.1. However, for small substrate dimensions, smaller

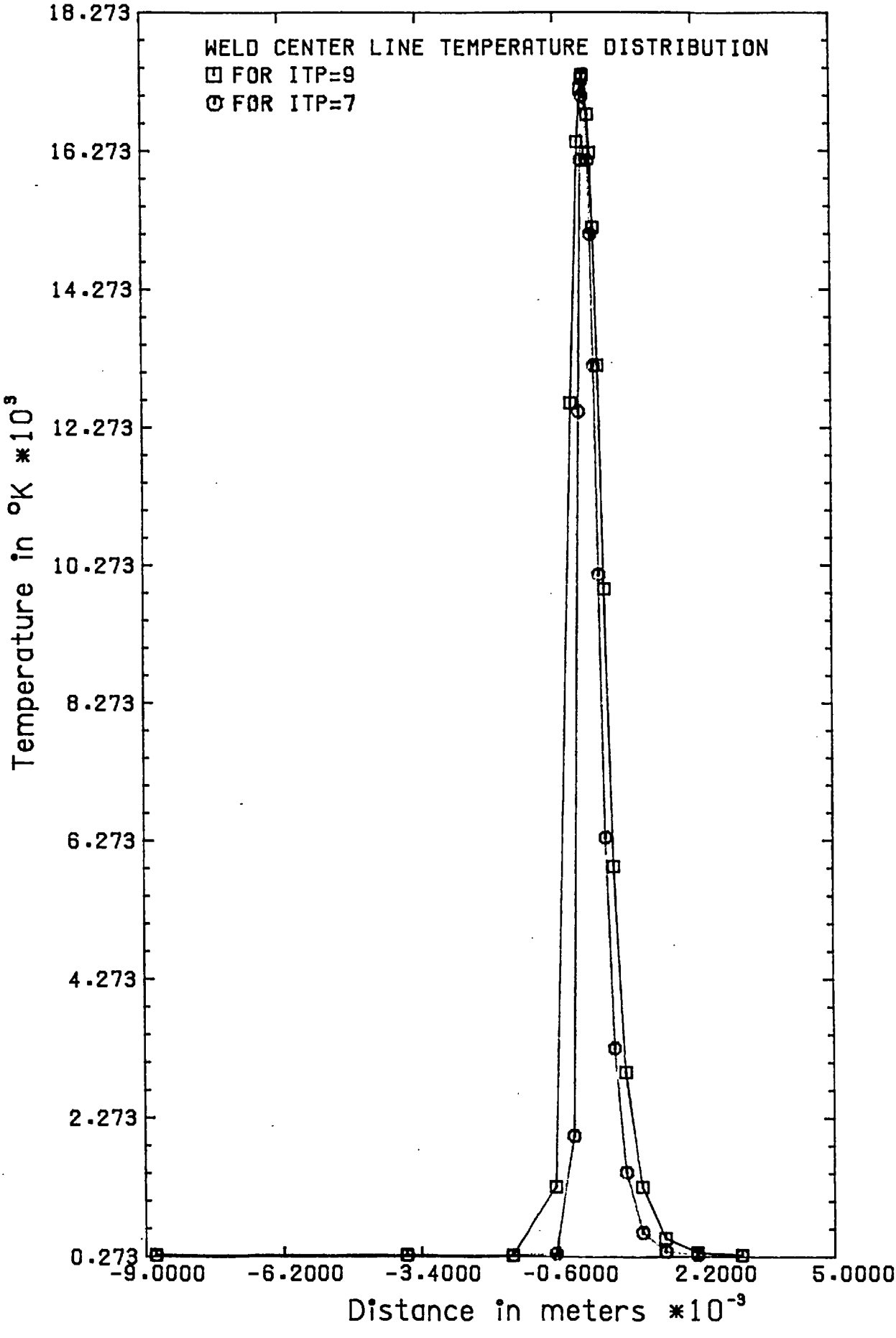

FIG. 3.7 Effect of grid size on weld center-line temperature distribution. Power 1.5 kW, Speed 9.5 mm/sec.

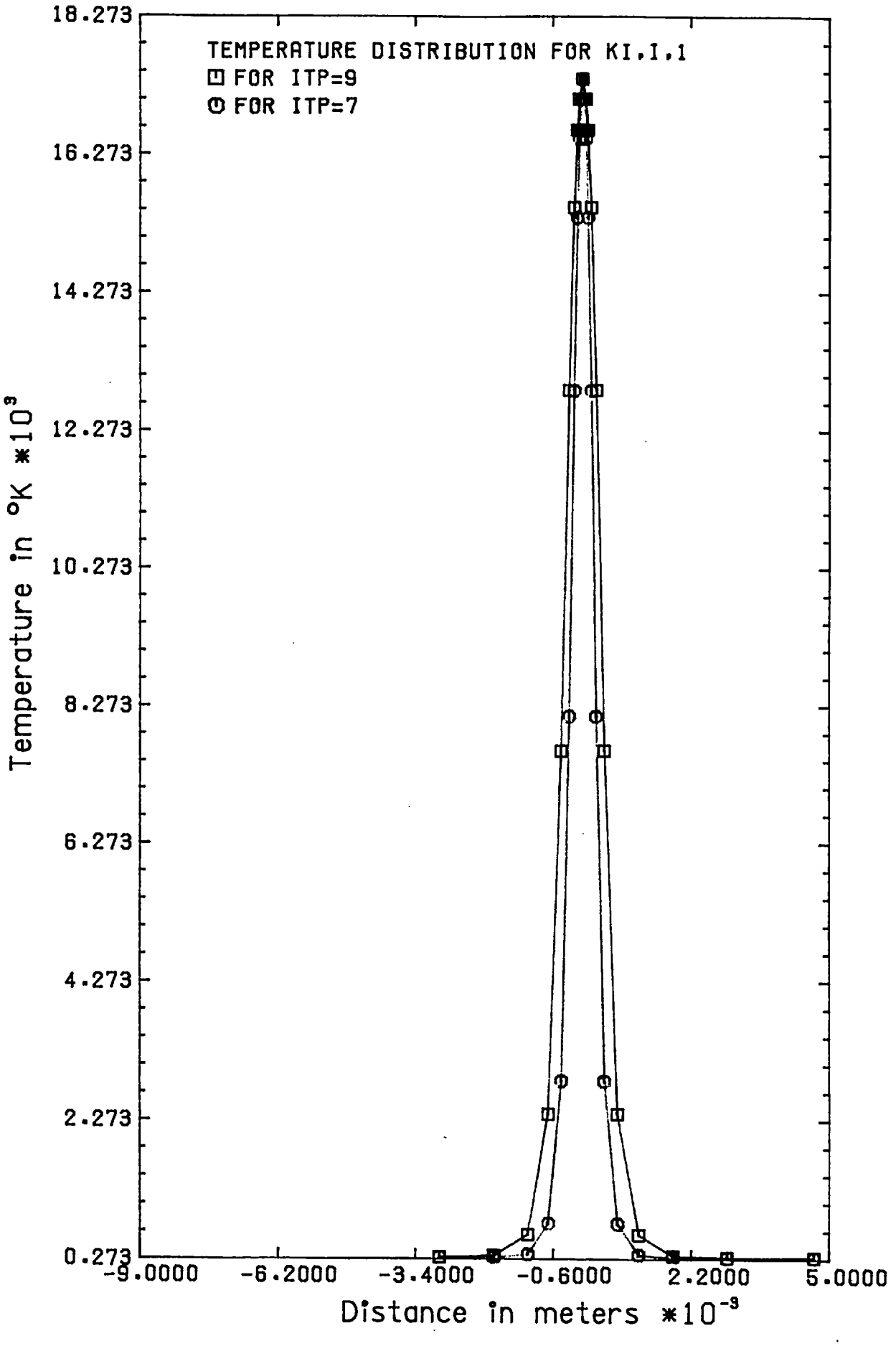

FIG. 3.8 Effect of grid size on surface temperature distribution along y-direction through the point of interaction Power 1.5 kW, Speed 9.5 mm/sec.

matrices could produce the solution. Approximately 1 micro second of computer time is needed for the calculations per grid point for all the cases. Naturally, for smaller grid sizes the computer time needed is less. But the penalty would be accuracy. For the present study even a matrix size of 26 x 23 x 4 for the same substrate dimension lead to convergency problems. A solution might have been derived by elaborate trial runs varying the weighting factor and the number of grid points under the beam but this was abandoned since convergency was achieved with a matrix size of 32 x 31 x 4.

3.8.3 Selection of Convergency Limit

Ideally, the convergency limit "BIG" could be reduced to a very small value near to zero. This will lead to a good accuracy at tremendous cost in computer time. In a system like laser welding when the temperature at the point of interaction exceeds 1.7×10^4K and falls down to room temperature within a short distance then a convergency limit of 10^3 should also give a reasonable accuracy. Therefore, for the present study a higher convergency limit considering the optimum computing time and accuracy was considered.

The convergency limit "BIG" was considered to be the biggest residue value among the points in the matrix. It was checked that the biggest residue value occurs near the points having a temperature in excess of 10^{4^0}K . Therefore, it was evident that the "BIG" value of 10^3 would give an error less than 10%. However, an analysis of iteration count and accuracy as a function of "BIG" for a 32 x 31 x 4 exponential matrix is given in Table 3.5.

Value of BIG	Iteration Count	Central Processor Time in seconds	Accuracy
732.4	963	3480.013	See fig. 3.9
861.8	623	1938.037	
1183	283	865.897	

TABLE 3.5

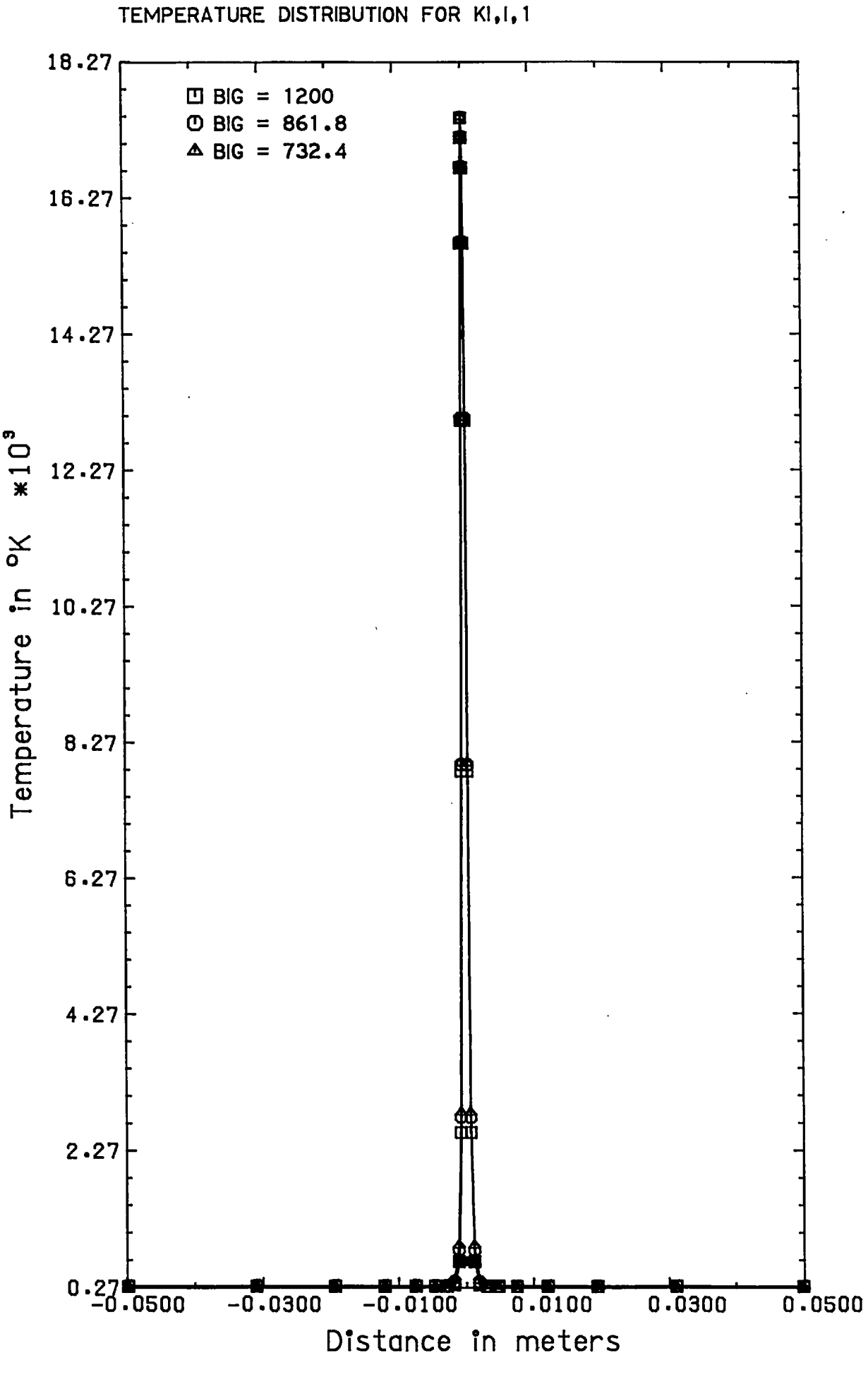

Fig. 3.9 Effect of "BIG" on temperature distribution

3.8.4 Effect of weighting factor on convergency

In order to speed up the convergence of the relaxation process used in the present study it was soon evident that "over-relaxation" was required. For a small weighting factors the residue values tend to increase continually. Therefore, the problem lies in selecting a weighting factor which will lead to relatively faster convergence with reasonable accuracy.

It was observed that with a greater number of grid points in the matrix convergency was more easily obtained and thus allowed a smaller weighting factor. But for a particular grid block size the effect of power and welding speed is not appreciable.

A weighting factor in the range of 40 x 128 was found to be suitable for a grid size of 32 x 31 x 4 used for a substrate dimension of 15cm x 10cm x 0.2cm. But while the program was being used for a substrate dimension of 15 x 10 x 0.1 cm^3 then it was found that an exponential weighting factor related with the biggest residue was very useful for relatively faster convergence. The weighting factor was related to "BIG" as follows

$$W = WW(0.5 + 0.5 \ln (BIG)) \qquad (3.59)$$

where WW = a constant multiplier
W = variable multiplier
WXWW = weighting factor.

The effect of weighting factor on convergency is summarised in Table 3.6.

W	Substrate dimension for matrix size of 32 x 31 x 4	BIG	Iteration count
64	15x10x0.2 cm^3	Does not converge (0.3044×10^{243})	8
128	"	1183	283
256	"	2221	404
301	15x10x0.1 cm^3	2892	417
128	"	4.18×10^7 (Does not converge)	424
263.8-175.7 (variable as 3.59)	"	2408	381

TABLE 3.6

3.8.5 Computation over extended lengths of time

The maximum run length allowed under the present J13 category job on the Imperial College CDC 6500/Cyber 174 is 1800 seconds of central processor time. But as shown in Table 3.5 to achieve a value of "BIG" equal to 861.8 requires 623 iterations which amounts to CP time equal to 1938.037 seconds.

As explained in section 3.8.3 a convergency limit of 1200 was sufficiently accurate for the present study. To achieve "BIG" equal to 1200 only 865 seconds of CP time was required. However, to run the program for even smaller "BIG" values the temperature profile obtained with a particular "BIG" value could be stored on magnetic disc as an indirect access binary file. This data file could be reloaded by a modified program to use the data as the initial temperature profile and so start execution from where the previous program had finished. In this way, by saving and reloading the data, the program could be run several times consuming considerable computing time but achieving lower values of BIG.

3.8.6 Accuracy

Generally the accuracy of a Numerical solutions is found by comparing it to that from an analytical solution. However, there is no analytical solution available for a meaningful comparison, since it is a three-dimensional non-linear problem with a finite heat source. An alternative way of checking the accuracy is by comparing the prediction obtained from the model with the data obtained from the actual process. This technique is also used by Paley and Hibbert[191].

Therefore, for the present study the calculated temperature profile is compared with the macro-structure of the weld which is shown in Plate 7.3. The prediction of welding speeds are also compared with the actual welding speeds obtained and shown in Fig. 7.2a.

During the above comparisons it was revealed that the predicted temperature profile reasonably correlates with the actual temperature profile. But while the molten zone correlates with the prediction very accurately the actual HAZ seems to be slightly bigger than that predicted. The comparison of the prediction and the experimental results obtained in the present study is given in Chapter 7.

It is also relevant to mention that the model when used for predicting temperature profile for laser heat treatment produced good correlation[241].

3.9 Presentation of Results

The results of the model were presented both in terms of different variables with relevant dimensions in SI units such as temperature in ^{o}K and in dimensionless groups as and when required.

Dimensional Analysis

The equations 3.25 to 3.51 reveals that the following parameters are required to solve the temperature profile.

Symbol	Description	S.I. Units
$P(1-r_f)$	The net power absorbed at the surface	Watt
ΔT	Temperature difference	^oK
K	Thermal conductivity	W/m^oK
V	Welding speed	m/s
X	Length	m
y	Width	m
z	Thickness	m
D_b	Beam diameter	m
h	Convective and radiative heat transfer coefficient ($h_r + h_c$)	$W/m^2\ ^oK$
α	Thermal diffusivity	m^2/s

The temperature is a function of the above 10 variables. Thus;

$$T_f = \int (P(1-r_f) \cdot K, \alpha, V, X, y, z, D_b, T, h)$$

The number of variable is 10 and we have to express these in terms of four dimensions (P, T, V, D_b). Then Buckingham's π theorem predicts the number of dimensionless groups as follows:

$$n = i - r$$

where n = number of dimensionless groups
i = number of variables
r = greatest number of variables that will not form a group.

Therefore, we have six dimensionless groups which are as follows:

$$\pi_1 = \frac{\Delta T K D_b}{P(1-r_f)} = T^* \qquad \text{Dimensionless temperature}$$

$$\pi_2 = \frac{U.D_b}{\alpha} = U^* \qquad \text{Dimensionless speed}$$

$$\pi_3 = \frac{X}{D_b} = X^* \qquad \text{Dimensionless length}$$

$$\pi_4 = \frac{y}{D_b} = Y^* \qquad \text{Dimensionless width}$$

$$\pi_5 = \frac{z}{D_b} = Z^* \qquad \text{Dimensionless depth}$$

$$\pi_6 = \frac{D_b^2 \,.\, h \,.\, \Delta T}{P(1-r_f)} = H^* \qquad \text{Dimensionless heat loss}$$

$$= \frac{T^* D_b h}{K}$$

These dimensionless groups are calculated and plotted one against another in section 3.10 for better understanding.

3.10 Operation of the mathematical model

The mathematical model could be used for the following:

1) To predict temperature profile
2) To predict welding speeds
3) To predict heat affected zone
4) To predict thermal cycle at any location or speed
5) To predict the effect of thickness on temperature profile
6) To predict the effect of supplementary heating or cooling.

The results from the model can either be represented in SI units after running it for relevant conditions or can be predicted from generalised curves produced using dimensionless groups as described in section 3.9. The advantage of generalised plots is that a reasonable prediction for temperature profile may be obtained for different operating conditions without further recourse to the computer. But due to there being too many variables involved it is difficult to represent the effect of all the variables in one single plot. Some

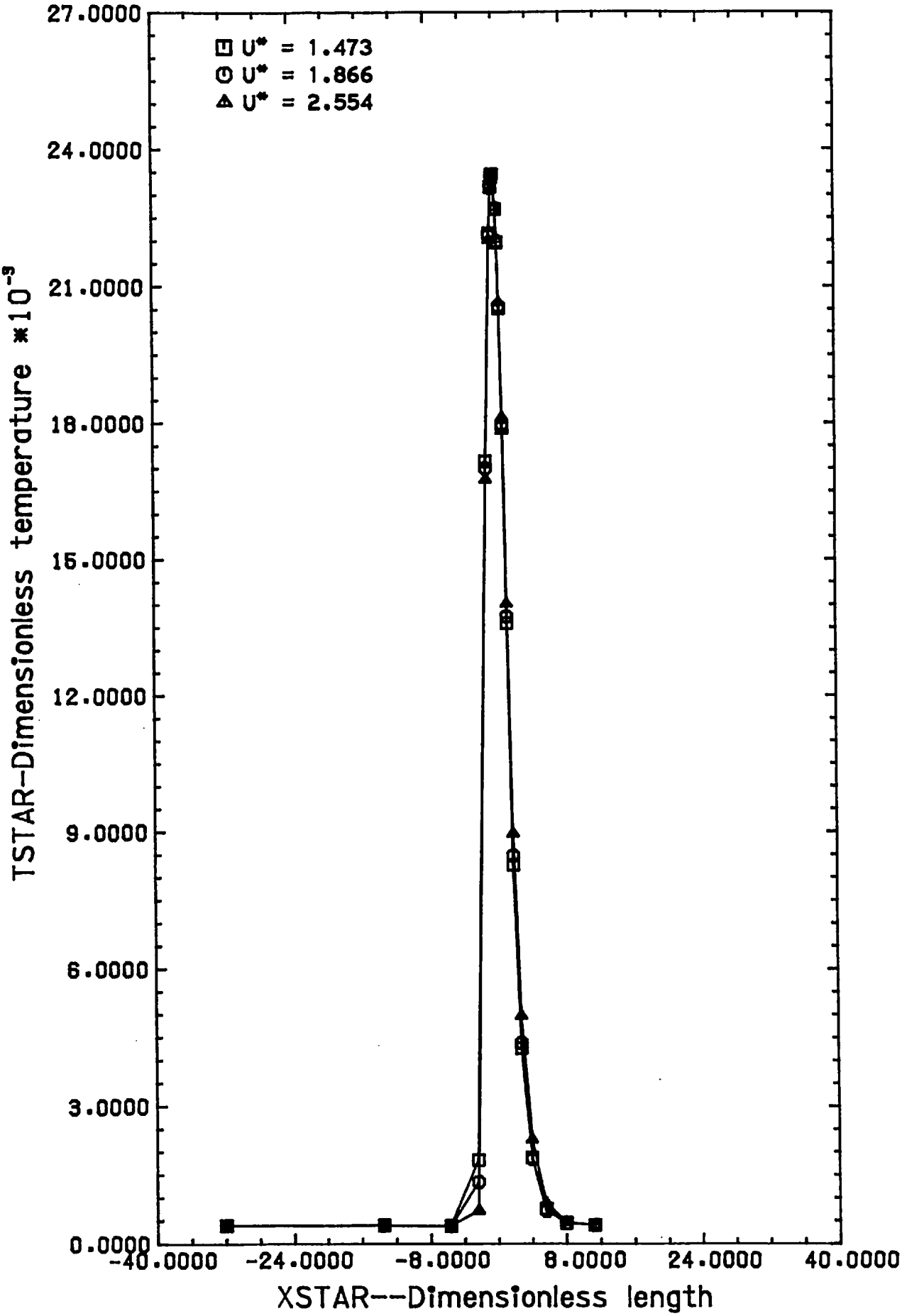

Fig. 3.10a Centerline T* VS. X*

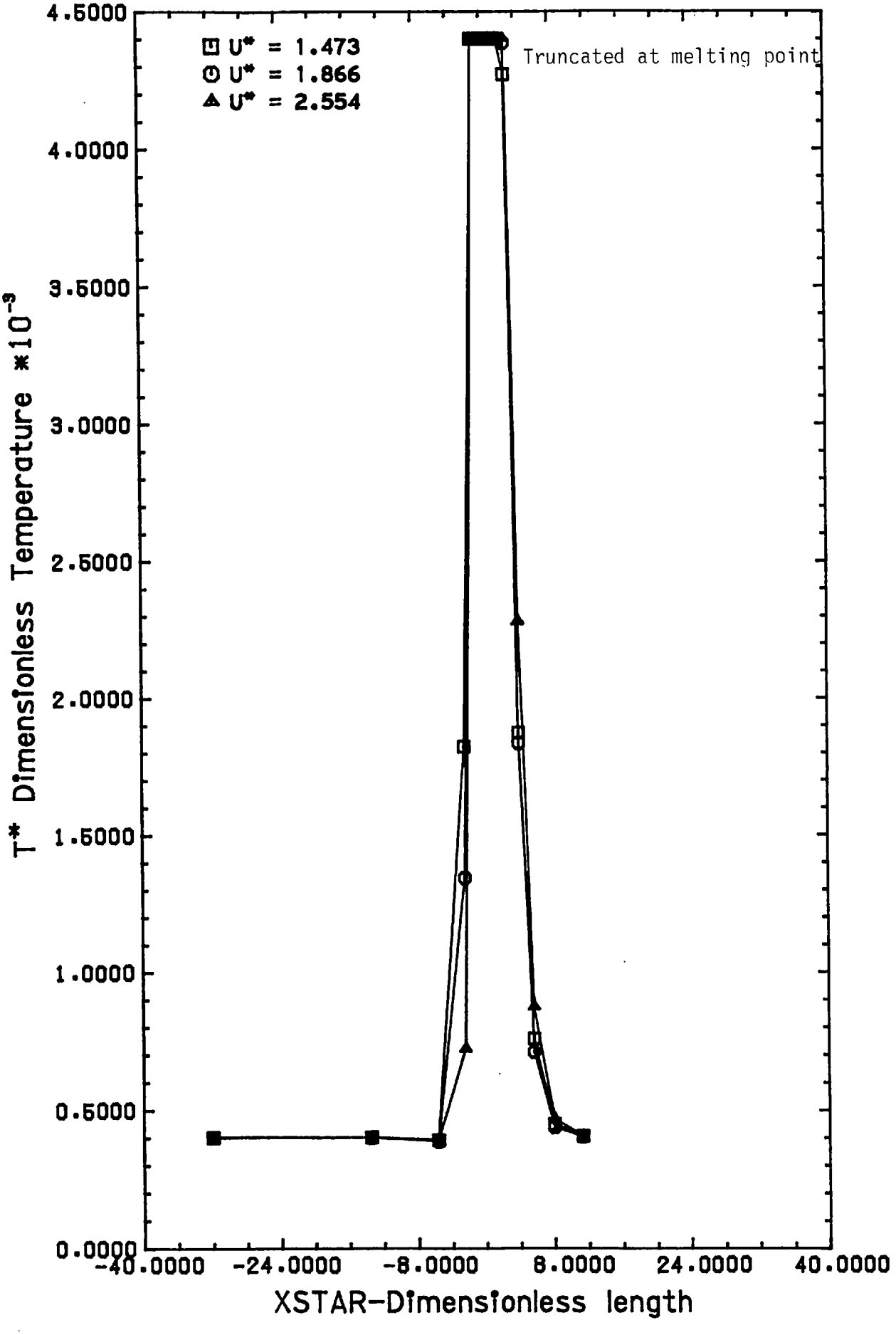

Fig 3.10b Centerline T^* VS. X^*

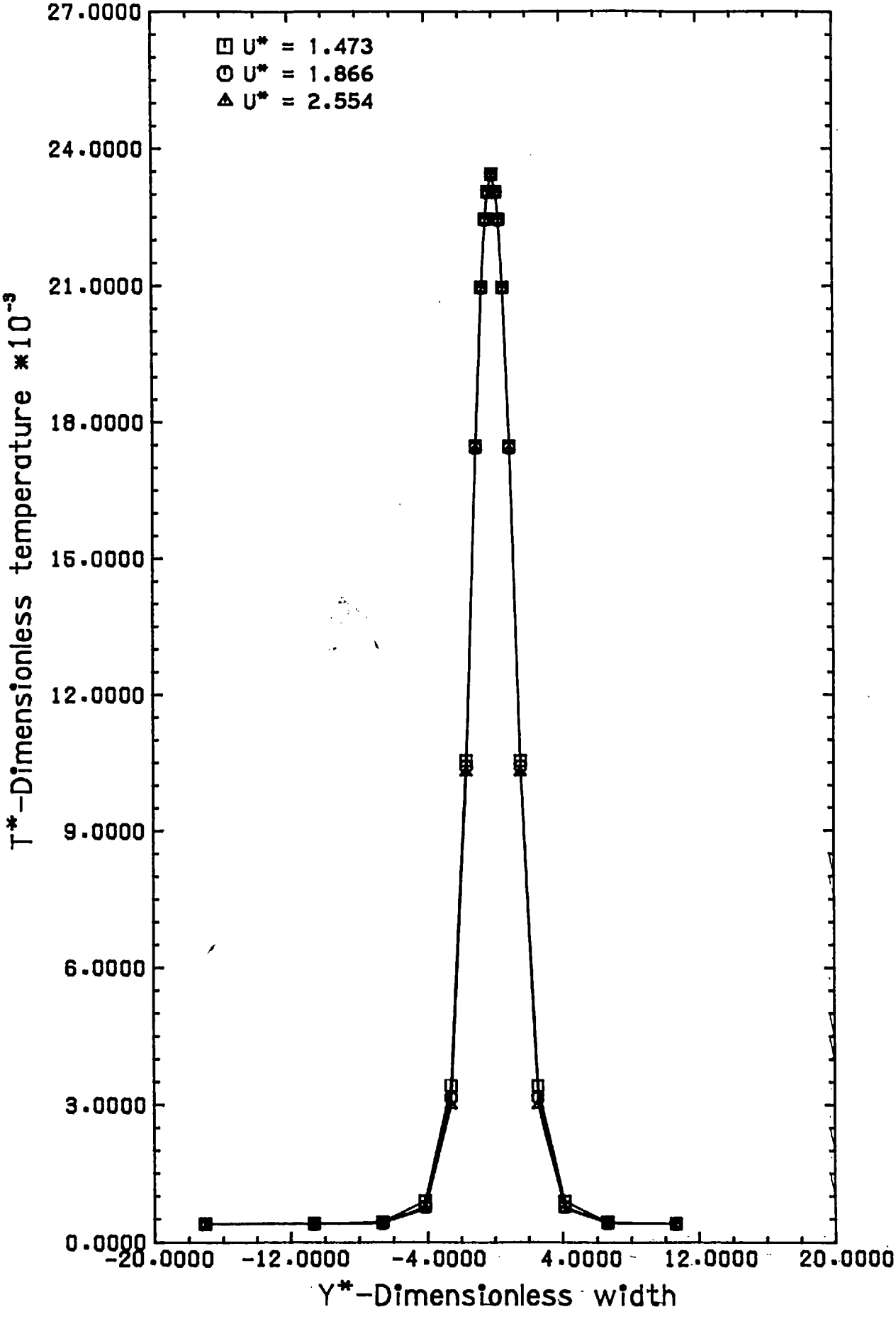

Fig. 3.11a T* vs. Y* through the point of interaction

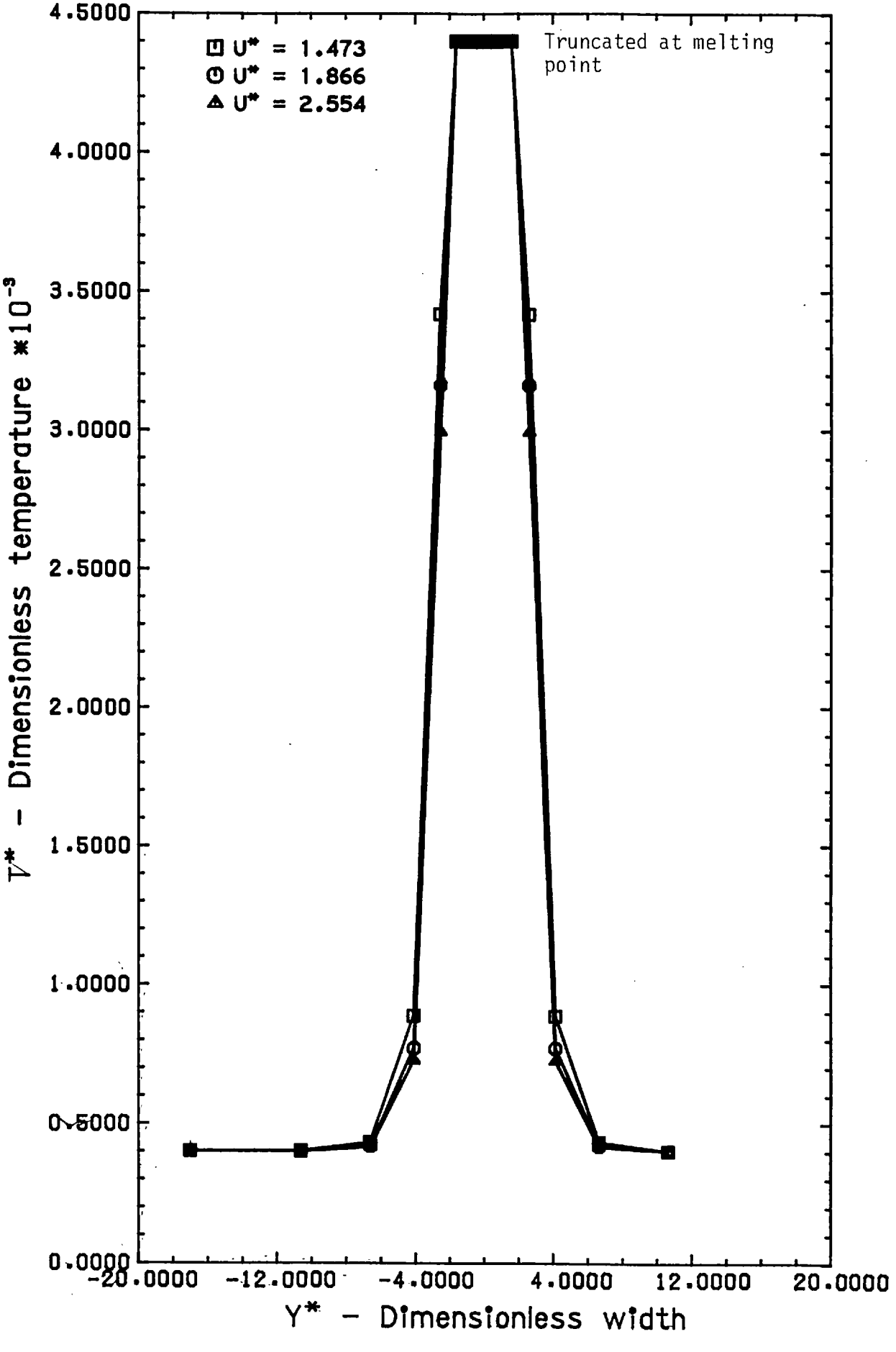

FIG. 3.11b T* vs. Y* through the point of interaction

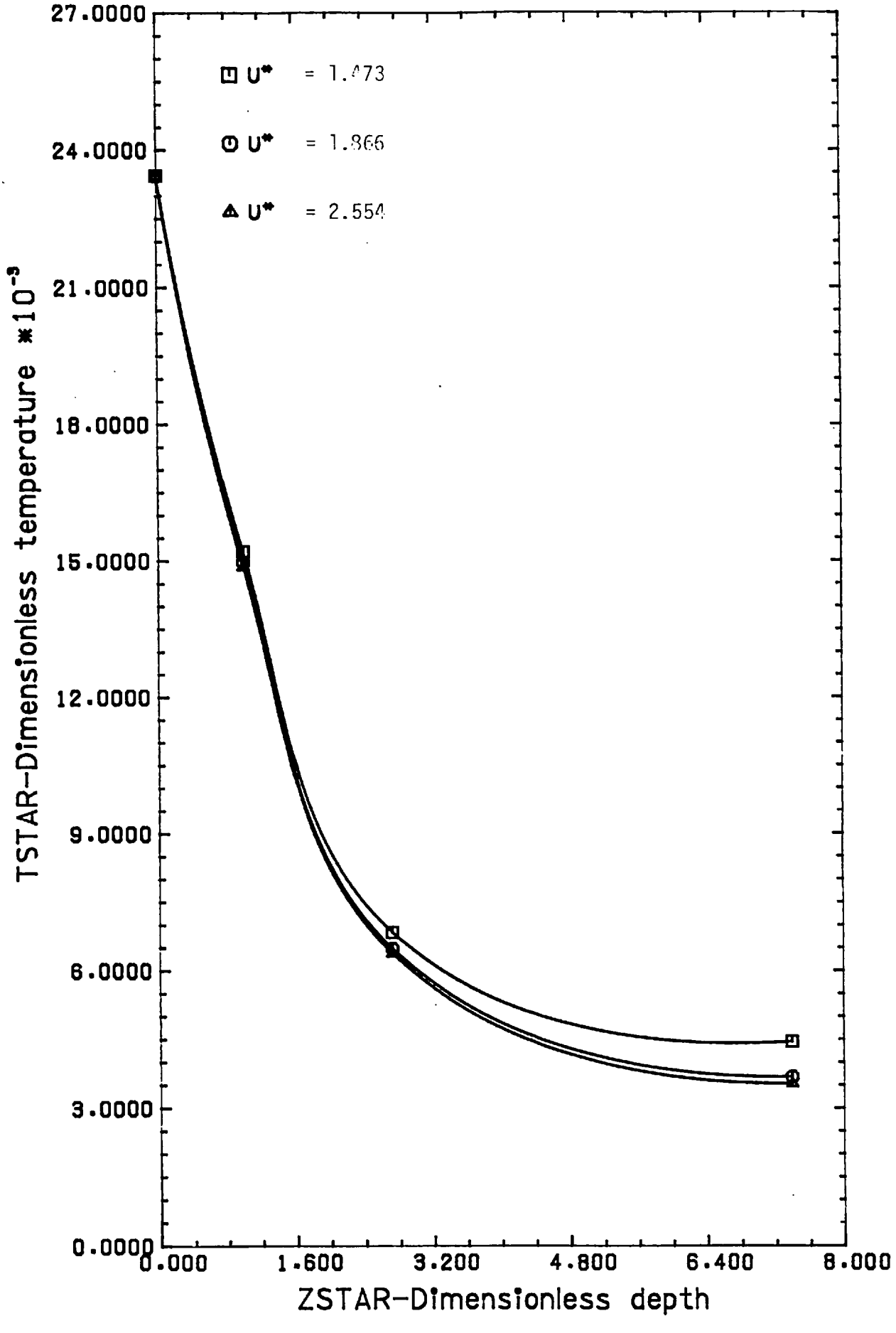

FIG. 3.12 T* vs. Z* through the point of interaction

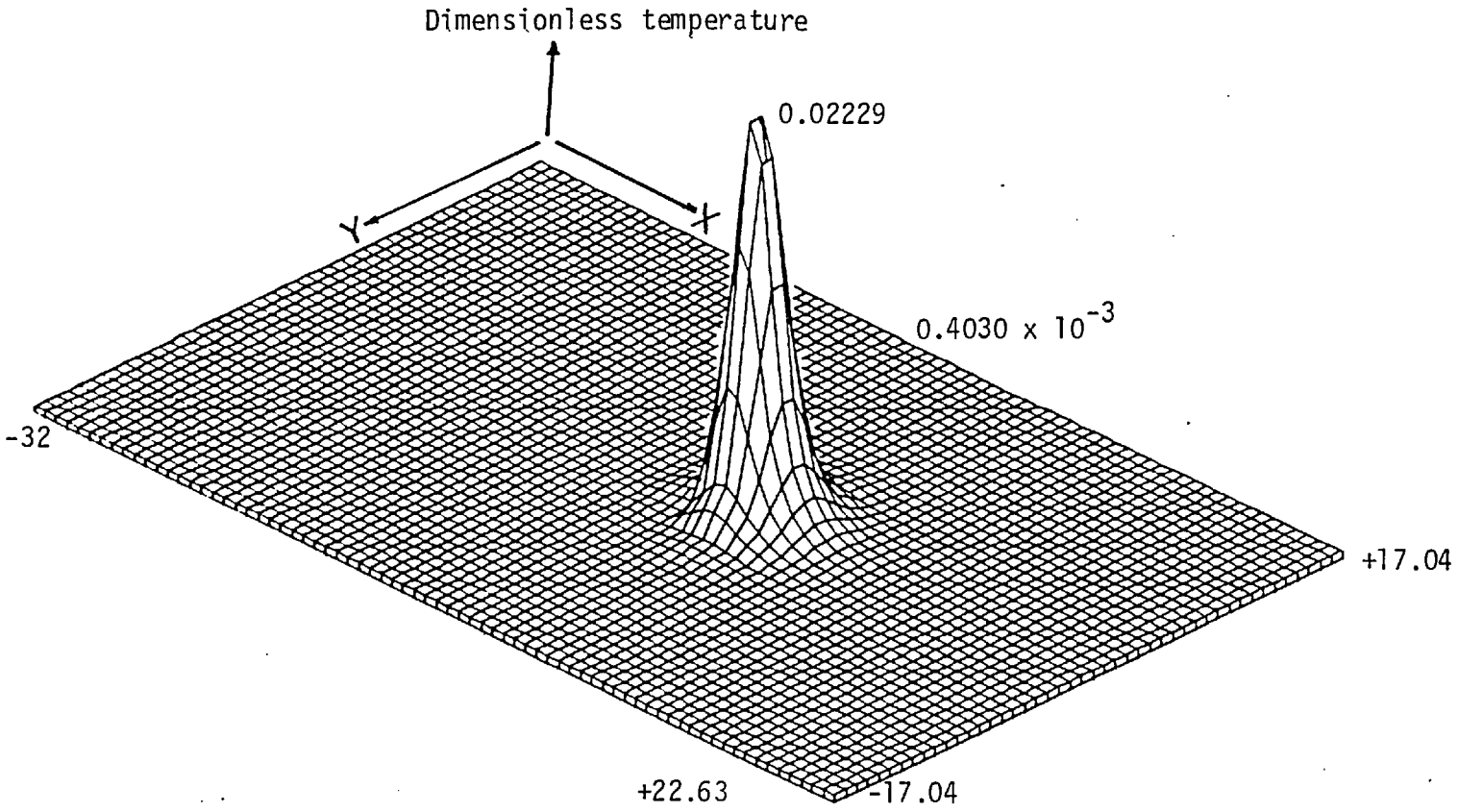

FIG. 3.13a Dimensionless temperature distribution

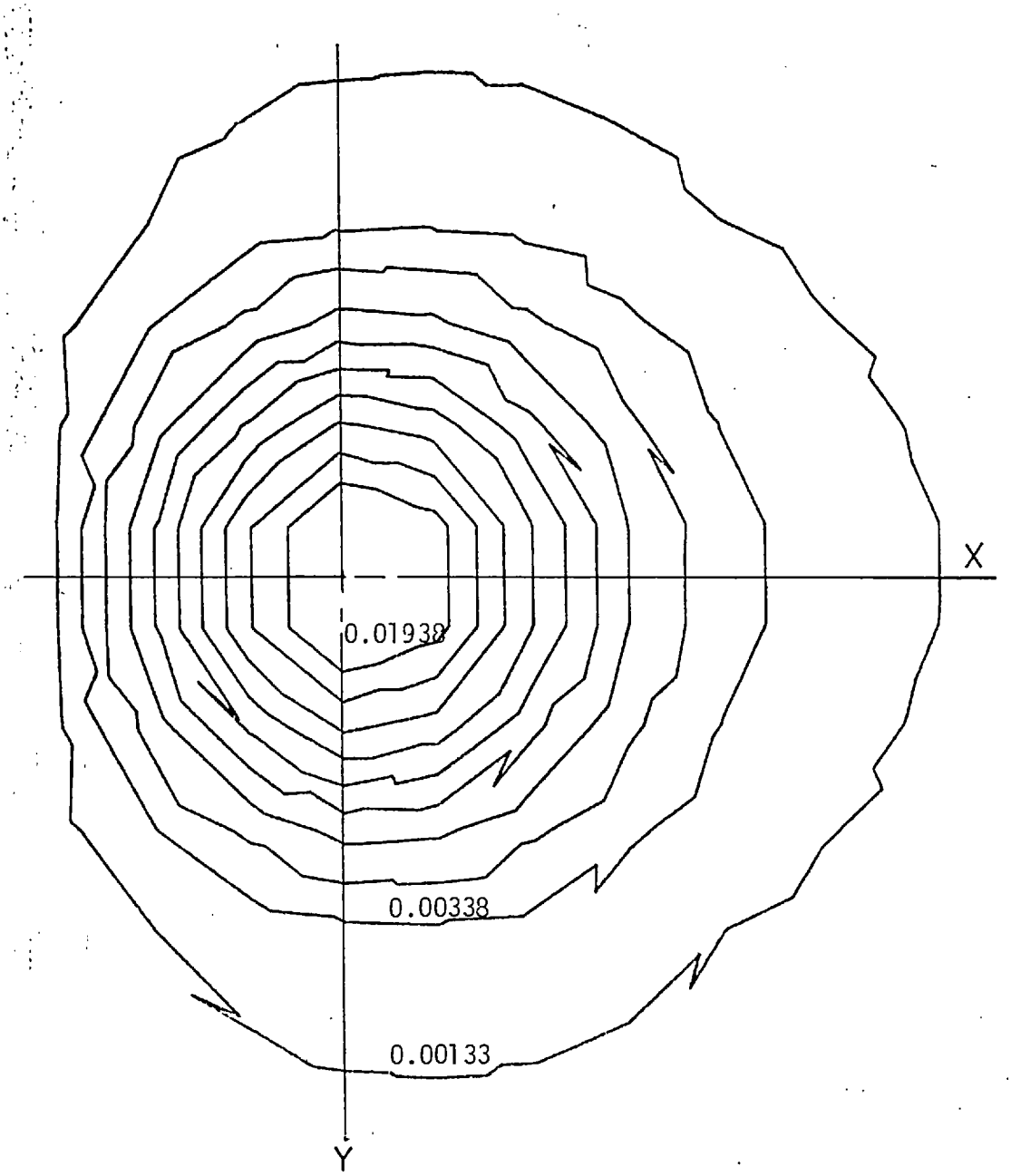

FIG. 3.13b Dimensionless temperature distribution

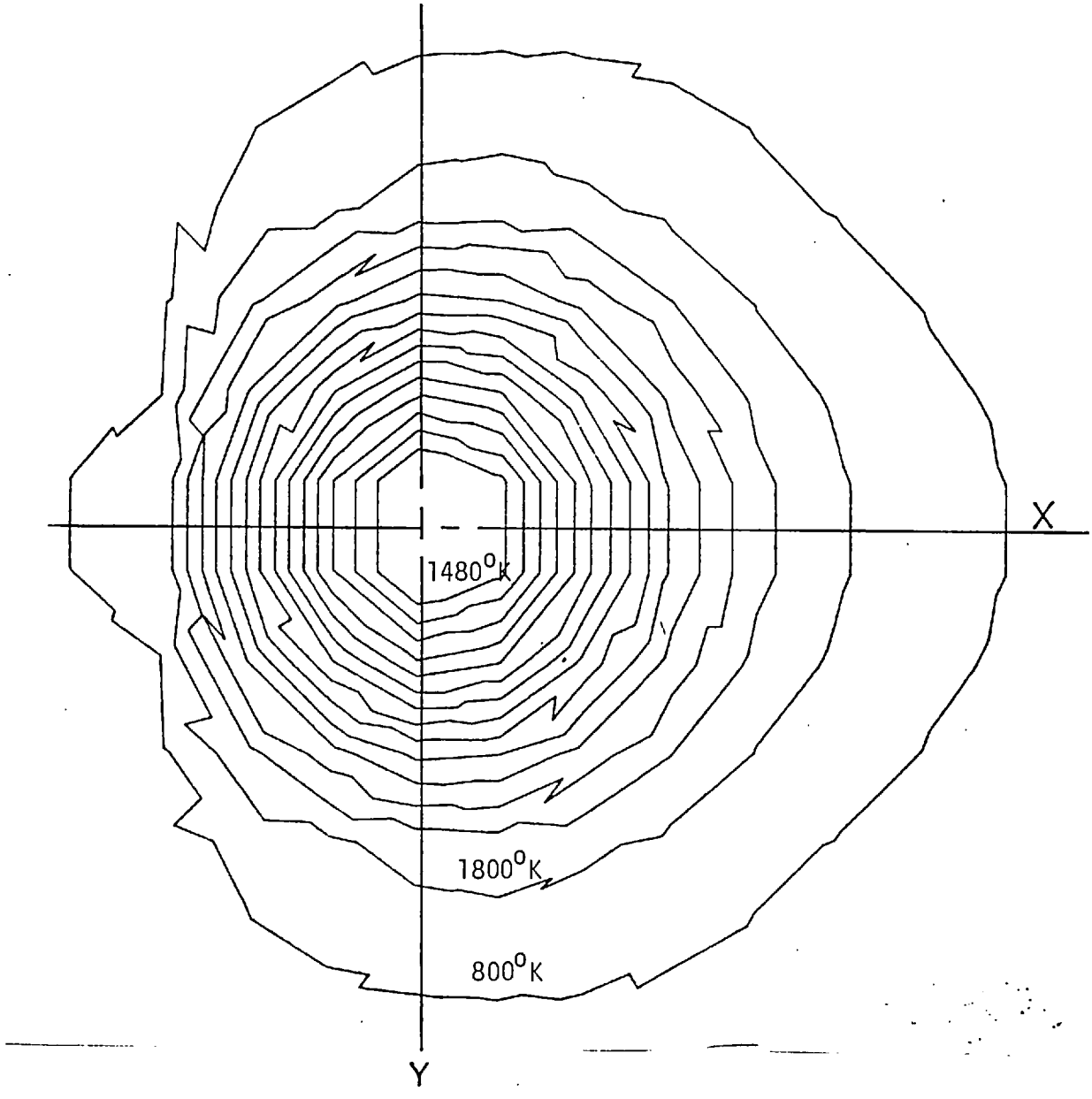

FIG. 3.14 Temperature distribution for a titanium weld

important generalised curves are shown in Figs. 3.10-3.14. The relevant predictions are compared with experimental results in Chapter 7 whenever possible.

3.11 Comparison with other mathematical models

Previous mathematical models for welding are discussed in Section 3.3.1 and 3.3.2 and their limitations are mentioned as and when found necessary. The solutions obtained from this present study are compared here with those from two of these models and with experimental observations.

The two models chosen for comparison are those of Rosenthal[178-179] and Swifthook et al[9]. The Rosenthal model was developed for conventional welding processes but it is the most used model for general welding purposes. Whereas the Swifthook and Gick model is specially developed for laser and electron beam welding.

Fig. 3.15 shows the prediction of the molten pool from these two models along with the prediction from the present study and the experimental observations.

It is evident from the figure that the prediction from the present study is relatively more accurate closely followed by Swifthook and Gick's[9] model.

The reason for the unrealistic prediction given by the Rosenthal's model is mainly due to the following:

1) It assumes a point heat source, whereas in reality the laser provides a finite heat source of gaussian power distribution.

2) There is no provision for convective and radiative heat loss.

3) There is no provision for a keyhole method of heat transfer.

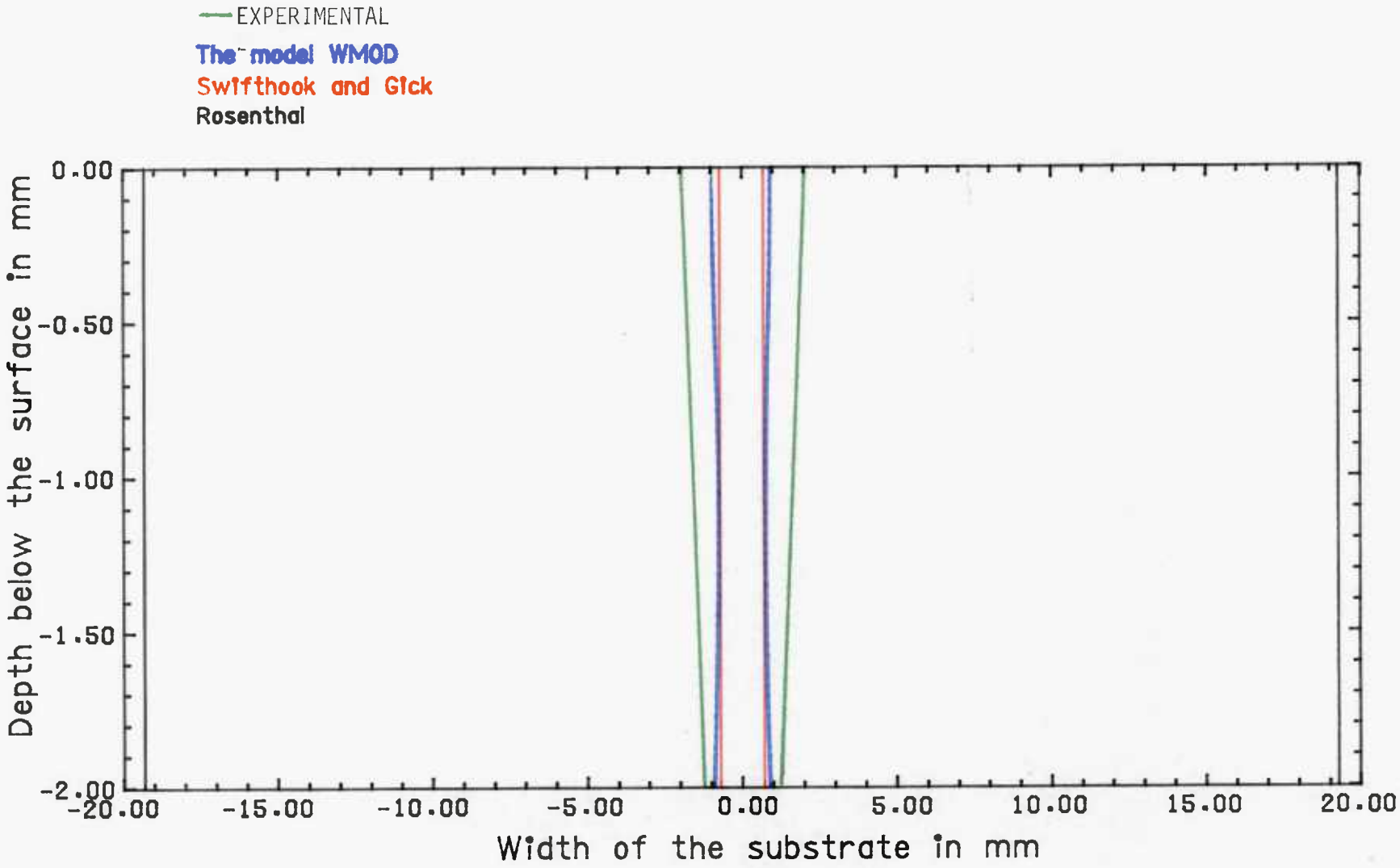

Fig. 3.15 Molten pool prediction from different mathematical models compared to experimental observation.

Therefore, Rosenthal's model is not suitable for modelling the laser welding in three dimensional heat transfer problems.

The main assumptions of the Swifthook and Gick's model which cause it to differ from the present study are:

1) It assumes a line heat source
2) There is no provision for convective and radiative heat transfer
3) There is a truncation of the Bessel functions.

The suggested model is the present study could be made even more accurate by incorporating the following:

1) Variation of physical properties with temperature
   e.g. thermal conductivity, specific heat, reflectivity.
2) Latent heat of evaporation
3) The convective movement of molten material within the weld pool. But it is obviously very difficult to quantify.

CHAPTER 4

THEORY AND DESIGN OF APPARATUS

4.1 Introduction

The basic requirements for welding processes are discussed in section 2.1. The advantages of the laser for welding are summarised in section 2.3.9. In summary, the essential considerations for laser welding are described below:-

1) Amount of power needed as energy source

2) Length of time for which the power is needed

3) Side effects anticipated for laser-substrate interaction.

4) An optical system to manipulate the power beam.

5) Work handling jigs to manipulate the substrate or workpiece with suitable arrangements to prevent atmospheric contamination.

Apparatus used to satisfy the above considerations are described and reasoning for their choice is furnished as and when required.

4.2 Selection of Laser

A laser is a device consisting of an optical cavity containing a medium, solid, liquid or gas, which when "pumped" to an excited state by some external energy produces coherent radiation as a result of stimulated emission. The wave length of the beam depends on the lasing medium. A brief summary of principal characteristics of various types of commercially available lasers are given in Appendix 4 .

For any full penetration welding steady and continuous energy source of several hundred watts is required. The CO_2 laser is the

only type at present which is capable of producing multikilowatt output continuously for any length of time.

Therefore, a CO_2 laser was chosen for this study of welding. A 2kW CW CO_2 laser (BOC Model-901), was made available by B.O.C. and the S.R.C. It was the most powerful commercial laser of its kind in Europe at the start of this work in 1974.

The essential features of the 2kW CW CO_2 laser is discussed in the next section.

4.3 2kW CW CO_2 Laser

Possibility of using CO_2 as a laser medium was first reported by Patel[207-209], since then considerable work was done to develop the system. Due to its high operational efficiency around 20% it had the potential to produce a high power radiant beam continuously.

CO_2 lasers use a mixture of $CO_2/N_2/He$ as the lasing medium. There are several publications[2-5,17,207-209] on the theory of these lasers, a very brief summary is included in appendix 5.

For the present study B.O.C. Model-901 2kW CW CO_2 laser was used.

4.3.1 Description of BOC 2kW CW CO_2 Laser (Model 901)

Basic features of the laser are shown in Plate 4.1 and described in detail in the BOC operating manual[210]. It operates on a fast axial flow design (i.e. gas velocities up to 500 m/s) with shock stabilisation of the plasma discharge by throttling the gas with the help of nozzles. It produces powers in excess of 2kW from a folded 8 meter active cavity.

The machine operates with a gas mixture of CO_2-He-N_2. Approximate gas composition with typical gas consumption on full power is given in Table 4.1.

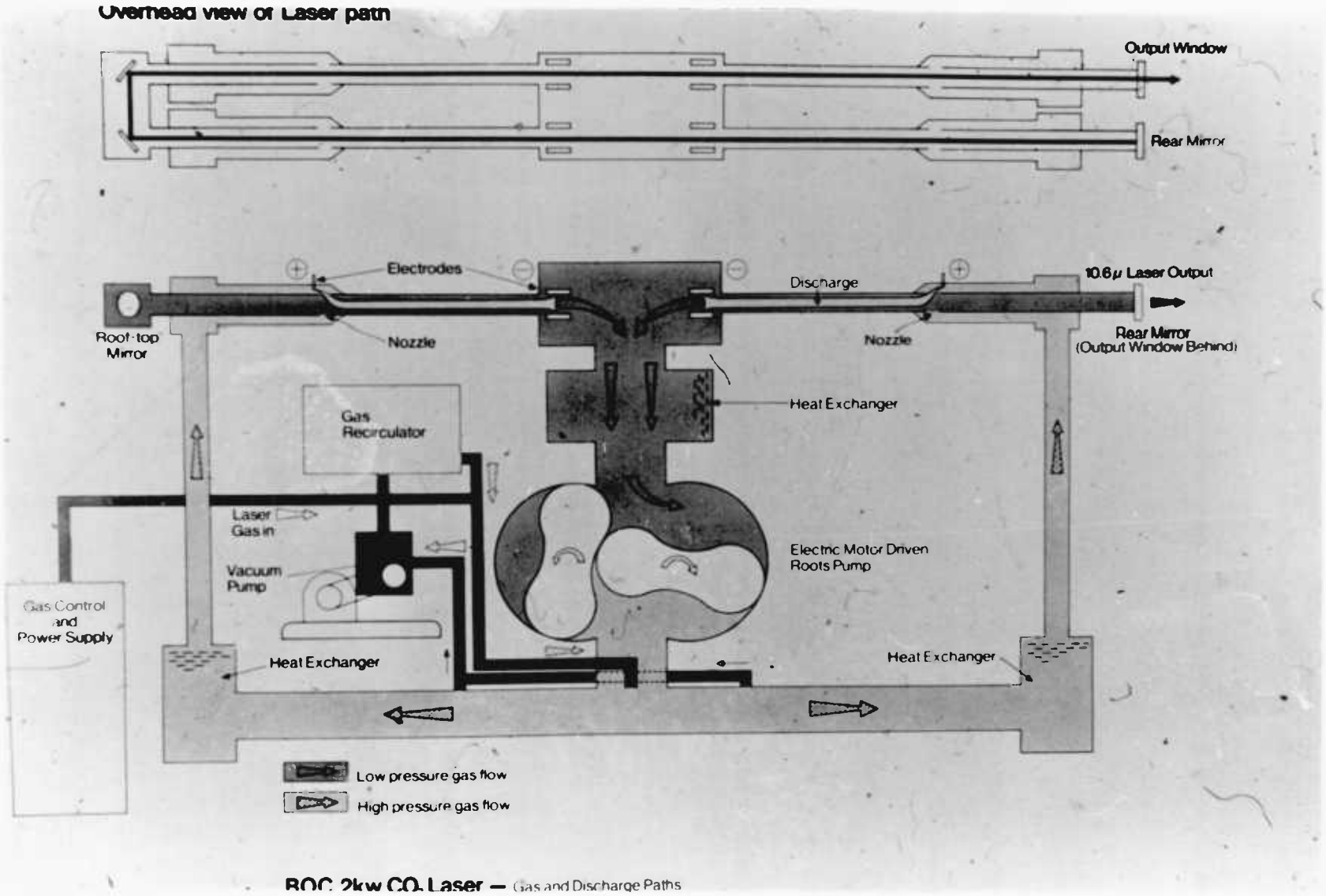

PLATE 4.1A Schematic diagram for BOC 2kW CW CO_2 laser system with gas and discharge paths

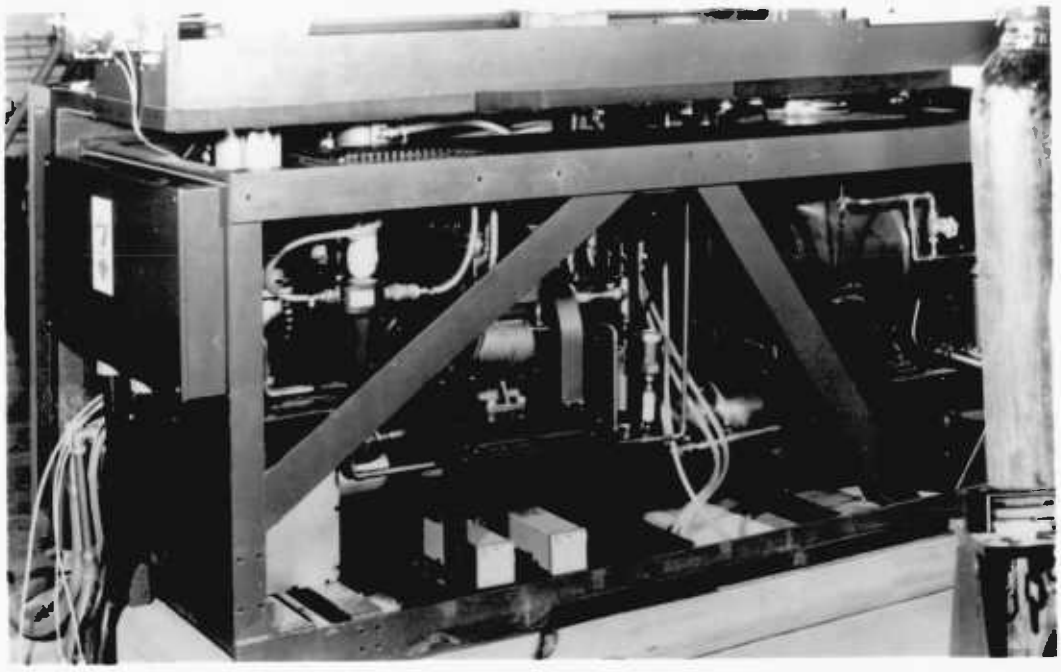

PLATE 4.1B BOC 2kW CW CO_2 laser with power supply and transformer

Constituent Gases	Composition wt %	Typical Gas Consumption at † Full Power with Recirculator Litre/hr.
Helium	75 - 85	170
Nitrogen	10 - 14	50
Carbon Dioxide	5 - 10	6

† From BOC Technical literature

TABLE 4.1

The machine is provided with gas recirculator for economic operation. The gas recirculator recovers Helium from used gas after passing through different catalysts at certain temperature. It reduces the consumption of Helium to less than 10% compared to the helium consumption without the recirculator.

The working gas pressure is 38-45 torr, depending on power required.

The cavity optics consists of one spherical total reflectance mirror and two plane mirrors of gold coated Beryllium-copper and an output window of Gallium arsenide which allows around 36% of beam to be transmitted. All optics are water cooled.

Circulating gases are cooled by gas/liquid heat exchangers shown in Plate 4.1 and the cathode assembly is also cooled with a water jacket.

A roots blower is used to circulate the gases through the plasma region at around 500m/s velocity which allows a stable discharge at these relatively high pressures by shock stabilization.

The gas mixture is electrically excited by low current and high voltage (700 ma D.C. total current with an open circuit voltage of 30kV.).

The discharge is converted to light energy of 10.6 μm wavelength as discussed in Appendix 4B. The cavity produces a 7 - 20mm diameter beam of low order mode. The actual size depends on the cavity optics and alignment.

The beam is focussed by a potassium chloride lens on to workpiece.

When the beam is not being used it is dumped into a totally absorbing copper cone calorimeter, which is water cooled, by a pneumatically operated gold coated shutter mirror. The purpose of the calorimeter is to obtain a continuous reading of the laser power.

Various safety circuits are incorporated to shut down the whole system automatically in the absence of any required service e.g. gas or cooling water or even cover lids.

A detailed description is available in the BOC Model 901 User's manual[210].

4.4 Design and Construction of Jigs and Fixtures

As summarised in Section 4.1 one of the main considerations for successful laser welding is a work handling jig capable of manipulating the workpiece in a steady and stable fashion with a uniform velocity. There should also be adequate arrangements for shielding the workpiece subsequent to welding to prevent atmospheric contamination. For that purpose several jigs and features were used. They are described below.

4.4.1 Work handling jigs

4.4.1.1 Welding jig with stepping motor (X-Y Table)

(Built by B.O.C. Industrial Power Beams Division)

The electric power driven X-Y table supplied by BOC was used for butt welding at relatively modest speeds up to 60mm/sec.

The rough sketch of the table is given in Figure 4.1. The workpieces were clamped between two heavy steel plates as shown in Figure 4.1

SKETCH FOR WELDING ASSEMBLY

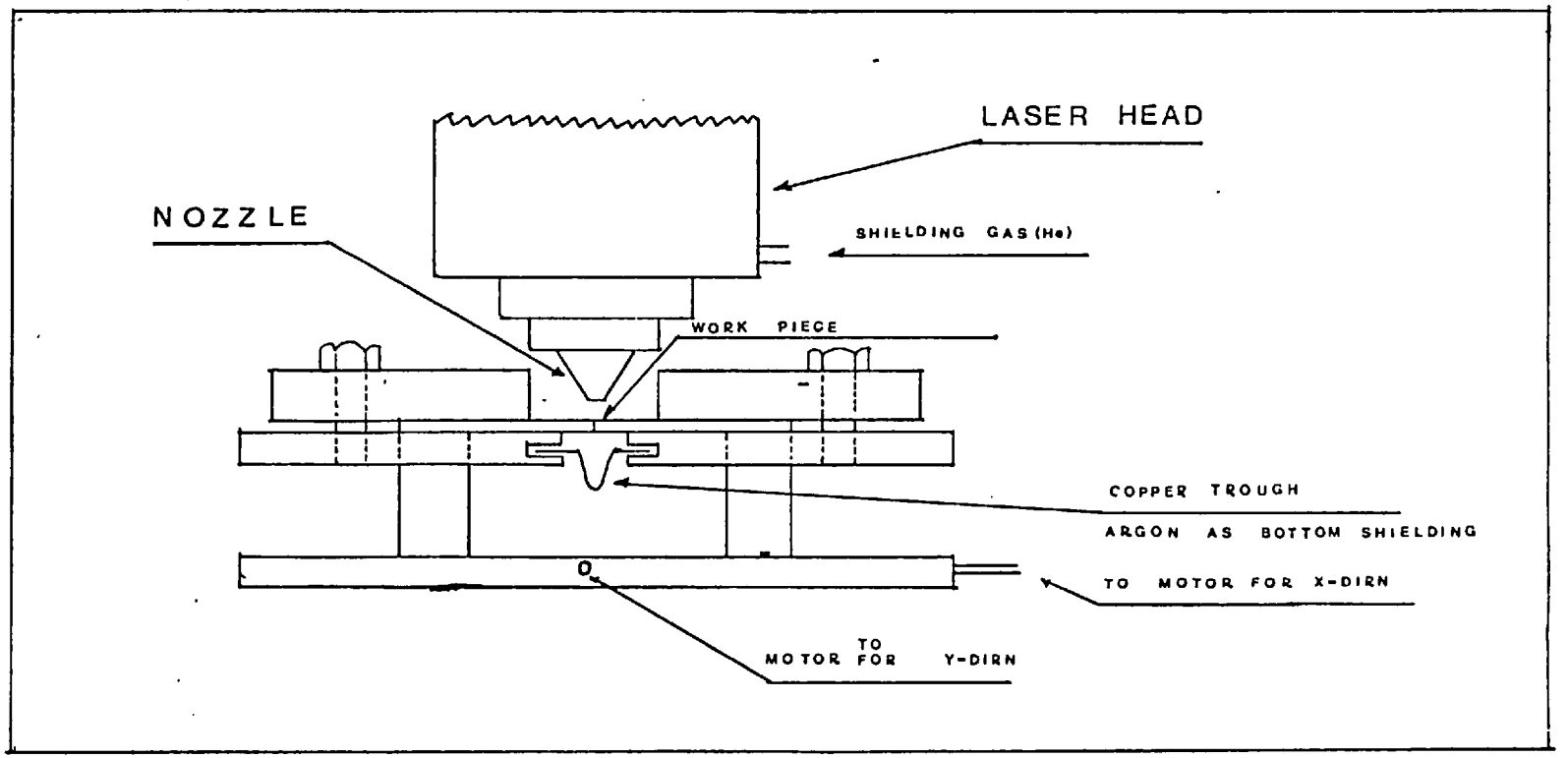

FIG. 4.1 Sketch of welding assembly

The whole assembly was arranged to move in both X and Y direction on spindles of 2.5mm pitch. For uniform speed stepping motors having a maximum torque value of 200 oz-inch was used. The motor was supplied by M/s Unimatic Engineers Limited and the model no. for the motor is 20-3437D20C-E075. The drive unit (Model USD853) was also supplied by the same company.

The Table has also got a provision to adjust the height manually.

4.4.1.2 Hydraulic jig (X-Y table built by M. Eboo, Royal School of Mines)

In view of the modest speed available in the X-Y table mentioned above necessity for an X-Y table with higher speed was felt.

An X-Y table for welding with hydraulic drive having a maximum speed of 368 mm/sec. was built in the department designed by Eboo[211]. The basic features are shown in Plate 4.2.

The hydraulic system was supplied by double A division of M/S Brown and Sharp Limited, United Kingdom.

The hydraulic system could be grouped in three main areas.

a) The Cylinders

In the x-direction the table was driven by a $1\frac{5}{8}$" diameter cylinder having a 15" storke. For the y-direction, a similar diameter cylinder with a 6" stroke was used.

b) Control Valves

Two control valves were needed for suitable operation of the table for each direction. One was required to control the flow of oil to the x-cylinder and thus control the speed. The other valve was used as a limit switch and acted as a safety device to slow down the movement of the trolley at the end of the stroke.

c) Power Unit

This included an electric motor, 4HP, 1500 r.p.m., suitable for 415V $\pm$ 6%, 3ph. 50hz. supply, mounted with a pump and the necessary valves

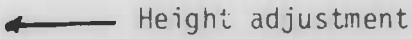
Height adjustment

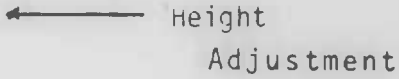
Height
Adjustment

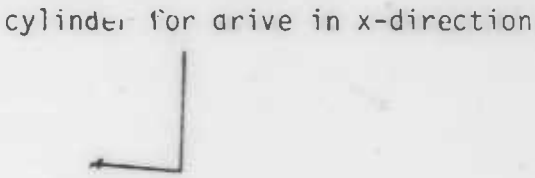
cylinder for drive in x-direction

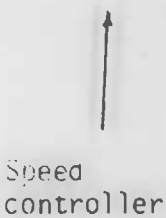
Speed
controller

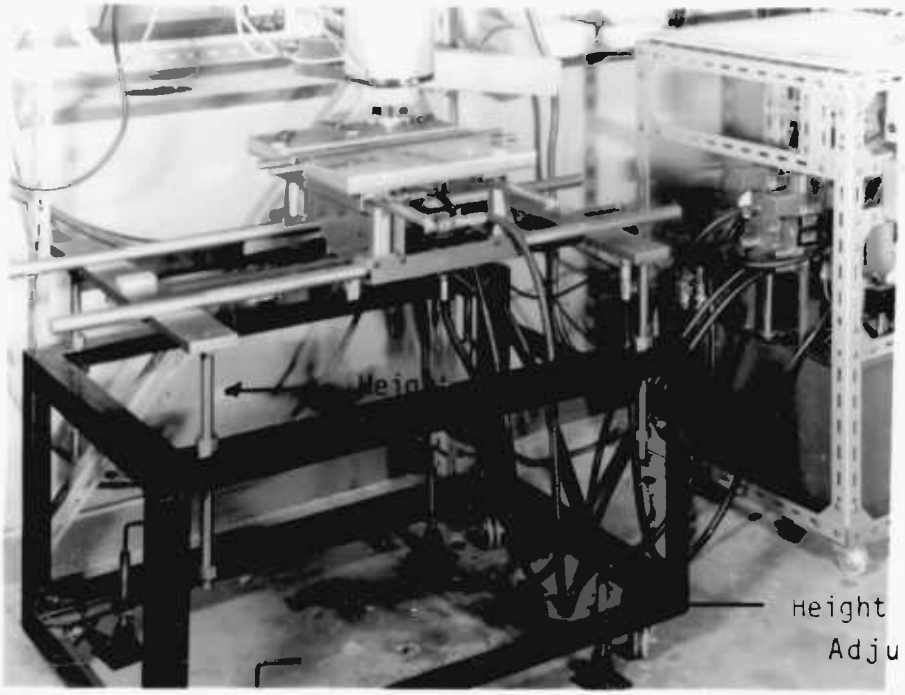

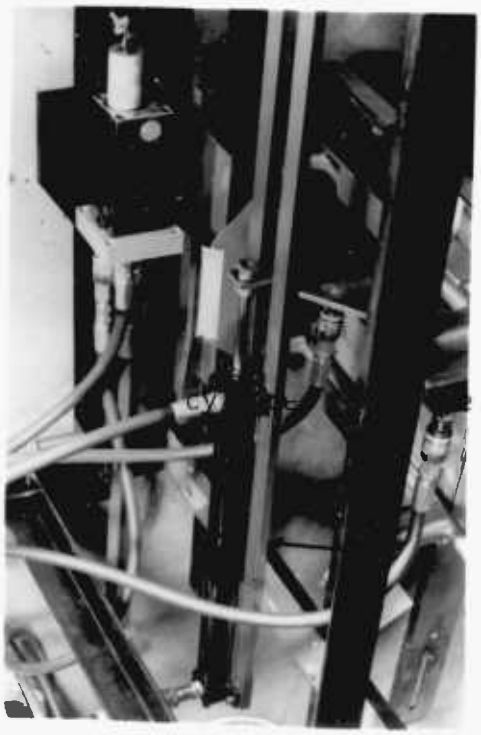

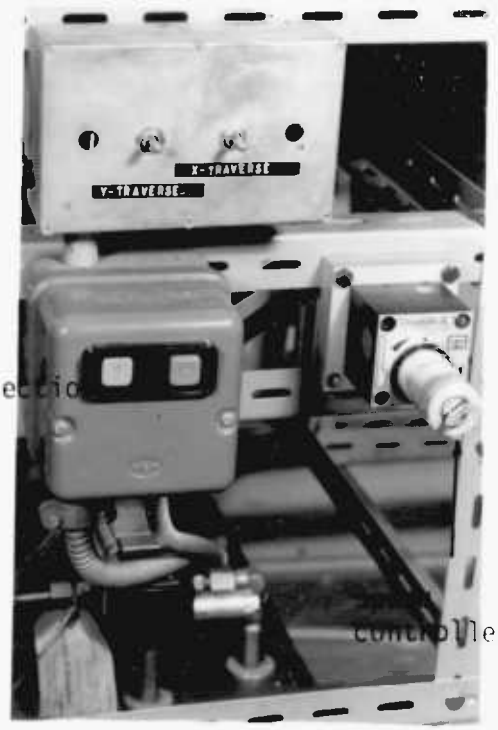

PLATE 4.2 Hydraulic x-y table

to control the hydraulic flow.

Additionally, the table had the facility to elevate or depress through 30 cms. This feature was to allow for the variation of optical systems in the laser and the type of workpiece to be handled. The table top was made up of aluminium and copper which acted as a heat sink. There was a water cooling facility in the copper plates whose relative position could be adjusted to allow for different amounts of bottom sheilding gas.

4.4.1.3 Rolling jig for butt welding thin sheets

Attempts to butt weld thin sheets (0.2mm and 0.4mm) using the above mentioned (Sections 4.5.1.1 and 4.5.1.2) workhandling jigs were unsuccessful because, clamping arrangements for the X-Y tables had to be more than one centimeter apart for the passage of the nozzles. Therefore, the clamping was ineffective in keeping the two sheets in a matched condition during welding. This was due to the thermal deformation caused by the large thermal graidents encountered in laser heating. The maximum speed achieved in the hydraulic table was 36cm/sec. whereas we needed the provision of higher speeds.

In order to overcome this problem a different jig was designed The essential features of the jig are shown in Plate 4.3. The main objective was to keep the material in focus with the matching edges. This was achieved by putting the strip under slight tension while moving it at high speed over a central roll fixed relative to the laser nozzle.

To achieve that objective a jig was designed resembling an ordinary rolling mill with the addition of a centre roll having two clamping collars, as shown in Plate 4.3, to press the sheets together.

Two sets of 2.5" diameter and 7" long rolls, as shown, were used to push or pull the material when required. The roll gap was adjusted by the gear system. The gear system was arranged to slide the upper roll up and down within a fraction of a millimeter precision.

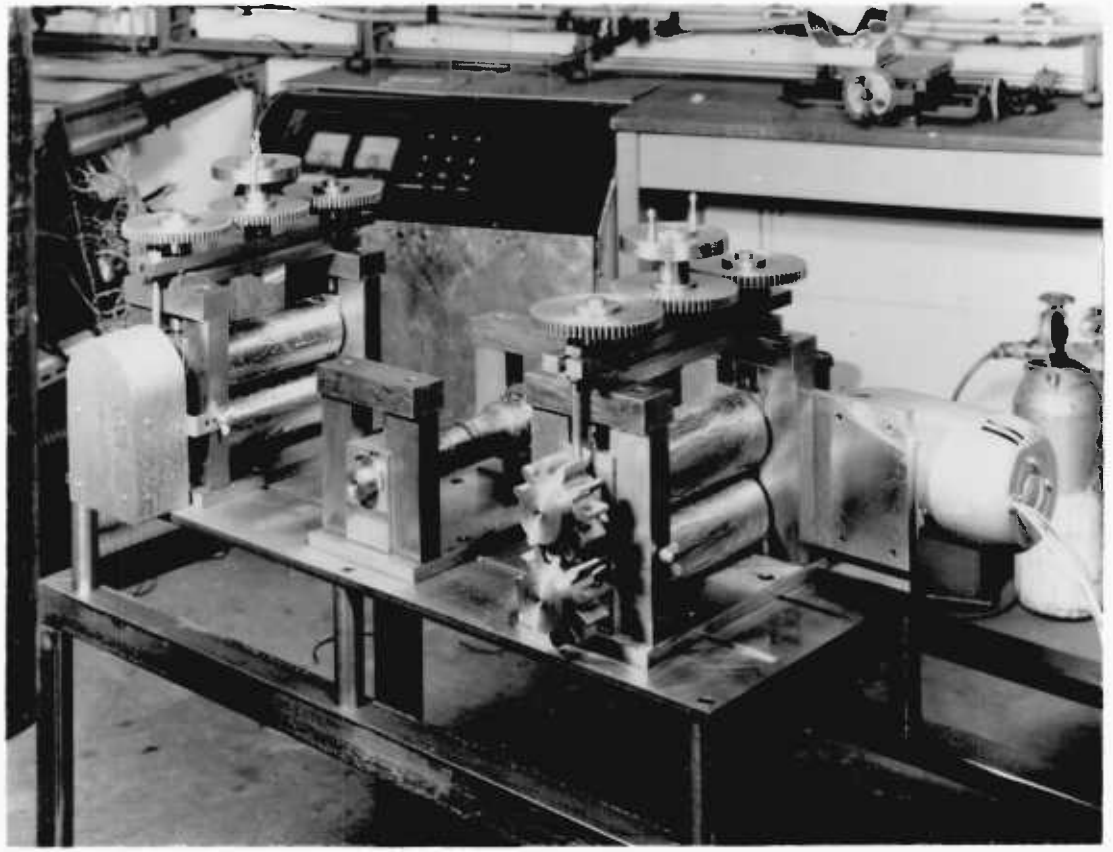

PLATE 4.3A Rolling jig for butt welding of thin sheets


Gear to adjust roll gap
Center roll
Controller
Slide for upper roll
Brake for lower roll

PLATE 4.38

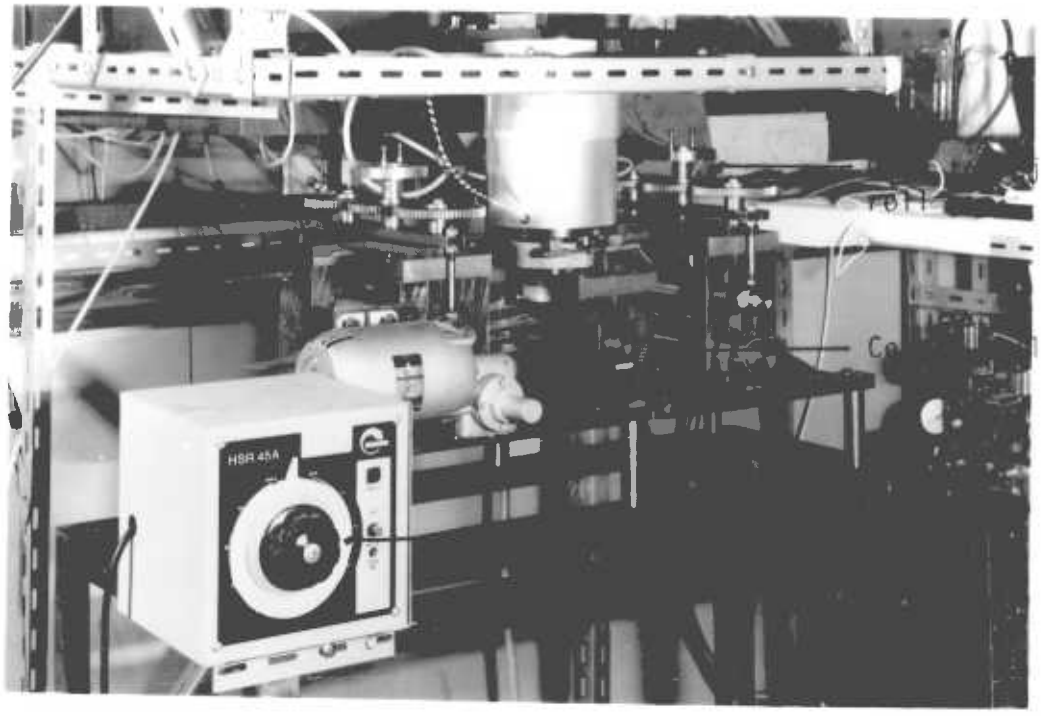

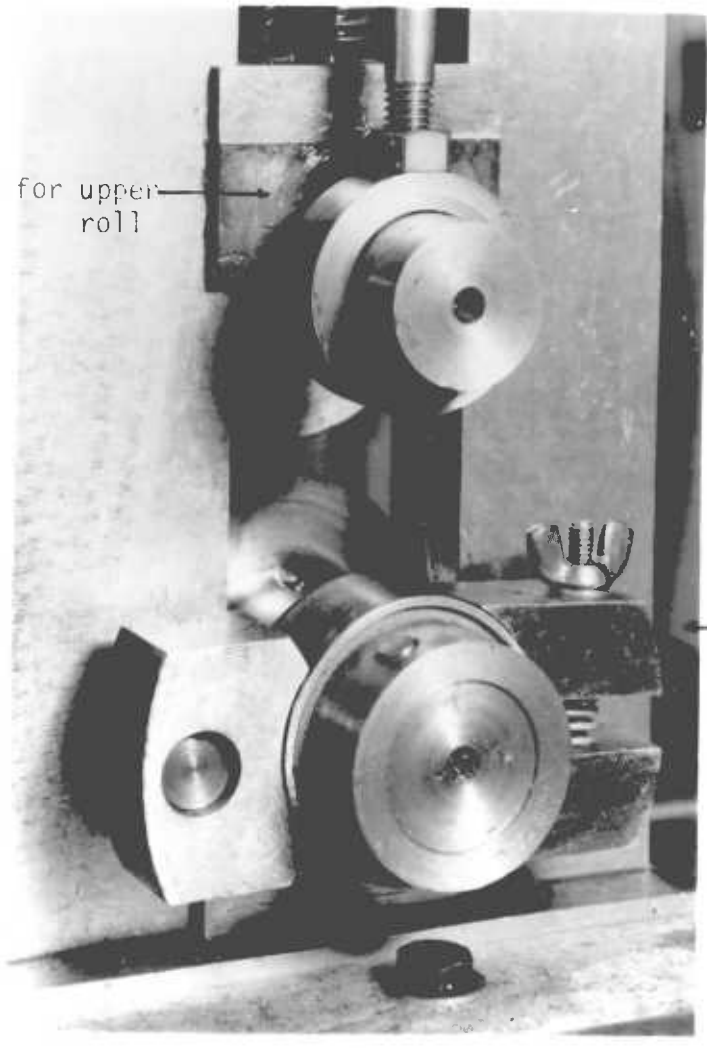

PLATE 4.3B Rolling jig

PLATE 4.3B

The maximum thickness it could handle was 1cm.

A 1.5" diameter and 7" long idle roll was used at the middle. Height of the roll could be varied. By varying the height we could set the centre roll at such a position that strips are under slight tension. The centre roll has two collars which can slide on it and could be fixed with the help of an allen screw. The position of the collars was adjusted to keep the edge of the two sheets level and close as required for butt welding. A 3/8" groove was provided in the central roll for the passage of the bottom sheilding gas.

A 0.25 HP D.C. shunt wound geared motor supplied by M/S Parvalux electric motors Limted, U.K., having a maximum speed of 960 r.p.m. was used to drive the bottom roll which in turn drove the upper roll via gear system as shown in Plate 4.3. The roll gap was limited by the gear system.

Two main considerations for choosing the motor were as follows:-

a) Power to drive

The power of the motor was derived by considering the torque required. The horse power was estimated for maximum available r.p.m. The rough calculation is given below:

Weight of the roll = volume of the roll x density
= 9.75 lb

Torque to drive the roll = load x radius
= 9.75 lb x 1.25" = 1.015 ft.lb

$$\text{Horse power required at 960 r.p.m.} = \frac{\text{torque x r.p.m.}}{5250}$$
$$= 0.186$$

Even for the present requirement the required r.p.m. was much less than 960 and consequently the required horse power. To be on the safeside the 0.25 HP motor was chosen for the purpose.

b) Control of speed

To achieve efficient speed control a D.C. motor was chosen so that the speed could be controlled by varying the input voltage.

Model HSR 45A motor speed controller, supplied by M/S Claude Lyons Controls Limited, was used to control the speed. This is basically a variable autotransformer and designed to provide constant torque throughout the speed range. This is suitable for D.C. shunt wound motors up to 3/4 HP and operates using A.C. mains. The electrical connection of the controller enables the motor to drive in both forward and reverse direction.

4.4.2 Shielding attachment for laser during welding

The primary shielding gas for the top surface of the work-piece was available as a concentric jet with the laser beam through the nozzle. While using the X-Y table with stepping motor the bottom shielding gas was sent through a trough as shown in Fig. 4.1.

But additional shielding at the top surface while welding titanium sheets of 2mm thickness or above was felt necessary to avoid surface oxidation. Therefore, a trailing shielding attachment was designed to be fitted with laser nozzle. Sketch of the attachment is given in Fig. 4.2. This was connected with Argon supply. This additional shielding gas was allowed to pass through a perforated tube of 1/4" diameter. This tube was enclosed in a box as shown in Fig. 4.2. Then the box had a number of holes with different sizes of hole to allow for the variation of velocity of the flowing gas with distance so that a reasonably steady trailing shield was available. The tube had also a small outlet to allow an annular sheilding gas near the nozzle.

While using the hydraulic X-Y table similar type of tube shown in Fig. 4.2 without an end of the stream outlet was used as bottom shielding arrangement.

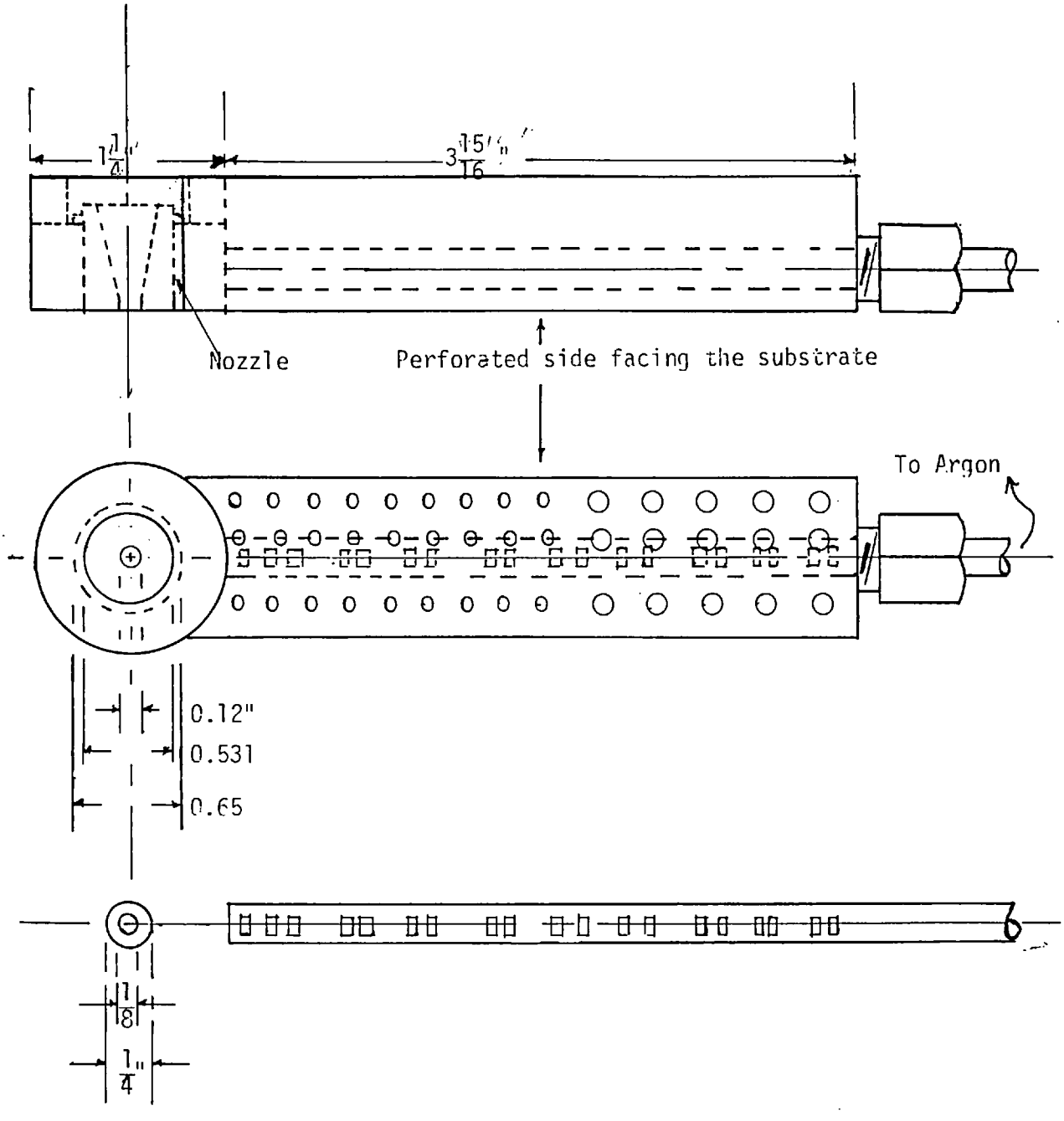

FIG. 4.2 Sketch for top shielding attachment

4.5 Photon drag detector

In spite of the low sensitivity, the photon drag detector was reported to be suitable for monitoring high power laser beam[212-215].

Under open circuit conditions a longitudinal e.m.f. is generated in a bar of p type Germanium exposed to 10.6μm radiation from CO_2 laser radiation due to the transfer of photon momentum to mobile holes[212-214]. This phenomenon is known as photon drag effect.

The photon drag detector uses this photon drag effect to monitor the laser beam.

The objective of the photon drag detector for our purpose is to try to obtain a better method of determining the beam diameter and if possible the mode structure of the beam. The design of the photon drag detector could be divided into three main areas depending on their respective functions and basic features as shown in Plate 4.4.

a) The detector

A 5mm sq. 100mm long p-type Germanium single crystal supplied by the Welding Institute was used as the detector. The crystal was mounted with araldite on a brass rod which was ground flat in area where crystal was mounted. Araldite was used for mounting because it would also act as an insulator. There was water cooling facility with the rod as shown in Plate 4.4. This single crystal used to produce 100 nanovolt for 1 watt of incident laser beam power[216]. An amplifier was needed to amplify the e.m.f. Lead to amplifier was soldered on the Germanium crystal with Indium Solder.

b) Beam chopper

The objectives of the beam chopper were as follows:-

1) To protect the Germanium single crystal from exposure to the whole laser beam of several hundreds of watts of energy which would in turn damage the crystal.

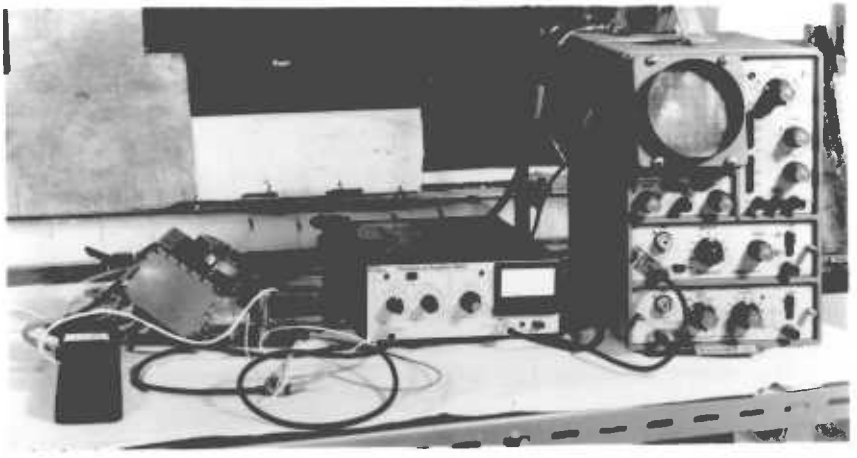

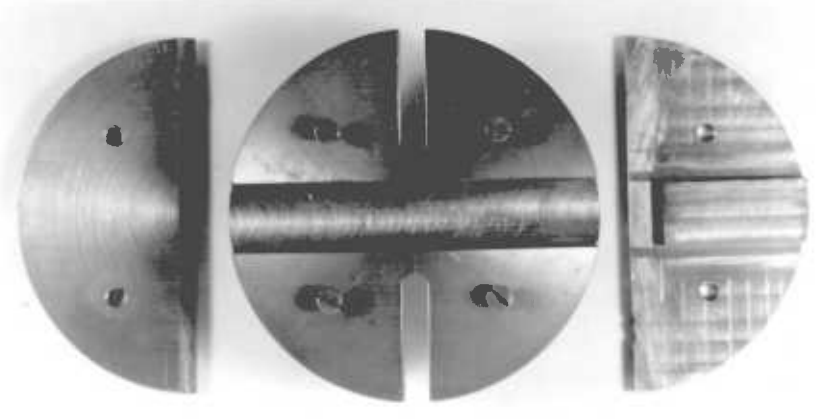

PLATE 4.4 Photon drag detector

2) To scan the beam with a definite slit width so that a portion of the total power incidents on the crystal as a function of the position within the beam. This was done with a view to get an idea of power distribution within the beam and thus the mode structure. For a known r.p.m. of the chopper and known slit width the power distribution and mode structure may be calculated by the circular argument of assuming the beam is gaussian and axisymmetric. The method of calculation is shown in Appendix 6.

The whole assembly of the beam chopper and the crystal is illustrated in Plate 4.4. The beam chopper was rotated at 3000 r.p.m. using a direct drive A.C. Motor supplied by M/S Crouzet England Ltd. The beam chopper was made of two semicircular brass plates and the slit width between the plates could be varied by sliding the two plates mounted on bare plate as shown in Plate 4.4. The position of the plates was secured by a pair of screws for each.

c) Amplifier and Output

For an accurate output a low noise precision amplifier of at least 80 dB gain was needed to amplify photon drag e.m.f. to microvolt range or more.

The amplifier used was model 9452 - a precision A.C. amplifier supplied by M/S. Brookdeal Electronics Ltd., U.K. important specifications are given below:-

Bandwith	+0, -3dB	1Hz to 1MHz
	+0, -1%	7Hz to 140 KHz
Gain - switched		30 to 100 dB in 10 dB steps
variable		0 to -11dB continuous
Linearity		0.001% typically
Power requirements		line only
voltage requirements		100 to 130V rms } switched 200 to 260V rms }
Frequency		50-60 Hz

Another advantage of the amplifier was automatic and almost immediate recovery from continuous overload.

The main limitations of the photon drag detector is that in order to analyse photon drag traces we have to assume that the beam is already axisymmetric and the power distribution is gaussian. However, the calculation method is given in appendix 6 for better understanding of the problem.

4.6 The Laser Head

The laser head was supplied as extra cavity optics as the part of B.O.C. Model 901 2kW CW CO_2 laser. The laser head was mounted on the main body of the laser.

In order to make more working area and to reduce the vibration of the head due to vibration of the body of the laser, the laser head was removed from the main frame and mounted on a separate dexion frame free from the laser structure. The mounting assembly is shown in Plate 4.5

The detailed description of the laser head containing the lens holder is available in the B.O.C. manual[210]. The basis of the laser head are illustrated in Fig. 4.3 and Plate 4.5.

The lens holder assembly was provided with facilities to adjust the position of the lens in height with respect to nozzle by means of a number of spacers. The nozzle position could be shifted in all the three directions (X-Y-Z) by means of screw winding adjustments.

4.7 The Lens

Bi-convex lenses were used to focus the beam for welding. They were made of polycrystalline potassium chloride ground and supplied by M/S Special Ltd., U.K. However, KCl suffers from rapid attack by moisture if the humidity exceeds 35%[217]. Therefore, a lens heater was fitted to the lens holder. Lenses not in use had to be stored in

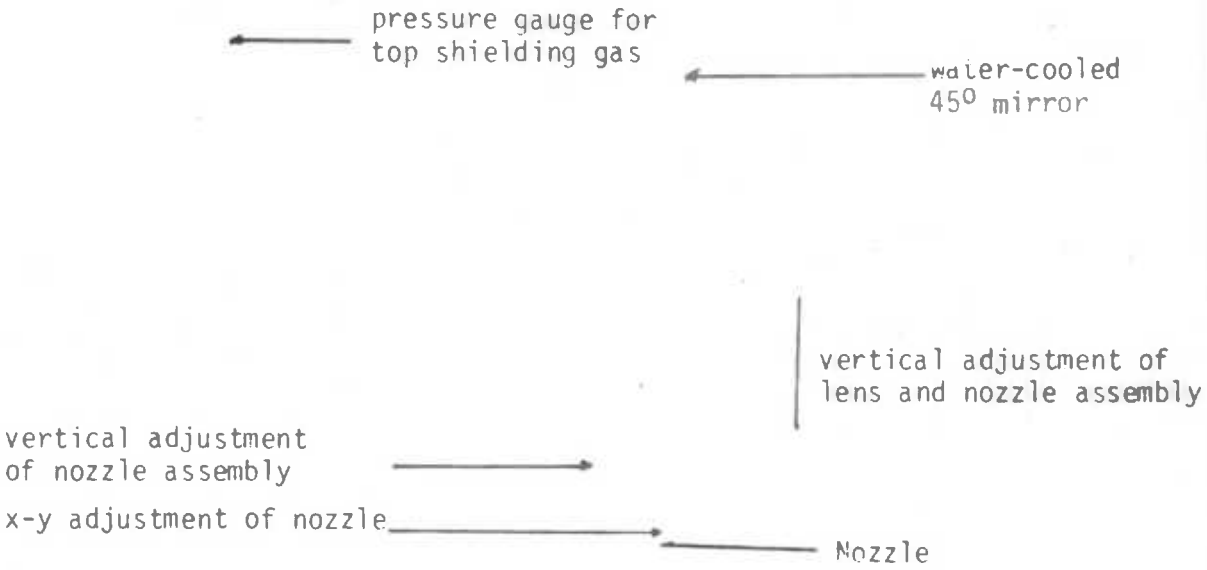
pressure gauge for
top shielding gas
water-cooled
45° mirror
vertical adjustment of
lens and nozzle assembly
vertical adjustment
of nozzle assembly
x-y adjustment of nozzle
Nozzle

PLATE 4.5

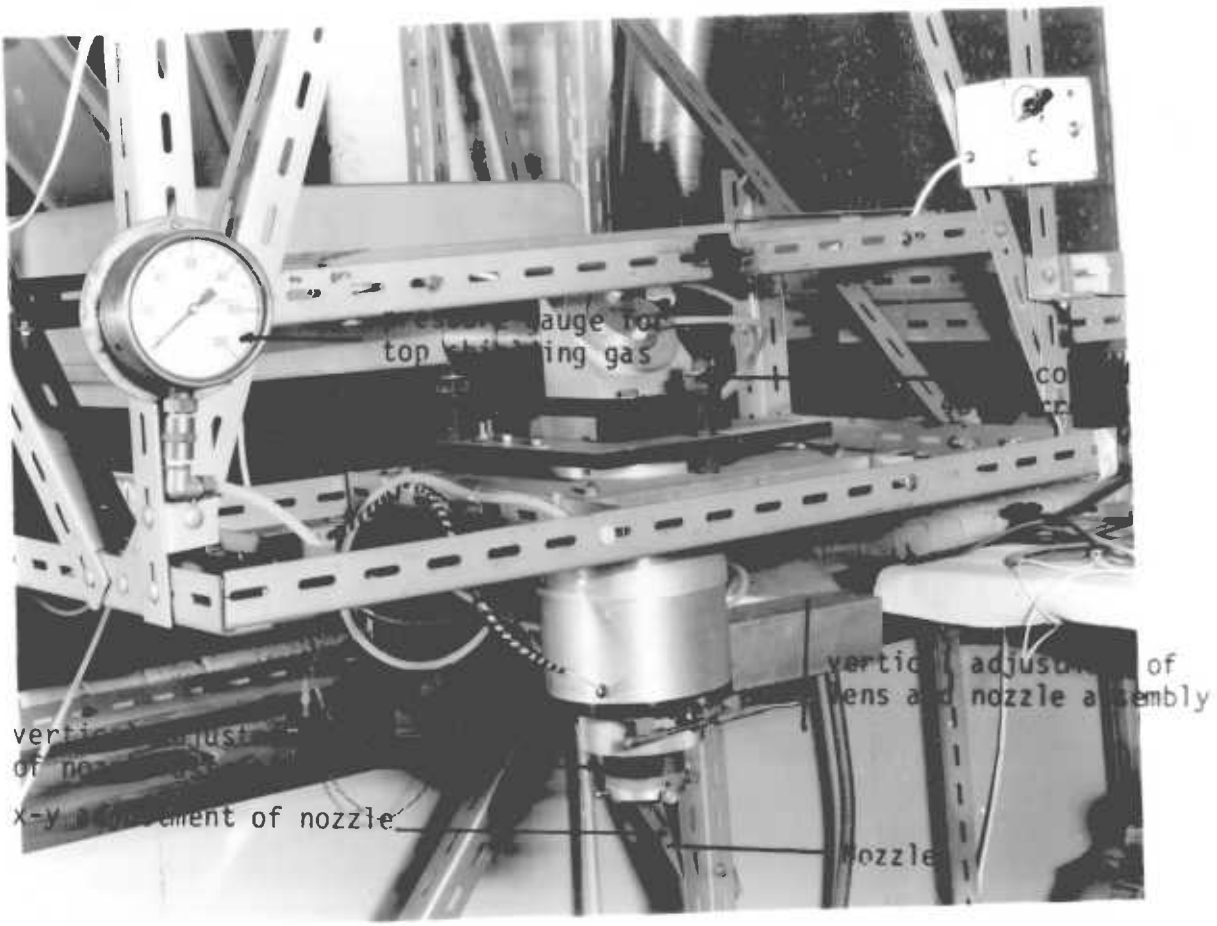

PLATE 4.5 Laser Head

PLATE 4.5

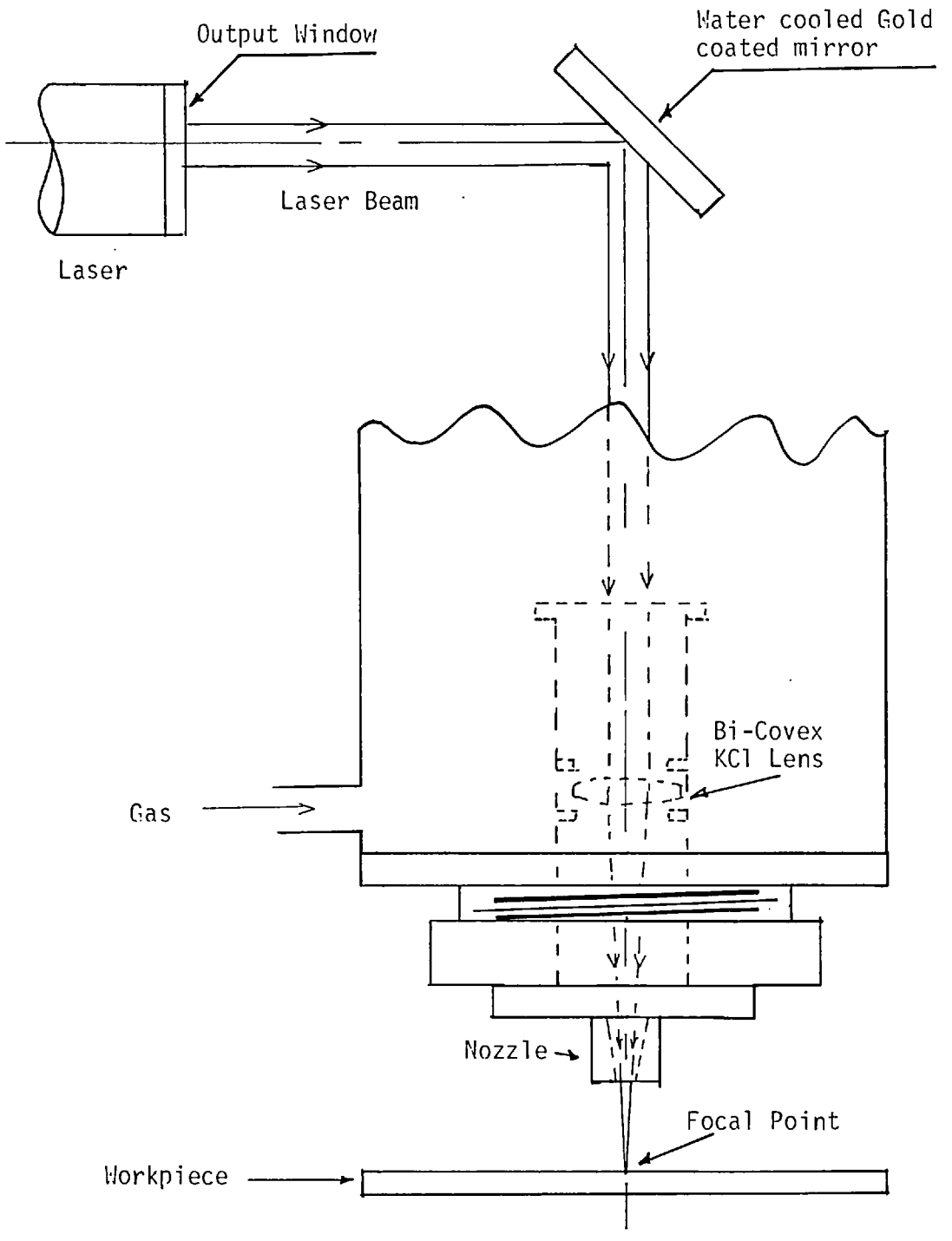

FIG: 4.3. Sketch for Laser head and lens assembly

dessicators or in an oven. Optical properties of different materials compared to KCl are given in Table 4.2. A comparison between competitive lens materials was given by Steen[17] (p112) KCl was chosen because it was relatively cheap and breakages at 2KW are not uncommon. It was also durable and transparent to 10.6 μm as well as ordinary light.

Possibly due to thermal warpage and divergence of the beam the focal length of the lens varies slightly with power. Therefore, after changing power some refocussing was required.

Gallium Arsenide and zinc selenide may have been better but were far more expensive.

Material Specification	Optimised Ge	CdTe	ZnSe	GaAs	NaCl	KCl
Bulk absorption @ 27°C to 10.6μ cm^{-1}	0.018	0.002	0.006	0.02	0.002	0.002
Specific heat J/cm^3 °C	1.65	1.23	1.87	1.42		
Thermal conductivity W/cm °C	0.60	0.07	0.21	0.46	0.07	0.07
Refractive index @ 10.6μ	4.0	2.64	2.4	3.3	1.50	1.50
Transmission range	2-23	1-30	.5-20	1-18	.2-21	.2-21
Flexural strength (rupture modulus) p.s.i.	13,500	3,200	8,500	20,000	350	330
Density grm/cm	5.323	5.86	5.27	5.32	2.17	2.00
Typical thermal distortion figure of merit† (AR coated window 5mm thick @ 100W throughput)	0.018	0.023	0.015	0.031		

† = Device absorption/(specific heat x thermal conductivity) low values being an advantage

* (After Ref. 217)

TABLE 4.2

Optically relevant properties of various lens materials

CHAPTER 5

OPERATION OF THE EQUIPMENT

5.1 The Laser

5.1.1 Operation of the Laser

The main objective in the successful operation of the laser is to obtain a steady desired output power of low order mode for a desired length of time. The details of switch-on procedure and operation procedure to vary the output power are given in BOC Model 901 CO_2 laser operating manual[210].

The important factors influencing the output power are discussed below.

5.1.2 Output Power

The power output from the laser was found to be a function of the discharge tube pressure, the gas composition and the tube current, together with the proper adjustment and cleanliness of the apparatus. The effect of each of these parameters is now discussed in term.

5.1.2.1 Effect of tube pressure

Laser power decreases with decrease of gas pressure. The laser was operated normally at 40-45 torr pressure but it could be reduced to 20-25 torr by altering all three gas regulators such that the gas mixture remains the same. The details of method of altering gas pressure is given in manual[210]. Again, discharge impedence reduces with the reduction of tube pressure and, therefore, readjustment of variac to keep a constant current is necessary.

5.1.2.2 Effect of gas composition

Gas composition may be varied by reducing the pressure of one or more of laser gases (He, N_2, CO_2). Thus a gas composition

less than optimum gas mixture may be produced which in turn would reduce the output power. CO_2 is the most important constitutive in the CO_2 laser gas mixture and responsible for lasing action though it is the smallest fraction of the gas mixture. Therefore, variation of CO_2 gas pressure would have least effect on tube pressure but large effect on output power, which means fine control of CO_2 pressure will give effective control on laser output power.

However, as power requirement for the present study was mostly around 1kW or above variation of gas composition was not required. For future reference the gas pressure setting generally maintained is given below, He - 16-17 psi, N_2 - 42 psi , CO_2 - 14 psi.

5.1.2.3 Effect of tube current and input voltage

Laser output power should saturate at approximately 160mA tube current[210] keeping gas pressure at a normal level (40-45 torr). This would give a maximum output of 2kW. Lower powerdown to 800W could be achieved by reducing the discharge current. But it should be noted that the discharge current depends on tube resistance which varies with gas pressure. Therefore, for lower pressure discharge current required would be less. However, details are available in the BOC manual[210].

5.1.2.4 Cleanliness of cavity optics

Unclean mirrors lead to serious fall of power due to scattering caused by foreign particles and scratches.

The gold coated fully reflected mirror was occasionally cleaned with alcohol for light cleaning. Otherwise, it was cleaned with liquid detergent and gently wiped with cotton wool and after that mirror was washed with distilled water and dried. Due to long 10.6μm wavelength of carbon dioxide laser beam it is less sensitive to optics cleanliness compared to lower wavelength lasers.

The output window has rather hard coatings which enables us to clean it in any detergent. But unless plasma tube is

seriously fouled light cleaning with alcohol was enough for the window. Output window had to be kept in a better cleaned condition. Because foreign matter or a scratch on window not only means reduction of power but also means absorbtion of localised power. That in turn heated up the GaAs window resulting in breakage which quickly leads to flooding of the plasma tube and thus considerably work and expense. Thus as routine maintenance this window was cleaned once every week.

5.1.2.5 Foreign matter in plasma tube

The two most common foreign materials contaminating the plasma tube are oil vapour and moisture.

Oil vapour generally comes in the recirculated gas from the exhaust of the vacuum pump. Though, the recirculated gas is passed through a series of alumina and activated charcoal filter[210] some times oil contamination exceeds the level to be coped with by the filters but these are very rare occasions. The presence of oil vapour leads to unclean optics and an interference with the excitation mechanisms and thus fall of power.

Water vapour generally enters the plasma tube when there is a leak in the system from either the heat exchanger or water cooled mirrors. Water vapour may lead to a breakage of the output window as explained in the previous section.

5.1.2.6 Alignment of optics

Fox and Li[218] report that a very small amount of tilt due to misalignment causes a significant perturbation which leads to asymmetric mode patterns and increase of diffraction loss. They also report that for relatively large values of Fresnel number and tilt angle, two of the lowest order modes become degenerate in loss. However, Fresnel number[229] "N_f" for the laser used is as follows

$$N_f = \frac{(\gamma_m)^2}{L_c \times \lambda} = \frac{(1.7 \times 10^{-2})^2}{8.0 \times 10.6 \times 10^{-6}} = 3.408$$

where γ_m = radius of mirror L_c = length of cavity
λ = wavelength of the radiation

Therefore, for such small fresnel number low order modes are expected unless there is a serious misalignment of the optics

The misalgnment of cavity optics are generally caused by:-

a) Erroneous alignment of the optical bench when setting up the laser

b) Thermal warping of the optics.

Therefore, extreme care should be taken during the setting up of the optical bench. There should also be adequate cooling arrangements for the cavity optics to offset thermal warping.

Extreme non-alignment would result in the over heating of the 'O' rings holding the output window which would foul the window, increase its absorption and so overheat and break.

Misalignment also causes edge truncation of the beam leading to a decrease in the output power. Care should also be taken while focussing the beam through the lens onto the workpiece The beam should be incident at the central area of the lens and perpendicular to the plane of the lens to avoid spherical aberration and coma effects. The focussed beam should emerge out of the nozzle without touching it i.e. without truncation of the beam which would reduce the power without this being recorded on the calorimeter.

5.1.2.7 Cooling of cavity optics

Efficient cooling of optical cavity is absolutely necessary to maintain the thermal stability of the cavity. Otherwise as explained in the preceeding section, thermal warping would lead to misaligned cavity optics.

For the BOC model 901 CW CO_2 laser cavity optics, external 45^{o} mirror and the calorimeter were water cooled, as shown in Fig. 5.1.

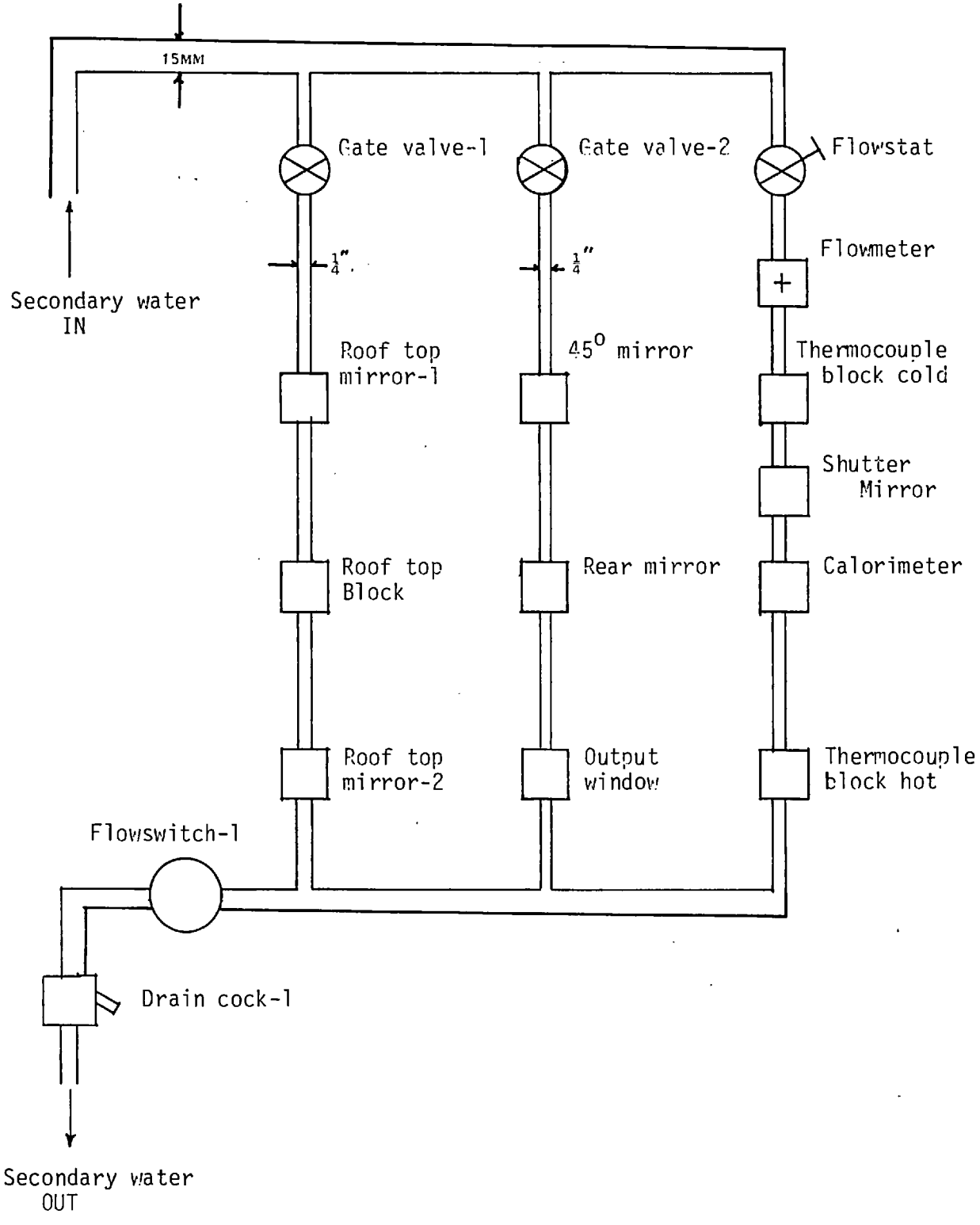

FIG: 5.1 Secondary water circuit for BOC 901 2kw CO_2 Laser (ref:210)

5.1.3 Modes of Oscillation

The spatial relation of intensity distribution transverse to the direction of propagation of the beam is defined as mode structure. The mode structure of a laser beam is determined by[15]

a) Geometry of the laser cavity optics
b) Gain of the cavity
c) Inhomogeneties in the laser medium
and d) Pumping power.

Several workers[14,203,218,220-2] have theoretically examined the causes of mode structure. Steen[17] recorded various mode structures from a carbon dioxide laser using char prints. In the present study the mode structure of the beam was checked also usually using char prints. An attempt was made to determine the mode structure more accurately by using a Photon drag detector. But due to the complicated unconvoluting calculation resulting from the cumulative output from Photon drag detector this method was not pursued in any great depth (See Section 5.3).

A series of typical char prints obtained are given in Plate 5.1.

5.1.4 Welding set up

Mainly three types of jigs (discussed in Section 4.5.1.1 - 4.5.1.3) were used for welding according to different needs.

All the jigs were adjustable in height so that the workpiece may be placed at the focal point of the beam. The lens system was also adjustable over a range of 4". The general sketch for the welding set up is given in Fig. 4.1.

For relatively modest speeds up to 60mm/sec. the lead screw jig (section 4.5.1.1) was used. For speeds up to 340 mm/sec. the hydraulic X-Y table (Plate 4.2 and Section 4.5.1.2) was used.

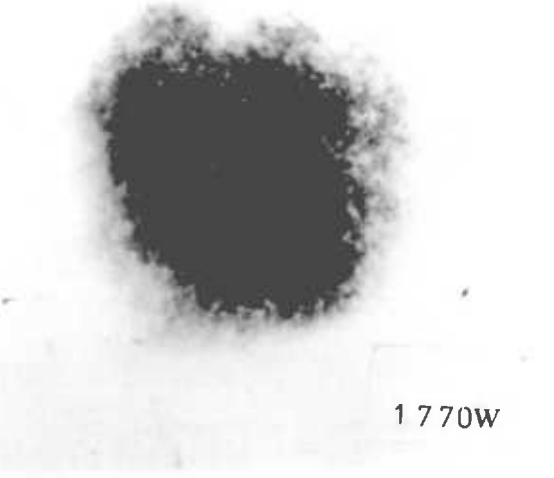

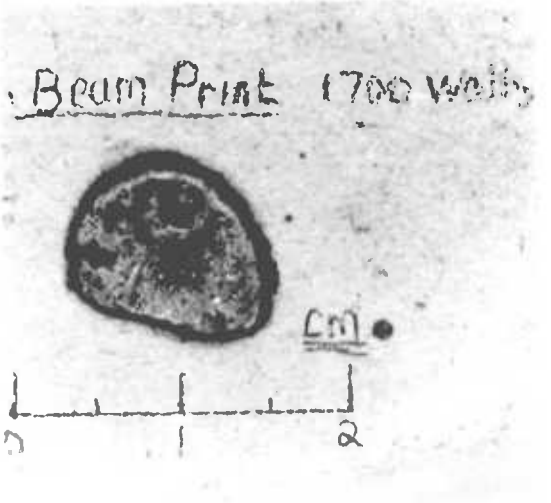

PLATE 5.1 Char prints for the beam showing different mode pattern

Whereas butt welding of thin sheets of 0.2mm was attempted in rolling jig (Plate 4.3 and Section 4.5.1.3) up to speeds of 148 cm/sec. Operation of each jig is discussed in the following sections. In all the three cases the beam remains stationary while the workpiece moves.

5.2 Work Handling Jigs

5.2.1 Welding jig with lead screw and stepping motors (X-Y table)

This jig was made available by M/S British Oxygen Limited. They also supplied the calibration curve for the table showing the linear speed against the controller setting. The calibration curve is illustrated in Fig. 5.2. Detail of the equipment is given in Section 4.5.1.1.

To use the jig the height of the table was first adjusted to be near the focal point of the beam. A small piece of metal was put on the table with a small slope. Then the piece of metal was made to travel under the laser beam at a slow speed. The position where a blue plasma was emitted from the metal was noted. The distance between that position and the nozzle end was measured using a feeler gauge. The cleaned workpieces to be welded were clamped between two heavy pieces of metal as shown in Fig. 4.1. The height of the lens was then adjusted to give the previously measured distance between the workpieces and the nozzle end. The trolley was moved in the Y-direction so that the beam fell on the joint between the two plates if they were to be butt welded. The laser power was fixed. The controller setting for the required speed was selected and the welding run performed.

5.2.2 Hydraulic jig (X-Y table)

The hydraulic jig was built at the Royal School of Mines[211]. Setting up the workpiece at focal point of the laser beam was similar as for the case of the lead screw X-Y table described in preceding section.

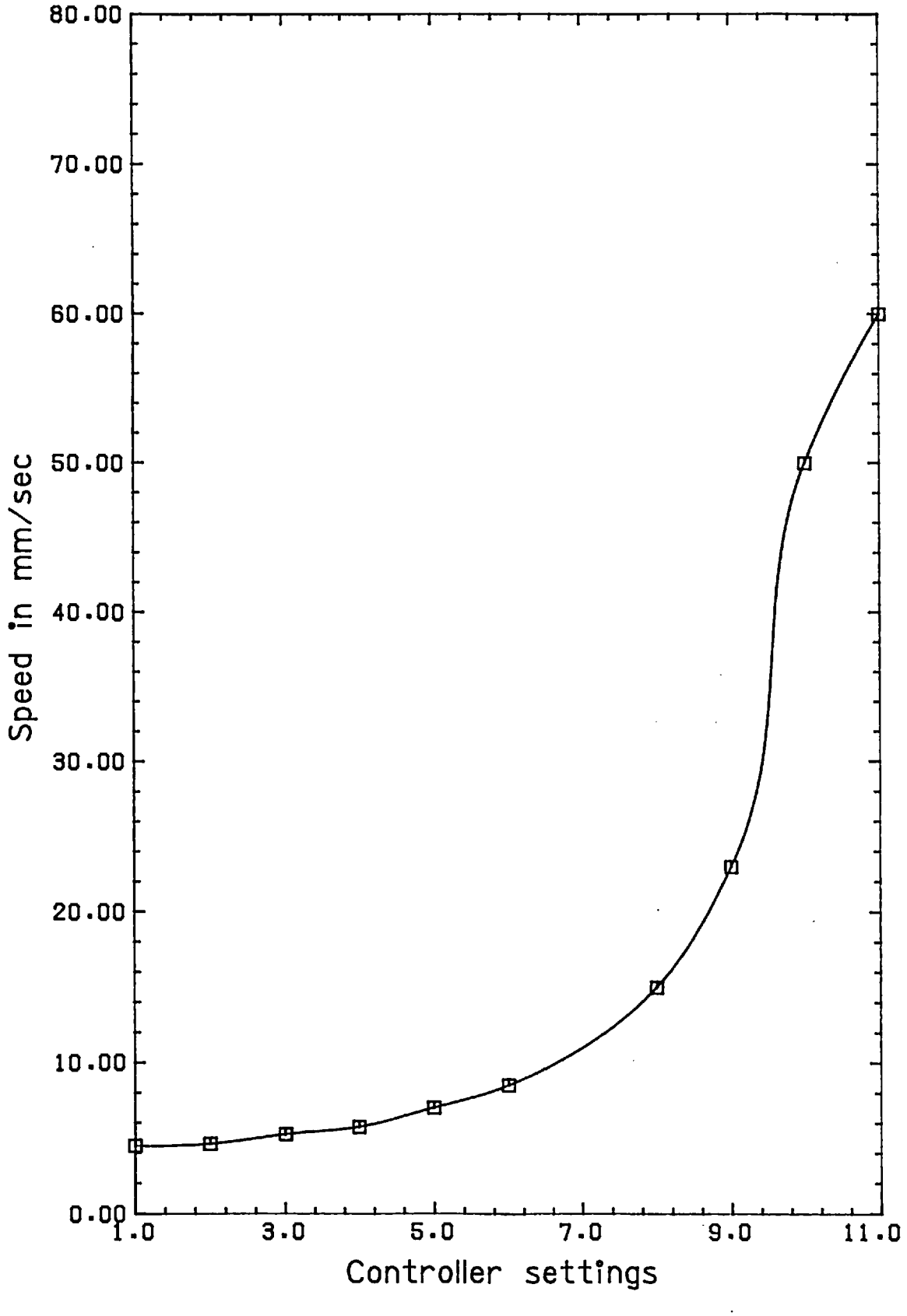

FIG. 5.2 Calibration curve for welding jig with stepping motor

The design of the table is discussed in Section 4.5.1.2. As explained in Section 4.5.1.2 the table was hydraulically driven. For x-direction movement a 15" stroke piston was used whose speed was controlled by controlling the oil flow using needle valve. Speed of the trolley was calibrated against controller setting using an electronic timing device. The calibration curve is illustrated in Fig. 5.3.

5.2.3 Rolling jig for butt welding thin sheets

Design of the jig is described in Section 4.5.1.3. For obtaining butt welds in this jig long strips of width of 2" to 3" were necessary. Before inserting the strip through the rollers the height of the whole trolley should be adjusted as before such that the focal point of the laser beam fell on the centre position of the central roll. Minor adjustments to the focus could be done by moving the lens assembly. Then using the gears shown in Plate 4.3 roll gap was increased to allow the sheets to be welded to slide through easily. First an ordinary sheet of equal thickness of that to be welded was pushed between the rolls and then the roll gaps were so adjusted that the strip was held with a slight pressure. But care had to be taken to adjust the roll gap of the idle roll set (i.e. roll set without drive) so that when the sheets were pushed or pulled they would move easily without loosing the slight tension. Two strips were slid through both sets of rolls. The two sheets were arranged to lie on the centre roll in such a way that the laser beam fell on the joint of the sheets. The sheets were fixed under optimum tension by adjusting the height of the centre roll and the roll gap. Pressure was applied from two sides by collars mounted on the central roll so that they were closely fitting. Two laser spot welds were made at the two ends of the required length of the weld to make sure that the entire length had a good alignment between the beam and the joint.

It should be noted that due to the extremely small volume of the weld ingot the accuracy of alignment was of the utmost importance. With the present arrangement a weld length of greater than 6" was difficult to achieve. This was mainly because the sheets

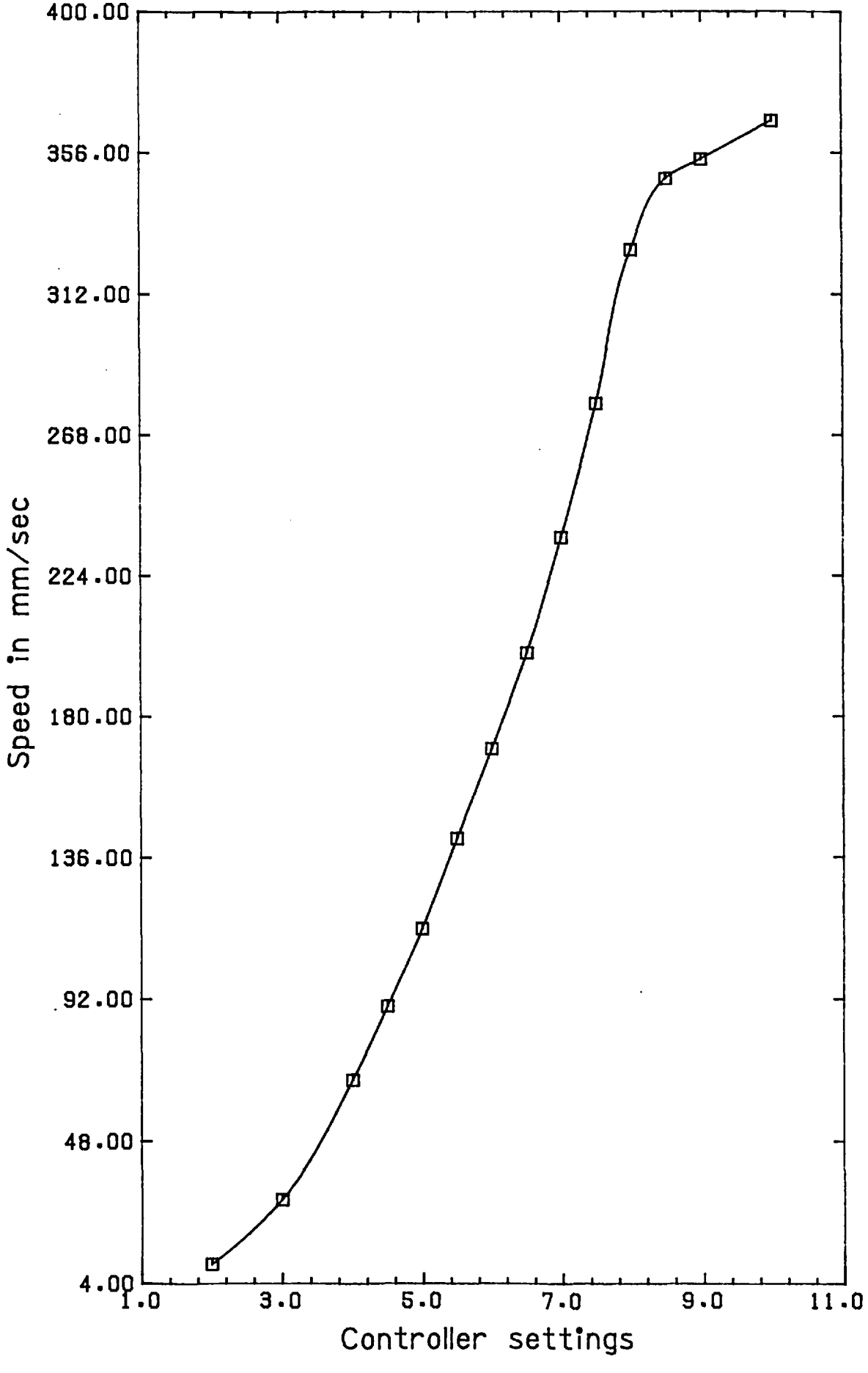

FIG. 5.3 Calibration curve for hydraulic X-Y Table

tended to slide one over the another if they were not very carefully set between the rolls.

The speed of the movement was controlled by controlling the input voltage to the DC motor. For that purpose an open loop motor speed controller (detail in Section 4.5.1.3) was used. The linear speed was calibrated by measuring the r.p.m. of the rolls using a tackometer for different controller setting and then calculating the linear speed from r.p.m. and diameter of the roll for different controller settings. The calibration curve is illustrated in Fig. 5.4.

5.3 Photon Drag Detector

The photon drag detector (Plate 4.4, Section 4.6) was operated as follows:

1) The germanium crystal mounting was placed approximately under the laser beam path so that the whole focused beam would fall perpendicularly on the polished end of the crystal.

2) Before focussing the beam, care was taken (a) that the beam chopper was working. Otherwise the full exposure to the high power beam would damage the crystal.
(b) output from the crystal was connected to the input of the amplifier and output of that to the oscilloscope.
(c) gain of the amplifier was fixed at 70 dB to 80 dB range.
(d) the frequency range was set at 100Hz to 10 kHz to cut down unwanted noise.

3) The output from the amplifier was connected to a storage oscilloscope.

4) The laser beam was turned on.

5) Visual display of the power distribution falling on the germanium single crystal as the beam was chopped by the rotating of the slit (5thou) of the chopper was obtained

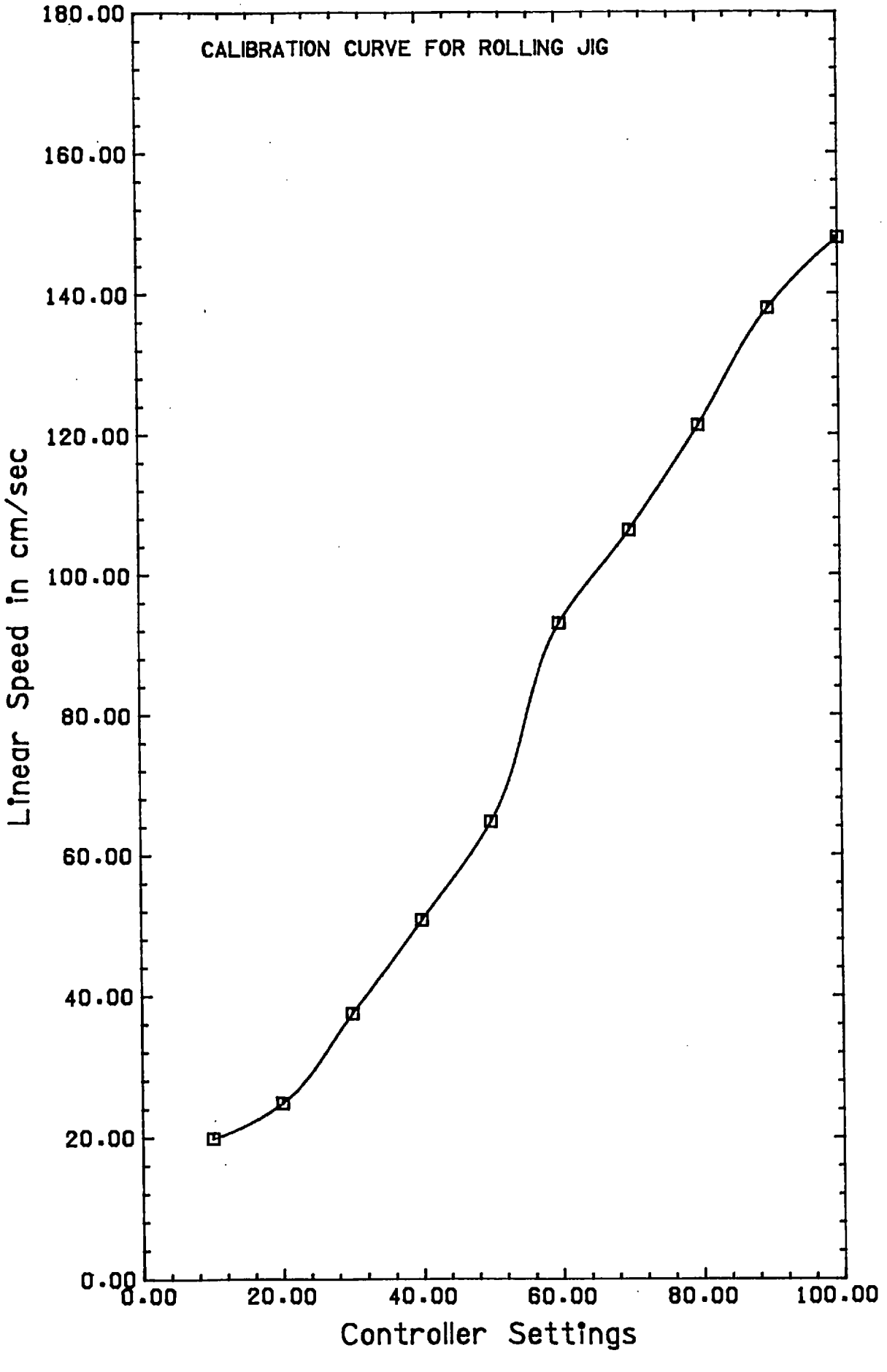

Fig. 5.4 Calibration curve for rolling jig

on the oscilloscope screen. A typical oscilloscope trace is shown in Plate 5.2.

6) Using the width of the slit and r.p.m. of the chopper the mode structure could be calculated if the beam was assumed to be axisymmetric (See section 4.5 or Appendix 4c).

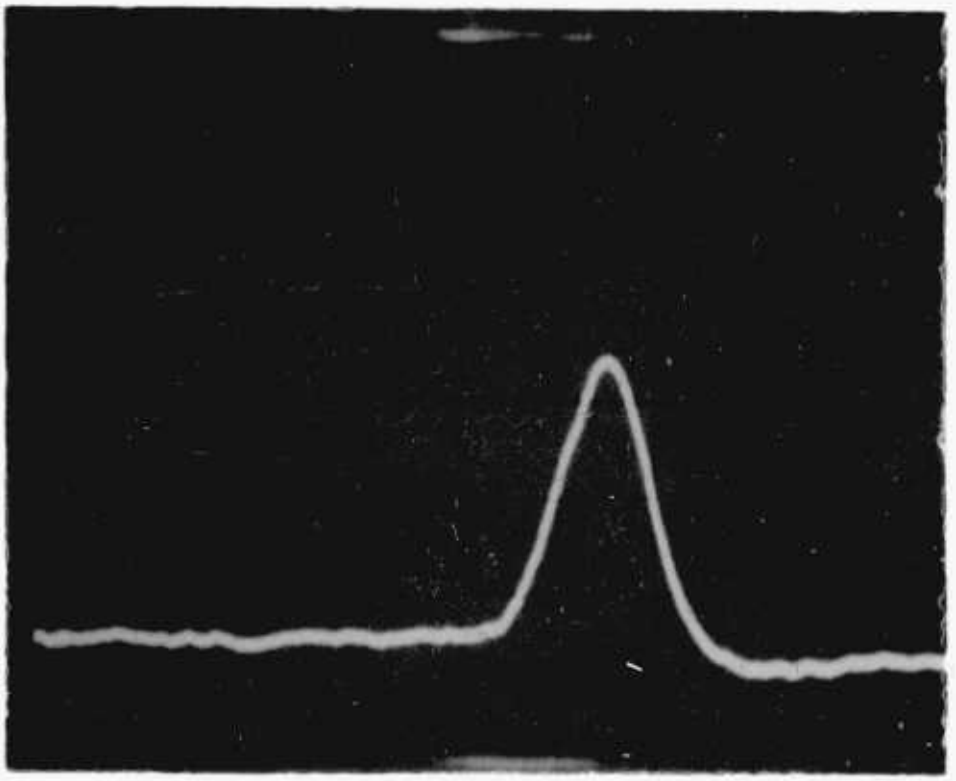

PLATE 5.2 Oscilloscope trace for CW CO_2 laser beam with using a photon drag detector

1.8 kW

50 s/div

0.1 V/div

70 dB

100 - 10 KHz

140 Am slit width

CHAPTER 6

EXPERIMENTAL METHODS

6.1 Experimental Strategy

The aims of the experiments performed were:

1) to establish whether sound welds could be achieved for titanium alloy and tin coated mild steel using a 2kW CW CO_2 laser.

2) To investigate the influence of different welding parameters during the laser welding.

3) To study the quality of the weld obtained, and to correlate the micro-structure and the mechanical properties of the laser weld materials

4) To determine the extent of the heat affected zone and to estimate the temperature cycle undergone by comparison with a theoretical model

Both the first and second objectives were achieved by making a series of welds with the laser using systematically varied process variables.

The third objective was achieved by performing several mechanical and chemical tests along with extensive metallographic examination on the welded specimens.

The fourth objective was achieved by measuring the HAZ revealed in macrographs , and the thermal cycle was estimated by comparing the microstructure with previous work on time-temperature-transformation of the alloy. This estimated temperature profile was compared with that obtained from a theoretical model

6.2 Experimental Procedure

Autogeneous butt welds and some bead-on-plate welds were made in titanium sheets whereas lap welds and bead-on-plate welds were mainly made in tinplate. Attempts were also made to butt weld thin tin plates.

The variables studied in the process were as follows:

1) Thickness of the material
2) Laser power
3) Welding speed

The procedure was:-

i) For each weld the specimens were degreased. A special proprietory solvent from ICI, designed to remove grease from titanium alloy, was used for titanium specimens (The basic composition was 6Al-4V-Ti and CP). Trichloroethylene and Acetone were used to degrease tin plates

ii) They were then mounted on a variable speed X-Y table (Sections 4.5.1.1, 4.5.1.2 and 4.5.1.3 - Fig. 4.1, Plates 4.2 and 4.3) so that they could be moved under the stationary laser beam. The type of X-Y table required and its operation for welding is discussed in sections 5.2.1, 5.2.2 and 5.2.3.

iii) The weld area was shielded with helium above (to remove oxygen and reduce plasma formation) and Argon beneath (Fig. 4.1) - (to remove oxygen and because it is cheaper than helium).

iv) The butt fit up of the workpiece edges needed to be reasonably matched but did not require extra side pressure for thicknesses down to 1mm.

v) The laser beam was focussed on the surface using 75mm focal length KCl lens and was necessarily carefully centred on the joint between the plates; off centering of the beam by more than half the focussed beam diameter (around 250μm) usually led to welding defects.

A typical weld defect in titanium butt weld resulting from off centering of the beam and ill butt fit up, is illustrated in Plate 6.1

vi) The laser power was monitored with a copper cone calorimeter (section 4.3.1 and 6.3.4.1)

vii) The mode structure checked by means of char prints

viii) The welds produced were examined in detail by
a) Radiography
b) Tension test
c) Fatigue test
d) Micro and Macro hardness tests
e) Corrosion test - Tafel extrapolation method
f) Metallography (optical, S.E.M., and transmission electron microscopy).

6.3 Measurement and Calculation of Parameters

6.3.1 Gas flow parameters

The significance of the jet exit Reynold's number on convective heat transfer is discussed in (Section 3.5.4.2.3). Reynold's number is given by the following expression:

$$Re = (GDENS \times GVEL \times D)/GVISC \qquad (6.1)$$

where GDENS = gas density at NTP in KG/m^3
GVEL = gas velocity m/sec
D = jet diameter metre
GVISC = gas viscosity at NTP $N.sec/m^2$

PLATE 6.1 Welding defect due to off-centering of the beam

Therefore, to determine the gas exit Reynolds number the velocity of the gas coming out of the nozzle has to be determined.

The difficulty of measuring the gas velocity arises due to the unknown pressure drop between the gas cylinder and the nozzle. During the experiments a slow flow of gas was felt near the nozzle.

In the beginning gas flow was roughly estimated to be 2.64 litres/min considering the time of usage of a cylinder. From this the velocity of the gas was estimated to be as follows:

$$2.64 \text{ litres/min} = 0.044 \text{ litres/sec.} = \pi \text{ GVEL} \times \left(\frac{D}{2}\right)^2$$

or

$$\text{GVEL} = \frac{0.044 \times 4}{D^2 \times \pi} = 6.228 \text{ m/sec.} \qquad (6.2)$$

This was a rough estimate so at a later date when the shielding gas flow system had been changed, the velocity of the gas coming out of the nozzle was determined, with similar pressure gauge setting as before, by using a Pitot tube made by J. Clarke of the Royal School of Mines. The pressure distribution for the 3mm diameter nozzle at a jet-plate distance of 1mm was obtained by shifting the pitot tube under the beam. The pressure distribution is illustrated in Fig. 6.1. As this distribution is for a 3mm diameter nozzle at a 1mm jet-plate distance, it can be safely assumed that the centre is within the potential core of the jet which usually extends four diameters beyond the jet exit. Assuming that the static pressure above the manometer is the same as the static pressure around the jet the pressure difference can be read directly from the manometer reading of the Pitot pressure.

Now applying Bernoulli's equation for an incompressible ideal fluid with the velocity at the impact tube being zero, the working equation for the Pitot tube can be written (Ref 206-p42) as:

$$u = \sqrt{\frac{2\,\Delta p}{\rho}} \qquad (6.3)$$

where u = velocity, m/sec. Δp = pressure difference in Pa (N/m^2)
ρ = density, Kg/m^3 (for air = $1 Kg/m^3$)

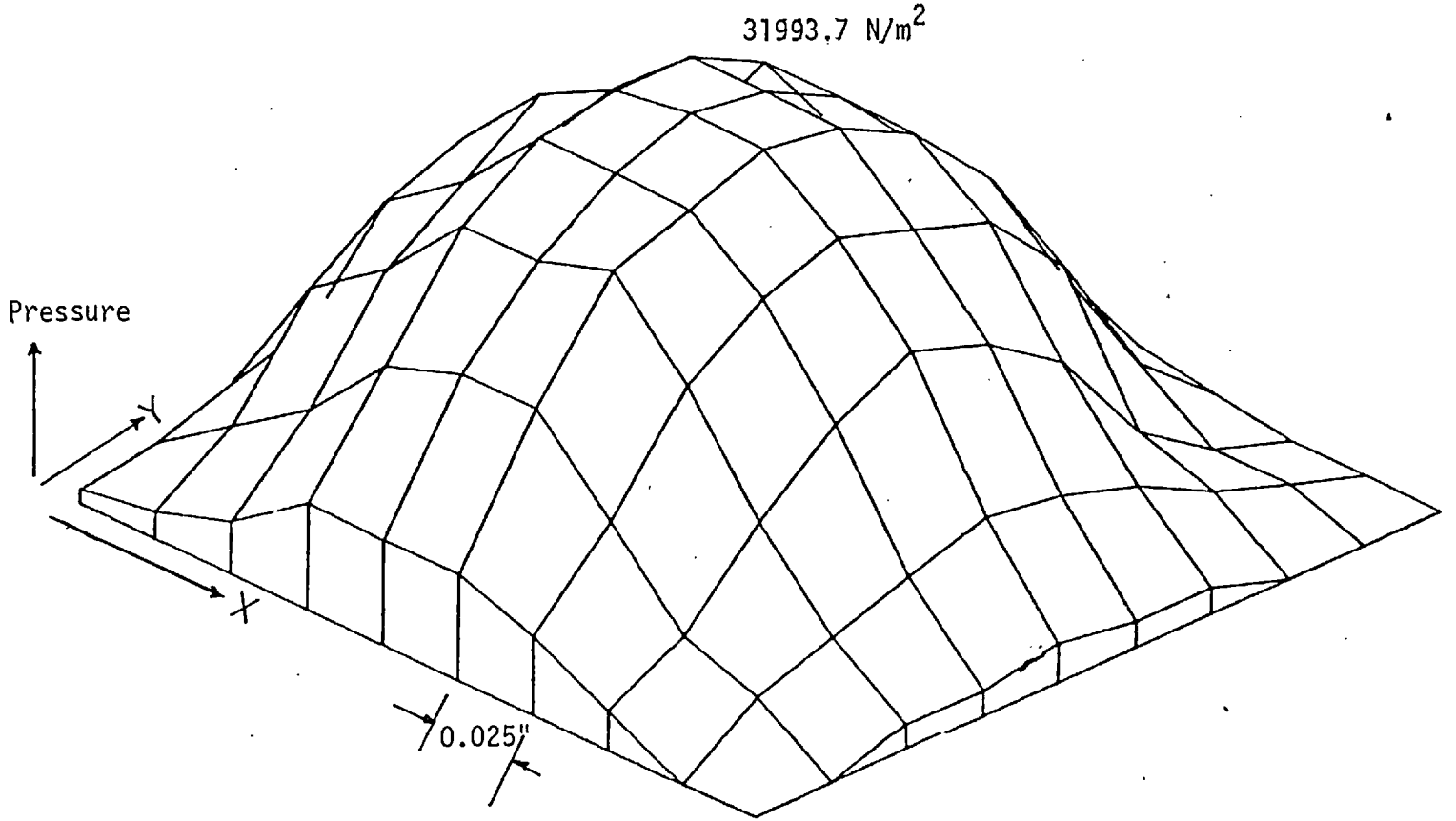

Fig.6.1 Stagnation pressure distribution for 3mm nozzle for 1mm jet plate distance.

Now using the maximum pressure difference at the core of the jet $\Delta p = 31993.7\ N/m^2$ we can calculate the velocity of the gas flow through the nozzle using equation 6.2.

$$u = \sqrt{\frac{2 \times 31993.7}{1}}$$

$$= 252.96\ m/sec. \qquad (6.4)$$

this does not correspond to the type of gas flow observed during the welding runs. Probably this change of flow rate for similar cylinder head pressure setting was due to the change of design for the gas flow.

However, as this flow rate was needed for the theoretical heat transfer calculations both these values of gas velocities were used for the temperature profile calculations. It was observed that as the convective heat transfer loss was very small the temperature profile is insensitive to the shielding gas velocity. Thus the experimental uncertainty in the precise velocity is not significant.

6.3.2 Laser Parameters

6.3.2.1 Laser power

To measure the laser output power beam coming out of the GaAs window was deflected by water cooled gold coated mirror at 45^{o} into the water cooled copper cone calrimeter which was mounted as an integral part of the BOC Laser. However, monitoring the power was only possible when the beam was not in use. During the use of the beam the above mentioned mirror was removed from the beam path using pneumatic control.

Water flow to cool the calorimeter was measured by the rotameter. The inlet and outlet temperatures of the cooling water was measured using copper-constantan thermocouple. The power enetering the calorimeter can be calculated from the temperature gain of the cooling water and thus laser output power was calibrated and displayed as watts of laser power by the digital voltmeter mounted on the power supply.

This direct calibration was checked at the Royal School of Mines by Clarke, using a black body copper sphere calorimeter.

6.3.2.2 Beam Diameter

6.3.2.2.1 Definition of beam diameter

The diameter of the laser beam is normally measured as the distance between points at which the amplitude is 1/e that of the centre and the intensity (Power density) is $1/e^2$ (Ref. 15, p14).

For stable cavity laser the fundamental TEM_{oo} mode structure is defined by

$$P(r) = P_o \exp(-2r^2/r_b^2) \tag{3.41}$$

$$= \frac{2 \times P_{TOT}}{\pi r_b^2} e^{(-2r^2/r_b^2)} \tag{3.44}$$

or

$$P(r) = \frac{8 P_{TOT}}{D_b^2} e^{(-8r^2/D_b^2)} \tag{6.5}$$

For the gaussian power distribution beam diameter is illustrated[14] in Fig. 6.2.

6.3.2.2.2 Different techniques to measure beam diameter

Different methods used by other workers in measuring beam diameter has been reviewed by Steen[17]. This is a common problem encountered in laser power work. It appears from the review[17] that most of the workers measured the contour of a single isotherm of char prints as in charring of card or heat sensitive paper, drilling holes[20,223] in black paper or thin metal films or the formation of glow images on thin asbestos sheet, or special fluorescent screens.

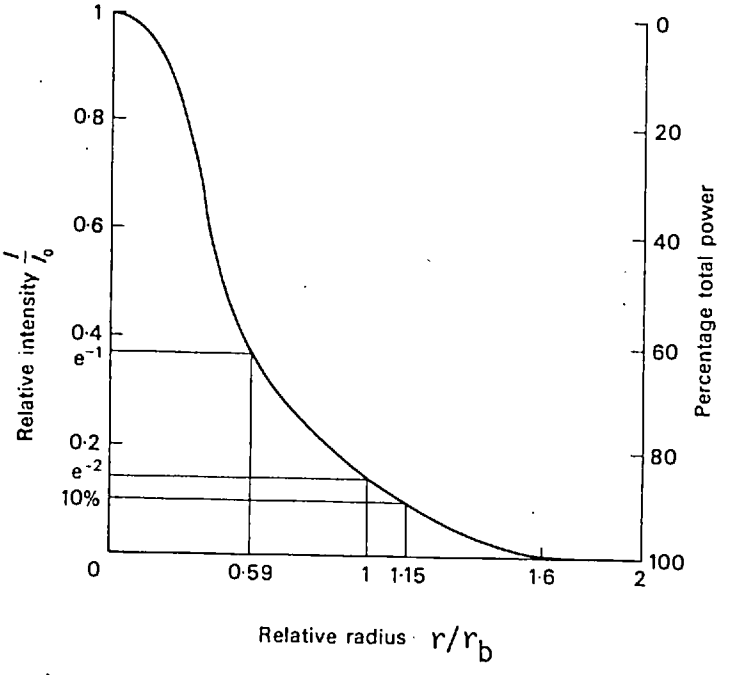

Fig. 6.2 Variation of relative intensity and percentage total power with radius for a Gaussian beam. (after Harry- Ref: 15)

Now a days the more sophisticated instruments like the "Pyroanalyser" made by Laser Precision Corporation[224] is available in the market to measure beam width, made structure etc. of the laser beam. Unfortunately, nothing of this sort is available for several hundred watts to multikilowatt range of the present study.

For high power study of 10.6μm beam Photon drag detector[212-214] (Section 5.3 and 4.6) appers to be more attractive, but it has its problems too.

There are also theoretical methods to measure diffraction limited spot size of laser beam.

Different methods to measure the beam diameter can be summarised as follows:

1) Theoretical calculation of beam diameter

If the beam power is assumed to be gaussian and that truncation effects at the aperture and spherical aberration within any lens are negligible then the following standard optical techniques to calculate the diffraction spread of the beam may be used.

(i) Ray transfer matrix methods described by Kogelnik and Li[203]

(ii) Analytical solutions of the Laguerre-Gaussian functions described by Boyd and Gordon[225] and Dickson[226].

(iii) Geometrical solutions described by Deschamp and Mast[227], Laures[228] and Sinclair and Bell[229] (P88).

out of the above three the geometrical solution is the simplest and is known as the'Propagation Circle'method for gaussian beams.

2) Experimental methods to measure beam diameter

(i) Single isotherm contouring as in char prints, drilling holes in metal foils[20,223] and acrylic plastics or forming glow images on asbestos sheets and fluorescent screens.

(ii) Multiple isotherm contouring

a) linear response photographic paper[230] but this is unsuitable for 10.6μm radiation because this would require special paper and liquid nitrogen cooling etc.

b) Photon drag detector[212-214]

c) Thermal rise time method[17].

Relative merits and demerits of the above methods are discussed in the following section.

6.3.2.2.3 Choice of technique to measure beam diameter

The theoretical techniques to measure the beam diameter is strongly affected by the following[17]:-

(i) The effect of diffraction on a Gaussian beam

(ii) The effect of truncation at the aperture on (i)

(iii) The effect of nongaussian modes

(iv) The effect of spherical aberration in the lens used.

Ignoring the above effects the diffraction limited spot size of focussed laser beam is given by the following expression (Ready[14]).

$$r_b = \frac{1.22f\lambda}{D_b} \qquad (6.6)$$

where r_b = radius of diffraction limited spot size
D_b = unfocussed beam diameter
λ = wave length of the laser radiation
f = focal length of the lens

However, for all the practical laser systems it is impossible to avoid the effects mentioned above and, therefore, the actual focussed beam diameter is always much greater than theoretically calculated diameter.

The truncation effect leads to the enlargement of focussed beam spot diameter. The truncation effect due to aperture is reviewed by Steen[17] and he quoted from Dickson[226] that $1/e^2$ intensity radius (i.e. 1/e power radius) could be enlarged by 50% due to this effect.

While reviewing the effect of mode structure Steen[17] noted an increase of 20% in beam radius for TEM_{01} mode compared to that of TEM_{00} mode. Amplitude distribution for TEM_{01} mode is given by the expression[17]:

$$P = \frac{P_{TOT}}{\pi r_b^2} \frac{\sqrt{2}\, r}{r_b} e^{(-r^2/r_b^2)} \sin\theta \qquad (6.7)$$

Increase of beam radius will be more for higher order modes.

Spherical aberration of lenses leads to increase of spot size. For F1.5 lens an increase of spot size by 35% has been reported[15,17]. Steen[17] reports that spherical aberration is negligible for lenses having F.NO ($F = f/D_b$) greater than 7.0. In the present study lenses of F.NO $\leq$ 7 (depending on unfocussed beam diameter incident on the lens) have been used. So some spherical aberration might be expected.

In view of the foregoing we find that a theoretical calculation will only give an idea of beam diameter and will require a suitable scaling factor or additional width. The actual beam diameter could be greater than double the theoretically calculated value at the minimum spot size.

Among the experimental techniques to measure the beam diameter the single isotherm method is mostly used due to its simplicity. Though, inaccuracies involved in the method are easily seen if a convergent gaussian beam is considered. For all single isotherm methods the recorded isotherm contour is a function of both exposure time and total power. In fact, the beam diameter will appear to grow with exposure time or increase in total power. In any case it is unlikely that the isotherm contour recorded will coincide with either

the contour for the 1/e or $1/e^2$ value of the central power density of the beam. The argument is best explained diagrammatically by Steen[17], as shown in Fig. 6.3.

Cohen and Epperson[20] drilled a series of holes in a thin film of tantalum nitride by using a ruby laser with various powers focussed with a 2.54 cm focal length lens. He then plotted the diameters against powers, as shown in Fig. 6.4. It was evident from the graph that the beam diameter depended on power, particularly at the low power range.

However, for the present study, experiments were completed at high power range where dependence of beam diameter on power was assumed to be less. Besides that for 10.6 μm radiation we can use transparent acrylic sheets to obtain a print of the beam profile, as shown in Plate 6.2. The exposure time was controlled by using a time switch for shutter operation. Although an element of error can be expected when using this process, it is made attractive as a quick method to estimate the beam diameter by the immense simplicity and speed of process. The beam diameter obtained from single isotherm contours in acrylic sheet can be checked by using more sophisticated methods, for example, a photon drag detector.

The multiple isotherm contouring method using photographic paper could not be used for high power 10.6 μm radiation because a new type of paper and liquid nitrogen cooling etc[17] would be required.

The photon drag detector[212-214] (section 5.3 and 4.6) scans the beam and produces a convoluted signal. The disadvantages associated with the method are as follows:-

1) The process is rather complicated to use
2) The beam characteristic is not available directly. A time consuming calculation has to be done to interpret the convoluted signal.
3) Before any calculations, it is necessary to assume that the beam is axisymmetric which is not always the case.

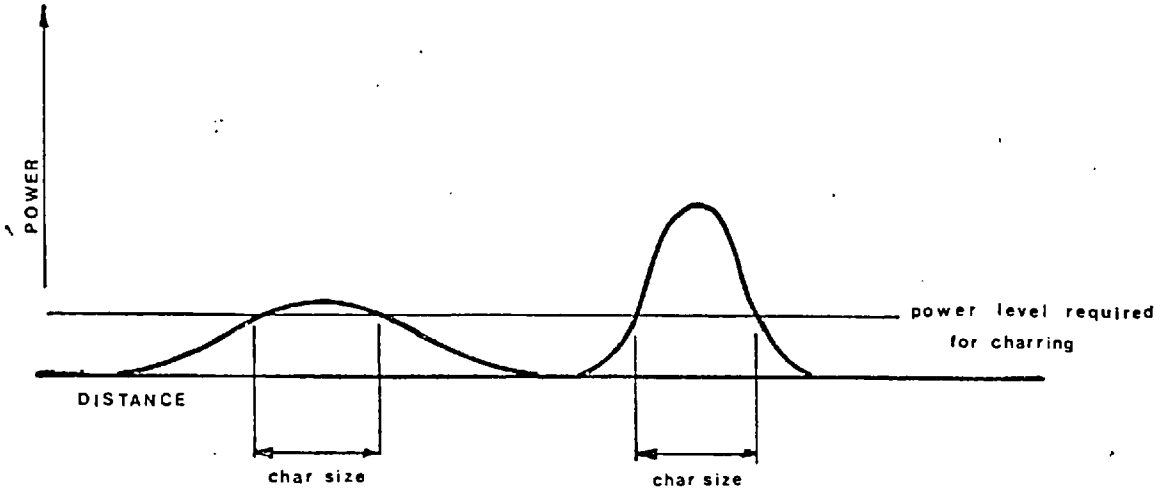

FIG. 6.3 Showing the error in using an isothermal technique to measure the gaussian beam diameter (Ref. 17)

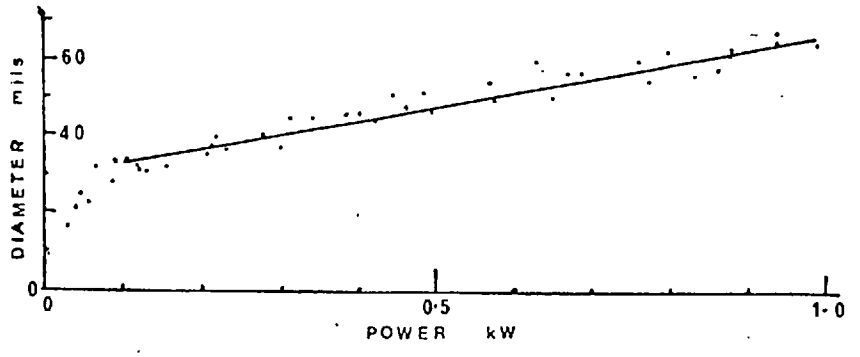

FIG. 6.4 The apparent variation in beam diameter with power by using an isothermal technique (Ref. 20)

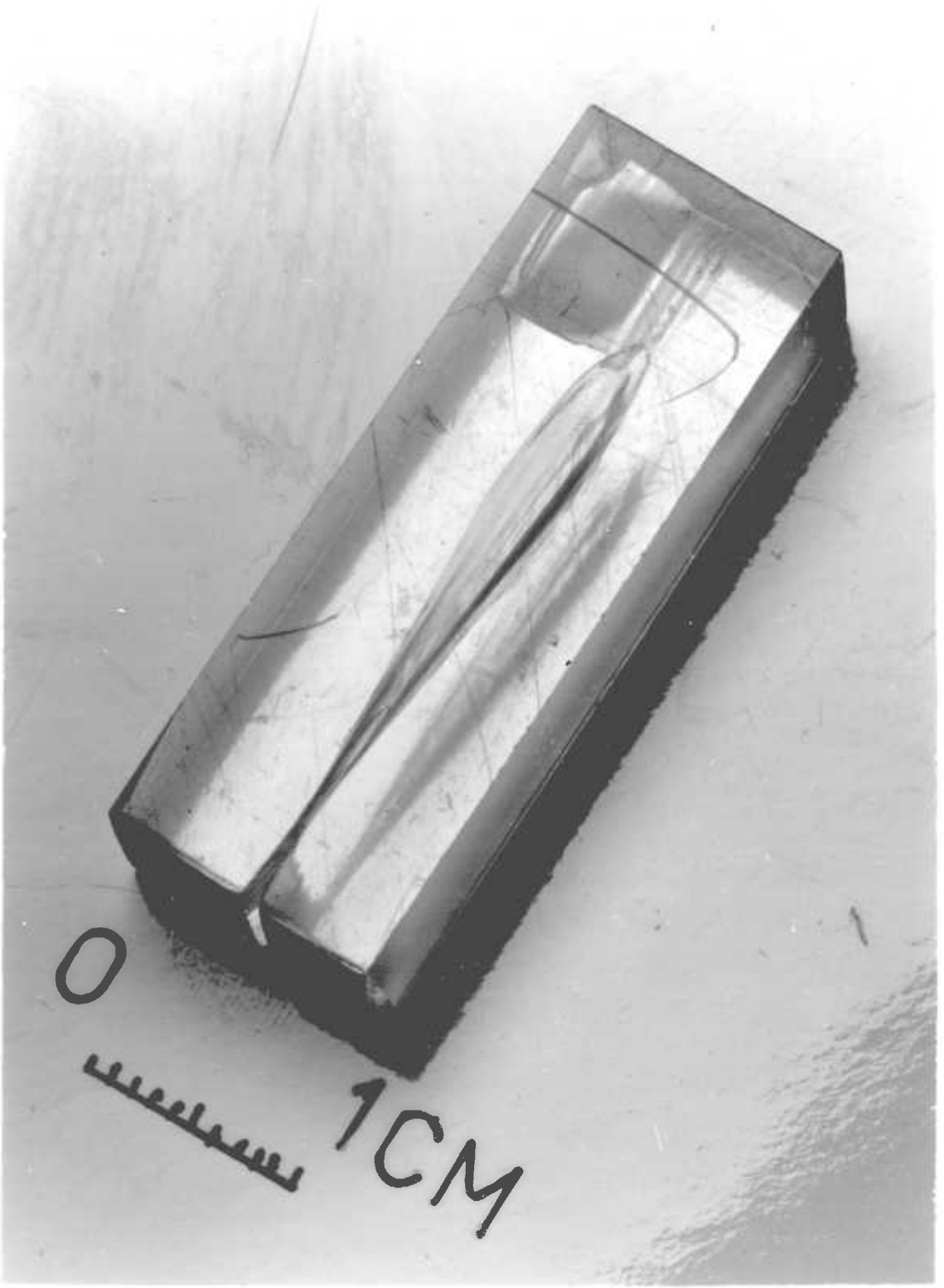

PLATE 6.2 Laser beam print on acrylic sheet

However, this method is the most accurate available at present.

In the thermal rise time method[17] basically the time required to raise temperature of a spot on a certain substrate to 90% of steady state is measured and then this value substituted into a mathematical mode[192] of a stationary spot heated by a laser to obtain a gaussian beam diameter equivalent to the incident beam. This process cannot be used if melting or evaporation occurs and so can only measure the beam size at a distance from the focal point of a high powered beam.

In view of the foregoing, the beam diameter was roughly estimated, for the present study, using a single isotherm technique in acrylic, assuming that the isotherm coincided with 1/e of central value. Then using the photon drag detector a more educated estimate of the beam diameter was obtained. It was found that there was reasonable correlation between the beam diameters measured by the two different processes.

6.3.3 Substrate parameters

6.3.3.1 Physical properties

Physical properties of the materials used (Titanium and tin plate) are obtained from different hand books[231-235]. However, as the substrates used were commercial materials and exposed to the severe thermal cycle a range of values was considered. It was also assumed that most of the physical properties remain constant during temperature change.

The physical properties of the substrate used for the calculation for the present study are given in Table 3.2 in Chapter 3.

6.3.3.2 Surface reflectivity

It is very difficult to measure the surface reflectivity due to the rapid formation of a keyhole and plasma. However, a keyhole, being conical, would be expected to behave as a black body whereas the reflectance of a plasma is unknown. Not all the beam would

fall over the keyhole so some will be reflected from the rapidly heating surface.

The reflectivity of the zone around the keyhole needs to be known if the process is to be modelled mathematically. The reflectivity of the substrate can be calculated from the emmissivity of the substrate using the following relationship[16]

$$\varepsilon_\lambda(T) = 1 - R_\lambda(T) \qquad (6.8)$$

for an opaque material.

where $\varepsilon_\lambda(T)$ = emmissivity of the substrate at T^oC temp for the radiation having λ wavelength

$R_\lambda(T)$ = reflectivity for λ wavelength radiation at T^oC temp.

Generally to determine the variation of $E_\lambda(T)$ with λ and T requires direct spectroscopic measurement. However, $E_\lambda(T)$ for metals in the infra-red spectral region ($\lambda > 2\mu m$) can be calculated from data on the temperature dependent resistivity of the metal[16]. Such a calculation will be valid only for metals heated in vacuum without a surface oxide layer. The presence of an oxide layer will increase the emmissivity and decrease the reflectivity. We can calculate emmissivity from electrical resistivity assuming that there is no surface oxide layer.

For perpendicular incidence of radiation of long wavelength Bramson[236] derived the relationship between the emmissivity and the electrical resistivity of the substrate, given as follows:

$$\varepsilon_\lambda(T) = 0.365\left|\frac{\rho_r(T)}{\lambda}\right|^{\frac{1}{2}} - 0.667\left|\frac{\rho_r(T)}{\lambda}\right| + 0.006\left|\frac{\rho_r(T)}{\lambda}\right|^{\frac{3}{2}} \qquad (6.9)$$

where $\rho_r(T)$ = electrical resistivity at absolute temperature T exposed in ohm-cm.

The calculation for reflectivity for titanium (6Al-4V) at $300^{o}K$ is given below.

Considering for Ti-6Al-4V[233] - $\rho_r(300) = 170 \times 10^{-6}\ \Omega\,cm$

$\lambda = 10.6 \times 10^{-4} cm$

then using equation 6.9

$$\varepsilon_\lambda(300) = 0.135860 \qquad (6.10)$$

Now using equation 6.8

$$R_\lambda(300) = 1 - 0.135860 = 0.864$$
$$\simeq 0.85 \qquad (6.11)$$

For mild steel $\rho_r(300) = 15 \times 10^{-6}\ \Omega$ cm (Ref 16)

$$\varepsilon_\lambda(300) = 0.03399 \qquad (6.12)$$

$$R_\lambda(300) = 1 - 0.03399 = 96.6 \text{ (approx)} \qquad (6.13)$$

6.3.4 Welding Variables

6.3.4.1 Laser power

It is a very important variable and measurement technique for output power is discussed in section 6.3.2.1. Different factors effecting the output power are discussed in section 5.1.2.

Laser power required for welding depends on the material, its thickness and the welding speed.

For titanium a series of welds were made for different thicknesses for various laser powers which fall in the range 770 watts to 2kW.

For tin plate the laser output power range used was 500-1950 watts.

6.3.4.2 Welding speed

Welding speed is a function of laser output power, the material and its thickness.

To establish the speed for a statisfactory weld, samples were run through the focussed beam at different speeds until a satisfactory weld was obtained. The speed of the work handling jig was measured as described in section 5.2

6.3.4.3 Thickness of the material

Thickness of materials were measured using Moore and Wright micrometers. But all the sheet materials used were found to be consistant with their specifications. Therefore, the measurement taken was more or less confirmatory. The thickness variation found was usually less than $\pm$ 0.05mm.

6.3.4.4 The materials

The materials used can be broadly divided into two groups:-

a) titanium b) mild steel.

Their specifications are given in turn.

6.3.4.4.1 Titanium alloy

Two types of titanium alloy were used for the present study.

a) Commercially pure titanium (DTD 5063)
b) Titanium 6Al-4V (AMS 4911).

Although, materials specifications were sent with the titanium alloys supplied by the British Aircraft Corporation, confirmatory analyses were carried out by the Analytical Services Laboratory of the Royal School of Mines.

Quantitative analyses for aluminium and vanadium in Ti-6Al-4V by x-ray fluorescence using NBS standard 654 were performed.

Whereas for semi-quantitative an XRF study was done for trace elements in both the commercially pure titanium and Ti-6Al-4V. The composition of 6Al-4V-Ti is given in Table 6.1.

MATERIAL	Al %	V %	TRACE ELEMENTS %					Titanium
			Si %	Fe	Ca & Zn	Ba & Mo	K & Sn	
Titanium Alloy AMS 4911	6.27 ±0.03	3.94 ±0.02	0.5 -0.05	0.5 -0.05	<0.05	<0.05		Rest

TABLE 6.1

The analysis of commercially pure titanium revealed silicon as the principal impurity along with the traces of K, Sn, Ca, Fe and Zn when titanium content is more than 99 wt per cent.

6.3.4.4.2 Tin plate

Two types of tin plate were used for the present study.

1) tin coated mild steel (≃ 0.2mm thickness)

2) drum quality mild steel plates (≃ 0.4mm thickness)

The materials were supplied by the British Steel Corporation Port Talbot, along with their compositions shown in Table 6.2.

MATERIAL	C wt%	P wt%	Mn wt%	S wt%	COATING
Tin coated mild steel	0.05-0.08	0.007-0.001	≃0.25	>0.02	coating of tin @ 2.8gm/in^2
Drum quality mild steel	←	same	→		none

TABLE 6.2

6.3.5 Metallurgical Properties

6.3.5.1 Radiography

The Muller-150 x-ray equipment facility at BOC-Murex Research and Development Laboratories, Waltham Cross, was used for the radiographic examination of weld joints. Details of the parameters used in the x-ray radiography for the present study are given in Table 6.3.

MATERIAL	Film Used	X-ray source	Exposure time in seconds	Current mA	Voltage KW	Screen used	Film (cm) focus distance
Titanium and tin plate	Kodak -C	Cu-cathod with w target	90	3	70	Pb	53

TABLE 6.3

6.3.5.2 Metallography

Microstructures of the welded specimen were systematically studied to evaluate the quality of the welds and to study the heat affected zone produced by the laser. This examination was done by optical microscopy, scanning and transmission electron microscopy.

6.3.5.2.1 Specimen preparation for optical microscopy

All the specimens were mechanically polished. The specimens were first roughly polished in emery paper starting at Grade 120 going up to 600 in stages. Then some of the tin plate specimens were polished up to 3 μm using diamond paste. But all the titanium specimens and some tinplate speciments were finally polished in vibromet using 0.5 μm alumina powder.

These polished specimens after being washed and dried were subsequently etched to reveal their microstructure. Swab etching was performed using the following etchants.

i) For titanium alloys

2% Hydrofloric acid
10% Nitric acid
Rest distilled water

Some times repolishing using a 0.5% hydrofloric acid solution was helpful to improve the clarity of the microstructure.

ii) For tin plate

2% Nital was used.

6.3.5.2.2 Optical microscopy

The Reichert MeF projection microscope was used for observation of microstructure and macrostructure and subsequent photographs and macrographs. But for routine checking of microstructure and HAZ a Vickers microscope (M41) was used where magnifications. of 100x to 1000x could be achieved.

6.3.5.2.3 Scanning electron microscopy

Examination at magnifications up to 5k was achieved using the Stereoscan-600 scanning electro microscope supplied by Cambridge Instruments Limited, U.K. At magnifications over 5K there was a loss of resolution. A specimen size of 1cm sq was preferred for movement within the microscope, but specimens up to 2cm long could be used with restricted movement.

6.3.5.2.4 Transmission electron microscopy

A Siemens 100 kV electron microscope was used. Maximum specimen size allowed in the stage was 2.3mm diameter disc. Only titanium alloys were examined this way. Thin foils were made by using the window technique.

6.3.5.2.5 Preparation of tin foils for titanium alloy

Thin foils were made by using the window technique.

Relevant details for the present study are given below:

Composition of Electrolyte

60% Methanol

30% Butanol

5% Perchloric Acid

Voltage - 30V Current 50mA
Working Temperature - Below (-45^{o}C)
Specimen - Anode (+ve)
Crucible - Cathode (-ve)

Description

Methanol was poured into a big trough placed on a magnetic stirrer. A stainless steel beaker was placed in it. The specimen after being ground to 0.12 to 0.18mm and lacquered at the sides was suspended in the stainless steel beaker, containing cooled electrolyte by a pair of forceps. The temperature of the electrolyte was kept below (-45^{o}C) by pouring liquid nitrogen in the big trough and the temperature of the electrolyte was measured by an alcohol thermometer. As the current passed between the specimen (anode) and the beaker (cathode) the specimen was slowly eroded in the unlacquered region. The process was carried on till the perforation is achieved in the specimen. Careful watch was needed to observe the perforation. The specimen was quickly removed after the perforation and it was washed and dried. In this way enough thin area suitable for transmission electron microscopy was produced.

6.3.6 Mechanical Properties

6.3.6.1 Tension test

The 5 tonne instron tensile testing machine was used. All the specimens were made carefully with a gauge length of 2.2 cm with

the weld transverse to the direction of tension as shown in Fig. 6.5.

For titanium alloy samples, a cross-head speed of 0.05cm/min was applied. For tin plate samples, a cross-head speed of 0.1cm/min was applied.

Two samples from most of the butt welded and lapwelded joints were drawn.

6.3.6.2 Hardness measurement

Micro-hardness test

Micro-hardness traverse across the weld zone was performed on some selected samples to investigate the effect of different welding variables on hardness within the weld zone and HAZ.

The Leitz micro-hardness tester was used for this purpose.

For mild steel and tin plate a load of 100 grammes was used.

For titanium it was noticed during micro-hardness traverse across the weld ingot that the knoop scale hardness difference between α and β phase is not appreciable. In fact variation of hardness was of the same order throughout, including the parent matrix and the weld ingot. Therefore, it was necessary to perform macro-hardness tests on titanium.

Macro-hardness test

The macro-hardness was measured on a Vickers hardness testing machine with a load of 5kgs.

6.3.6.3 Fatigue test

Some confirmatory fatigue tests were carried out on samples of interest. The usual statistical procedure was not followed, because of the impracticability of the time and quantity of materials required for the purpose.

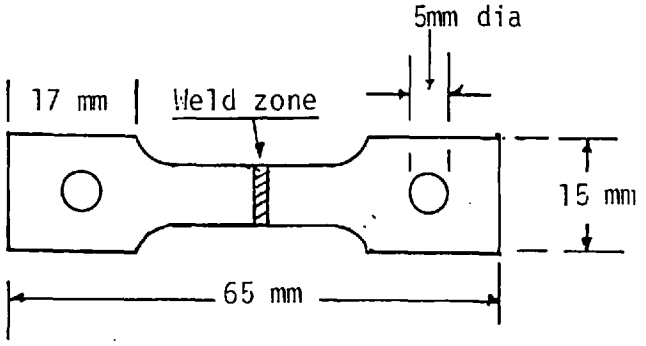

Fig: 6.5 Sketch for Tension Test specimen

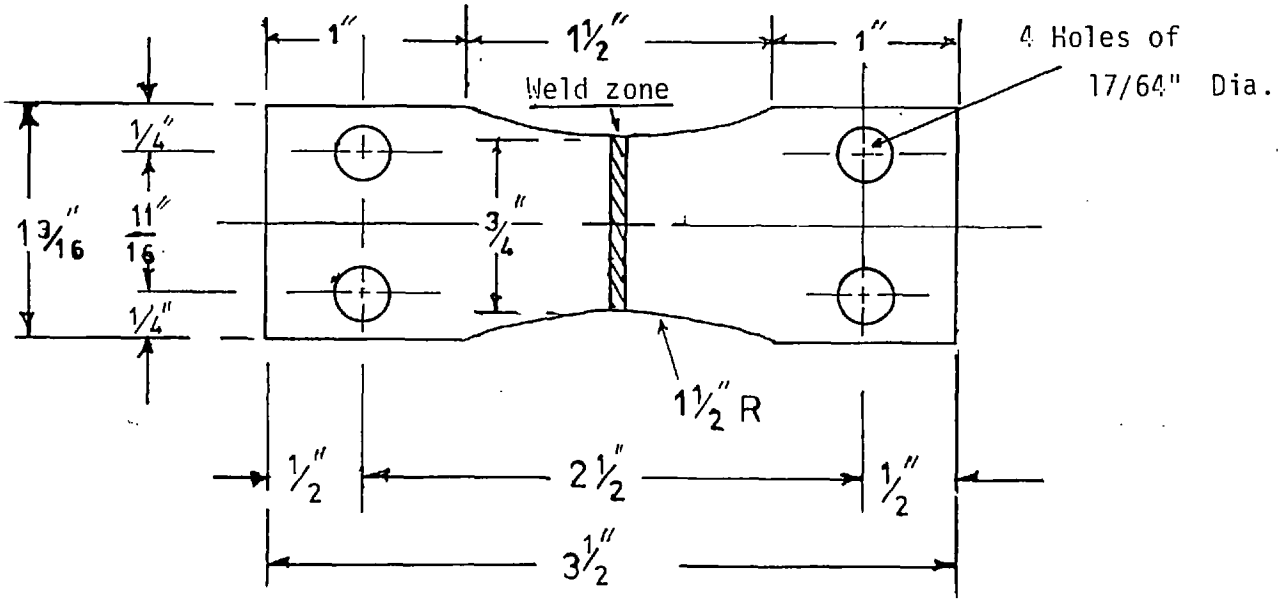

Fig: 6.6 Sketch for Fatigue Test specimen

However, a fatigue limit was predicted from the fatigue limit of the parent material, tensile strength and few sample tests around that limit. Then about four samples were tested around that predicted limit to confirm the prediction of the endurance ratio.

The simple bending type fatigue tests was performed using the Avery Dynamic Fatigue Testing machine (Type 7303). Fatigue specimens were machined carefully keeping the weld zone at the middle as shown in Fig. 6.6.

6.3.7 Corrosion Properties

The corrosion property of the welded joints in tin plate was a matter of interest due to the application of welded joints in the making of tin cans used for storing foods and chemicals. This was also true for titanium due to its increasing use in the chemical industry.

The corrosion resistance of some laser welds and parent material was measured by the Tafel extrapolation method[237-8].

It is possible to measure extremely low corrosion rates using this method. It can also be performed rapidly and with high accuracy but numerous restrictions must be met before this method can be used to get this accuracy. The principle of the method is discussed below.

6.3.7.1 Principle of Tafel extrapolation method for corrosion rate measurement

The Tafel extrapolation technique[237] uses data obtained from cathode or anodic polarisation measurements. Cathodic polarisation data are preferred, since these are easier to measure experimentally. For the present study cathodic polarisation data was used.

A schematic diagram for conducting the cathodic polarisation experiment is shown in Fig. 6.7.

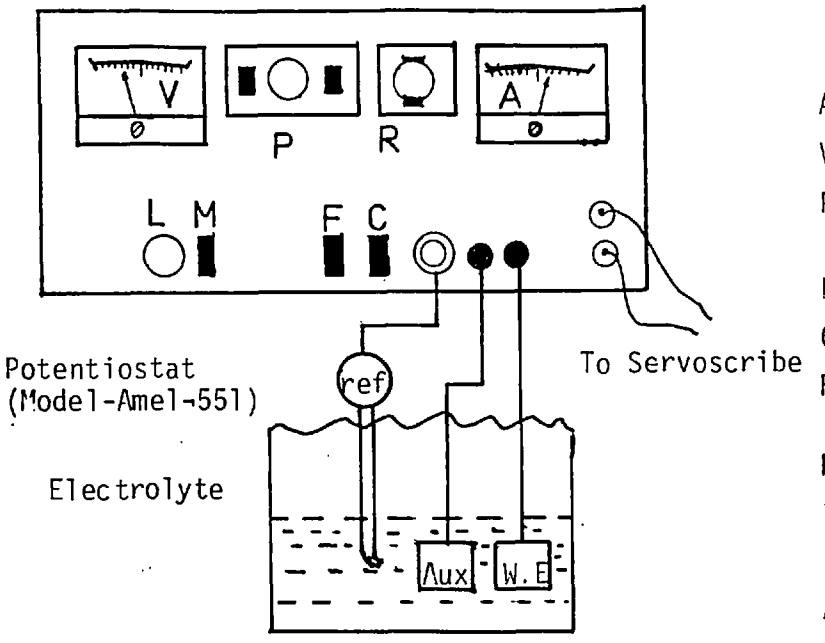

A- Ammeter
V- Voltmeter
P- Voltage & Current presetting
R- Current range
C- Cell switch IN-OUT
F- Function: Potentiostat-Galvanostat
M- Power-ON-OFF
L- Indicator Lamp
ref:-Reference electrode
Aux- Auxiliary electrode
W.E.-Working electrode (The sample)

Fig: 6.7 Electric circuit for Cathodic polarisation measurement for Corrosion rate measurement.

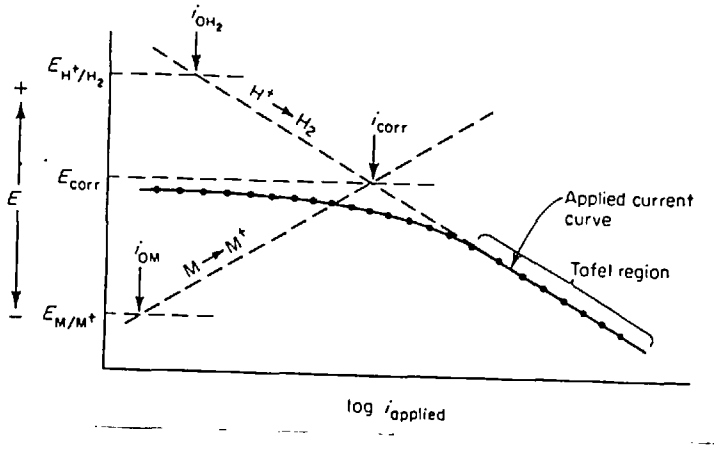

Fig. 6.8 Applied current cathodic polarisation curve of a corroding metal showing Tafel extrapolation (Ref. 237)

The metal sample is termed the working electrode and the cathode current is supplied to it by means of an auxiliary electrode composed of inert material such as platinum. The current is measured by means of an ammeter A, and the potential of the working electrode is measured with respect to a reference electrode indicated at voltmeter, V of the potentiostat . The micrometer dial "m" serves to adjust continuously the voltage or current within the range. The current and voltage are continuously measured.

To understand the process it is necessary to consider the results[237] obtained during the cathodic polarisation of a metal, M, immersed in an air-free acid solution. Prior to the application of cathodic current, the voltmeter indicates the corrosion potential of the specimen with respect to the reference electrode. If the potential of the electrode is plotted against the logarithm of the applied current, a figure similar to that shown in Fig. 6.8 is obtained. The curve is nonlinear at low currents, but at higher currents it becomes linear on a semilogarithmic plot of log current versus potential.

Since mixed-potential theory is based on the assumption of the conservation of charge the applied anodic current density is equal to the difference between the total reduction rate and total oxidation rate[237].

$$i_{app(cathodic)} = i_{reduction} - i_{oxide} \qquad (6.14)$$

Referring to both Eqn. 6.14. and Fig. 6.8, it is apparent that at high applied current densities, the applied current begins to approach total actual cathodic current, since the corresponding total anodic current becomes negligible. In actual practice, an applied polarization curve becomes linear on a semilogarithmic plot at approximately 50 mV more active than the corrosion potential. This region of linearity is referred to as the Tafel region. In Fig. 6.8 the total anodic and cathodic polarization curves corresponding to hydrogen evolution and metal dissolution are super-imposed as dotted lines. It can be seen that at relatively high applied current densities

the applied current density and that corresponding to hydrogen evolution have become virtually identical.

To determine the corrosion rate from such polarisation measurements, the Tafel region is extrapolated to the corrosion potential. At the corrosion potential, the rate of hydrogen evolution is equal to the rate of metal dissolution and this point corresponds to the corrosion rate of the system expressed in terms of current density. To ensure reasonable accuracy, the Tafel region must extend over a current range of at least one order of accuracy.

6.3.7.2 Corrosion test for tin plate

The electrolyte used for corrosion rate measurement for tin plate was 10% NaCl. This particular electrolyte was chosen considering that tin plates would be used for food cans. The auxiliary electrode was platinum whereas the reference electrode was saturated calomal. The set up is as shown in Fig. 6.7

6.3.7.3 Corrosion test for titanium alloys

The electrolyte used for corrosion rate measurement of titanium alloys was 2% HCl. The reason for corrosion testing of titanium alloy was its increasing use in the chemical industry particularly in sea water heat exchangers at power stations. The auxiliary electrode was platinum and the reference electrode was saturated calomel (saturated solution of KCl rubbed with $HgCl_2$) connected through Agar salt bridge drawn into lugging capillary. This capillary end was placed near the specimen to reduce the ohmic resistance of the electrolyte. The set up is already shown in Fig. 6.7.

6.3.8 Composition variation of weld ingot

To study the variation of composition of weld ingot with respect to the parent metal electron probe micro-analysis was carried out in a few samples. The test was carried out by the Analytical Services Laboratory of the Royal School of Mines.

6.3.9 Measurement of undercut of the welds

Undercut and underbead of the welds are the parameters of importance because excessive presence of those may act as stress raisers. They are illustrated in Fig. 6.9.

The undercut and underbead of the selected samples of the welds were measured using a projecttina microscope with graduated projection screens. The accuracy was ± 0.02mm. More sophisticated methods for measuring surface irregularities such as the talysurf were found to be too sensitive.

6.3.10 Oxygen contamination of titanium weld

Due to inadequate shielding arrangements surface of some of the welds were oxidised. To study the extent of oxygen contamination chemical analysis of total oxygen for a doubtful sample was carried out at Imperial Metal Industries, Birmingham.

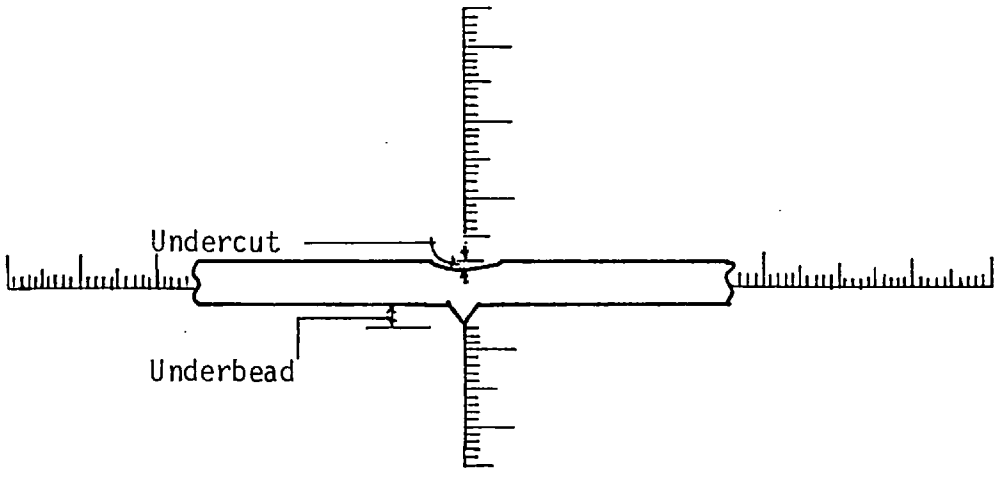

Fig: 6.9 Sketch showing Undercut and Underbead

CHAPTER 7

EXPERIMENTAL RESULTS AND DISCUSSION

7.1 Summary

The experiments were carried out to study

a) The effect of different welding variables
b) The metallurgical and mechanical properties of the laser welded materials.

The materials for welding can be broadly divided in three following groups:

1) Titanium alloys
2) Tinplate (tin coated mild steel)
3) Drum quality mild steel sheets.

Results and observations from the experiments are discussed in following sequences.

1(a) Welding variables for titanium alloys

i) Effect of laser power
ii) Effect of welding speed
iii) Effect of material thickness
iv) Effect of composition
v) Extrapolation up to 5kW
vi) Discussion and comparison with other processes

1(b) Metallurgical properties of titanium alloy welds

i) Radiography
ii) Metallography
iia) Optical microscopy
iib) Scanning electron microscopy
iic) Transmission electron microscopy
iii) Grain size
iv) Discussion and comparison with other processes

1(c) Mechanical properties of titanium alloy welds

i) Hardnesss measurement
ii) Tension test
iii) Fatigue property
iv) Discussion and comparison with other processes

1(d) Microstructure and mechanical properties of titanium alloy welds

1(e) Corrosion properties of titanium alloy welds

1(f) Composition variation of weld ingot

i) Electron probe micro-analysis

1(g) Undercut and underbead of titanium welds

1(h) Oxygen diffusion in titanium alloy welds

1(i) Thermal efficiency of laser welding and titanium

i) Melting efficiency
ii) Process efficiency

2(a) Welding variables for tinplate

i) Type of welds
ii) Effect of laser power
iii) Effect of welding speed
iv) Discussion and comparison with other processes

2(b) Metallurgical properties of tinplate welds

i) Radiography
ii) Metallography
iia) Optical microscopy
iii) Discussion and comparison with other processes.

2(c) Mechanical properties of tinplate welds

i) Micro-hardness measurement

ii) Tension test

iii) Fatigue properties

iv) Discussion and comparison with other processes

2(d) Microstructure and mechanical properties of tinplate welds

2(e) Corrosion properties of tinplate welds

2(f) Composition variation of weld ingot

i) Electron probe micro-analysis

2(g) Undercut and underbead of tinplate welds

2(h) Thermal efficiency of laser welding of tin plates

i) Melting efficiency

ii) Process efficiency

3(a) Welding variables for drum quality mild steel plates

i) Effect of laser power

ii) Effect of welding speed

iii) Discussion and comparison with other processes

3(b) Metallurgical properties

i) Radiography

ii) Metallography

iia) Optical microscopy

iii) Discussion and comparison with other processes

3(c) Mechanical properties

i) Microhardness measurement

ii) Tension test

iii) Fatigue properties

iv) Discussion and comparison with other processes

3(d) Micro-structure and mechanical properties of drum quality mild steel welds

3(e) Undercut and underbead of the welds

3(f) Thermal efficiency of laser welding of drum quality steel

i) Melting efficiency

ii) Process efficiency

7.2 Results and Discussion of Titanium Alloy Welding

7.2.1 Welding variables for titanium alloys

The range of welding runs on titanium alloys for various welding conditions which is illustrated in Fig. 7.1. Details are given in Appendix 7 .

7.2.1.1 Effect of laser power

The variation of welding speed with laser power for different thicknesses is shown in Fig. 7.2a.

It is evident that the welding speed for a particular thickness increases with the increase of power. But there is a certain threshold power below which welding is not possible for particular thickness.

In Figure 7.2a a trend of maximum welding speed and minimum welding speed possible for the thicknesses are shown. It is worth noting that the range of welding speed for successful weld decreases with the increase of thickness.

Maximum welding speeds for 2mm Ti-6Al-4V predicted by the mathematical model for different laser powers are also shown in Fig. 7.2a. It is evident that the prediced values are higher than actual values in the low power region which is probably due to the fact that there is more unaccounted heat loss at low power than that for high power. Incorporation of latent heat of fusion, moving boundary for solid/liquid phase etc. may improve the prediction given by the model. However, the model is useful for selecting process variables for new sets of materials.

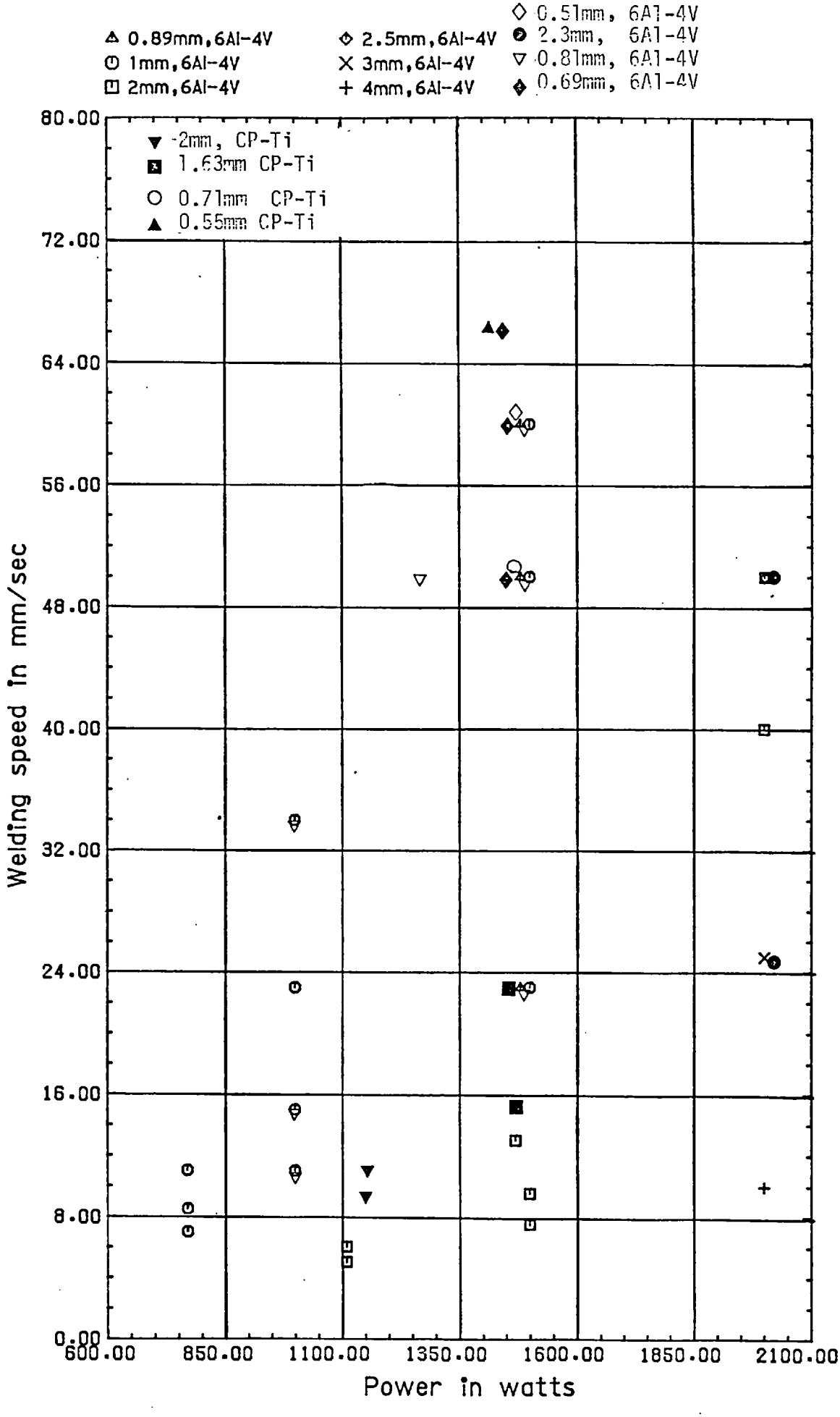

Fig. 7.1 The range of welding runs in titanium alloys for various welding conditions

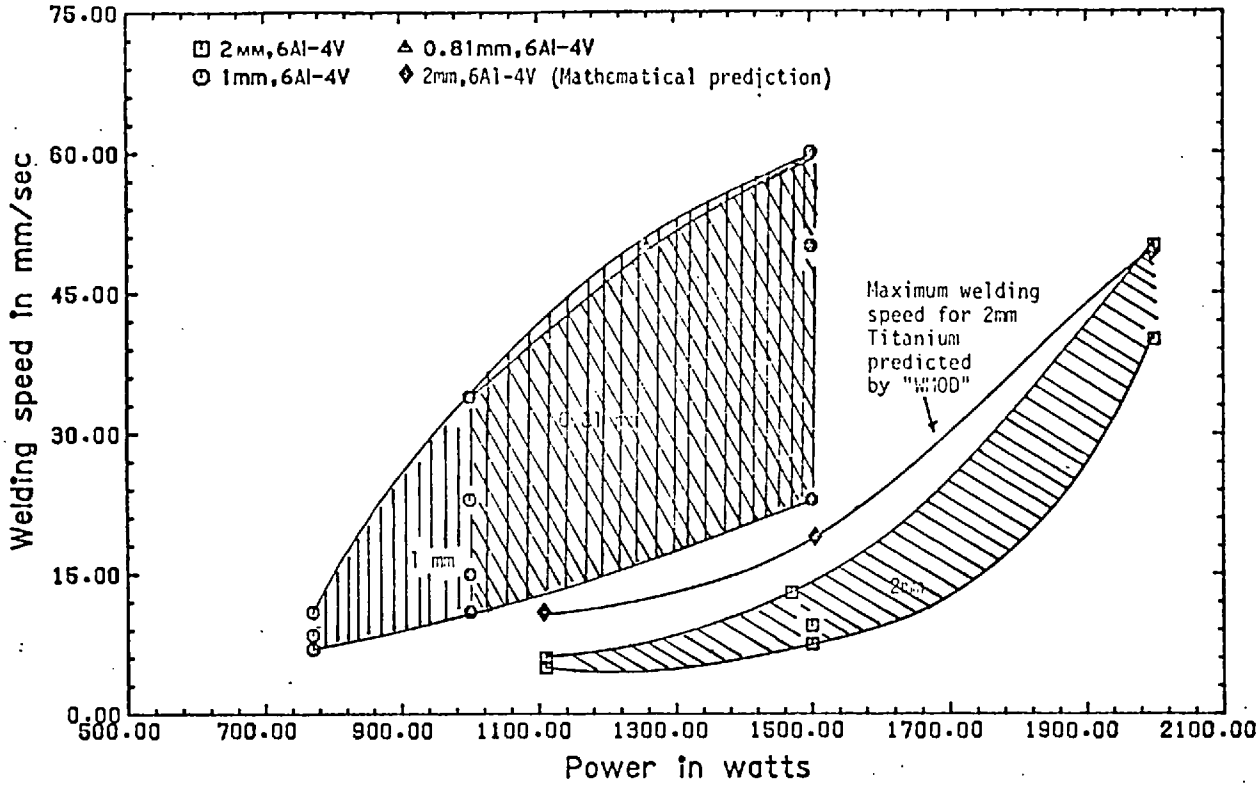

Fig 7.2a Variation of titanium welding speed with power
(Experimental and mathematical prediction from wmod)

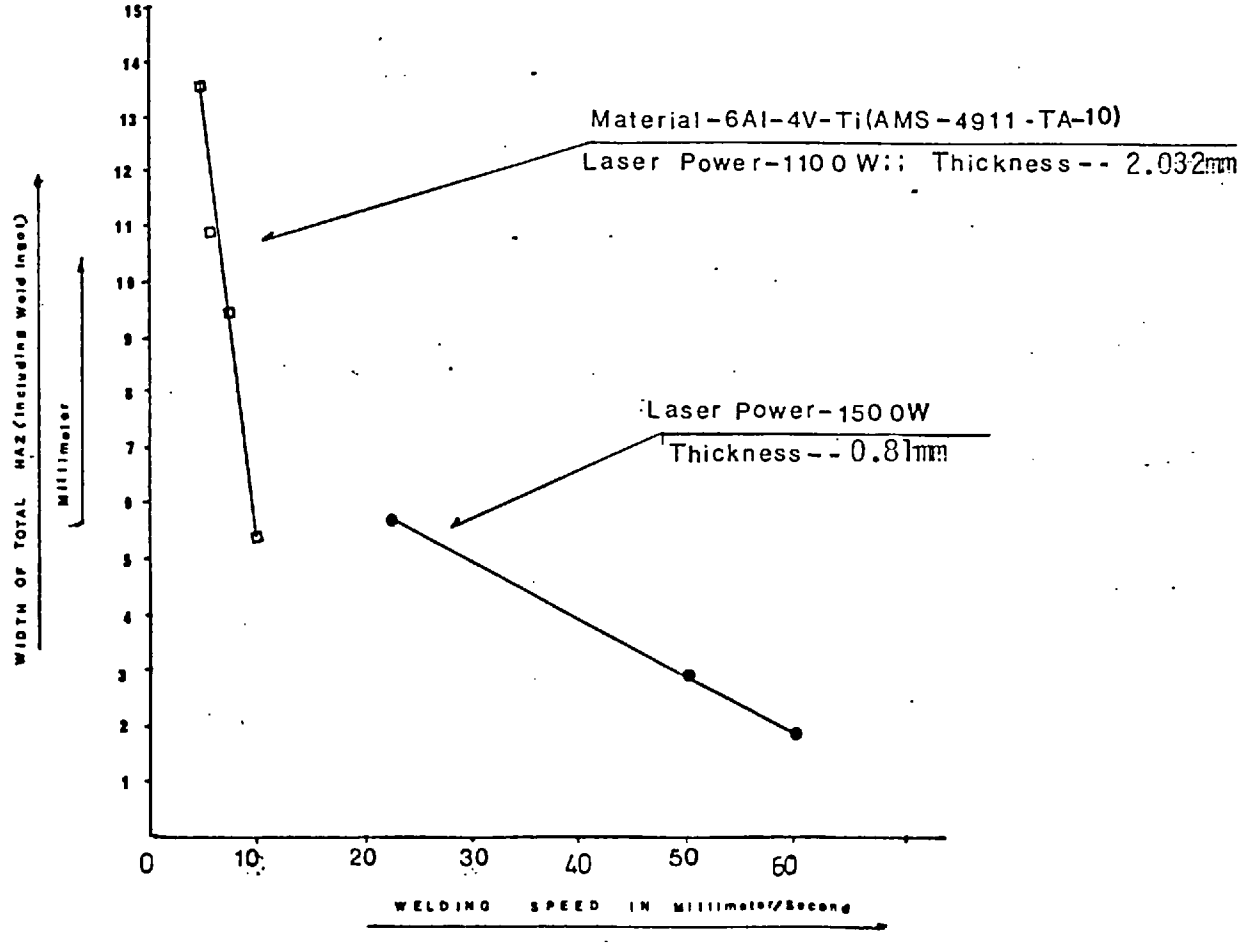

FIG. 7.2b Variation of HAZ with titanium welding speed

7.2.1.2 Effect of welding speed

Fig.7.2a also shows that for a particular power welding can be performed for a range of speed for a particular thickness. But beyond that range full penetration welding is not possible. Higher speeds may lead to improper penetration as shown in Plate 7.1

Plate 7.1 represents the macrograph of 2mm (0.08") thick Ti-6Al-4V alloy welded at 1100W ± 20W laser power and traverse speed of 9.5mm/sec. leading to improper penetration; whereas the same material could either be welded, with full penetration, with 1100 watts at 5mm/sec. or 1500 watts at 9.5 mm/sec.

Fig 7.2b shows the variation of HAZ against the welding speed. It is evident that the HAZ varies inversely with welding speed which means that at lower speeds more energy is wasted to heat up the workpiece.

7.2.1.3 Effect of material thickness

The variation of welding speed with thickness for a laser power of 1000 ± 10W, 1500W ± 20W and 2000 ± 40W is shown in Fig. 7.3. It is evident that for the same power a slower speed is required for greater thicknesses.

7.2.1.4 Effect of composition

Change of composition leads to change of physical properties such as thermal conductivity, thermal diffusivity etc. These changes in properties affect the welding conditions. Table 7.1 shows the welding speeds of C.P. Titanium and Ti-6Al-4V of same thickness and welded with same power.

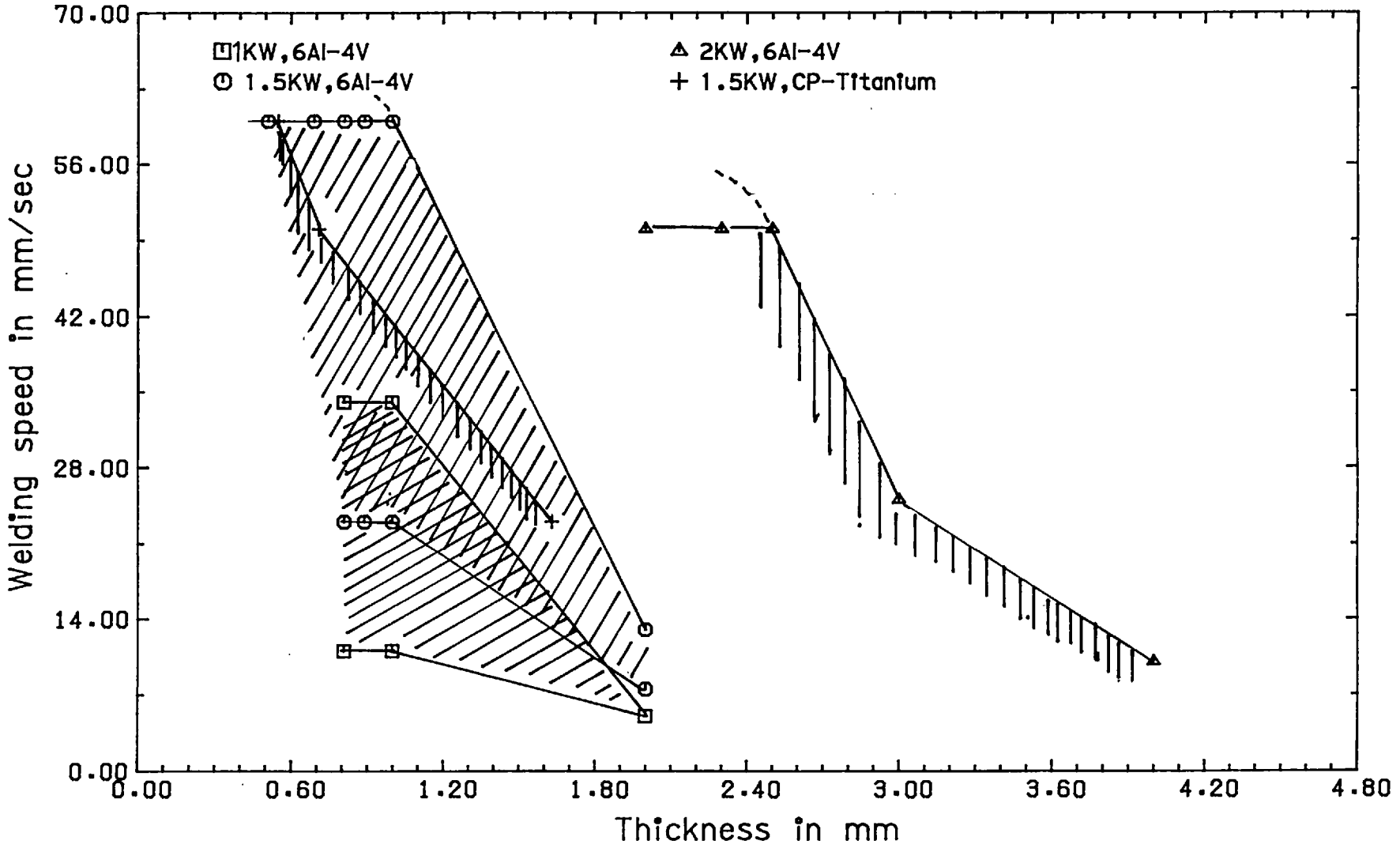

Fig.7.3 Variation of titanium welding speed with thickness

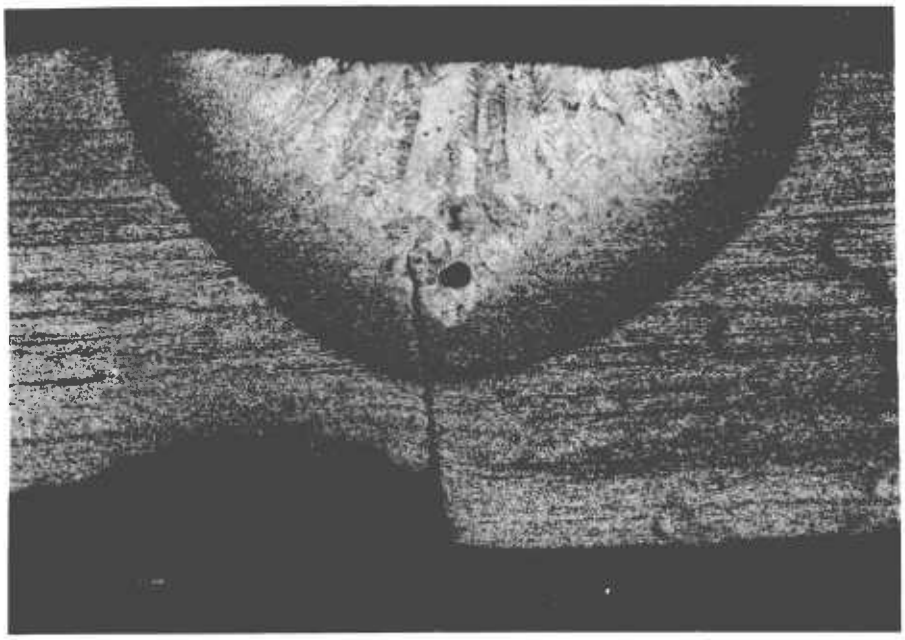

PLATE 7.1 Showing the defect in welding due to traverse speed greater than the optimum range

Weld	Thickness	Material	Laser power	Welding speed	Thermal* conductivity at 300°K
	mm		Watts	mm/sec	$W.M^{-1}.K^{-1}$
2	2.032	CP Titanium	1140±10	9.5	20.93
4	"	"	"	13	"
10	"	Ti-6Al-4V	1110±10	6	7.33
12	"	"	"	5	"

* Thermal conductivity data obtained from Ref. 233 and values at room temperature ($300^{o}K$) are quoted.

TABLE 7.1

It is evident from the above table that high welding speed could be achieved for material of higher thermal conductivity for the same power and thickness.

For materials of exceedingly high thermal conductivity such as copper (385 $WM^{-1}\ K^{-1}$), aluminium (201 $WM^{-1}\ K^{-1}$) reflectivity for 10.6 m radiation is also very high. Therefore, these materials can not be welded at the power density level ($10^{6}W/cm^{2}$ - $10^{7}W/cm^{2}$) of the present study.

7.2.1.5 Extension of laser welding work with 5kW CO_2 laser

In a recent study carried out by the author laser welding variables for Ti-6Al-4V have been extrapolated up to 4.7kW. For this study a series of bead-on-plate welds were done on 6Al-4V-Ti using the CL5 5kW CW CO_2 laser designed and developed by Culham laboratories, U.K.A.E.A. This particular laser has an unstable resonator with an output of ring shaped beam, 43mm in diameter The focussed beam diameter was around 500μm using an F6 mirror. Therefore, the focussed beam diameter was comparable for both the lasers.

Welding speeds are plotted against output power for different substrate thicknesses in Figure 7.4, and welding speed against substrate thickness for different powers is shown in Figure 7.5.

It is evident from the above figures that the relationship between the variables is the same as observed in the 2kW study. The data for powers of 2kW for both the lasers used here were found to be comparable. The slightly higher values obtained with the 5kW laser may be explained by the fact that bead on plate welding was performed with the 5kW laser as opposed to butt weld which was done with the 2kW laser.

7.2.1.6 Discussion and comparison with other processes

The total cross-sectional area of metal joined in unit time per unit of applied energy is suggested as a useful practical method of comparing processes and their performance. This is known as the joining rate of the process.

The joining rate for a given process and joint design frequently tends to start well below average with thin material, to rise as the thickness is increased and optimum welding conditions are established and finally to drop as the thickness becomes too great for the process to handle[12]. The same tendency is observed in this study for the laser welding of titanium alloys. Fig. 7.6 shows the trend of the variation of joining rate (mm^2/KJ) against thickness (mm) for three different laser welding powers one obtained from the present study along with two obtained from Banas[157-164]. The peak joining rate for the thicknesses and the powers are plotted. However, it should be noted that only some four weldings describe the trend of each variable of significance due to the lack of availibility of the material.

There are very few published data available for the welding of titanium alloy at any power level and nothing for the power level used for the present study.

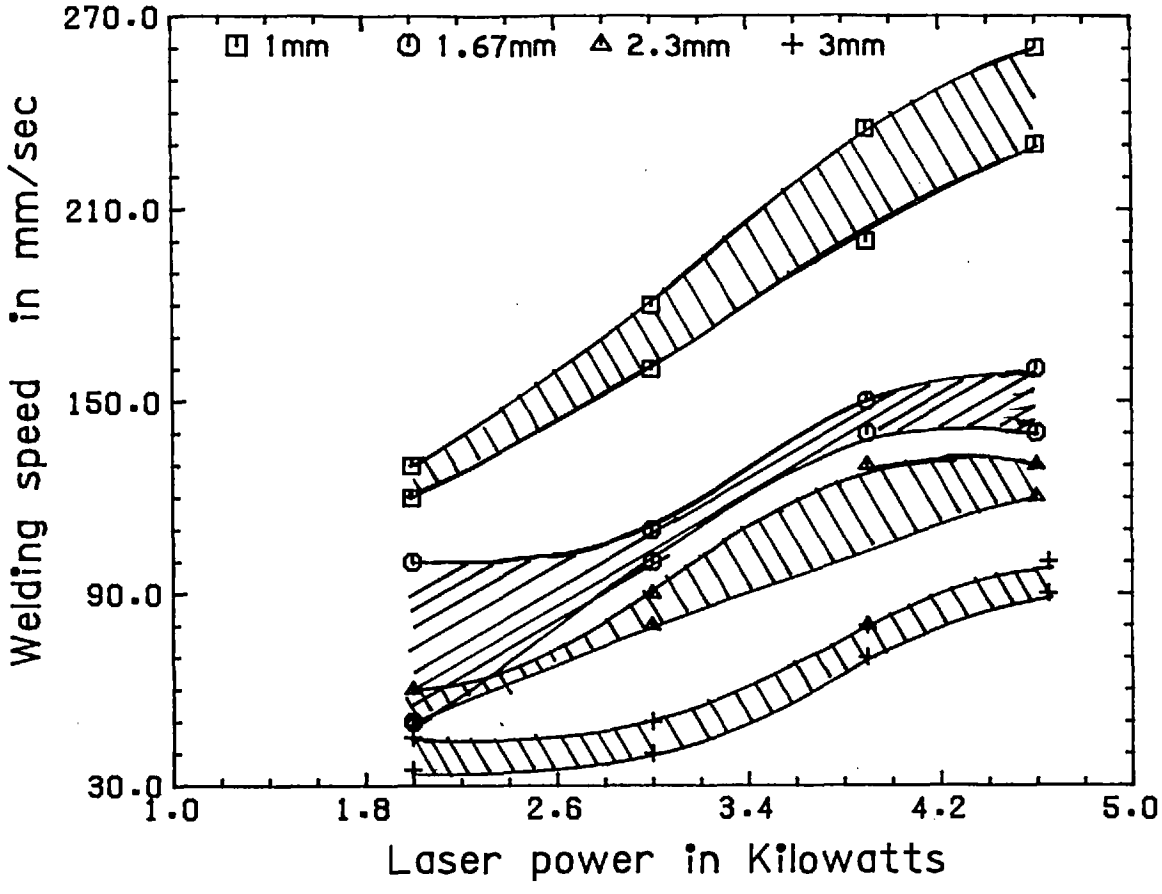

Fig. 7.4 Titanium welding speed vs. power for Culham 5kW CO_2 laser

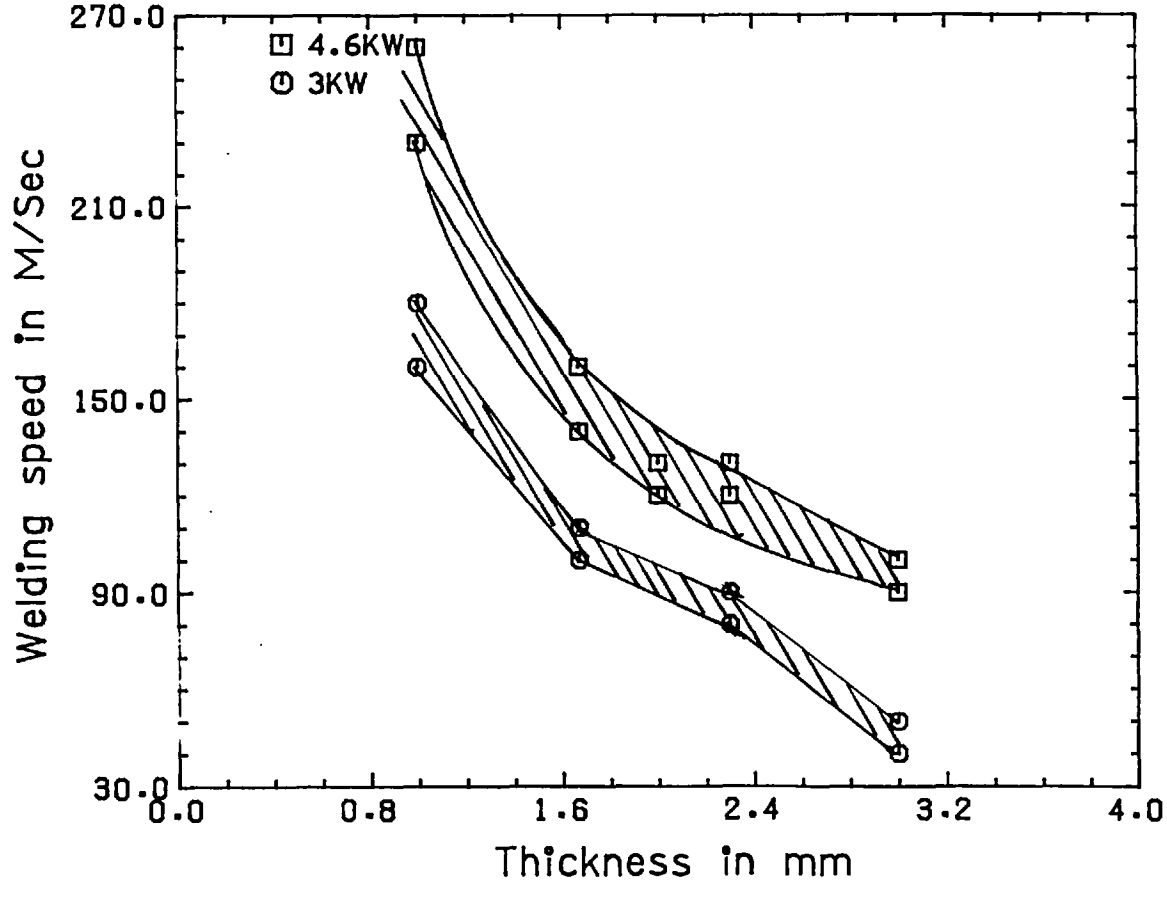

Fig. 7.5 Titanium welding speed vs. thickness for Culham 5kW CO_2 laser

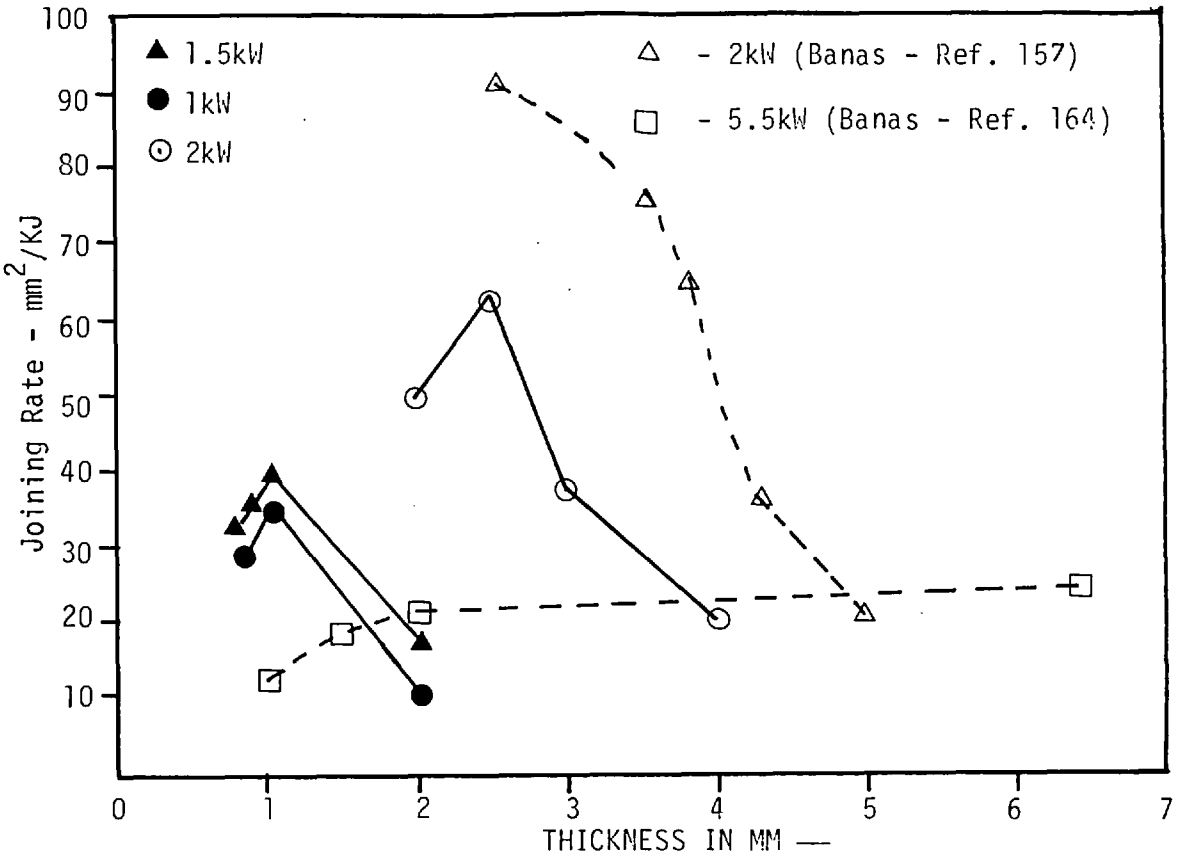

FIG. 7.6 Joining rate vs. thickness for titanium

EFFECT OF LASER WELDING SPEED ON PENETRATION

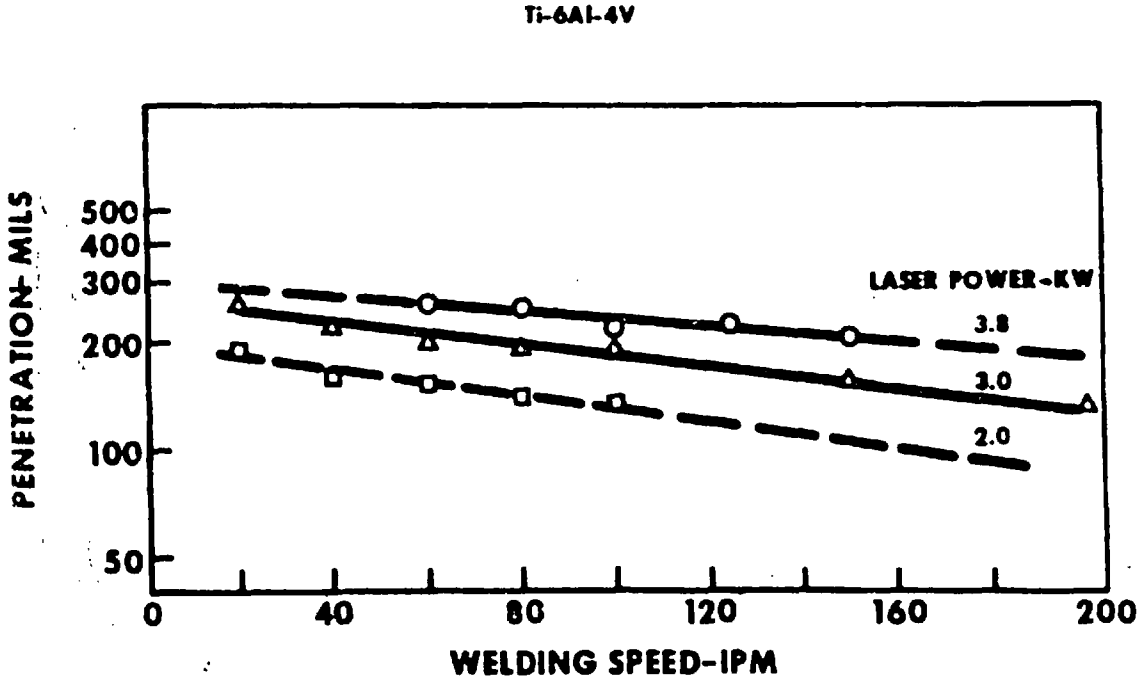

FIG. 7.7 Penetration vs. titanium welding speed (Ref.157)

However, Banas[7,157,164] published some data on welding of Ti-6Al-4V using a CO_2 laser in the power range of 2 to 5.5 kW. In his earlier work[7,157] he reported a penetration versus welding speed as shown in Fig. 7.7. From this figure we find that for 2mm thick 6Al-4V-Ti the joining rate is 90.77 mm^2/kJ for a laser power of 2kW. But in his later work[164] he reported a joining rate of 21.56 mm^2/kJ for 2mm 6Al-4V-Ti welding using 5.5 kW laser power. The joining rate variation with thickness using Banas's[157,164] experimental values is also shown in Fig. 7.6. Th-ough, it is somewhat artificial to compare the joining rates obtained from different power levels even for the same thickness range, the trends of joining rates against thickness reported by Banas[157,164] in two different reports seem to be quite confusing. The joining rates reported by Banas[157] in 1972 are higher than that observed in the present study whereas that reported by Banas[164] in 1974 are lower.

Any comparison of laser welding with other processes is always somewhat artifical because each welding process has its own optimum range of metal thickness, power dissipations, joining rates, and joint geometry. However inadequate it may appear, when a comparison is called for it should be restricted to similar powers applied to similar metals of similar thickness to make it as meaningful as possible[160]. Keeping this in mind the laser welding data for Ti-6Al-4V are compared with the published data of other processes in Table 7.2.

TABLE 7.2

Process	Thickness mm	Material	Power kW	Welding Speed mm/sec.	Joining Rate mm^2/kJ
Laser	2	Ti-6Al-4V	1.5	13	17.33
Plasma Arc Ref. 164	2	Ti-6Al-4V	0.5	1.2	4.8
Plasma Arc Ref. 164	2	Ti-6Al-4V	0.76	2.3	6.05
EBW* (Ref 164)	2	Ti-6Al-4V	1.17	16.9	28.83
Laser	1	6Al-4V-Ti	0.77	11	14.29
GTA (Ref 164)	1	6Al-4V-Ti	0.76	1.5	1.97
EBW* (Ref 164)	1	6Al-4V-Ti	0.78	16.9	21.67

* Filler material added - 0.76mm Ti-6Al-4V wire

We can observe from the table that the laser welding speed and joining rate are better than that for arc welding but slower than that for EBW. However, numerical comparison should be treated with caution.

Other parameters will also be compared in the relevant sections.

7.2.2 Metallurgical properties of titanium alloy welds

7.2.2.1 Radiography

Most of the butt welds were x-rayed to study the discontinuity of the welds.

Plate 7.2 shows radiographs of three successful welds welded at different powers and speeds. No crack, porosity or inclusion were observed in successful welds. Undercut was also not prominent. But defects like incomplete penetration of unsuccessful welds which can be detected by visual inspection was confirmed from radiographs.

These observations lead us to believe that the process itself does not cause any contamination. Porosity is, however, a problem in EBW vacuum welding[6] and so this suggests that welding at atmospheric pressure has other advantages than mere convenience.

7.2.2.2 Metallography

To study the macro and micro structural change of the HAZ and fusion zone of the welds optical microscopy, SEM and transmission electron microscopy were used. Observations from these studies are discussed in turn.

7.2.2.2.1 Optical Microscopy

Titanium alloys were received in the annealed condition. The variation of microstructure for a typical Ti-6Al-4V weld as seen in an optical photomicrograph in comparison with its macrostructure is represented in a composite - Plate 7.3.

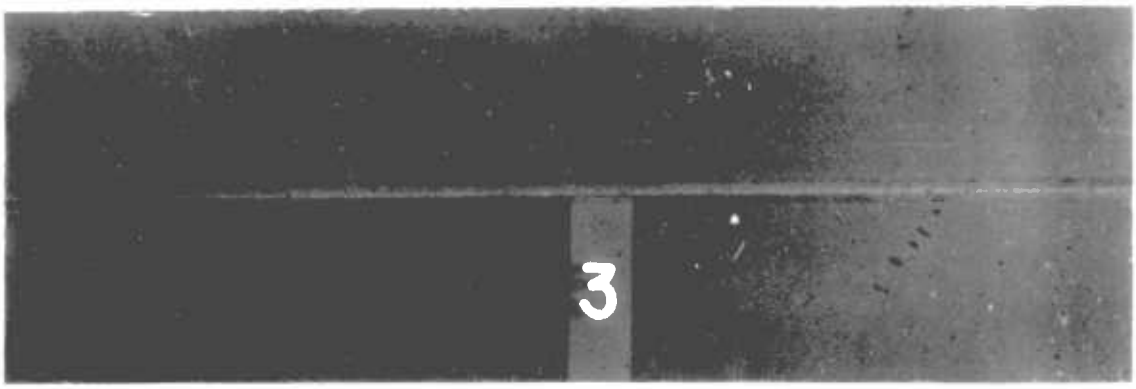

Commercially pure titanium (DTD 5063), 2mm thick
Butt weld - 1110 watts, 8.5 mm/sec

Ti-6Al-4V (AMS 4911-TA.10), 2mm thick
Butt weld - 1110 watts, 5 mm/sec

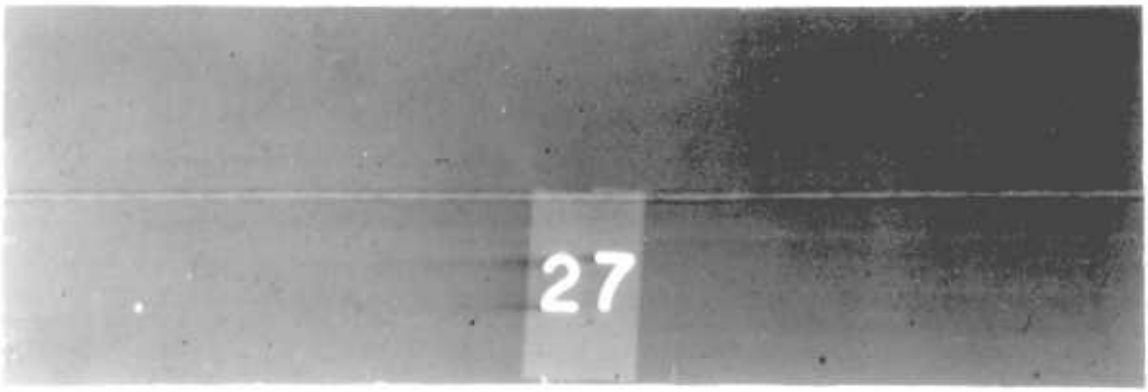

Ti-6Al-4V (AMS 4911 - TA.10), 2mm thick
Butt weld - 1000 watts, 23 mm/sec

PLATE 7.2 Representative radiographs for titanium welds

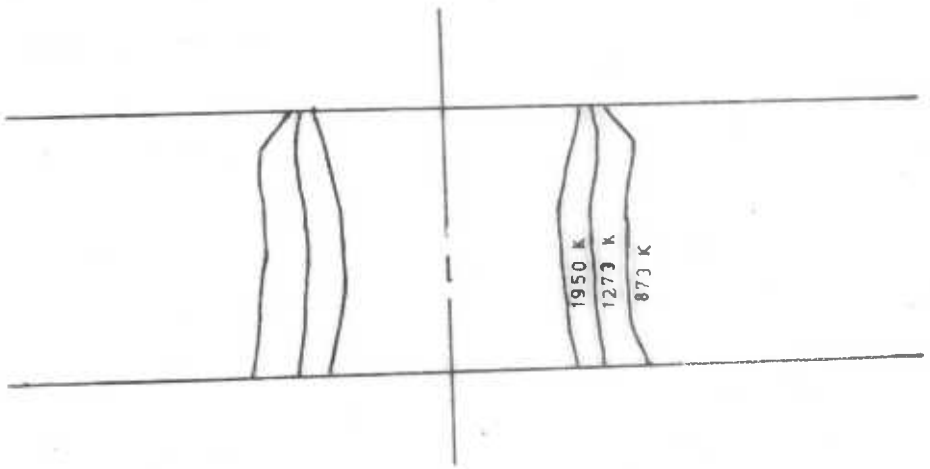

Predicted temperature contour

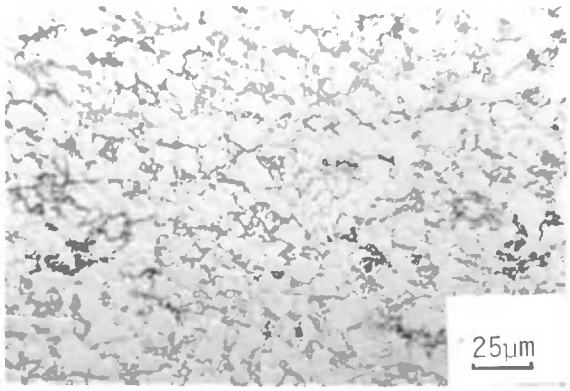

(A) Parent matrix

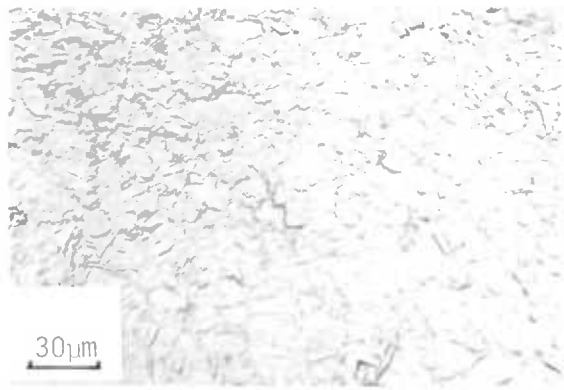

(B) HAZ

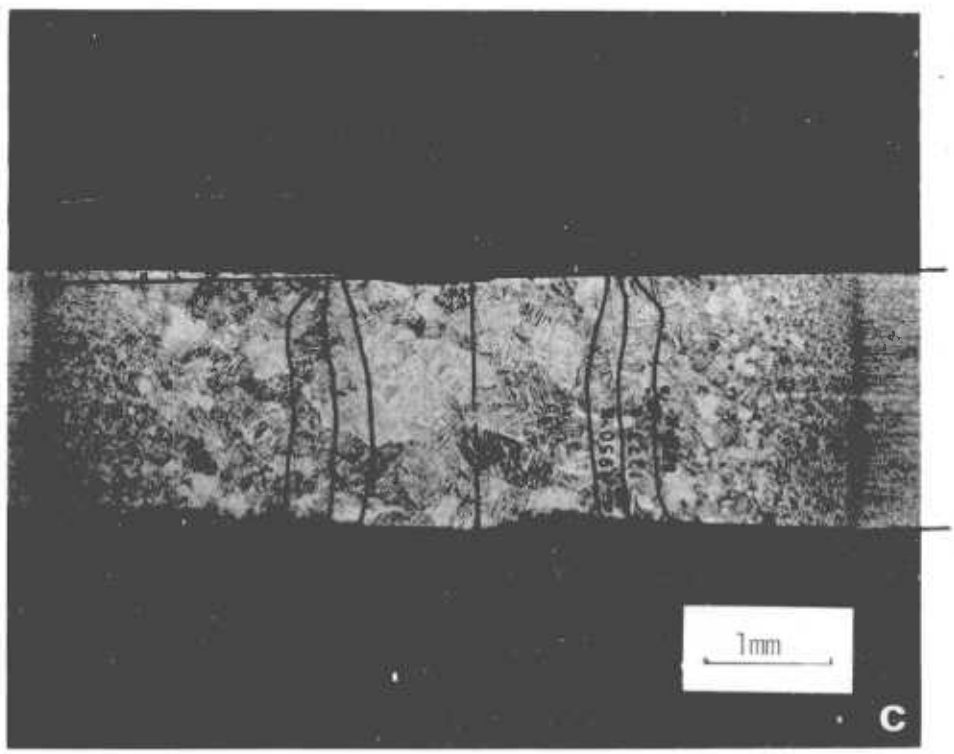

(C) Macrostructure of the weld
Predicted temperature contour

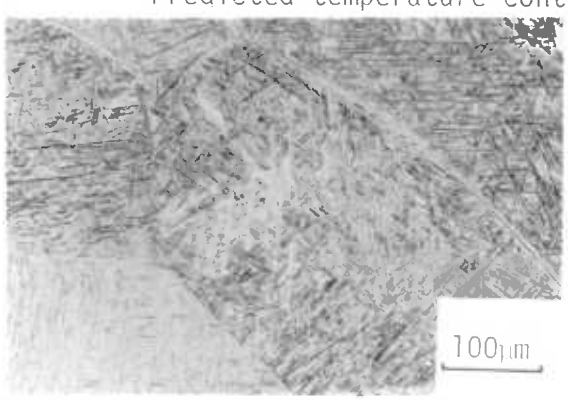

(D) Fusion zone

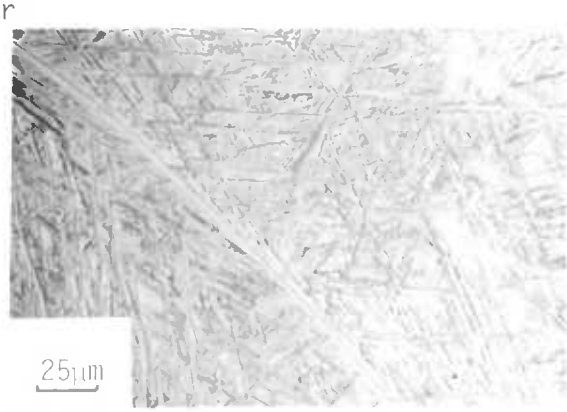

(E) Fusion zone

PLATE 7.3 Composite showing structural variation 2mm thick 6Al-4V-Ti alloy with CW CO_2 laser. Welding speed 7.5 mm/sec, laser power 1500W.

The parent metal (Plate 7.3a) shows dark β in a bright α matrix, which is a typical annealed structure for α-β titanium.

The heat affected zone consists of a mixture of α' (martensitic α) and primary α, which corresponds to a structure quenched from the range 980-720°C[239]. The HAZ is shown in Plate 7.3b. Right hand side of the micrograph, Plate 7.3b, is near the fusion zone. In that area traces of α' (martensitic α) can be observed, whereas at the left hand side i.e. further away from the fusion zone a relative increase of primary α is noticed. This observation is confirmed by scanning electron microscope study dicussed in the next section.

The fusion zone consists mainly of α' (martensitic α). Both the plates 7.3d and 7.3e represent the fusion zone of the same specimen. Abundance of α' (martensitic α) with the prior β-grain boundary is evident in this micrographs. This is confirmed by the structure revealed under both scanning and transmission electron-micrscopes. This kind of microstructure corresponds to a structure quenched from the β phase above 985°C[239]. This is also confirmed by comparison with the hardness values of others[239].

The variation of microstructure for a typical C.P. Titanium (DTD 5063) weld as seen in an optical photomicrography in comparison with its macrostructure is represented in a composite - Plate 7.4.

The parent metal (Plate 7.4a) shows equiaxed α grain which is a typical structure for annealed (around 700°C) commerically pure titanium. The black spots represents TiH formed during etching.

The heat affected zone (Plate 7.4c) consists mainly of recrystallised zones of "primary" α and some traces of transformed β in the form of plate like α.

The fusion zone (Plate 7.4d) consists mainly of α' (martensitic α) and plate like α with some "primary" α. That shows that the cooling rate for the fusion zone is higher than that for HAZ, and both HAZ and fusion zone are quenched from β region.

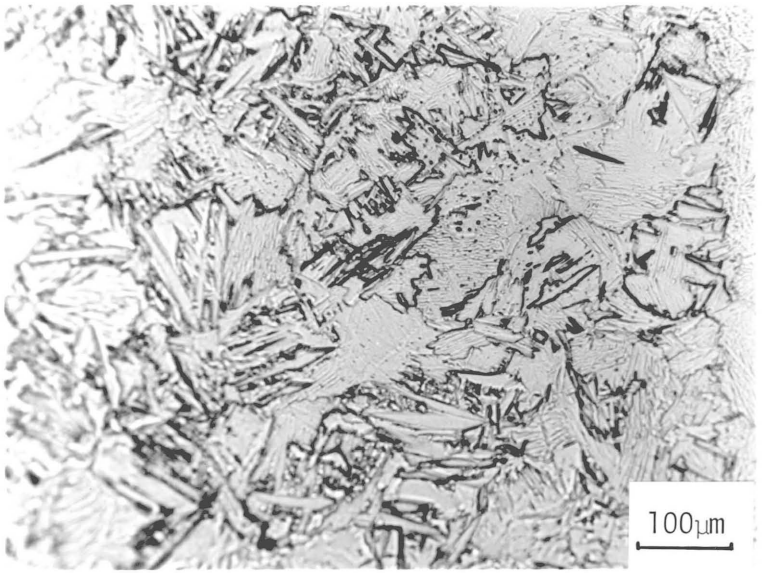

C

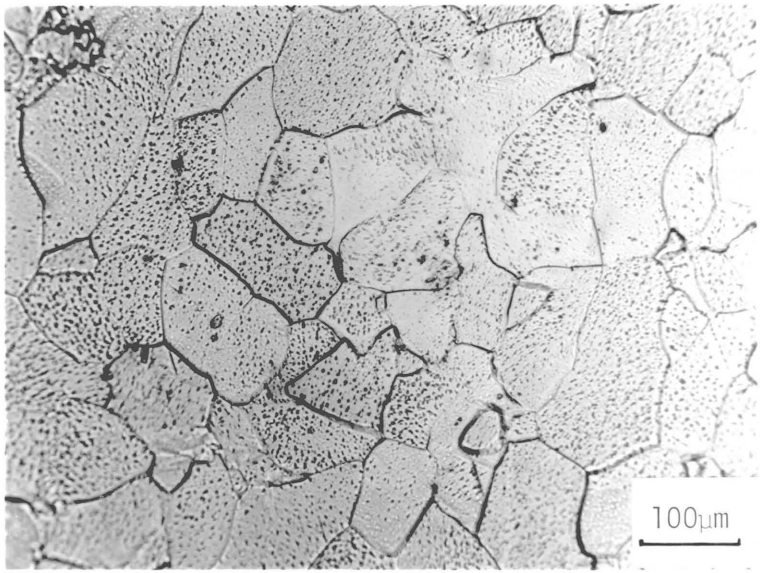

A

D

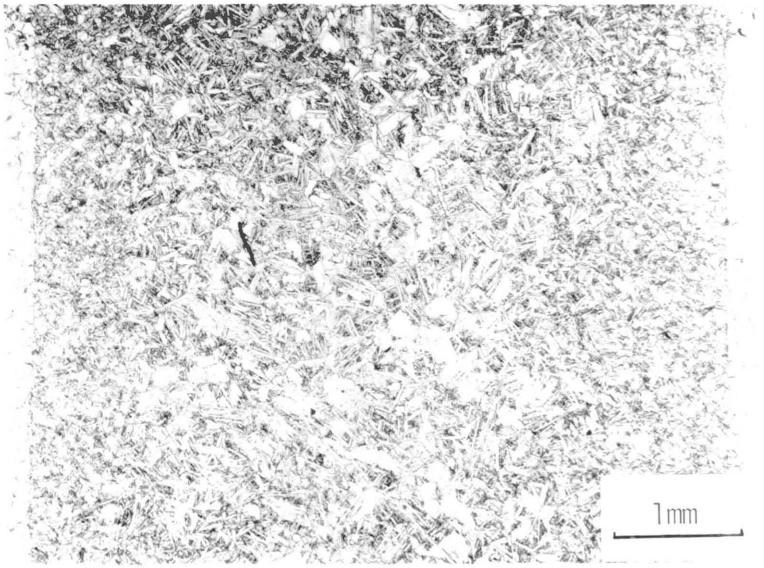

B

PLATE 7.4 Composite showing structural variation for butt welded 2mm thick CP-titanium (DTD 5063) with CW CO_2 laser welding speed. 11mm/sec, laser power 1110 watts

7.2.2.2.2 Scanning electron microscopy

Scanning electron micrographs of HAZ and fusion zone of the Ti-6Al-4V weld, shown in macrograph (Plate 7.3c), are represented in a composite - Plate 7.5.

Plate 7.5a represents the HAZ near the fusion zone, corresponding to the right hand side of the micro-structure shown in Plate 7.3b, as seen under SEM. It shows that this zone is a mixture of "primary" α with a fair amount of α' (martensitic α).

Plate 7.5b represents the HAZ further away from fusion zone. This zone mainly consisted of "primary" α with some transformed β. This confirms the observation from optical microstructure and we can generally infer that HAZ was below $985^{o}C$[239].

Plates 7.5c and 7.5d represent the fusion zone of the Ti-6Al-4V weld as seen under SEM.

Plate 7.5c is a scanning electron micrograph of the fusion zone near a prior β grain boundary as shown in optical photo-micrograph Plate 7.3e. This confirms that the fusion zone consists mainly of acicular α'(martensitic α) within prior β-grain boundaries.

Plate 7.5d is a scanning electron micrograph of the fusion zone near a point where three prior β-grain boundaries are joining. It can be seen that the α' (martensitic α) has a random orientation. This was subsequently confirmed by transmission electron microscope study.

7.2.2.2.3 Transmission electron microscopy

Plate 7.6 shows the transmission electron micrographs of Ti-6Al-4V welds.

The transmission electron micrograph (Plate 7.6a) of the weld zone also confirms the observations of the optical and scanning electron microscopy that the fusion zone consists mainly of α'

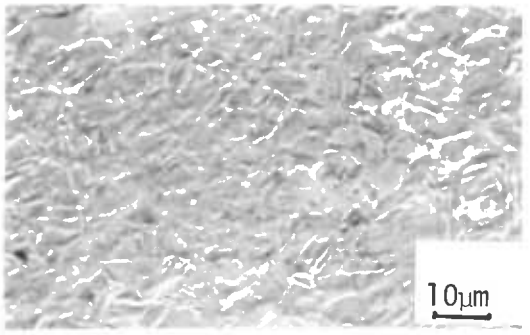

A

B

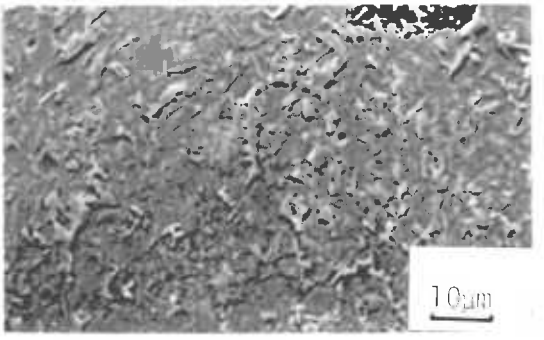

C

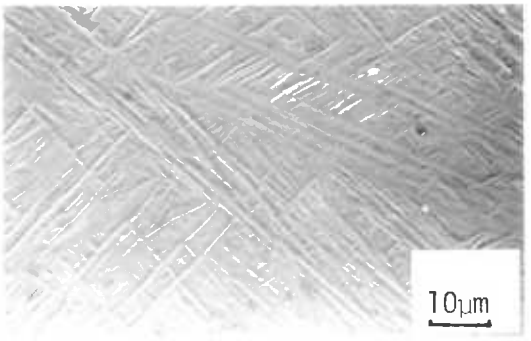

D

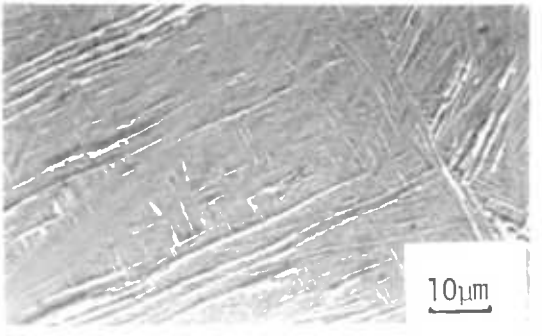

PLATE 7.5

Composite showing the scanning electron micrographs for butt welded 2mm thick 6Al-4V-Ti alloy with CW CO_2 laser welding speed 7.5 mm/sec, laser power 1500W

A) and B) HAZ

C) and D) Fusion zone

(martensitic α) of acicular morphology. This α' (acicular martensitic α) is characterised by large "primary" plates and smaller "secondary plates". The primary plates extend for large distances across the parent β grain and effectively partition the untransformed β. The partitioned β subsequently transforms to a series of short, acicular, secondary plates of martensite (Plate 7.6b and 7.6c). Similar microstructure was observed by Zaidi[244] for water quenched 6Al-4V-Ti from above 1000°C which also correlates with Hochied[239] et al. The selected area diffraction pattern (Plate 7.6b) of a martensite plate shown in Plate 7.6b indicates that the zone axis is $[10\bar{1}1]$ hcp. But the martensite plates are randomly situated. In another sample zone axis of the martensite plate was found to be [0001].

The parallel martensite plates (Plate 7.6e) observed in the fusion zone indicate that the cooling rate is high. The theoretical prediction from the mathematical model discussed in Chapter 3 indicated a cooling rate of 10^2 to 10^4 °C/sec. depending on the distance from the weld centerline. The theoretical cooling rates are shown in Fig 7.8. These rates compare well with the rates measured by Zaidi[244] and Hochied[239] for the observed microstructure; (viz at least 10^2 °C/sec for the areas heated above 1000°C).

7.2.2.2.4 Grain size measurement

The grain size at the fusion zone was measured for a few welds to study the effect of the welding speed on grain coarsening. Results are given in Table 7.3.

Laser Power in watts	Welding speed in mm/sec	Thickness in mm	Grain Size No of grains/sq. mm
1100	6	2.03	16.875
1100	5	2.03	14.666
1500	7.5	2.03	7.875
1500	9.5	2.03	13.5
1000	23	1.0	56.0
1000	15	1.0	34.67

TABLE 7.3

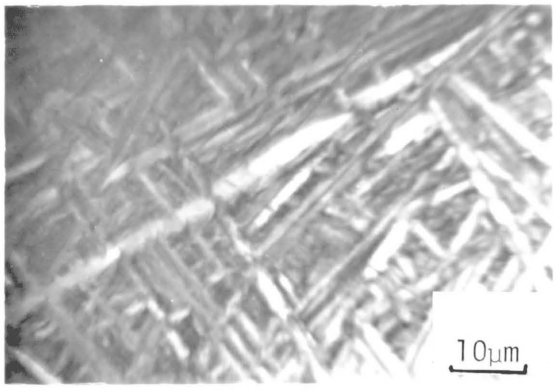

(A)

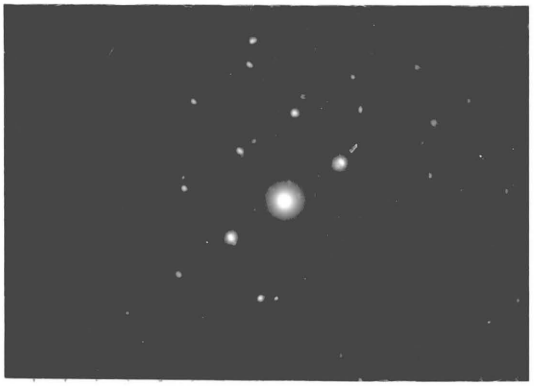

(D)

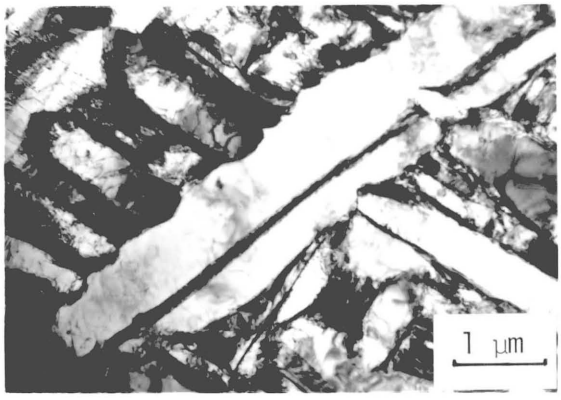

(B)

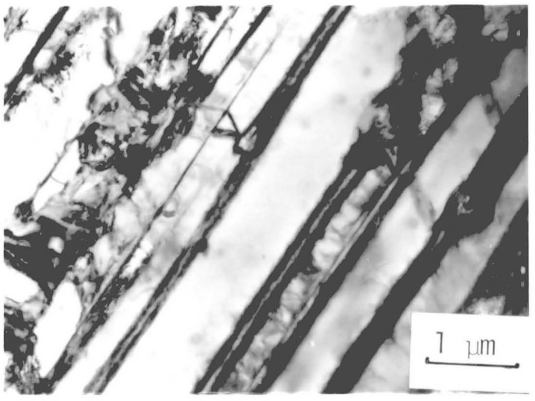

(E)

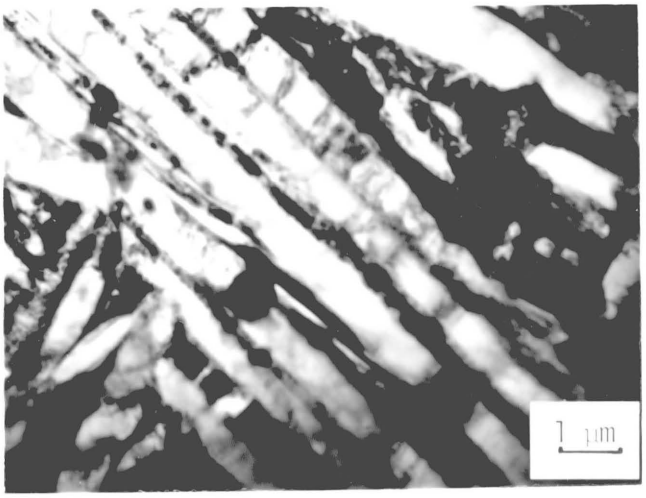

(C)

PLATE 7.6 Composite showing the transmission electron micrographs of the 6Al-4V-Ti weld

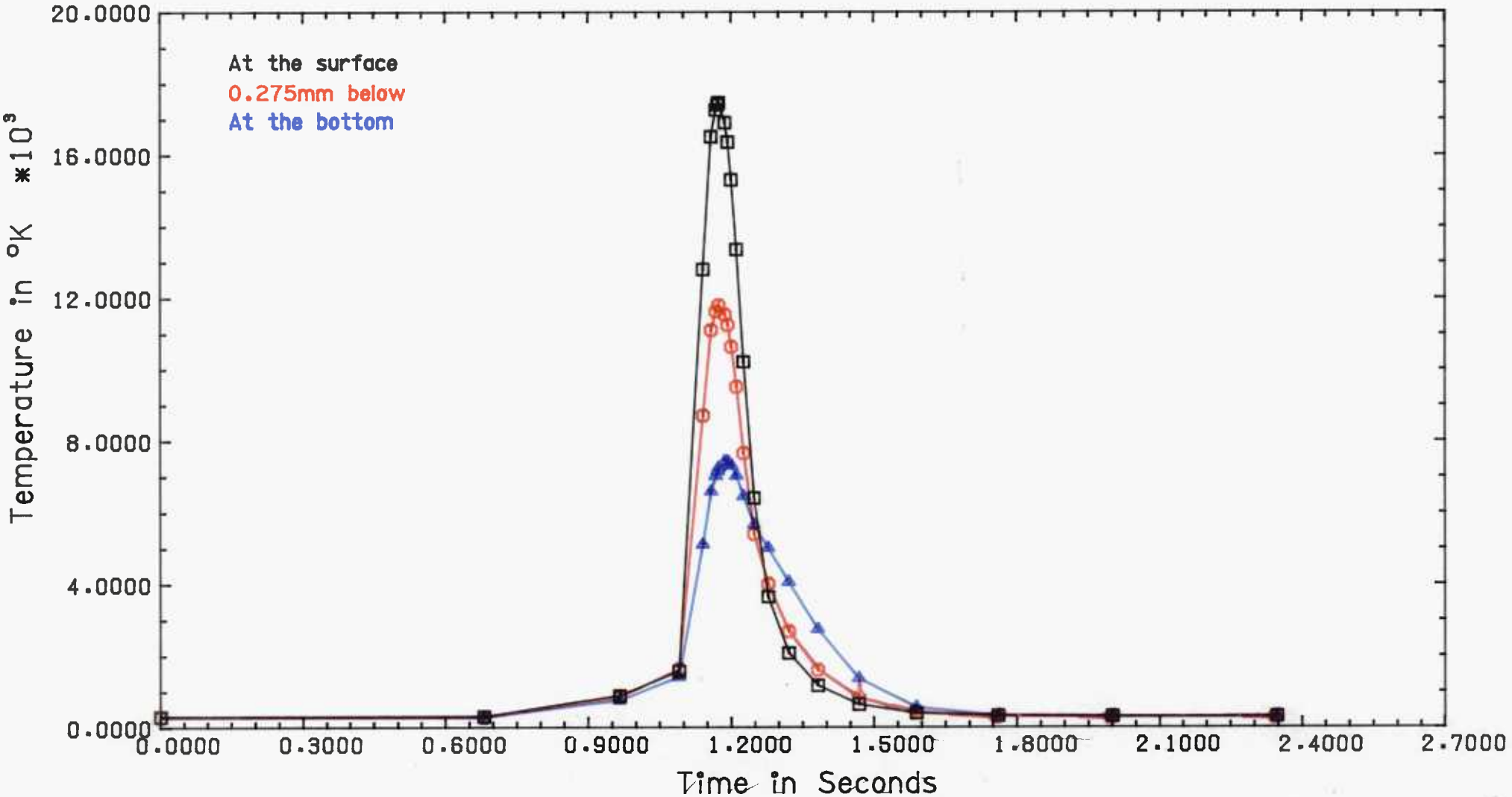

Fig.7.8 Mathematically predicted cooling rate for Ti-Weld;1500 watts,7.5mm/sec

It is evident from the data that for a particular power the higher the speed the less will be the grain coarsening.

7.2.2.3 Discussion and comparison with other processes

Banas[164] reports that 6Al-4V-Ti electron beam welds are quite narrow and exhibit a somewhat non-uniform radiographic appearance due to the lower surface weld spatter, whereas arc welds are considerably broader but also quite uniform in density. The laser welds of the present study exhibit uniform radiographic appearance and narrow welds. But the width of the weld is a function of the welding speed. After comparing with Banas's[164] it could be noted that the laser welds are narrower than arc welds and comparable to EBW. As previously mentioned in Section 7.2.2.1 porosity is also less in laser welds compared with EBW.

The microstructure of the laser welds consists mainly of α' (martensitic α) within prior β-grain boundary. Banas[164] reports the same microstructure for EBW. Banas also reported a Widmanstätten structure for plasma arc welds whereas Hill and Choi[253] reported the same structure for submerged arc welds.

This shows that beam welding processes involve much higher cooling rates compared with arc welding processes. In general, the beam welding processes can be considered as low specific energy input, high speed processes while the arc processes involve substantially higher specific energy inputs and slower welding speeds.

7.2.3 Mechanical properties of titanium alloy welds

7.2.3.1 Hardness measurement

Microhardness traverse across the weld ingot and HAZ reveals that in the knoop scale hardness the difference between α and β phase is not appreciable. In fact the variation of hardness is of the same order throughout, including parent matrix and weld ingot, showing no apparent increase in hardness in the weld ingot which mostly contains

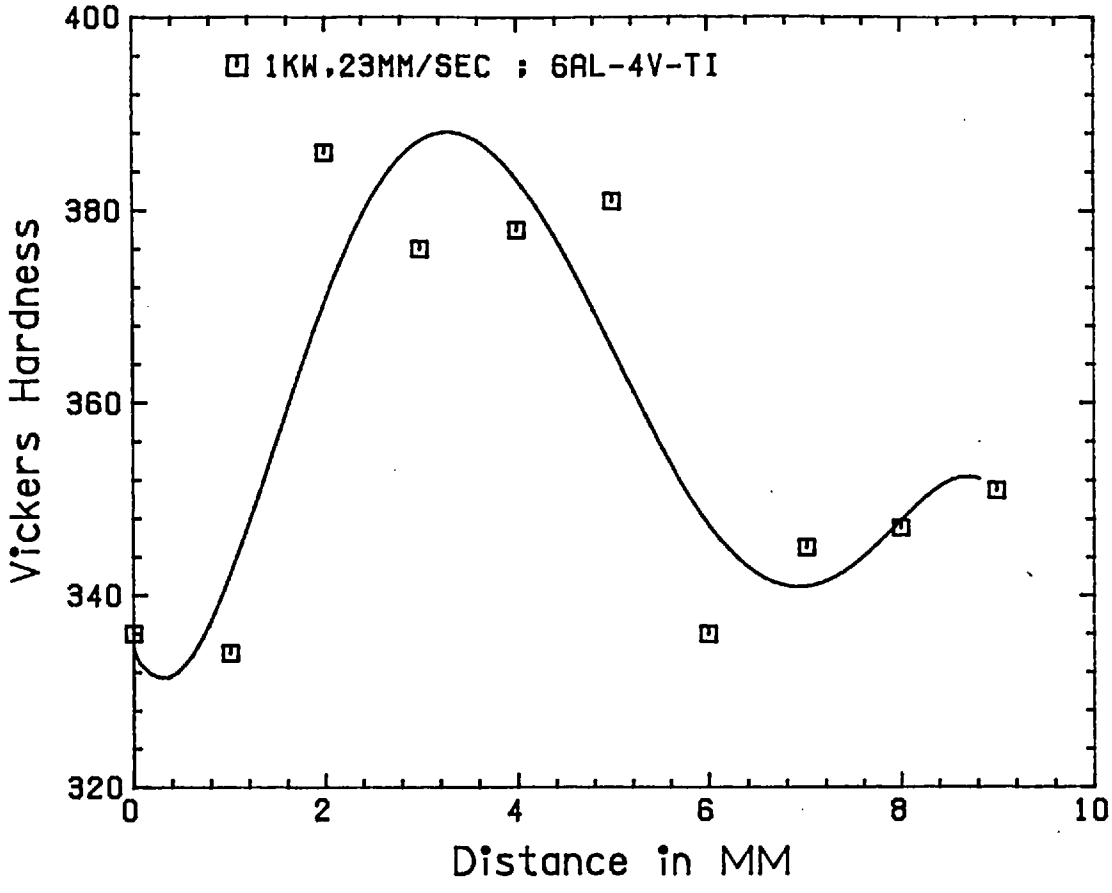

Fig. 7.9a Macro-Hardness traverse across the weld zone

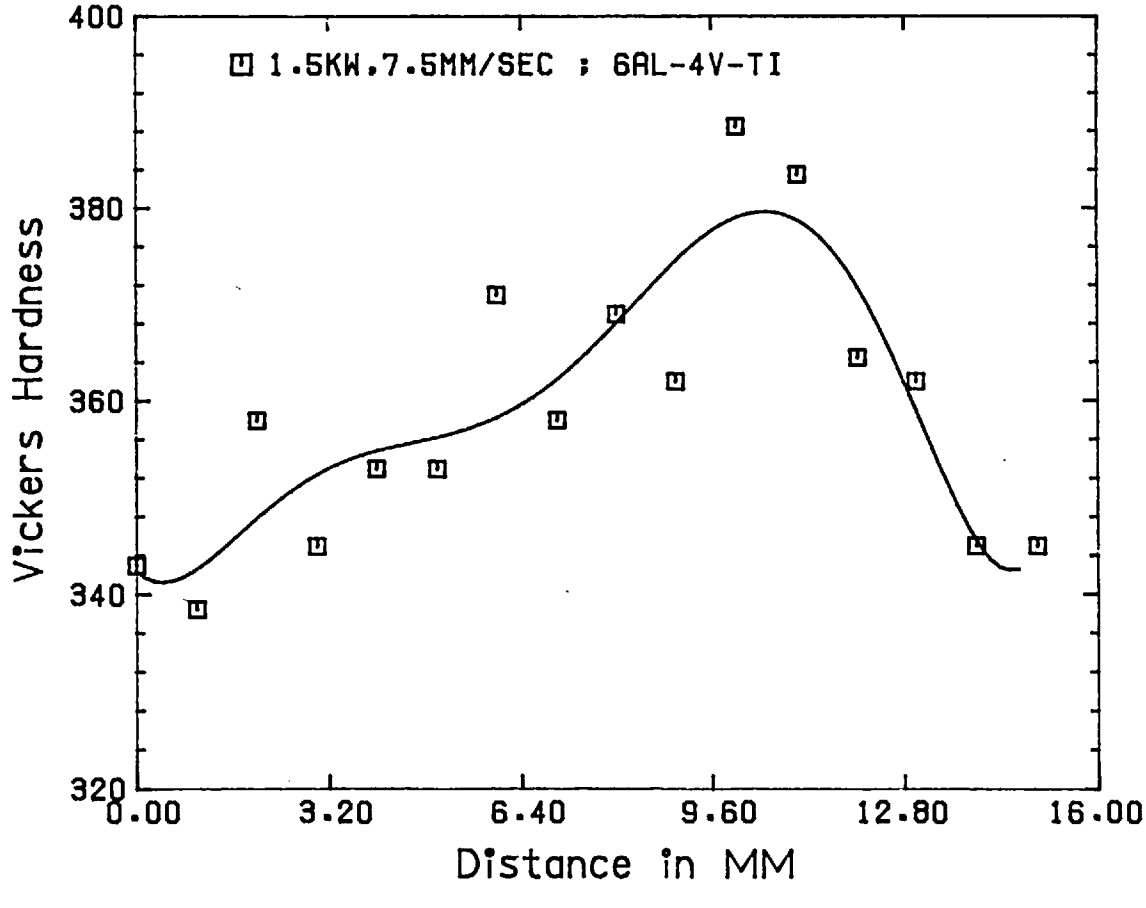

Fig 7.9b. Macro-Hardness traverse across the weld zone

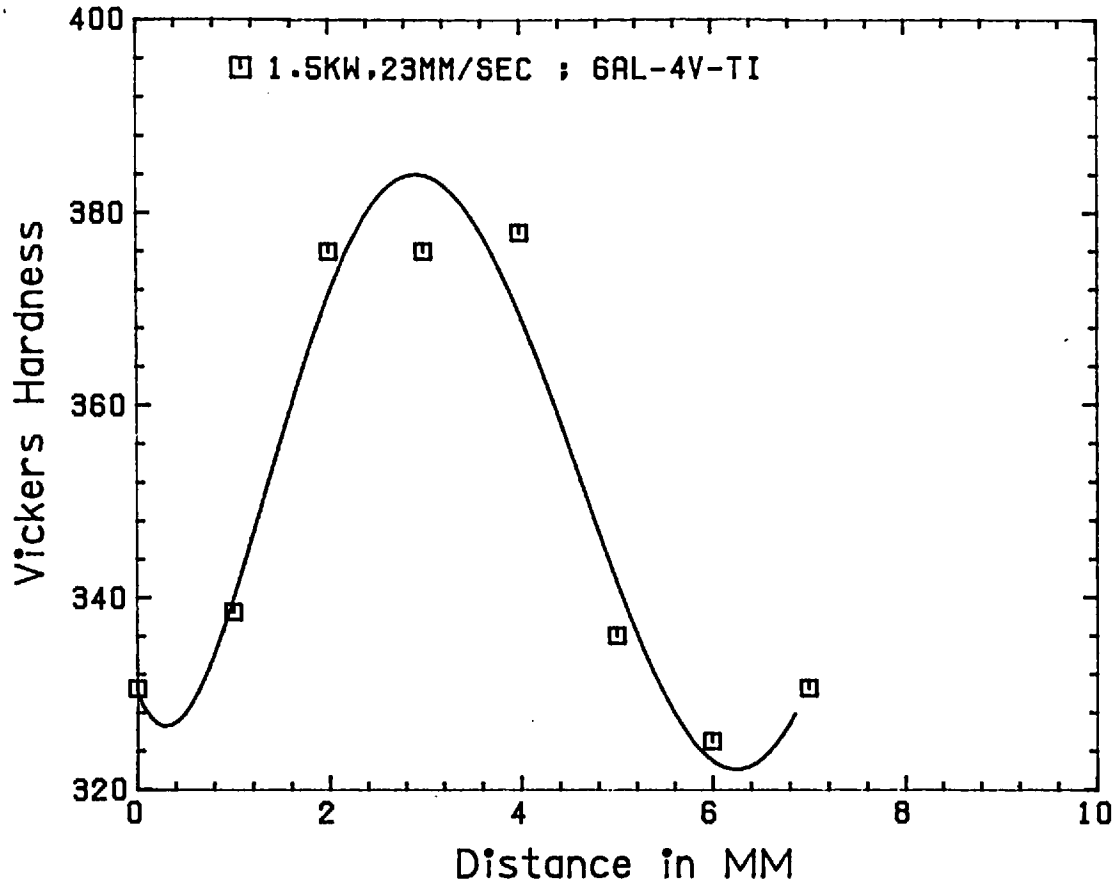

Fig 7.10a. Macro-Hardness traverse across the weld zone

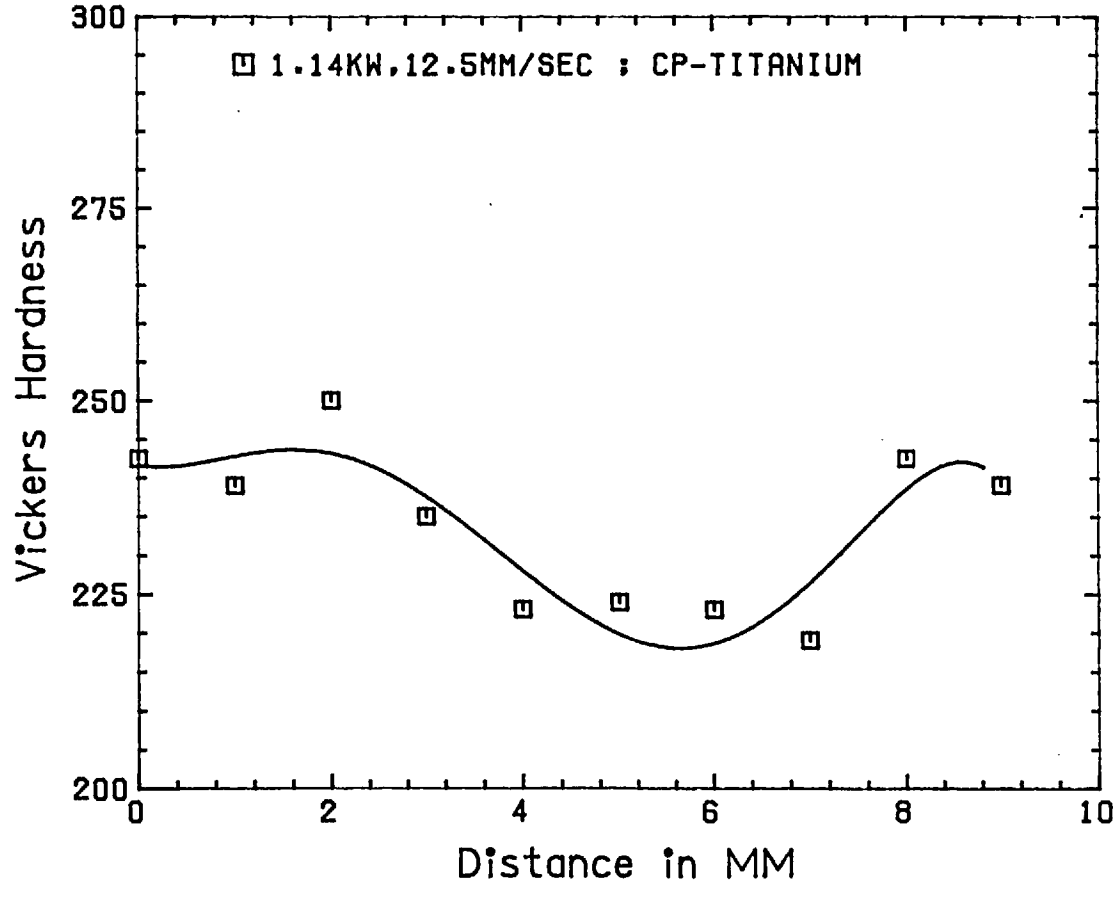

Fig 7.10b. Macro-Hardness traverse across the weld zone

α' (martensitic α) as quenched from β phase. Hochied et al[239] have also encountered the same difficulty with the 6Al-4V-Ti alloy.

However, measurement of macrohardness using the Vickers scale showed a slightly higher value (380-385 VHN) for the weld ingot than the parent matrix (340-350 VHN) for 6Al-4V-Ti alloy. Whereas, for commercially pure titanium the weld hardness of a weld ingot showed a slightly lower value (220-230 VHN) compared to that of parent matrix (240-250 VHN).

Figures 7.9 and 7.10 illustrate the variaton of Vickers hardness across the weld ingots (starting from partent matrix and ending in the parent matrix) for welds of different power and welding speed. Polynomials are fitted to the data points to show the tendency.

7.2.3.2 Tension test

The UTS, 0.2% proof stress and percentage elongation were measured and for successful welds they were found to be relatively independent of the laser power or welding speed used to make the welds. UTS 0.2% proof stress and elongation values are plotted against power and welding speeds as shown in Figures 7.11 and 7.12 respectively. Typical values of the mechanical properties are shown in Table 7.4. Details of tension test results are given in Appendix 7A It is seen that the weld properties are similar to the unwelded, as annealed material, a conclusion found with other welding processes for Ti alloys [245].

7.2.3.3 Fatigue Property

Under simple bending fatigue the endurance ratio for welded specimens (with a transverse central weld) was found to be 0.40-0.47 whereas that for unwelded specimen was 0.50. Stress is plotted against number of cycles (S-N curve) and shown in Figure 7.13.

These figures were obtained without following the full statistical procedure, however, they are in agreement with those

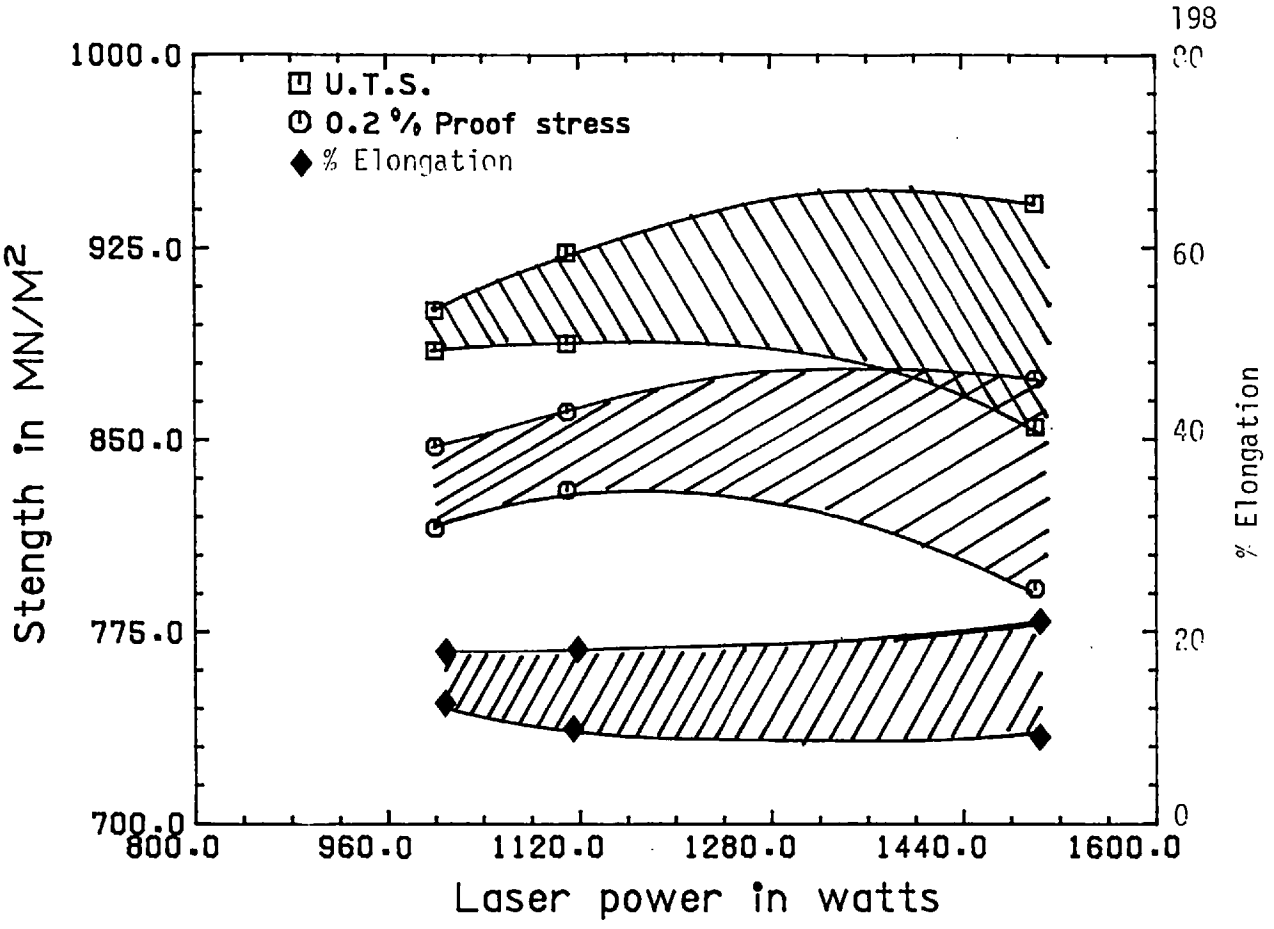

Fig. 7.11 UTS, 0.2% Proof stress and % elongation vs. welding speed for titanium welds

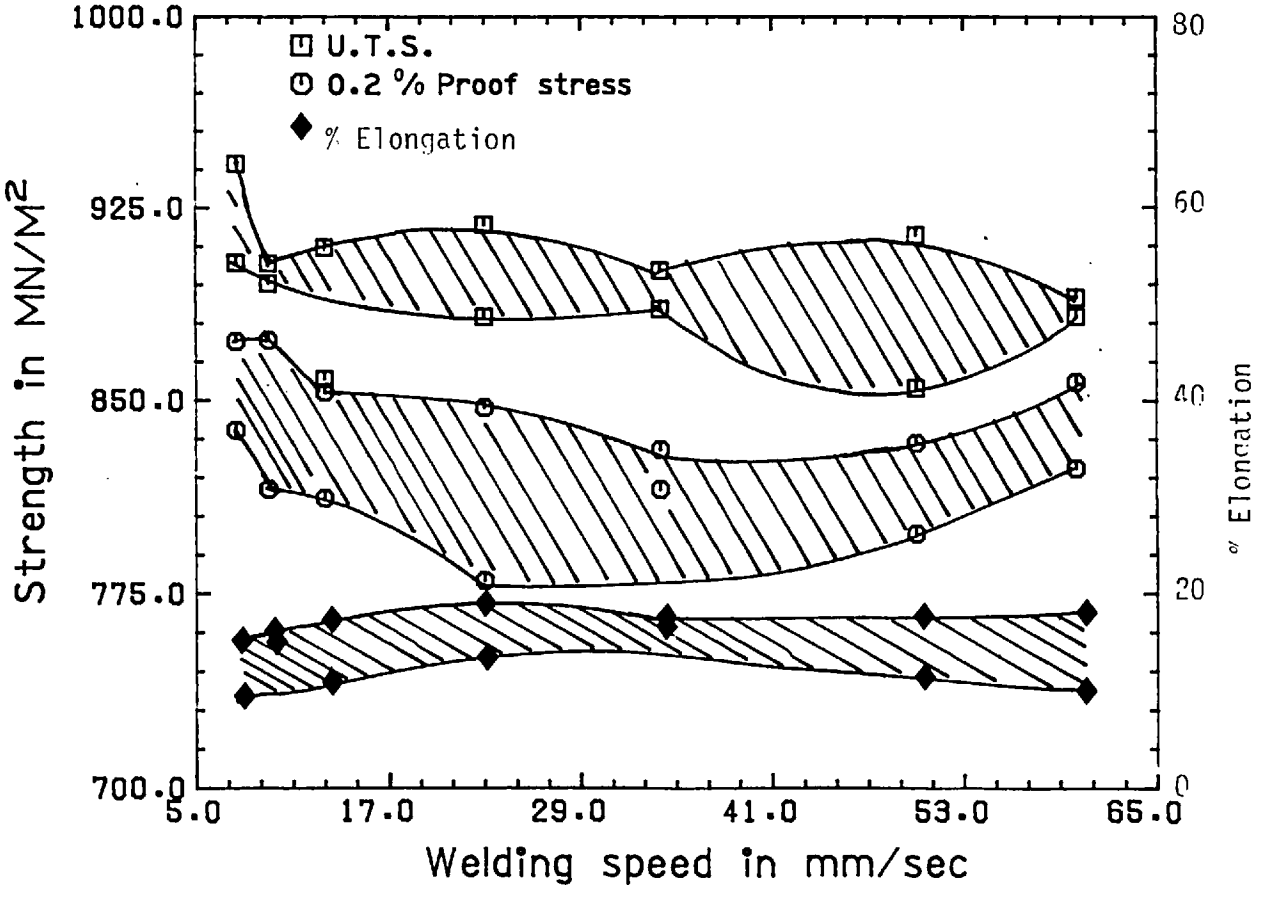

Fig. 7.12 UTS, 0.2% Proof stress and % elongation vs. welding speed for titanium welds

MATERIALS	WELDED MATERIAL			ORIGINAL MATERIAL		
	UTS MN/m^2	0.2% Proof Stress MN/m^2	Elongation %	UTS MN/m^2	0.2% Proof Stress MN/m^2	Elongation %
AMS 4911-TA -10 (6Al-4V-Ti)	≃860-923	≃800-860	11-14	895-1004	834-895	10-15
Commercially Pure Titanium	≃530-573	≃460-503	≃27	>494	>416	27-28

TABLE 7.4

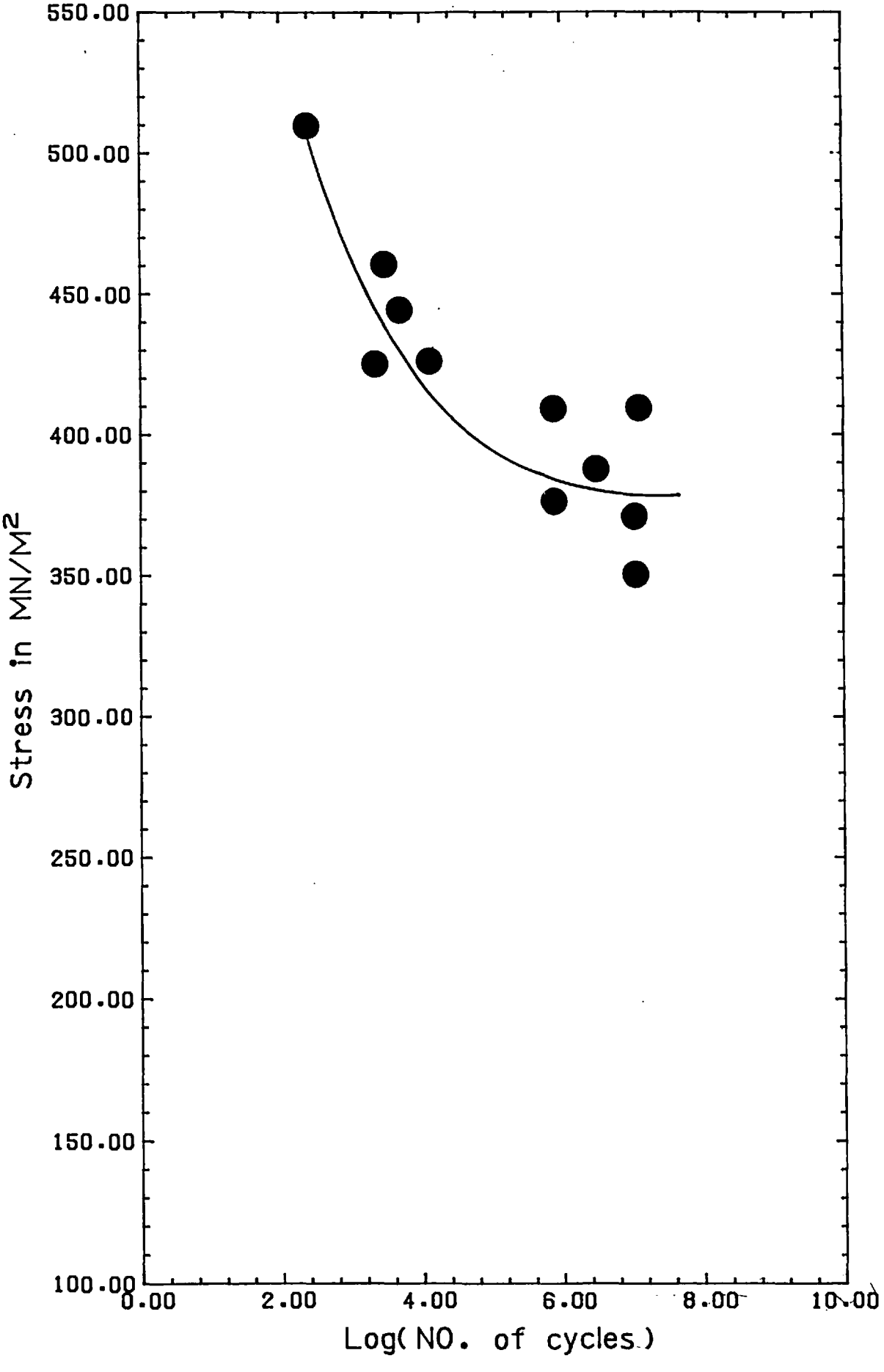

Fig. 7.13 S-N Curve for Titanium

of Bartlo[246] of 0.40-0.62 for different micro-structures of the same Ti alloy and 0.5-0.62 for titanium quenched from β phase which is the structure of the weld zone. However, it should be noted that his specimens were both surface and side ground whereas those reported here were only side ground.

7.2.3.4 Discussion and comparison with other processes

The slight increase in hardness in the weld zone in laser welds is caused by the α' (martensitic alpha) micro-structure of the weld zone. Therefore, this phenomena is also observed for EBW[164] it is even smaller (345-350 VHN).

Tensile properties are the same for all EBW, arc and laser welds. Fatigue property compares favourably with plasma arc welds reported by Banas[254]. However, the effect of micro-structure on mechanical properties is discussed in Section 7.2.4.

7.2.4 Microstructure and mechanical properties of titanium alloy welds

Hockeid et al[239] have reported that mechanical properties of 6Al-4V-Ti alloys are little affected by different heat treatments. Hickey[247], while working on mechanical properties of titanium alloys as a function of heat treatment, found that the mechanical properties of the Ti-6Al-4V alloy were least affected by different heat treatments. But extreme cases like unusual grain coarsening due to prolonged exposure over 985°C would effect the mechanical properties.

In the present study it is observed that the rapid change of microstructure (Section 7.2.2) near the weld zone did not change the mechanical properties (Section 7.2.3) to any large extent.

However, Bartlo[246] reports that the microstructure with α' (martensitic α) as principal phase (produced by β-quenching), which is similar to the weld zone, exhibits good fatigue strength but has low tensile ductility. Whereas the microstructure consisting of a mixture of fine primary alpha and α' (martensitic α), which is similar to the HAZ, results also in a high fatigue strength but this time with

good tensile ductility. Thus, both the principal structures within the weld zone are expected and found to have good fatigue properties due to the rapid quenching which is inherent in laser welding. But it was observed that the fatigue crack was always through the fusion zone and HAZ. According to Neal and Blenkinsop[248] this failure could be a result of simple cleavage of alpha grains due to restricted slip and to the relationship between the operative slip system $\{10\bar{1}0\}$ the cleavage plane $\{10\bar{1}7\}$ and the calculated plane of maximum stress.

However, the ductility of the fusion zone is expected to be reduced. Margolin et al[249] observed that voids form at the α/β interfaces in aged beta, at low tensile strains. As the strain is increased these voids readily grow along the interface before they by necessity must grow through the equiaxed alpha. As the mean free path between equiaxed alpha particles decreases, a growing void encounters more alpha particles which act as obstacles and growth is impeded. This results in greater strain to fracture and higher attainable ductility. In microstructure consisting of relatively long alpha plates, as observed in fusion zone, a greater area for void nucleation exists and fracture should occur at lower strains. The fact that this was not observed when applying the tension test transversely to the weld may be due to the very narrow fusion zone and HAZ reducing its influence.

7.2.5. Oxygen diffusion in titanium alloy welds

Oxygen[250-252] is a strengthening additive to titanium and some of its alloys, and to some extent it also improves corrosion resistance. It acts as an α-stabiliser in titanium. The presence of oxygen above a certain limit reduces the mechanical properties by forming oxide inclusions. For 6Al-4V-Ti alloy oxygen around 3000 ppm is present as an additive.

The total oxygen analysis of a weld sample is given in Table 7.5. This indicates that there is no significant oxygen contamination taking place during laser welding.

MATERIAL	OXYGEN IN PPM		
	Parent Metal	Weld zone with surface oxide	Weld zone after removing surface oxide
6Al-4V-Ti	3200	3400	3250
Commercially Pure Titanium	1600	1900	1700

TABLE 7.5 TOTAL OXYGEN ANALYSIS OF WELD SAMPLES

7.2.6 Corrosion properties of titanium alloy welds

The data for corrosion rates are given in table 7.6. They showed surprisingly, that the weld ingot corrodes more slowly in 2% HCl than the unwelded region.

Residual thermal stress in the weld region would be expected to increase the corrosion rate. In this case, however, it may be that the surface oxide is inhibiting the corrosion, or, as previously noted, oxygen within certain limits, is responsible for increasing the corrosion resistance[250-252].

7.2.7 Composition variation of titanium weld

Electron probe microanalysis was carried out in order to find out the distribution of alloying elements in the weld ingot as compared with that of the parent matrix.

It was observed that the parent metal was inhomogeneous - traces of vanadium and aluminium opposing each other. This was due to the α-β microstructure of the annealed parent matrix. Aluminium being an alpha stabiliser was present in higher concentrations in the α-phase whereas vanadium being a β-stabiliser was present in higher concentration in the β-phase. The vanadium content varied between 1.96% to in excess of 4.4% in the parent metal. Whereas the aluminium content varied between 3% to in excess of 5% in the parent metal.

Material	Corrosion rate in 2% HCl of original material	Corrosion rate in 2% HCl of welded material
	$\mu A/cm^2$	$\mu A/cm^2$
Ti-6Al-4V (sample 45)	37.63	5.7
Ti-6Al-4V (sample 27)	37.63	6.375
CP-Ti (sample 3)	22	0.5

TABLE 7.6

However, as the traces moved towards the fusion zone this opposing tendency between Al and V was found to decrease. Near the centerline of the weld the distribution of aluminium and vanadium seemed to be relatively homogeneous. Here, vanadium varied between 2.45% to 3.4% whereas aluminium varied between 2.8% to 4%. The relative homogeniety near the centerline of the weld could be due to the fact that the microstructure in that area mainly contained α' (martensitic α) within prior β-grains. EPMA trace of Al and V at parent metal and fusion zone is given in Fig. 7.14.

7.2.8 Undercut and underbead of titanium welds

The undercuts observed in the welds were not appreciable but they were coarse enough to be studied by a talysurf. The undercut for 1mm thick welds was too small to be measured using a project tina microscope. A few data for 2mm thick welds are given in Table 7.7

The maximum undercut observed was around 3.75% which was believed to be much better than that observed for EBW. But there are hardly any published data to confirm this.

7.2.9 Thermal efficiency of the laser welding of titanium

As shown in Fig. 7.15 only part of the total laser energy available is transferred to the weldment. Also, only part of the energy which enters the weldment is used to melt the bead, the remainder heats up the base metal and forms the heat affected zone. A typical macrostructure of fusion zone and heat affected zone is shown in Plate 7.3 with the predicted isotherms from the mathematical model discussed in Chapter 3.

An accurate prediction of the quantity of heat or energy entering the base metal is needed to predict the metallurgical response. For a given laser energy input, the ratio between the total input energy and the heat entering the base metal is significant. However, this is explained by using thermal efficiency

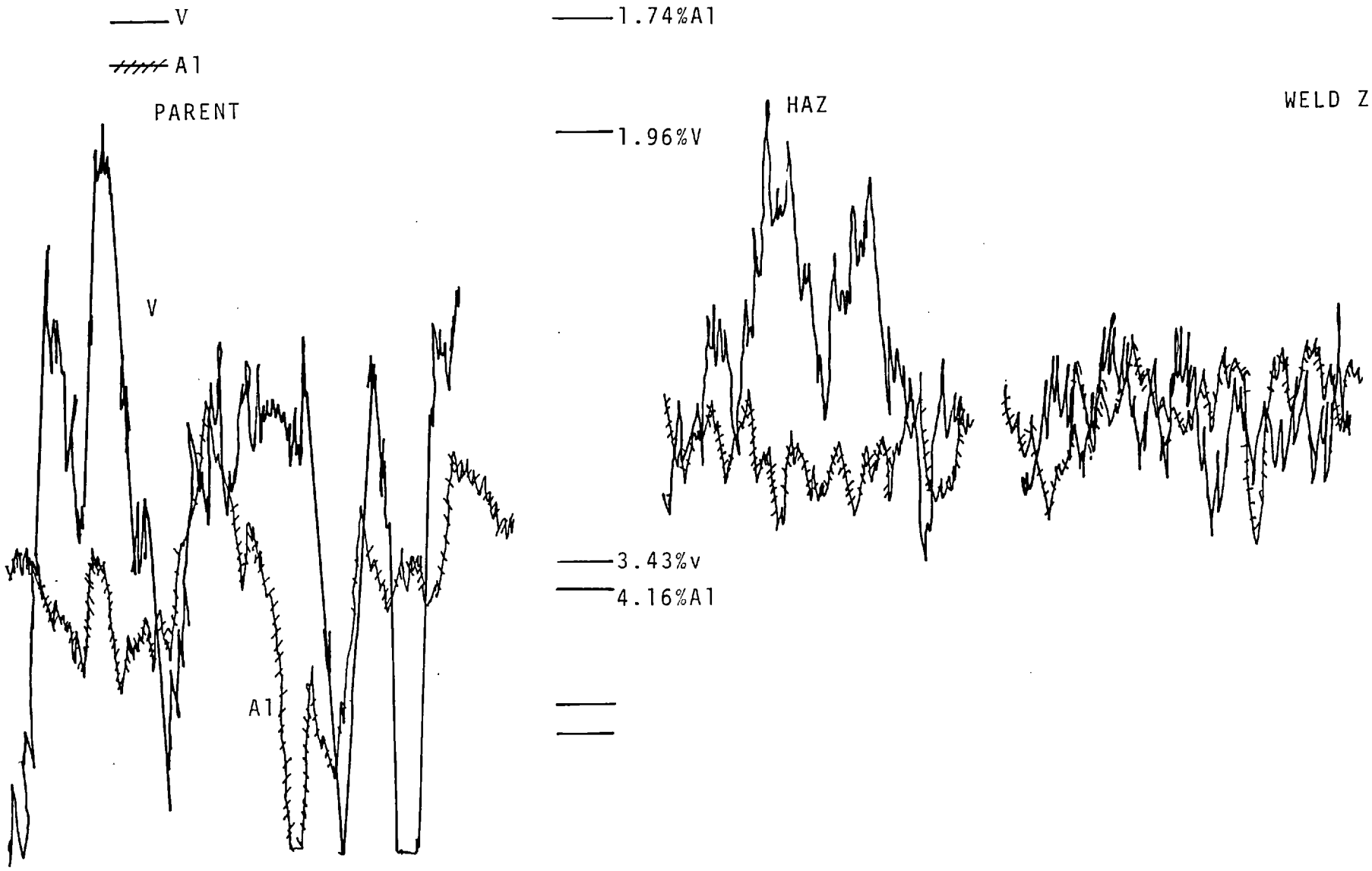

Fig.7.14 Electron probe micro-analyser trace of Al and V at parent metal and fusion zone.

Laser Power	Welding Speed mm/sec	Thickness mm	Undercut mm	% Under-cut	Underbead	Material
1140	9.5	2	0.01	0.5	Negligible	Cp-Titanium
1140	13	2	0.02	1	Negligible	Cp-Titanium
1110	5	2	0.075	3.75	Negligible	6Al-4V-Ti
1500	7.5	2	0.075	3.75	Negligible	6Al-4V-Ti
2000	40	2	Negligible			

TABLE 7.7

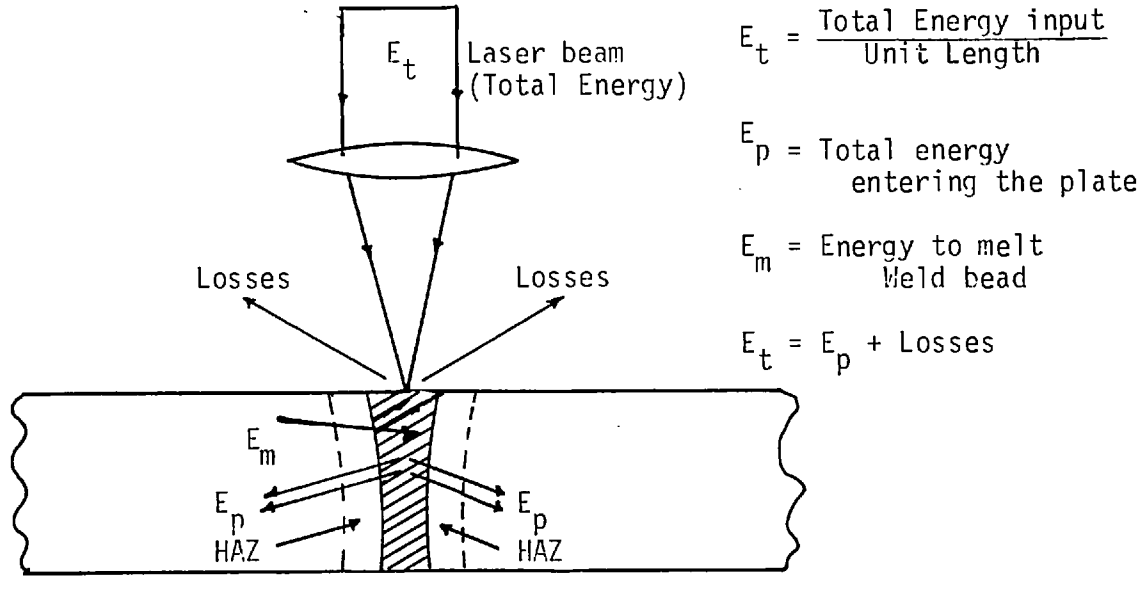

Fig: 7.15 Energy distribution at the Laser beam and material interaction point.

terms. In general, the efficiency is expressed as the ratio of output to input energies. In this investigation two thermal efficiencies are used to describe the energy distribution in the laser welding. These are referred to as the melting efficiency and the process efficiency. They are discussed in turn in the following sections.

7.2.9.1 Melting Efficiency

The melting efficiency, Z_m, can be defined as being the ratio of the energy required to melt the weld bead to the total energy input over the same distance[255]. This relationship can be expressed as:

$$Z_m = (E_m/E_t) \times 100$$

$$= \frac{N_A \times \rho[C_p(T_m - T_a) + L]}{(P_{TOT}/V)} \times 100$$

$$= \frac{V \times N_A \times \rho[C_p(T_m - T_a) + L_f]}{P_{TOT}} \times 100 \qquad (7.1)$$

where, V = weld speed in m/s
N_A = Nugget area m^2
ρ = density kg/m^3
C_p = specific heat - J/kg ^oK
L_f = latent heat of fusion J/kg
T_m = melting point in ^oK
T_a = ambient temperature in ^oK
E_m = energy per unit length
E_t = total laser energy available per unit length
Z_m = melting efficiency

The melting efficiency is calculated for a few titanium welds using Eqn 7.1 and values are given in Table 7.8.

TABLE 7.8

TABLE 7.8 TABLE FOR MELTING EFFICIENCY FOR TITANIUM

Power watts	Welding speed mm/sec	Thick-ness mm	Melt width @ surface mm	Width of HAZ @ surface mm	Melt width @ bottom mm	Width of HAZ @ bottom mm	Nugget area mm^2	HAZ area mm^2	Melting effic-iency %
1000.00	23.00	1.00	1.85	3.75	.90	2.50	1.38	1.75	21.37
1000.00	34.00	1.00	1.65	3.30	.80	2.50	1.22	1.67	28.14
1000.00	15.00	1.00	2.15	4.70	1.60	3.40	1.88	2.17	19.00
1000.00	11.00	1.00	2.65	6.40	2.00	4.60	2.33	3.17	17.28
1480.00	60.00	.89	1.00	2.20	.60	1.50	.71	.93	19.50
1480.00	50.00	.89	1.35	3.00	.90	2.00	1.00	1.22	22.66
1480.00	23.00	.89	1.60	3.10	1.35	2.75	1.31	1.29	13.78
1500.00	60.00	.81	1.00	2.00	.90	1.50	.77	.65	20.80
1500.00	50.00	.81	1.20	2.20	.90	1.75	.85	.75	19.16
1500.00	23.00	.81	1.35	5.60	1.25	4.00	1.05	2.83	10.91
1500.00	7.50	2.03	4.30	10.00	3.00	5.50	7.41	3.32	25.03
1500.00	9.50	2.03	3.85	8.35	2.15	4.00	6.09	6.45	26.06
1500.00	13.00	2.03	3.25	6.25	2.00	4.00	5.33	5.08	31.20
1110.00	6.00	2.03	3.75	8.25	.75	8.25	4.57	12.18	16.68
1500.00	23.00	1.00	1.75	3.00	1.45	2.75	1.60	1.27	16.58
1540.00	50.00	1.00	1.45	2.50	.95	2.45	1.20	1.27	26.36
1540.00	60.00	1.00	1.15	2.25	.85	2.00	1.00	1.12	26.32

TABLE 7.9

TABLE 7.9 TABLE FOR PROCESS EFFICIENCY FOR TITANIUM

Power watts	Welding speed mm/sec	Thick-ness mm	Melt width @ surface mm	Width of HAZ @ surface mm	Melt width @ bottom mm	Width of HAZ @ bottom mm	Nugget area mm^2	HAZ area mm^2	Process effic-iency %
1000.00	23.00	1.00	1.85	3.75	.90	2.50	1.38	1.75	27.77
1000.00	34.00	1.00	1.65	3.30	.80	2.50	1.22	1.67	37.20
1000.00	15.00	1.00	2.15	4.70	1.60	3.40	1.88	2.17	24.19
1000.00	11.00	1.00	2.65	6.40	2.00	4.60	2.33	3.17	22.84
1480.00	60.00	.89	1.00	2.20	.60	1.50	.71	.93	25.53
1480.00	50.00	.89	1.35	3.00	.90	2.00	1.00	1.22	29.42
1480.00	23.00	.89	1.60	3.10	1.35	2.75	1.31	1.29	16.98
1500.00	60.00	.81	1.00	2.00	.90	1.50	.77	.65	24.92
1500.00	50.00	.81	1.20	2.20	.90	1.75	.85	.75	23.12
1500.00	23.00	.81	1.35	5.60	1.25	4.00	1.05	2.83	17.83
1500.00	7.50	2.03	4.30	10.00	3.00	5.50	7.41	3.32	31.65
1500.00	9.50	2.03	3.85	8.35	2.15	4.00	6.09	6.45	32.56
1500.00	13.00	2.03	3.25	6.25	2.00	4.00	5.33	5.08	38.20
1110.00	6.00	2.03	3.75	8.25	.75	8.25	4.57	12.18	27.16
1500.00	23.00	1.00	1.75	3.00	1.45	2.75	1.60	1.27	19.64
1540.00	50.00	1.00	1.45	2.50	.95	2.45	1.20	1.27	32.91
1540.00	60.00	1.00	1.15	2.25	.85	2.00	1.00	1.12	33.30

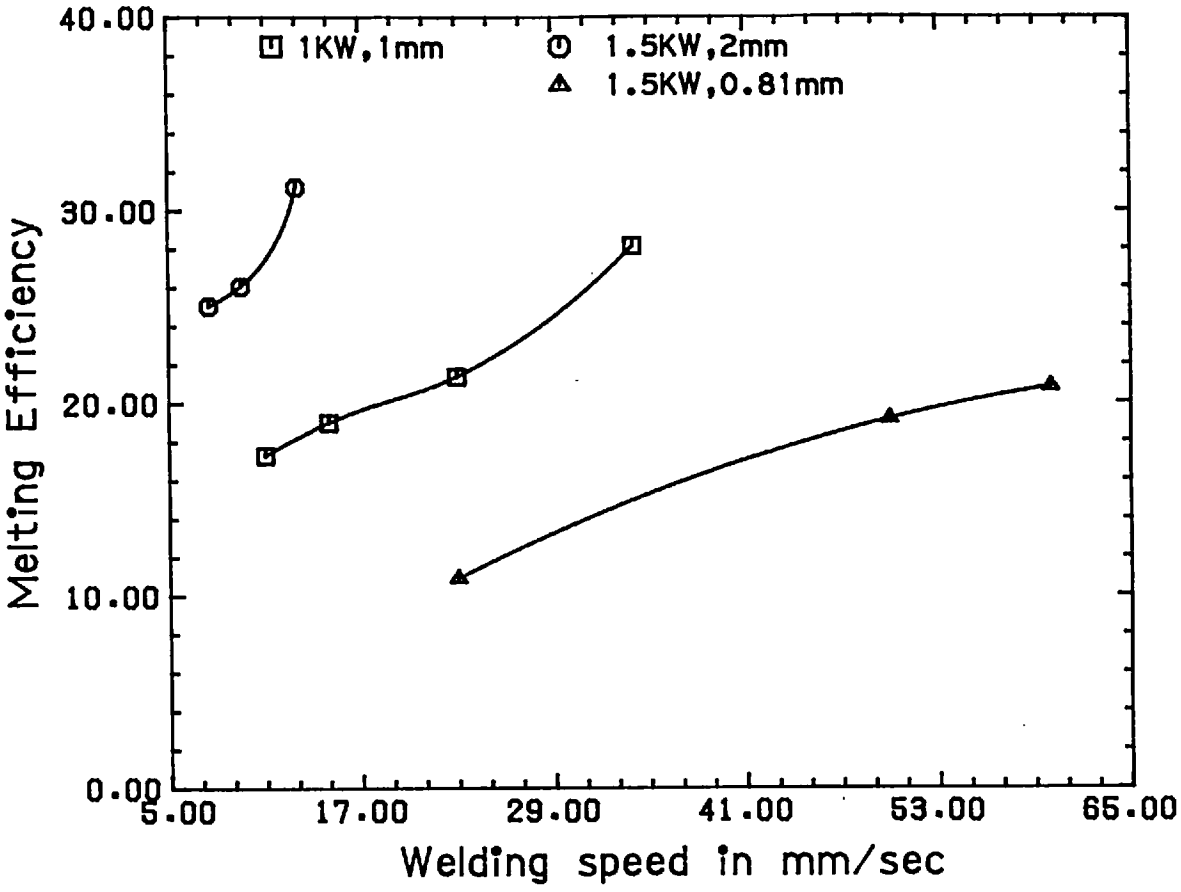

Fig. 7.16 Melting efficiency vs. welding speed for titanium welds

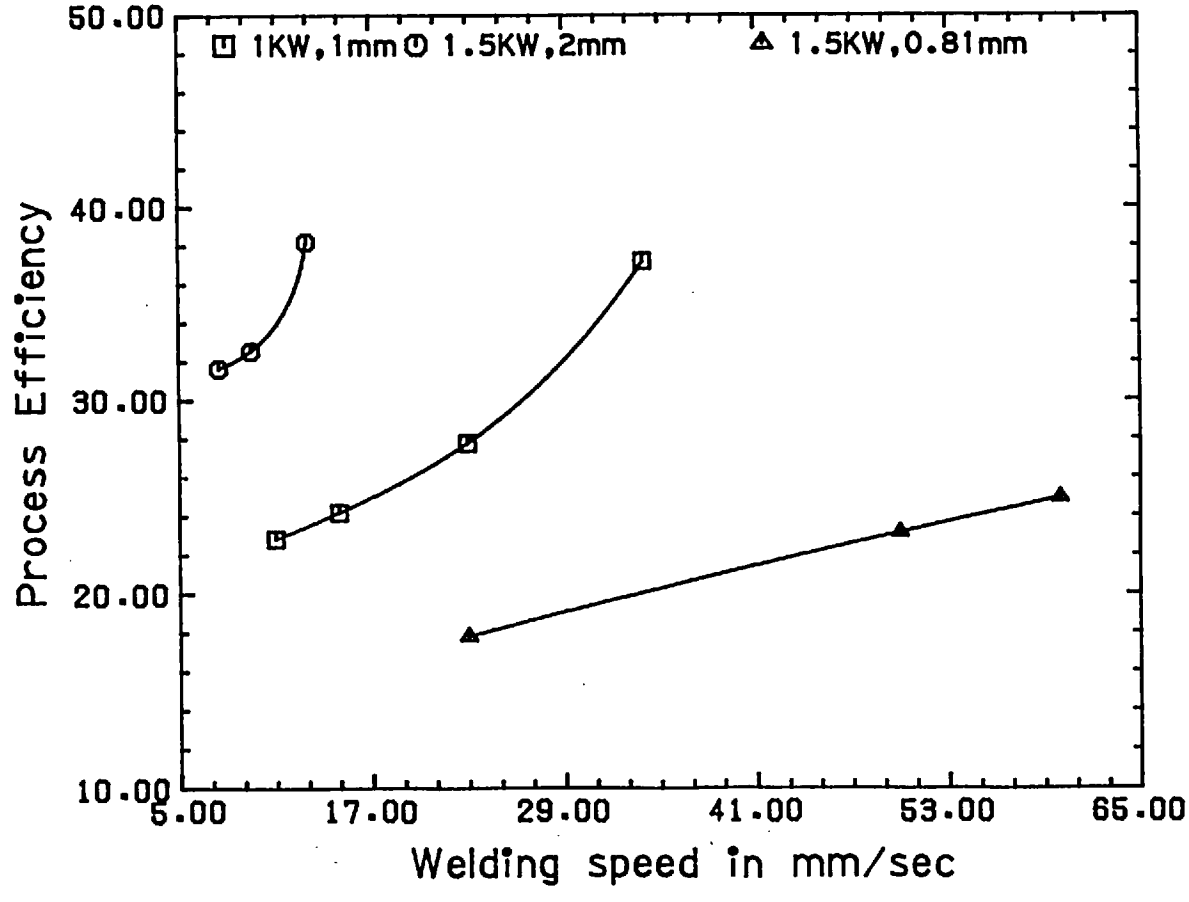

Fig. 7.17 Process efficiency vs. welding speed for titanium welds

The melting efficiency (Z_m) is plotted against welding speed in Fig. 7.16. It is evident from the figure that Z_m increases with welding speed. It is also noted that the melting efficiency increase with thickness of the material.

7.2.9.2 Process efficiency

The process efficiency (Z_p) is defined [255] as the ratio of the total energy which enters the plate or section being welded per unit distance travelled, to the total energy input of the laser over the same distance. The relationship is stated as follows:

$$Z_p = (E_p/E_t) \times 100$$

where E_p = energy per unit distance entering the workpiece

E_t = total energy available per unit length

Z_p = process efficiency

This relationship is important since the heat transfer phenomenon determining the welding temperature distribution and cooling rates depend on the energy absorbed instead of available energy. Therefore, if the transfer efficiency of the total energy input is not considered, the energy input term does not represent the actual energy entering the plate.

Niles and Jackson[253] used Rosenthal's[178-179] equation and measured the temperature far removed from the weld bead to calculate the process efficiency. But for the present study Rosenthal's equation can not be used as explained in section 3.11. An approximate value can be obtained by calculating the total energy used to heat up the workpiece. The process efficiency calculated in this way is given in Table 7.9. The data is plotted in Fig. 7.17.

It is evident from Figure 7.17 that the process efficiency increases with the increase of welding speed showing that the loss of energy entering the workpiece decreases for an increase in speed. In some cases a fall of process efficiency observed at the highest speed but that is within experimental scatter.

7.3 Results and discussion of tin plate welds

7.3.1 Welding variables for tin plate

The range of welding runs on tin plates for various welding conditions is illustrated in Fig. 7.18. Details are given in Appendix 8 .

7.3.1.1 Type of welds

Type of welds done on tin plates are as follows:-

1) Lap welding
2) Bead on plate welding
3) Butt welding

The major part of the tin plate weld study involved lap welds. Some bead on plate welds were performed to get an idea of welding speed range for butt welds. Some butt welding was attempted but due to its small thickness (0.2mm), jigging was difficult and thus only few butt welds were produced.

7.3.1.2 Effect of laser power and welding speed

It was quite evident from the wide spread in values of the laser powers and welding speeds used that there was a maximum speed for a given power and workpiece thickness above which incomplete penetration or an intermittent weld was produced. Also that there was a minimum speed below which the fusion zone was so large that material was lost and the weld showed irregular holes. The same behaviour was also observed with titanium welds.

Figure 7.19 and 7.20 respectively show the permissible range for sound lap welds and bead on plate welds on 0.2mm thick tin plates. It is evident from these two figures that the welding speed increases with power. In the initial stages (up to 1250 W) the welding speed increased exponentially with power but after 1500 watts power the maximum welding speed increased less rapidly with power. This agrees with the results of most other laser workers[152-153]. Probably when operating near the maximum power level the laser induced plasma causes more interference with beam/workpiece interactions ,also some degeneration

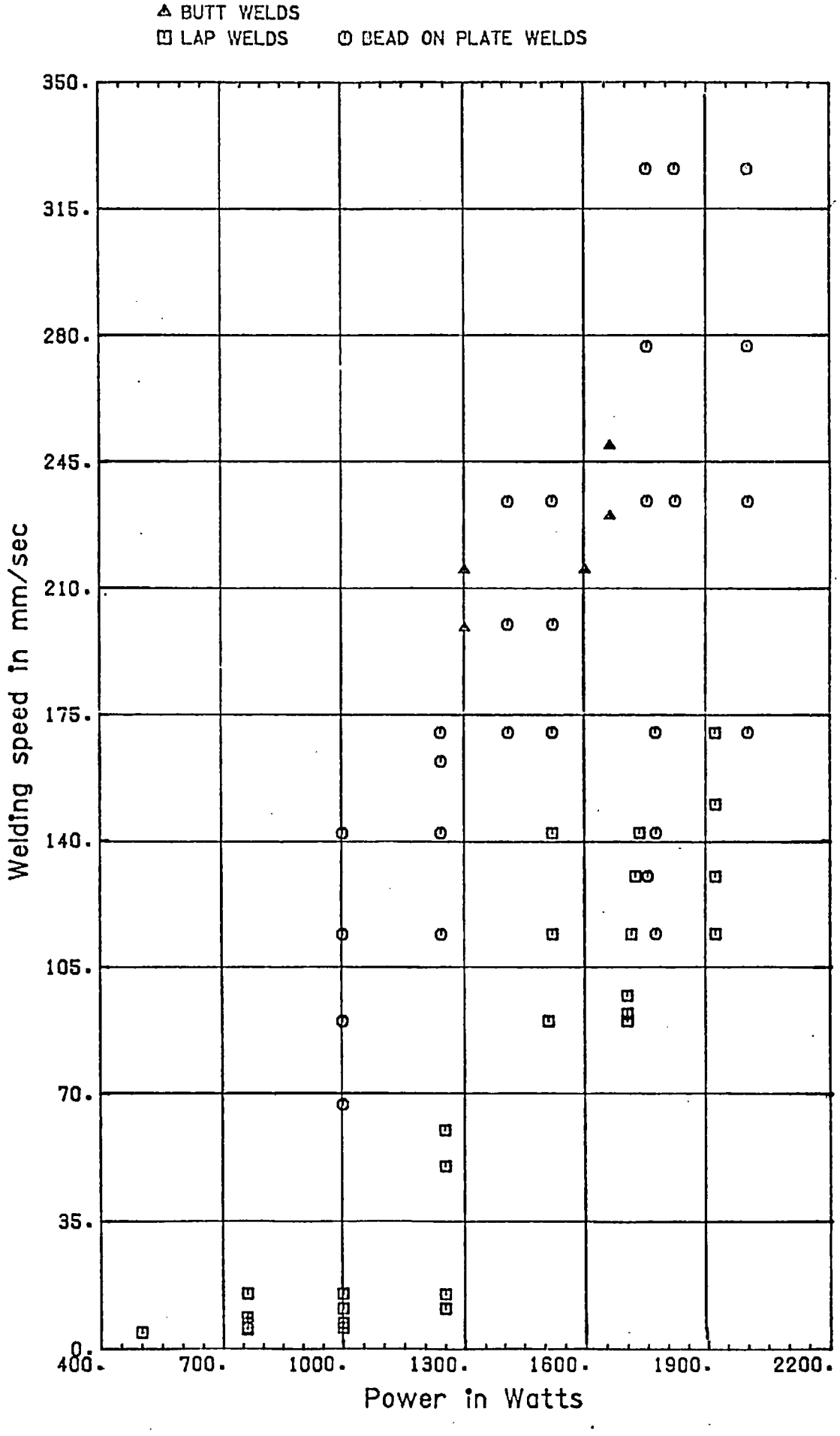

Fig. 7.18 The range of welding runs on tin plates for various welding conditions

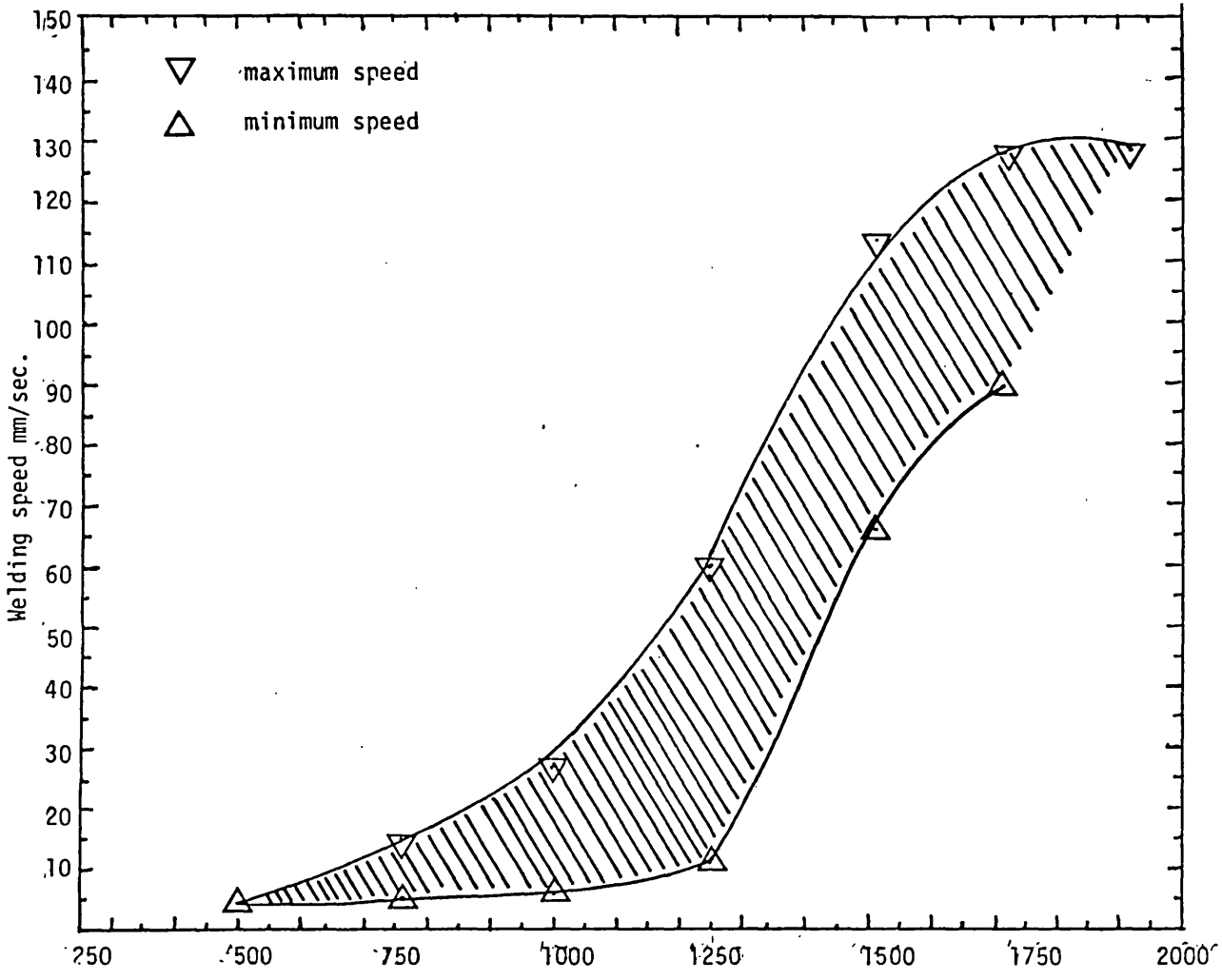

FIG. 7.19 Variation of tin plate lap welding speed with laser power

FIG. 7.20 Variation of tin plate bead on plate welding speed with laser power

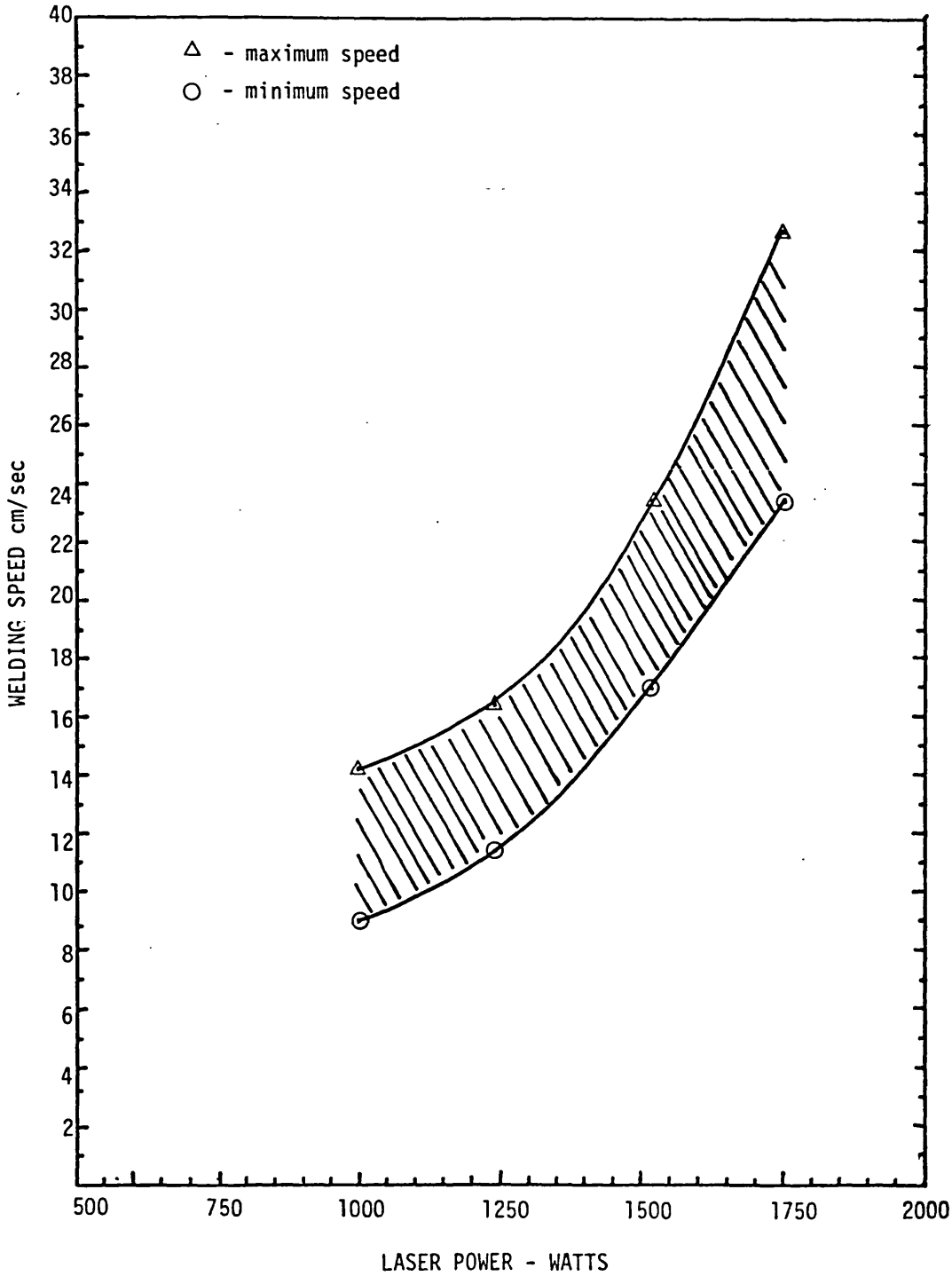

of mode structure could be expected from a laser at its maximum output. Baardsen et al[154] observed an exponential increase of speed with power for the whole range while welding 0.035" rimmed steel sheets with a 5kW laser. This observation, however, does not agree with the present study.

It should also be noted that above a certain threshold power (1000W for 0.2mm lap weld) the rate of change of welding speed with respect to laser power increases (up to 1700 watts for 0.2mm lap weld) up to an optimum power level.

As it can be observed from the two figures 7.19 and 7.20, welding speeds for bead on plate welds are higher than that for the lap welds for the same power, which shows that the welding speed decreases with thickness.

It is also observed that the HAZ and the width of the weld ingot varies with laser power and welding speed. Some representative values are given in Table 7.10.

Material	Width of Weld ingot mm	Width of Total HAZ mm	Power in Watts	Welding Speed in mm/sec	Thickness in mm
Tin coated mild steel	0.9	2.1	1000	5.75	0.4
	0.45	1.05	1000	15	(Lap weld for
	0.75	1.95	760	5.25	0.2mm)
	0.5	1.5	760	5.75	"
	0.45	1.25	760	8.5	"
	0.5	1.0	760	15	"
	0.4	0.55	1250	60	"

TABLE 7.10

It is evident from the data that for the same power the HAZ decreases with increase of speed whereas for the same speed HAZ increases with power. This phenomena is also observed with titanium

7.3.1.3 Discussion and comparison with other processes

The purpose of studying the laser welding of tin plate was to find an alternative method of making cans. The comparison between different processes of can making is given in Appendix 2, Table III. The other welding process for making cans is the soudronic welding method. It is observed that the welding speed available with the soudronic method is higher than that available with 2kW laser machine. This might be overcome by using a higher powered laser or an arc augmented laser welding as in the Imperial College/NRDC patent no: 6008/78. The soudronic method may be in this way surpassed since it has problems such as electrode contamination, porosity of the welds[10,11] etc.

7.3.2 Metallurgical properties of tin plate welds

7.3.2.1 Radiography

Most of the lap welds were radiographed and indicated that the sound welds having no porosity were produced in the permissible welding region indicated in Fig. 7.19. Two representative radiographs, respectively for 500W, 4.5 mm/sec weld and 1250W, 60 mm/sec weld, are presented in Plate 7.7. The welds exhibit narrow and uniform weld zone characteristics.

7.3.2.2 Metallography

All the specimens were mechanically polished and etched with 2% Nital,. The structure was studied under the optical microscope.

Tin plate was received in the annealed condition. The variation of micro-structure as seen in an optical photomicrograph after welding is represented in a composite - Plate 7.8.

Plate 7.8b represents a macrograph of a typical laser welded tin plate (tin coated mild steel). Plate 7.8a represents the micrograph of the parent matrix (marked "P" in the macrograph 7.8b). It predominantly shows equiaxed ferrite grains.

Plate 7.8c represents the micrograph of the heat affected zone (marked "H" in the macrograph 7.8b). Some ferrites (bright areas)

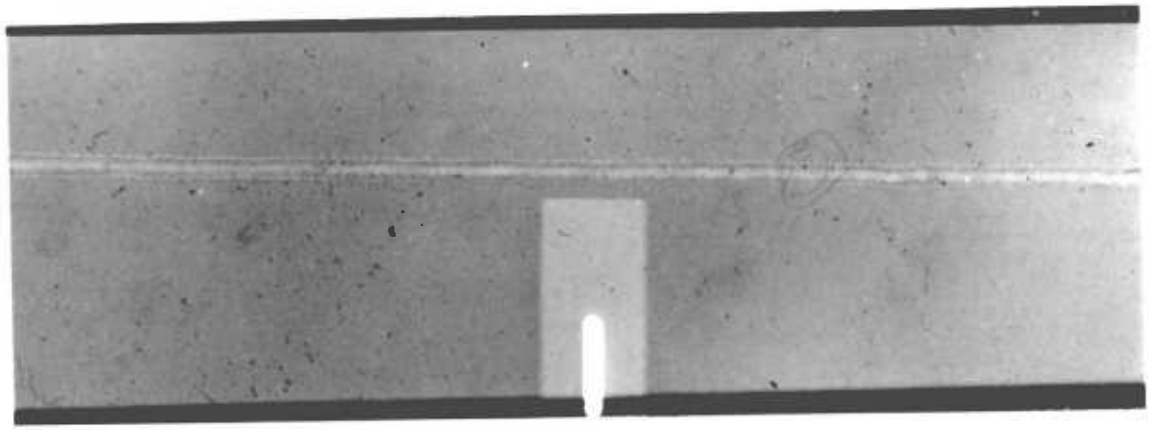

a) 4.5 mm/sec speed with laser power of 500W

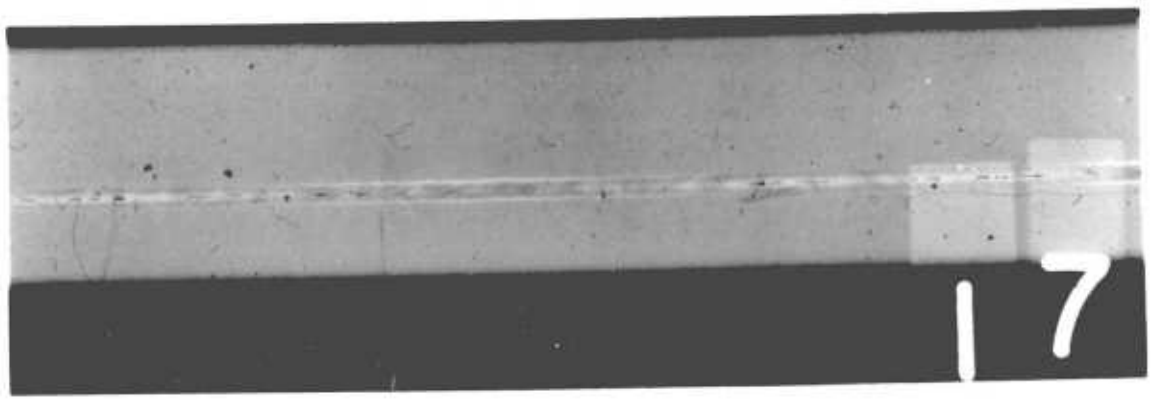

b) 60 mm/sec speed with laser power of 1250W

PLATE 7.7 Radiographs for tin plate welds

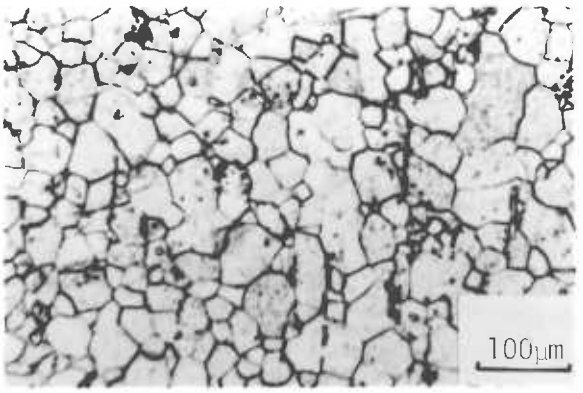

A

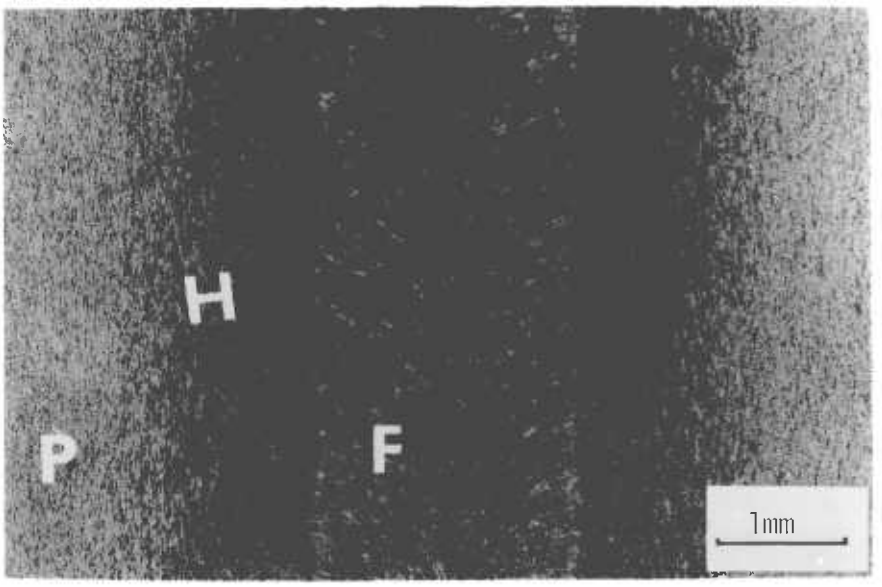

B

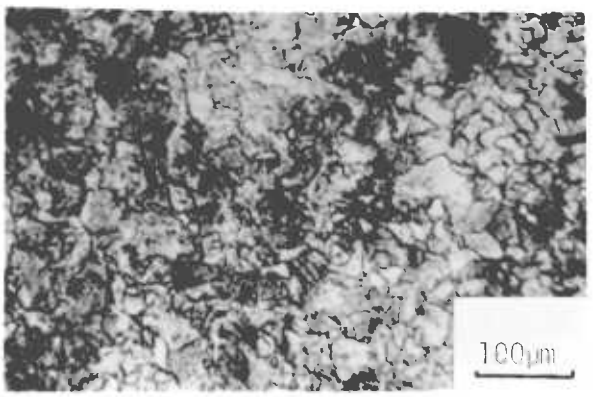

C

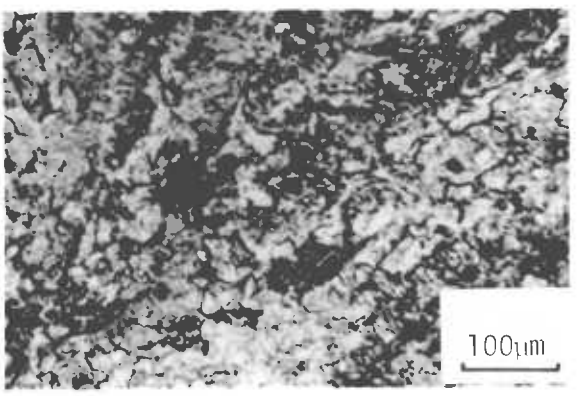

D

PLATE 7.8 Composite showing structural variation for lap welded 0.2mm tin plate; laser power 1000W, welding speed 6 mm/sec.

A) Parent matrix
B) Macrostructure
C) HAZ
D) Fusion zone

are still observed in the HAZ. The dark areas are not properly resolved but they seem to be mostly lamellar carbides.

Plate 7.8d represents the micrograph of the fusion zone (marked "F" in the macrograph 7.8b). The columnar nature of the weld pool is evident from the Plates 7.8b and 7.8d. Plate 7.8d reveals the presence of some ferrite (bright area) even at the weld zone. Like HAZ dark areas of weld pool is also not properly resolved under the optical microscope, but, one or two pockets of martensite type transformation product may be observed showing that the cooling rate is higher than that for HAZ. Probably this area mostly contains upper and lower bainite but they are extremely difficult to resolve with an optical microscope.

7.3.2.3 Discussion and comparison with other processes

Williams et al[10-11] report that they have observed similar microstructures for soudronic welds done on the same material.

However, this is to be expected because the material is basically a mild steel of extremely low carbon (0.05-0.08%) content and, therefore, a large variation of microstructure is not possible.

The weld nugget produced by the soudronic weld seemed to be irregular, if not intermittant at high speeds (20m/min and onwards Ref. 11). Whereas the laser weld produced a continuous weld bead and therefore, better mechanical properties would be expected.

All other can making processes either use deep drawing or lock seam and solder. Therefore, no comparison of weld microstructure is possible. Inspite of this the relative advantages and disadvantages are furnished in Appendix 2 (Table III).

7.3.3 Mechanical properties of tin plate welds

7.3.3.1 Micro-hardness measurement

Micro-hardness traverse across the weld ingot revealed that the hardness at the weld ingot was higher than that of the parent material. Maximum hardness recorded in the weld zone was 2178 in knoop scale whereas the hardness at the parent matrix was around 1200 in knoop scale.

However, some representative data are shown in Figure 7.21 Details are in Appendix 10.

It is evident from the micro-hardness traverse that, th-ough, there is a hardness increase in the weld zone it is not of the order of the hardness of a martensitic structure for this percentage carbon steel. Therefore, there is less chance of drastic deterioration of the tensile ductility. A fact which is confirmed by the elongation values from the tension test.

7.3.3.2 Tension Test

The U.T.S. , 0.2% proof stress and percentage elongation were measured and they were found to be relatively independent of the laser power or welding speeds as shown in Figure 7.22a and 7.22b respectively. Typical values of the mechanical properties are shown in Table 7.11. Details of tension test results are given in Appendix 7B.

Materials	WELDED MATERIAL			ORIGINAL MATERIAL		
	U.T.S MN/m^2	0.2% Proof Stress MN/m^2	Elong-ation %	U.T.S. MN/m^2	0.2% Proof stress MN/m^2	Elong-ation %
Tin plate (Tin coated mild steel)	≈310 -355	≈267-316	17-27	313 -319	≈267	≈28

TABLE 7.11

It is observed that the weld properties are similar to the unwelded, and in most cases rupture takes place at the original material instead of the weld ingot. A similar observation was made for the titanium welds.

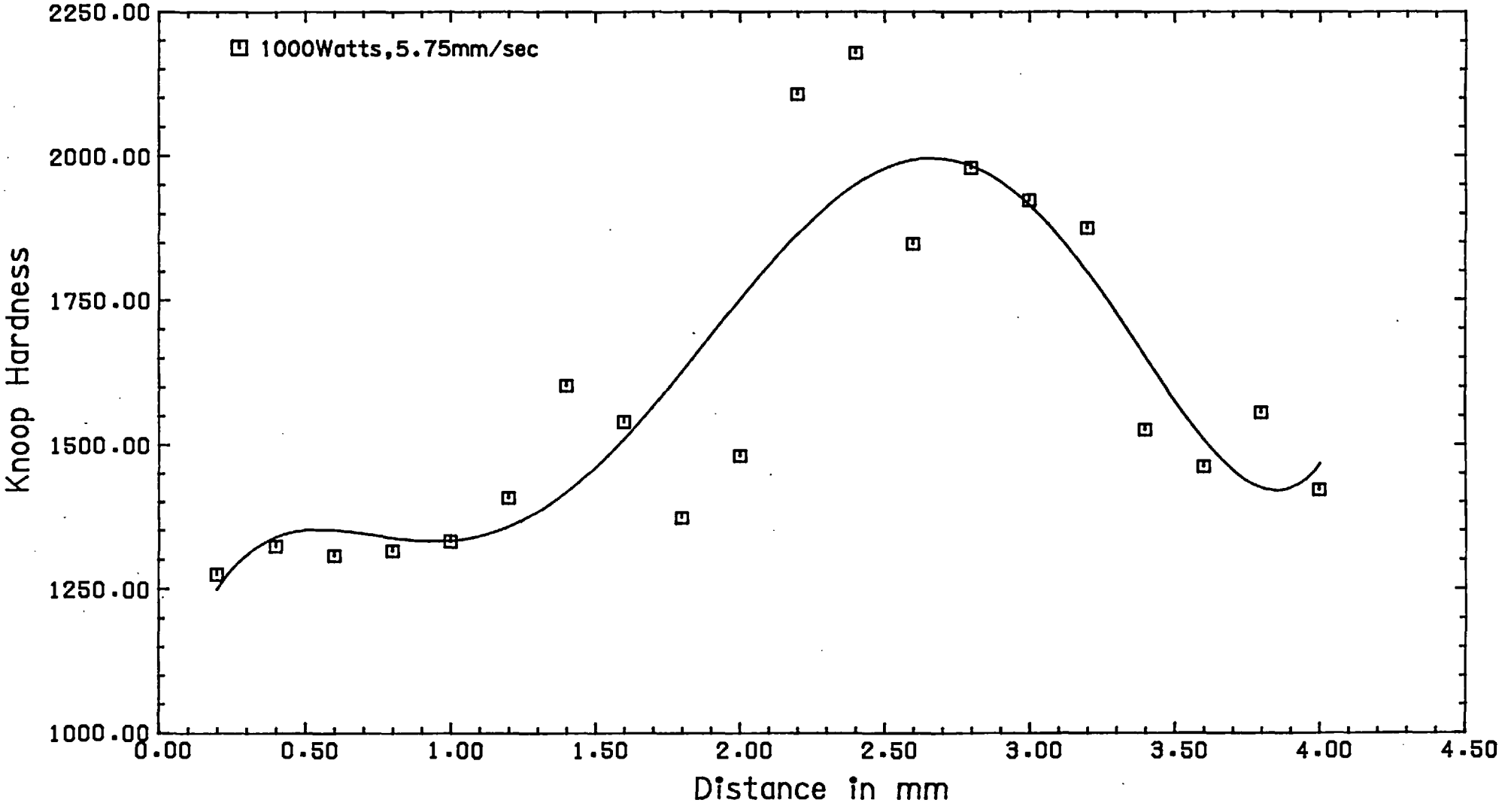

Fig. 7.21 Microhardness traverse accross Tin plate weld

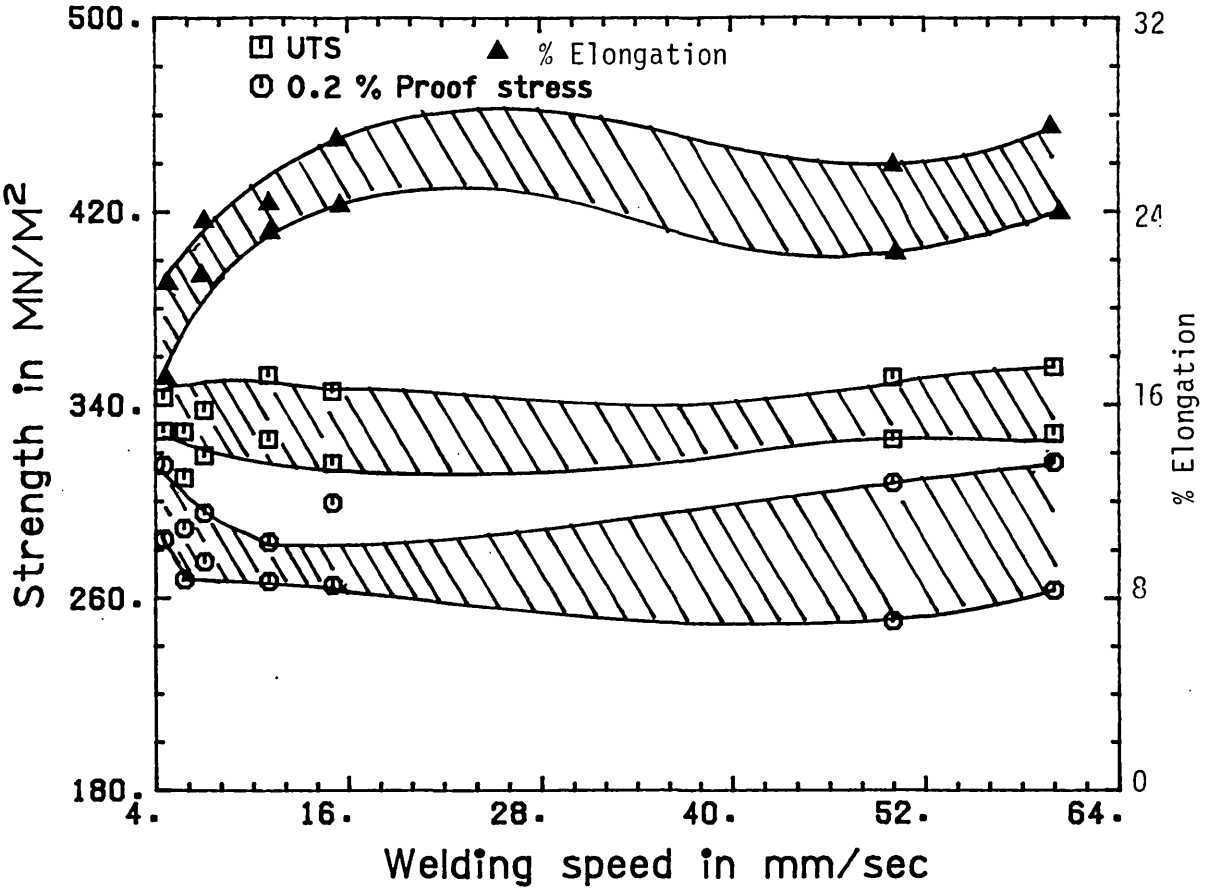

Fig 7.22b UTS, 0.2% Proof stress and % elongation vs. welding speeds for tin plate welds

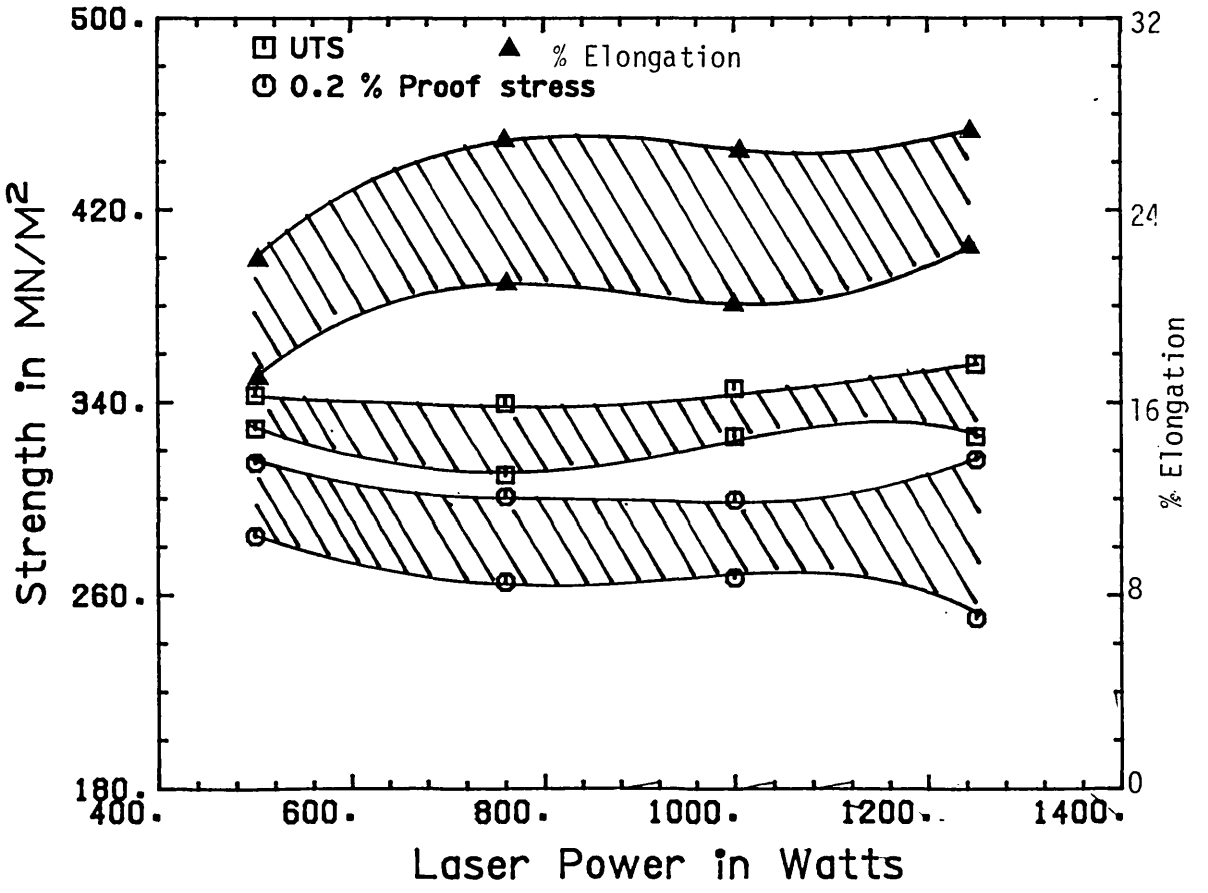

Fig 7.22a UTS, 0.2% Proof stress and % elongation vs. power for tin plate welds

7.2.3.3 Fatigue property

Under simple bending fatigue the endurance ratio of welded specimens (with a transverse central weld) was found to be 0.45-0.5 i.e. the endurance limit was 45% to 50% of the static tensile strength.

These figures were obtained without following the full statistical procedure. The stress is plotted against the number of cycles as shown in Figure 7.23. It also should be noted that the fatigue crack did not always pass through the weld.

7.3.2.3 Discussion and comparison with other processes

Williams et al[11] reported that they observed a maximum hardness of 350-370 VHN at the weld zone of a soudronic weld in tin plate the original hardness was 200 VHN to 250 VHN. In the present study a maximum hardness of 2100 knoop was observed in the weld ingot compared to 1200 knoop in the original metal. This shows that the percentage increase in hardness was the same for both soudronic and laser welding.

There is no published tension test results for soudronic welds. However, their discontinuous weld nuggets would be expected to have a lower U.T.S. than that for laser welds which have a continuous and uniform weld nugget.

The relationship between mechanical properties and microstructure is dicussed in the next section.

7.3.4 Microstructure and mechanical properties of tinplate welds

The very low carbon content (0.05% - 0.08%) of the material reduces any possibility of a large change in microstructure and, therefore, the mechanical properties.

However, the increase of hardness observed in the weld ingot is due to the presence of lamellar carbides and possibly some bainite.

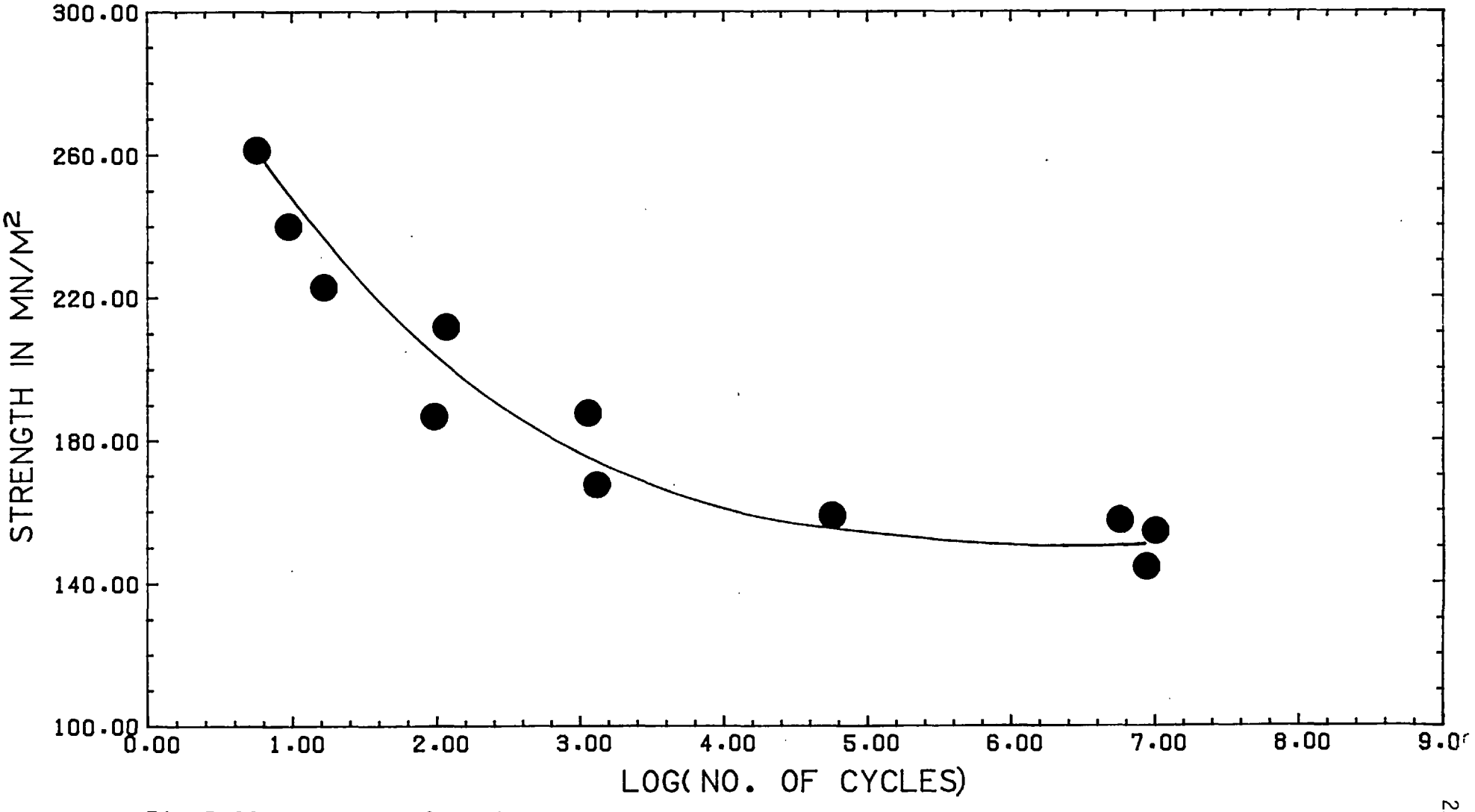

Fig.7.23 S-N Curve for Tin plate welds

The presence of carbides increases the tensile strength of steel but decreases the tensile ductility. This explains the observation that the U.T.S. for a welded sample is the same as that for the parent material and the failure occurs in the parent material. But no significant reduction in tensile ductility was observed. This is probably due to the fact that the weld ingot and HAZ is extremely small compared to the gauge length of the specimen and thus has little effect on ductility.

The presence of bainite improves the fatigue property of steel whereas the presence of carbide lamellae results in lower fatigue property[270]. Grain size does not have an important influence on the unnotched fatigue properties of heat treated steel[270]. Therefore, possibly lamellar carbide and bainite counteract each other resulting in the almost unaffected fatigue properties (endurance ratio ≃ 0.45 to 0.5) of the welded material compared to the parent material.

7.3.5. Corrosion properties of tin plate welds

The data for corrosion rates are given in Table 7.12. They show surprisingly that the applied corrosion current values for welded

Material Tin coated mild steel	Corrosion rate at 10% NaCl of original material	Corrosion rate in 10% NaCl of welded material
	mA/cm^2	mA/cm^2
Sample TP-1	11.0	8.831
Sample TP 15	7.2	0.666

TABLE 7.12

samples in 10% NaCl solution are lower than that for the parent metal. This shows that the corrosion rate is higher for the unwelded material than that for the welded material.

Residual thermal stress in the weld region would be expected to increase the corrosion rate. But the apparent anomaly of better corrosion resistance of welded material may be due to the formation

of Fe-Sn solid solution - a possibility explored in the electron probe microanalysis.

7.3.6 Composition variation of weld ingot

Williams et al[10] observed micro-cracking at the tin rich areas of soudronic welded tin plates. But in the present study of laser welding the phenomenon was absent. That leads to the question of behaviour of the tin coating in laser welding of tin plates. Therefore, electron probe microanalysis (EPMA) was carried out to detect the tin in the weld zone and the HAZ.

EPMA across the weld reveals that it contains about 0.33 to 0.46 percent tin in the weld ingot, when continuous trace has been carried out on a longitudinal section of a weld. But surprisingly it did not show any significant element distribution of tin. The continuous trace was more or less uniform which apparently discards the possibilities of the formation of intermetallic compounds. When count per minute (CPM) standard element tin was 70,000 CPM of tin across the weld were between 500 to 600. Then correcting for oxygen by difference method and considering other correction factors, the average tin content for the weld was estimated as 0.33-0.46% depending on the welding speed. At this range of tin content it is quite probable that they may have formed a solid solution with iron, which is guessed from iron -tin phase diagrams. Considering 0.375 µm film thickness it can be concluded that most of the tin has gone into weld pool instead of vapourising.

EPMA of a transverse section shows that up to 250 µm from the surface tin content is quite low compared with rest of the weld ingot. This is probably due to the entrapment of the tin coating in the lap weld.

Absence of any significant elemental distribution of tin in the weld ingot was also confirmed by the British Steel Corporation Laboratory, Port Talbot, when the same set of samples were sent for their analysis.

7.3.7 Undercut and underbead of tin plate welds

Undercuts observed in the welds were not appreciable and could not be resolved under the microscope used. In some cases underbeads were observed. Few data are given in Table 7.13.

Laser Power Watts	Welding Speed mm/sec	Thickness mm	Undercut mm	Underbead mm	% underbead
500	4.5	0.407	nil	nil	--
760	15	0.48	---	nil	nil
1000	5.75	0.3885	---	0.0185	4.76
1250	60	0.48	---	nil	--

TABLE 7.13

It is evident from the data that the underbead observed with slow speed welds is also small.

7.3.8 Thermal efficiency of laser welding of tin plate

Importance of thermal efficiency in welding processes is discussed in section 7.2.9. The behaviour of the melting efficiency and process efficiency for laser welding of tin plate are discussed in the following sections.

7.3.8.1 Melting efficiency

The melting efficiency is calculated for a few tin plate welds using eqn. 7.1 and values are given in Table 7.14

Melting efficiency (Zm) is plotted against welding speed in Fig. 7.24. It is evident from the figure that Zm increases with welding speed. The same was observed for laser welding of titanium. This agrees with GTAW work of Niles and Jackson[255] with steel.

7.3.8.2 Process efficiency

The process efficiency for tin plate welding is calculated using equation 7.2 and the data are given in Table 7.15. The data are plotted in Fig. 7.25.

TABLE 7.14 TABLE FOR MELTING EFFICIENCY

Power Watts	Welding speed mm/sec	Thick-ness mm	Melt width @ surface mm	Width of HAZ @ surface mm	Melt width @ bot-tom mm	Width of HAZ @ bottom mm	Nugget area mm^2	HAZ area mm^2	Melting effic-iency %
500.00	4.50	.40	.60	1.00	.25	1.00	.17	.23	1.14
760.00	5.25	.40	.80	1.40	.80	1.30	.32	.22	1.64
760.00	5.75	.40	.80	1.20	.75	1.20	.31	.17	1.74
760.00	7.00	.40	.70	1.30	.60	1.15	.26	.23	1.75
760.00	8.50	.40	.65	1.00	.40	.90	.21	.17	1.74
760.00	15.00	.40	.50	.75	.30	.75	.16	.14	2.34
1000.00	5.75	.40	1.00	1.60	1.00	1.60	.40	.28	1.71
1000.00	7.00	.40	.80	1.50	.80	1.40	.32	.26	1.66
1000.00	11.00	.40	.65	1.10	.40	.85	.21	.18	1.71
1000.00	15.00	.40	.55	.85	.30	.60	.17	.12	1.86
1250.00	50.00	.40	.65	2.00	.45	.90	.28	.34	6.52
1250.00	60.00	.40	.50	.75	.30	.30	.16	.05	5.70

TABLE 7.15 TABLE FOR PROCESS EFFICIENCY

Power watts	Welding speed mm/sec	Thick-ness mm	Melt width @ surface mm	Width of HAZ @ surface mm	Melt width @ bot-tom mm	Width of HAZ @ bottom mm	Nugget area mm^2	HAZ area mm^2	Process effic-iency %
500.00	4.50	.40	.60	1.00	.25	1.00	.17	.23	1.55
760.00	5.25	.40	.80	1.40	.80	1.30	.32	.22	1.94
760.00	5.75	.40	.80	1.20	.75	1.20	.31	.17	2.00
760.00	7.00	.40	.70	1.30	.60	1.15	.26	.23	2.20
760.00	8.50	.40	.65	1.00	.40	.90	.21	.17	2.13
760.00	15.00	.40	.50	.75	.30	.75	.16	.14	2.89
1000.00	5.75	.40	1.00	1.30	1.00	1.60	.40	.28	2.03
1000.00	7.00	.40	.80	1.50	.80	1.40	.32	.26	2.02
1000.00	11.00	.40	.65	1.10	.40	.85	.21	.18	2.11
1000.00	15.00	.40	.55	.85	.30	.60	.17	.12	2.25
1250.00	50.00	.40	.65	2.00	.45	.80	.22	.34	8.32
1250.00	60.00	.40	.50	.75	.30	.30	.16	.05	6.17

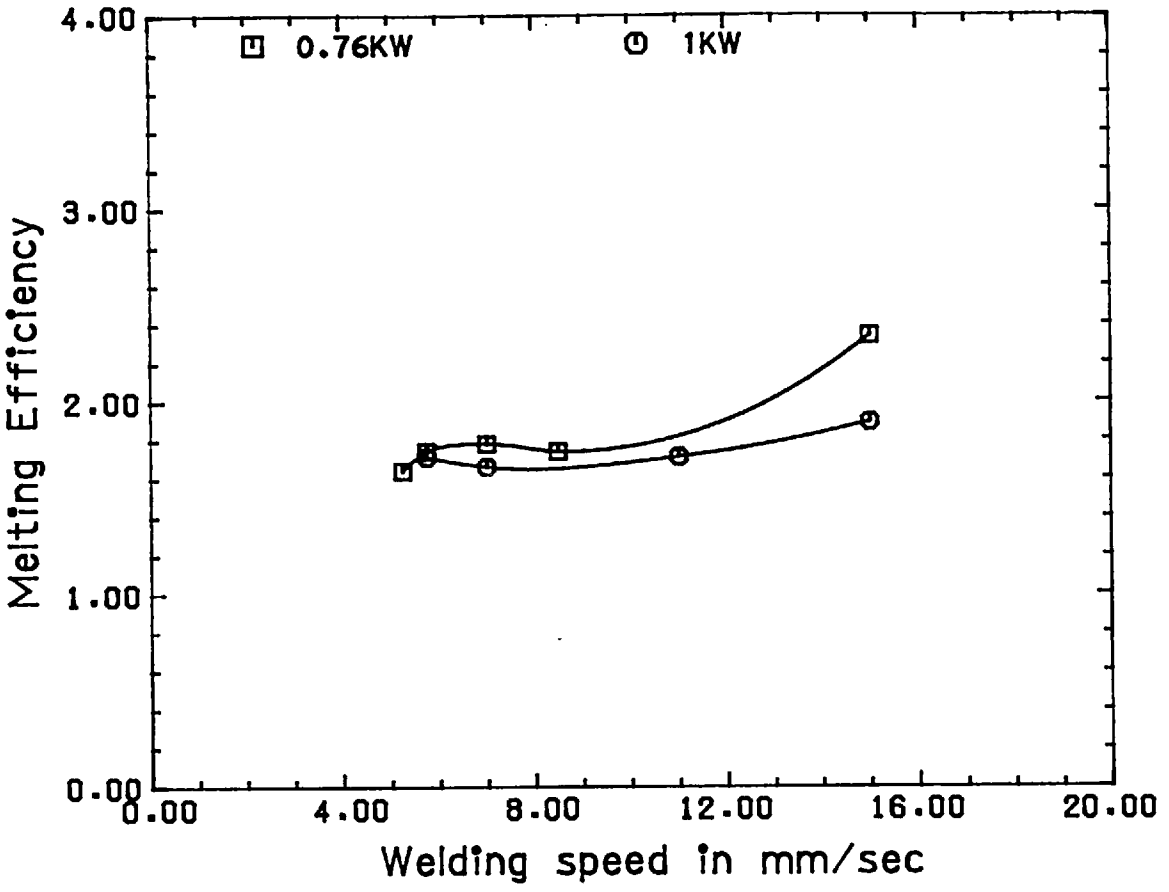

Fig. 7.24 Melting efficiency vs. welding speed for tin plate welds

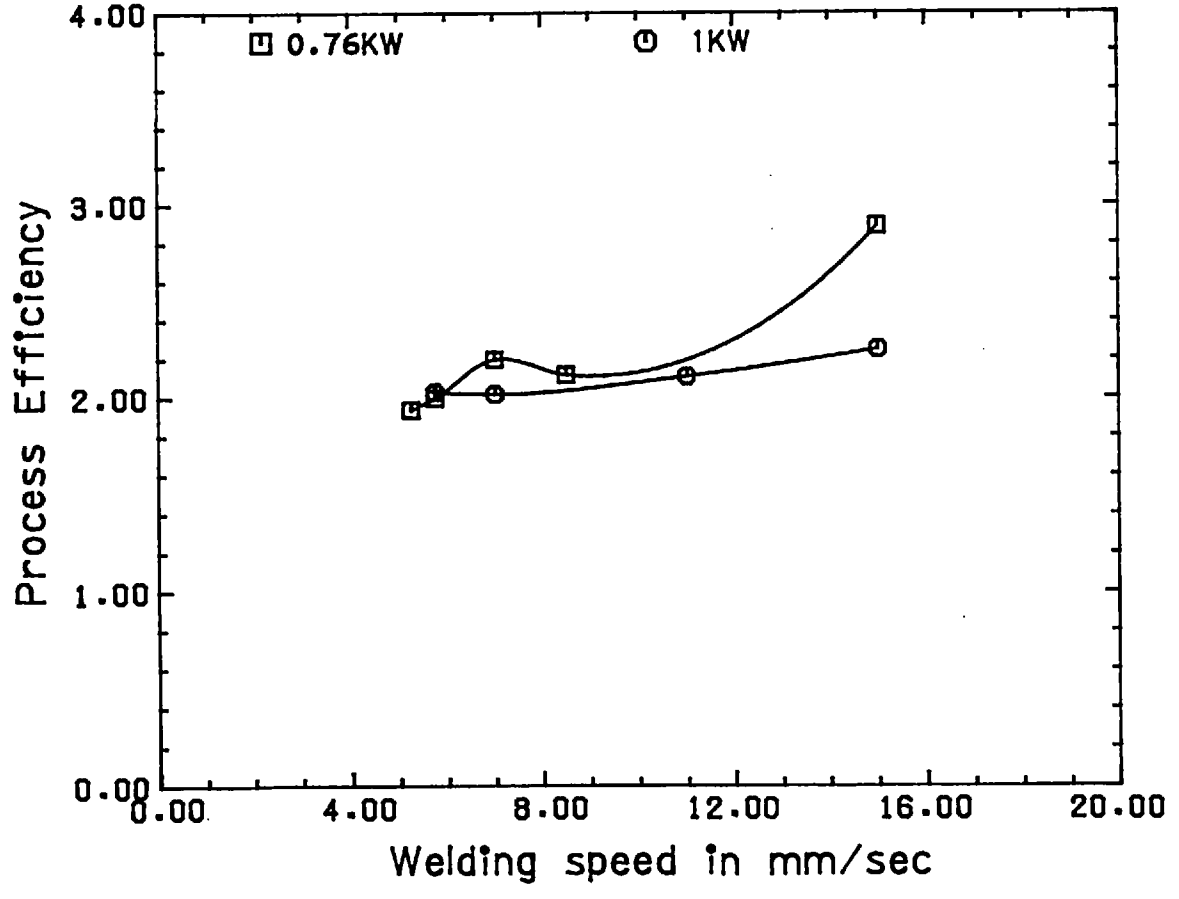

Fig. 7.25 Process efficiency vs. welding speed for tin plate welds

It is evident from the figure 7.25 that the process efficiency increases with the increase of welding speed showing that the loss of energy entering the workpiece decreases for an increase in speed. The same phenomena is observed with titanium welds. But this contradicts the GTAW work of Niles and Jackson[235] on steel. Probably this is due to the keyhole phenomena in laser welding.

7.4 Results and discussion of drum quality mild steel

7.4.1 Welding variables for drum quality mild steel plates

The range of welding runs on drum quality steel plates (Trade name - Hi-top) for various welding conditions is illustrated in Figure 7.26. Details are given in Appendix 9.

7.4.1.1 Effect of laser power and welding speed

All the welding runs on Hi-top were confined to lap welding of 0.4mm sheets. As the base materials are almost the same as the tin coated mild steel except there is no tin coating. It was thus assumed that the bead on plate welds on Hi-Top would have similar welding variables as found for the lap welding of 0.2mm tin coated mild steel sheets.

Similar to titanium welds and tin plate welds it is quite evident from the wide spread in values of the laser powers and welding speeds used that there is a critical range of speeds for a given power in which sound welds are produced.

Figure 7.27 shows the permissible range for sound lap welds on 0.4mm thick Hi-top sheets. It is evident from the figure that the welding speed increases exponentially with power up to 1750 watts. This agrees with Baardsen et al[154]. But as observed before with tin plate welds this only applied for the lower power range. This is discussed in section 7.3.1.2.

It was also observed that similar to the tin plate and titanium welds the HAZ and the width of the weld ingot varied with laser power and welding speed. Some representative values are given in Table 7.16.

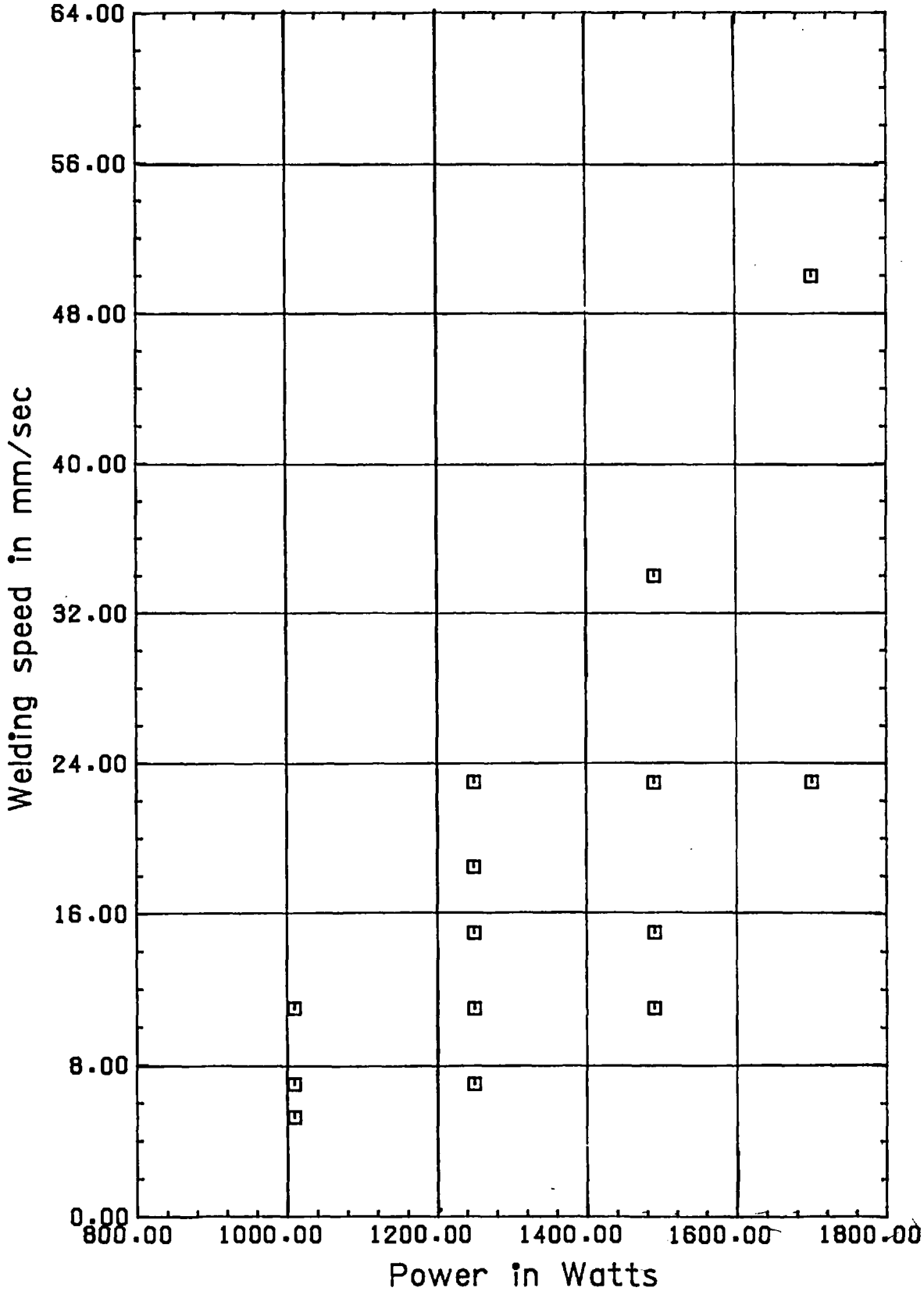

Fig. 7.26 The range of welding runs on tin free drum quality steel for various welding conditions

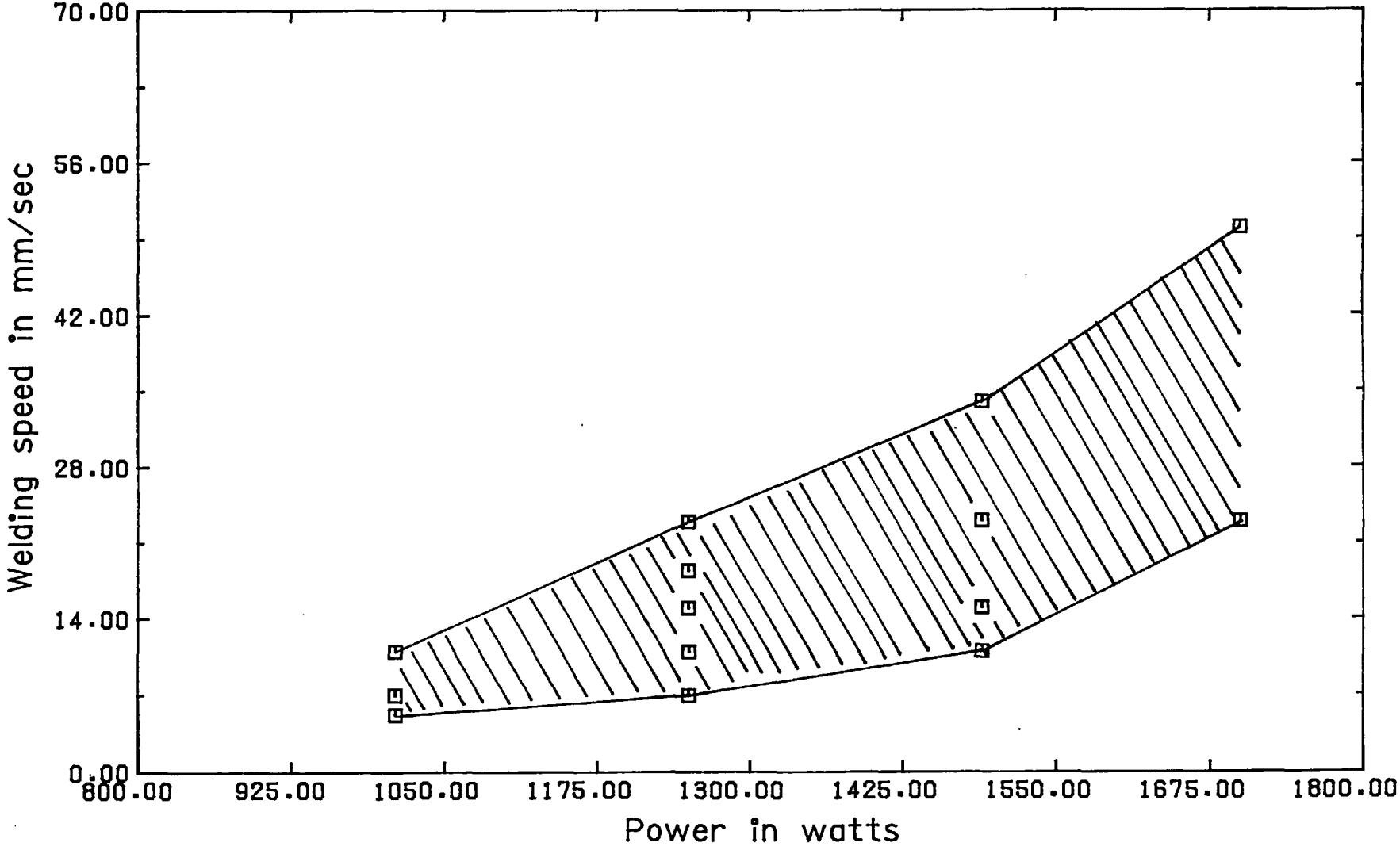

Fig 7.27 Variation of tin free steel lap welding speed with laser power

Material	Width of weld ingot mm	Width of Total HAZ mm	Power in watts	Welding Speed in mm/sec.	Thickness in mm
Mild steel	1.5	3.0	1490	11	0.8
	0.8	2.1	1490	34	(Lap weld of 0.4 mm)
	1.0	1.6	1010	11	"

TABLE 7.16

It is evident from this data that for the same power the HAZ decreased with increase in speed.

7.4.1.2 Discussion and comparison with other processes

The purpose of studying the laser welding of tin free drum quality steel was to find an alternative method of making cans. The comparison between different processes of can making is given in Appendix 2, Table III. The other welding process for making cans is the soudronic welding method which is not able to handle this type of material due to the electrode problem produced by the chromium oxide coating which is present on this material. Therefore, laser welding may be an important process for making cans from tin free steels.

7.4.2 Metallurgical Properties

7.4.2.1 Radiography

The radiographs indicated that sound welds having no porosity are produced in the permissible welding region indicated in Fig. 7.27. Two representative welds are presented in Plate 7.9. The welds exhibited a narrow and uniform weld zone similar to that observed for tin plate welds.

7.4.2.2 Metallography

All the specimens were mechanically polished and etched with 2% nital. The structure was studied under the optical microscope.

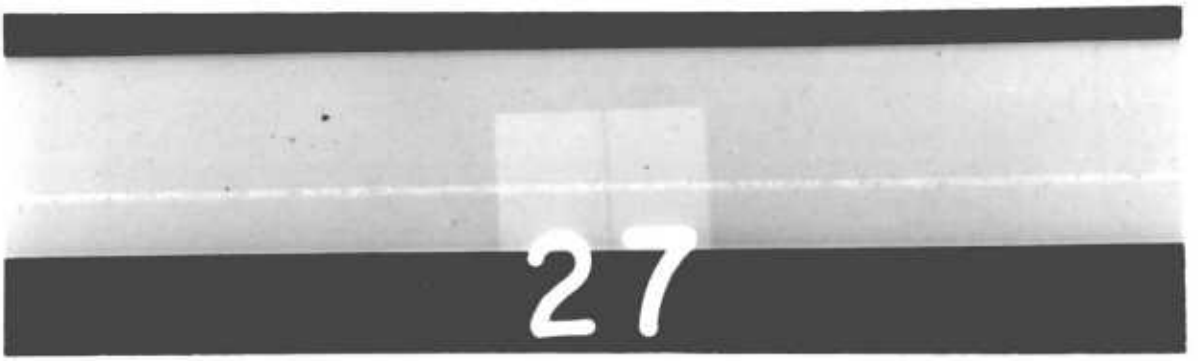

a) 1250 watts, 23 mm/sec

b) 1700 watts, 50 mm/sec

PLATE 7.9 Radiographs for drum quality steel welds

Tin free steel sheets were received in the annealed condition. The variation of microstructure as seen in an optical photomicrograph after welding is represented in a composite Plate 7.10. The microstructure variation observed is similar to that observed for tin plates because the base mild steel has a similar composition.

Plate 7.10b represents a macrograph of a typical laser welded tin free mild steel. Plate 7.10d represents the micrograph of the fusion zone. Both 7.10b and 7.10d revealed the columnar nature of the weld pool. Presence of lamellar carbide is also noted in the weld pool. Besides that it consists mainly of ferrite, two or three pockets of dark areas are observed but they are not properly resolved under the optical microscopy. Probably they are a martensite type transformation product like a bainite, but they are beyond the resolution of the optical microscope.

Plate 7.10a shows the parent matrix which consists mainly of equiaxed ferrite grains.

Plate 7.10c shows the heat affected zone (HAZ). Some grain coarsening is observed in this area.

It is evident from the micrographs that the cooling rate is highest in the fusion zone.

7.4.2.3 Discussion and comparison with other processes

The alternative can making process which involves welding is the soudronic process but it cannot weld tin free steel due to electrode problems. It is very difficult to weld such thin materials unless one uses an electron beam welding technique with ancillary vacuum chambers, which makes this process not commercially feasible.

Laser welding, however, provides an unique opportunity to weld tin free steel successfully.

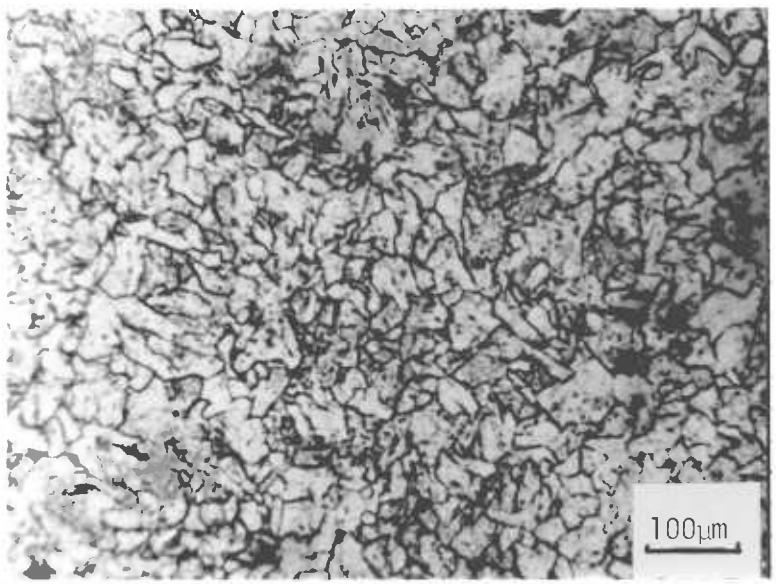

C

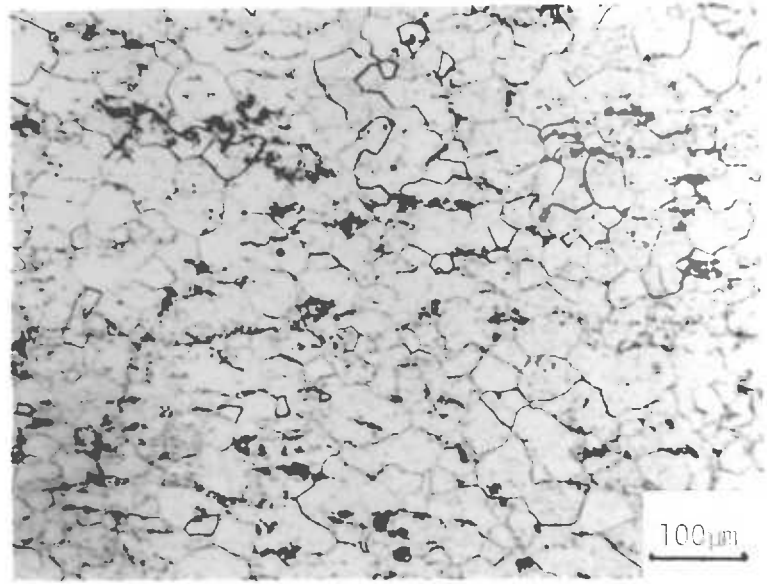

A

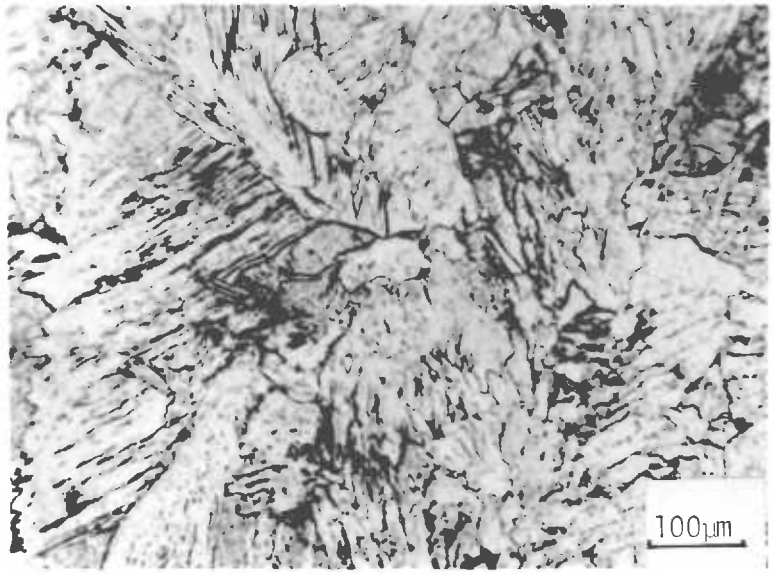

D

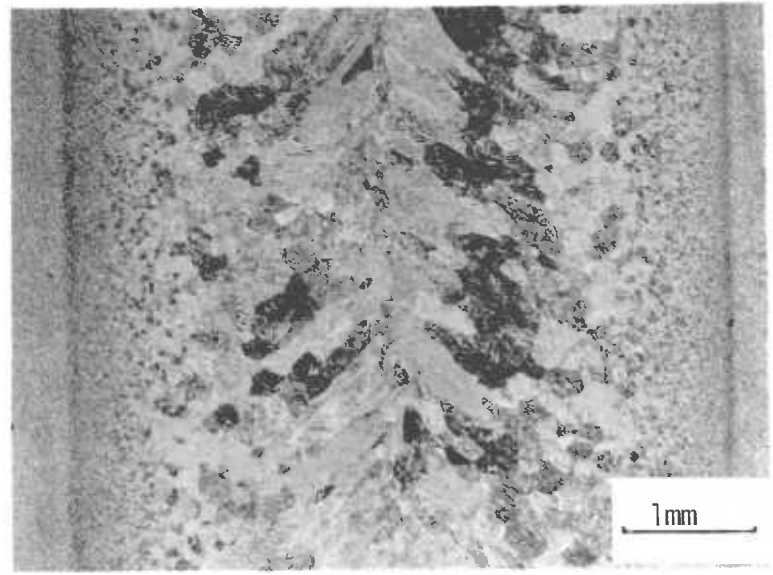

PLATE 7.10 Composite showing the structural variation for lap welded 0.4mm drum quality steel. 1010 watts, 5.25 mm/sec

7.4.3 Mechanical Properties

7.4.3.1 Micro-hardness measurements

A micro-hardness traverse across the weld ingot revealed that the hardness at the weld ingot was higher than that of the parent material. Maximum hardness recorded in the weld zone was 2066 knoop whereas the hardness at the parent matrix was around 1200 knoop.

Some representative data are plotted and shown in Figures 7.28a and 7.28b with fifth order polynomial regression curves fitted. The details are given in Appendix 10.

It should be noted that for the same power (Fig. 7.28a) the increase of hardness is higher for higher welding speeds. Whereas for the same welding speed (Fig. 7.28b) the increase of hardness is higher for lower power. This shows that for higher cooling rates the hardness increase is greater.

7.4.3.2 Tension test

The U.T.S., 0.2% proof stress and percentage elongation were measured and they were found to be relatively independent of the laser power or welding speeds as shown in Figures 7.29 and 7.30 respectively. Typical values of the mechanical properties are shown in Table 7.17 Details of tension test results are given in Appendix 9 .

MATERIALS	WELDED MATERIAL			ORIGINAL MATERIAL		
	U.T.S. MN/m^2	0.2% Proof Stress MN/m^2	Elongation %	U.T.S MN/m^2	0.2% Proof Stress MN/m^2	Elongation %
Hi-Top drum quality mild steel (tin free steel)	386-426	340 - 380	21-27	≃353-380	284 ≃ 328	≃30-32

TABLE 7.17

It is observed that the weld properties are similar to the unwelded and in most cases rupture takes place at the original material

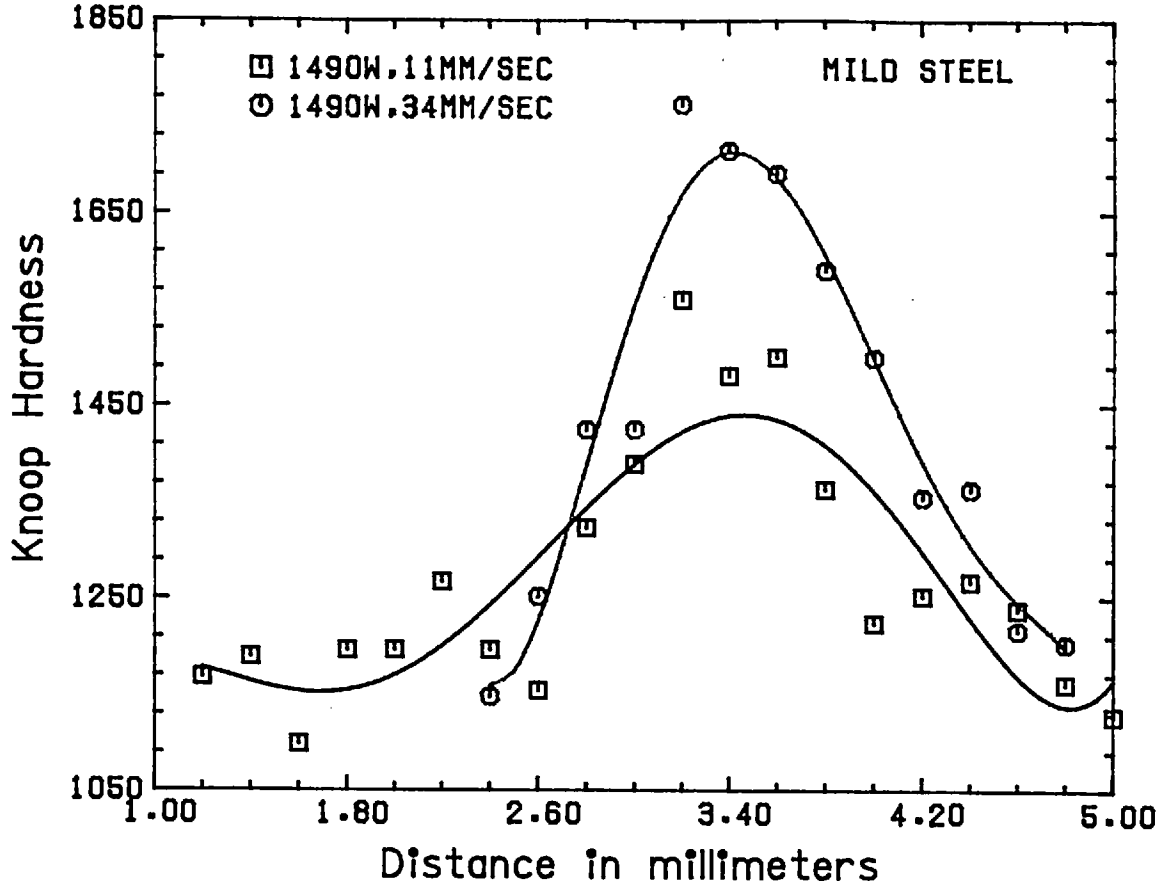

FIG. 7.28a Micro-hardness traverse for tin free steel welds

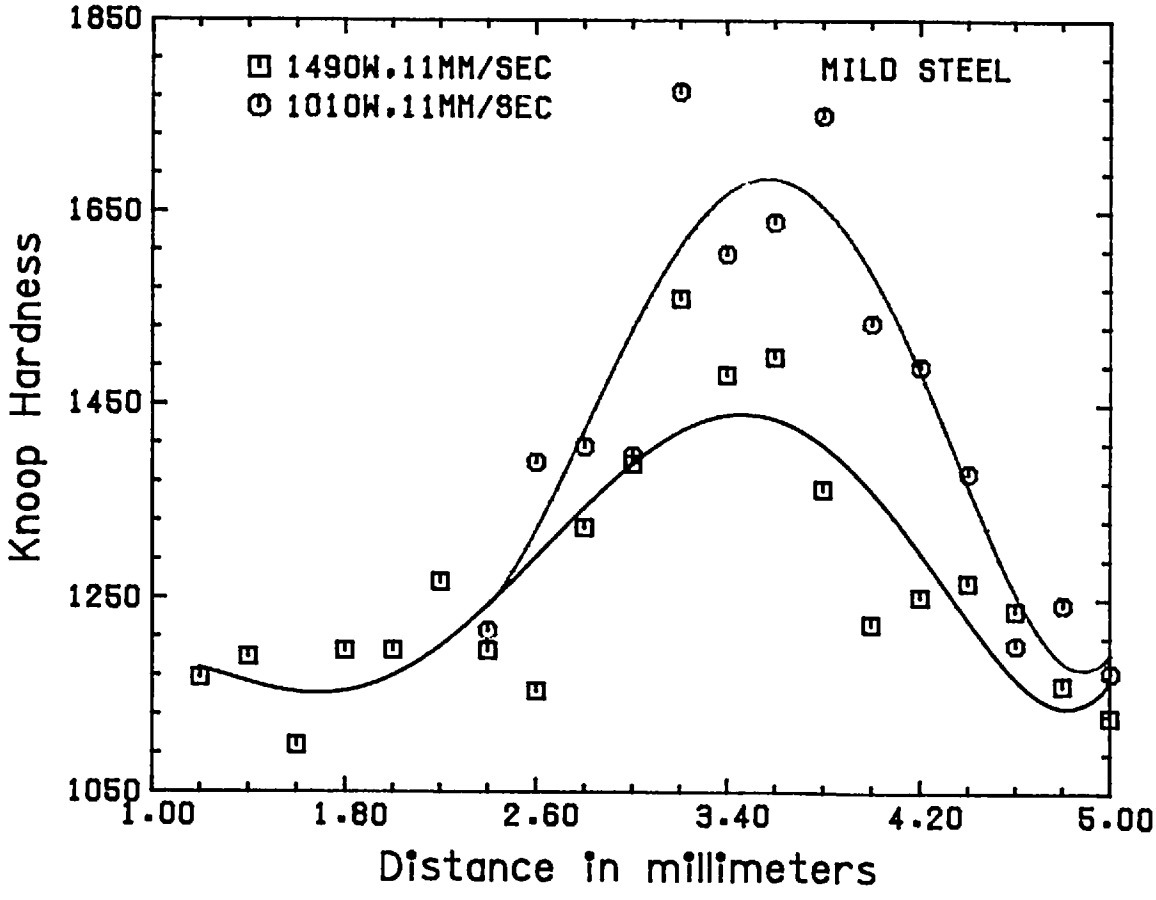

FIG. 7.28b Micro-hardness traverse for tin free steel welds

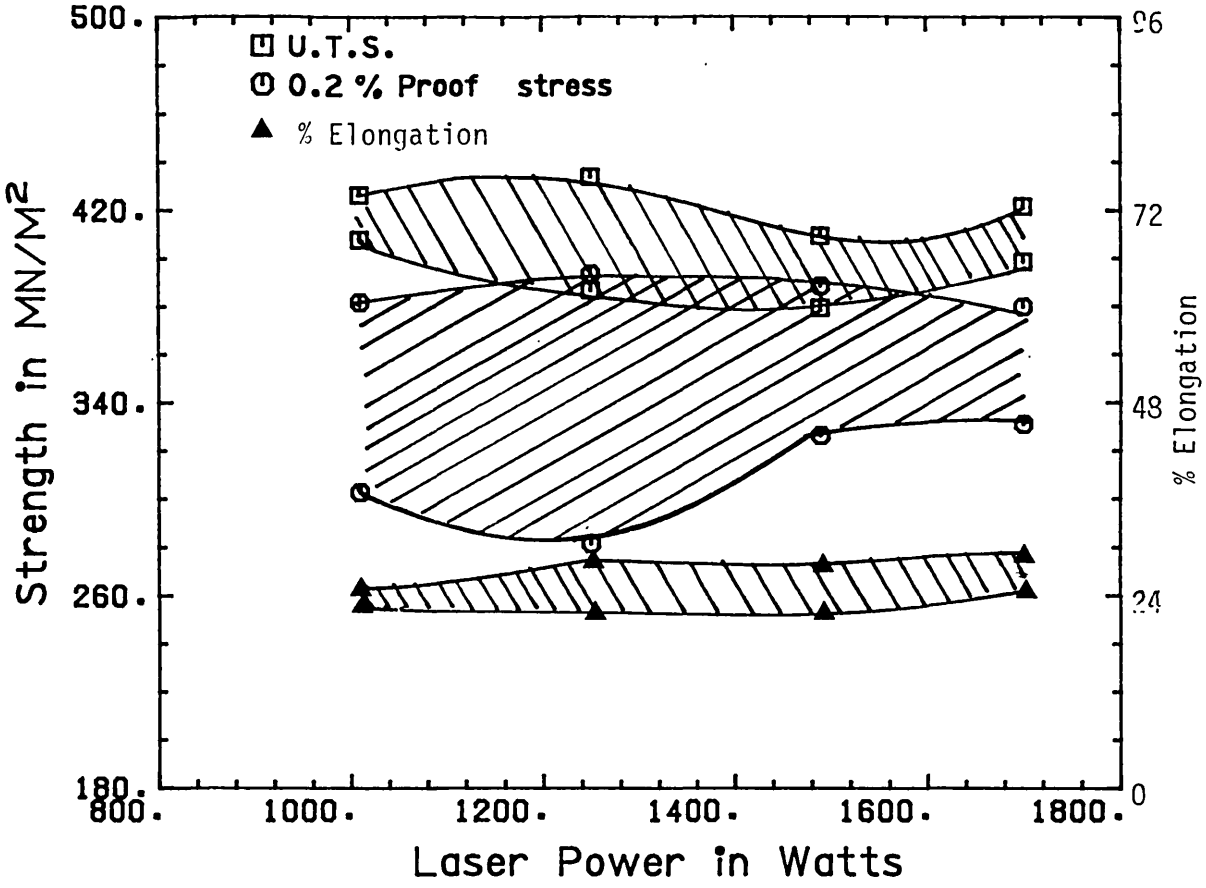

Fig 7.29 UTS, 0.2% Proof stress and % elongation vs. welding speeds for tin free steel welds

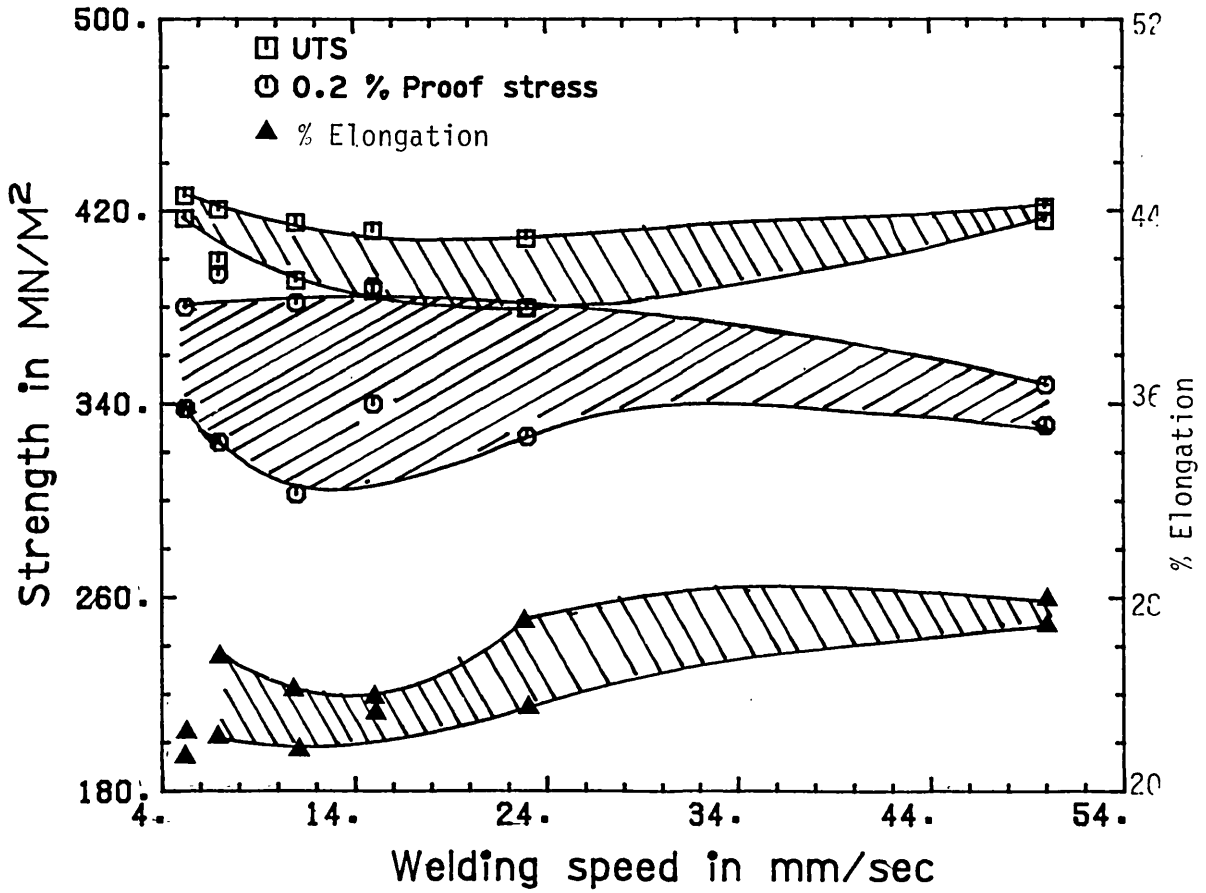

Fig 7.30 UTS, 0.2% Proof stress and % elongation vs. welding speeds for tin free steel welds

instead of the weld ingot. A similar observation was made for titanium and tin plate welds.

7.4.3.3 Fatigue properties

The endurance ratio for welded specimens (with a transverse central weld) was found to be 0.45-0.5 under simple bending fatigue test. This is similar to the tin plate welds.

These figures were obtained without following the full statistical procedure. Even so, the stress is plotted against the number of cycles and is shown in Figure 7.31 . It also should be noted that the fatigue crack did not always pass through the weld. These show that having the same composition tin plate and tin free steel show similar mechanical properties.

7.4.3.4 Discussion and comparison with other processes

There are no published results for the welding of tin free steel. However, as the compositions of tin free steel and tin plate are the same except for the difference in surface coating, it is expected that both should have similar properties after being welded. This is confirmed.

Most of the other can making processes either face difficulties or cannot handle tin free steel at all. Comparisons are given in Table III. Appendix 2. Therefore, by producing reasonable mechanical and metallurgical properties laser welding provides an unique opportunity for an alternative process.

7.4.4 Microstructure and mechanical properties of drum quality mild steel welds

The very low carbon content (0.05-0.08%) of the material reduces any possibility of a large change of microstructure and, therefore, the mechanical properties. However, both tin plate and tin free steel have the same composition and, therefore, mechanical and metallurgical properties. Consequently, the relationship between microstructure and mechanical propeties of tin free steel is similar to that for tin plate which is discussed in Section 7.3.4.

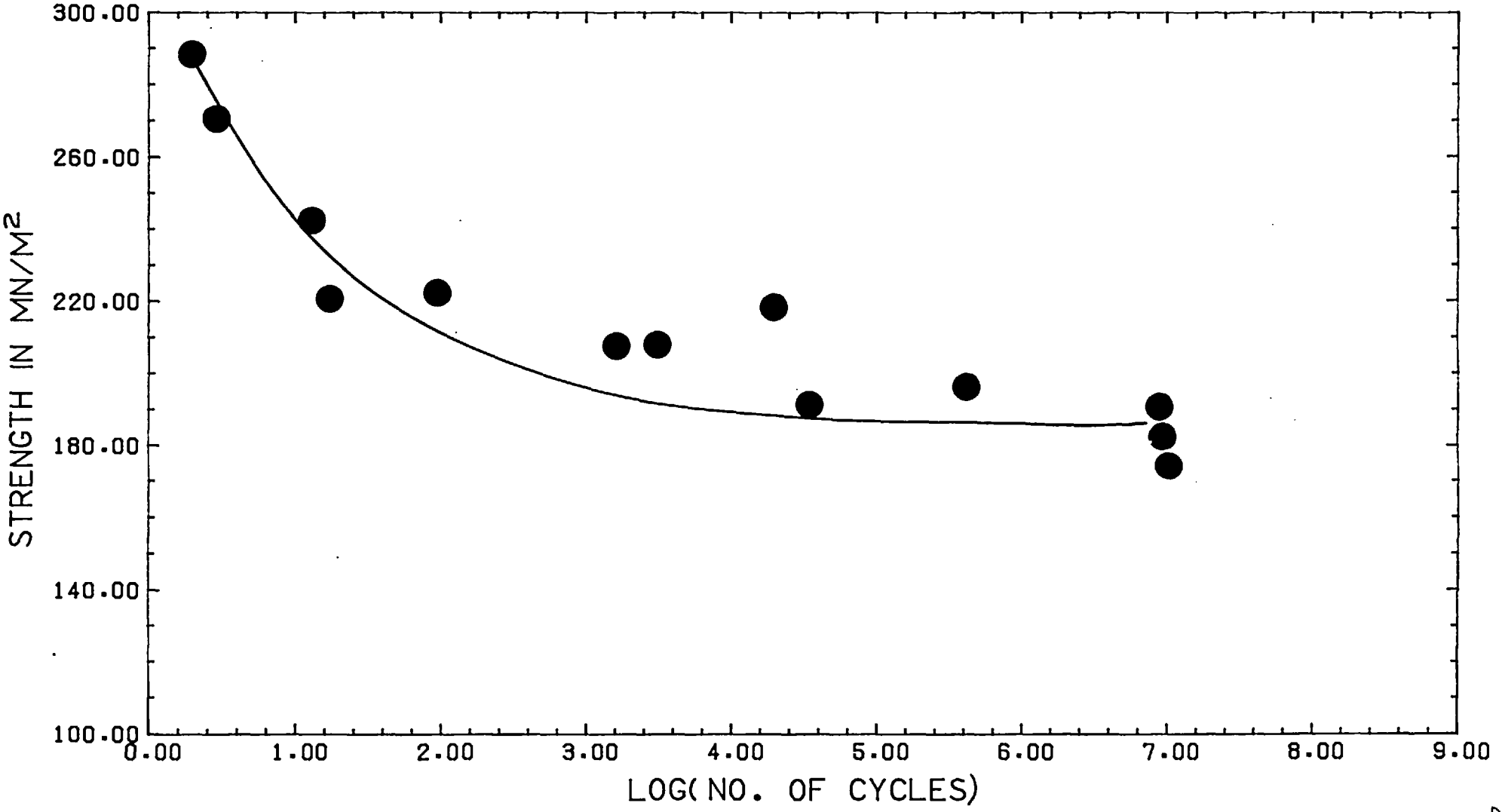

Fig.7.31 S-N Curve for Tin free steel Welds.

7.4.5 Undercut and underbead of the welds

Similar to tin plate welds undercuts were almost absent. Underbeads observed are bigger than those observed for tin plate welds probably because the stock is thicker. A few data are given in Table 7.18.

Laser power watts	Welding Speed mm/sec	Thickness mm	Undercut mm	Underbead mm	% underbead
1250	7	0.814	--	0.0555	6.818
1490	11	0.851	--	0.037	4.34
1490	34	0.814	--	0.01850	2.27
1700	50	0.8695	--	0.019	2.12

TABLE 7.18

7.4.6 Thermal efficiency of laser welding of tin free steel

Importance of thermal efficiency in welding processes is discussed in section 7.2.9. The behaviour of the melting efficiency and process efficiency for the laser welding of tin free steel are discussed in the following sections.

7.4.6.1 Melting efficiency

The melting efficiency is calculated for a few tin free steel welds using equation 7.1 and values are given in Table 7.19.

Figure 7.32 shows that melting efficiency (Zm) increases with welding speed. The same was observed for the laser welding of titanium and tin plate. This also agrees with GTAW work of Niles and Jackson[235] with steel. This shows that at the lower welding speeds more of the available energy is lost enlarging the molten pool and heating up the workpiece.

TABLE 7.19 TABLE FOR MELTING EFFICIENCY

Power watts	Welding speed mm/sec	Thick-ness mm	Melt width @ surface mm	Width of HAZ @ surface mm	Melt width @ bottom mm	Width of HAZ bottom mm	Nugget area mm^2	HAZ area mm^2	Melting effic-iency %
1010.00	5.25	.80	1.75	3.60	1.75	3.50	1.40	1.44	5.40
1010.00	7.00	.80	1.65	3.25	1.65	3.50	1.32	1.38	6.79
1010.00	11.00	.80	1.25	2.30	.75	2.30	.80	1.04	6.47
1250.00	5.25	.80	1.65	3.25	1.65	3.25	1.32	1.28	4.11
1250.00	11.00	.80	1.45	3.00	1.20	3.00	1.06	1.34	6.92
1250.00	15.00	.80	1.30	3.00	.90	2.50	.88	1.32	7.84
1250.00	18.50	.80	1.25	2.55	.65	2.10	.76	1.10	8.35
1250.00	28.00	.80	1.10	2.15	.45	1.40	.62	.80	8.47
1490.00	11.00	.80	1.35	2.80	1.25	2.50	1.04	1.08	5.70
1490.00	15.00	.80	1.25	2.75	1.10	2.50	.94	1.16	7.06
1490.00	23.00	.80	1.20	2.30	.60	1.75	.72	.90	8.25
1490.00	34.00	.80	1.00	2.00	.40	1.35	.54	.78	9.49

TABLE 7.20 TABLE FOR PROCESS EFFICIENCY

Power watts	Welding speed mm/sec	Thick-ness mm	Melt width @ surface mm	Width of HAZ @ surface mm	Melt width @ bottom mm	Width HAZ @ bottom mm	Nugget area mm^2	HAZ area mm^2	Process effic-iency %
1010.00	5.25	.80	1.75	3.60	1.75	3.50	1.40	1.44	6.88
1010.00	7.00	.80	1.65	3.25	1.65	3.50	1.32	1.38	8.68
1010.00	11.00	.80	1.25	2.30	.75	2.30	.80	1.04	8.71
1250.00	5.25	.80	1.65	3.25	1.65	3.25	1.32	1.28	5.18
1250.00	11.00	.80	1.45	3.00	1.20	3.00	1.06	1.34	9.26
1250.00	15.00	.80	1.30	3.00	.90	2.50	.88	1.32	10.97
1250.00	18.50	.80	1.25	2.55	.65	2.10	.76	1.10	11.57
1250.00	28.00	.80	1.10	2.15	.45	1.40	.62	.80	11.38
1490.00	11.00	.80	1.35	2.80	1.25	2.50	1.04	1.08	7.28
1490.00	15.00	.80	1.25	2.75	1.10	2.50	.94	1.16	9.34
1490.00	23.00	.80	1.20	2.30	.60	1.75	.72	.90	11.00
1490.00	34.00	.80	1.00	2.00	.40	1.35	.54	.78	13.01

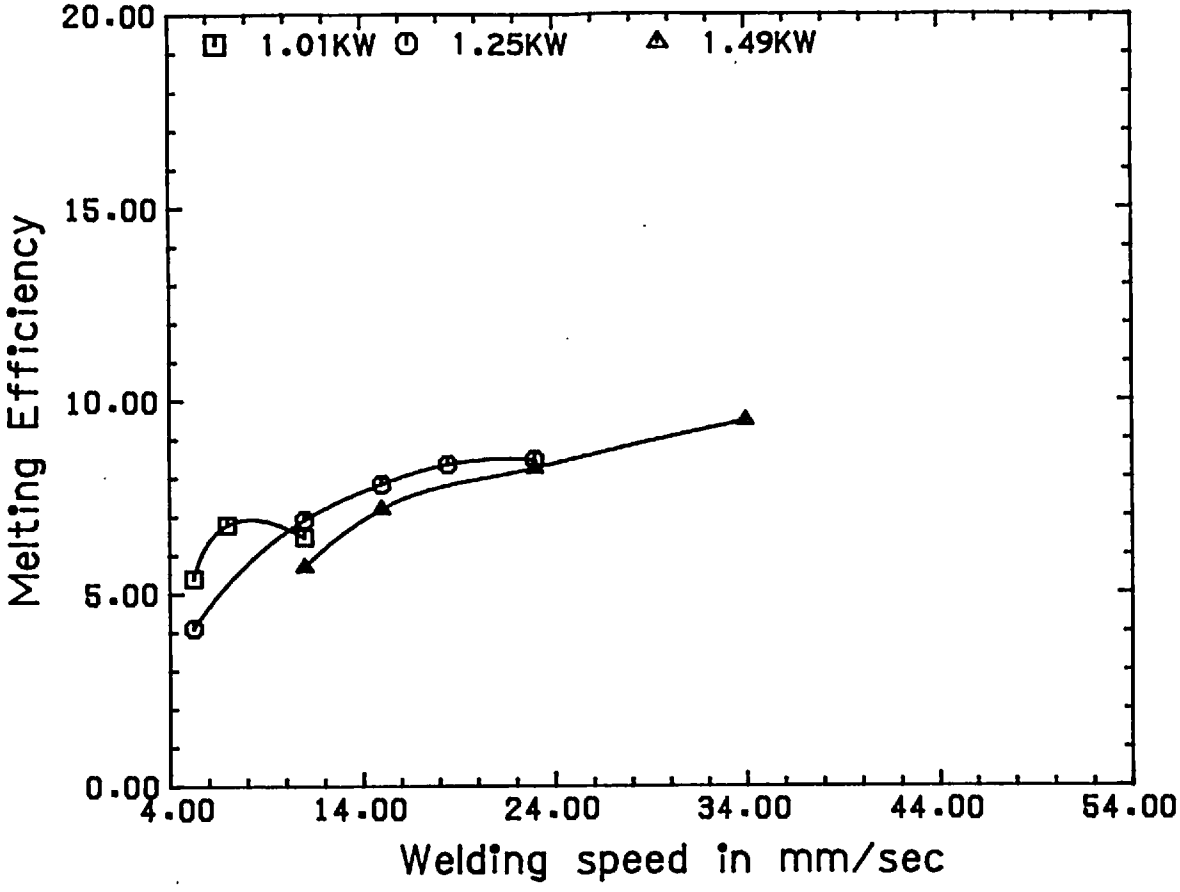

Fig. 7.32 Melting efficiency vs. welding speed for tin free steel welds

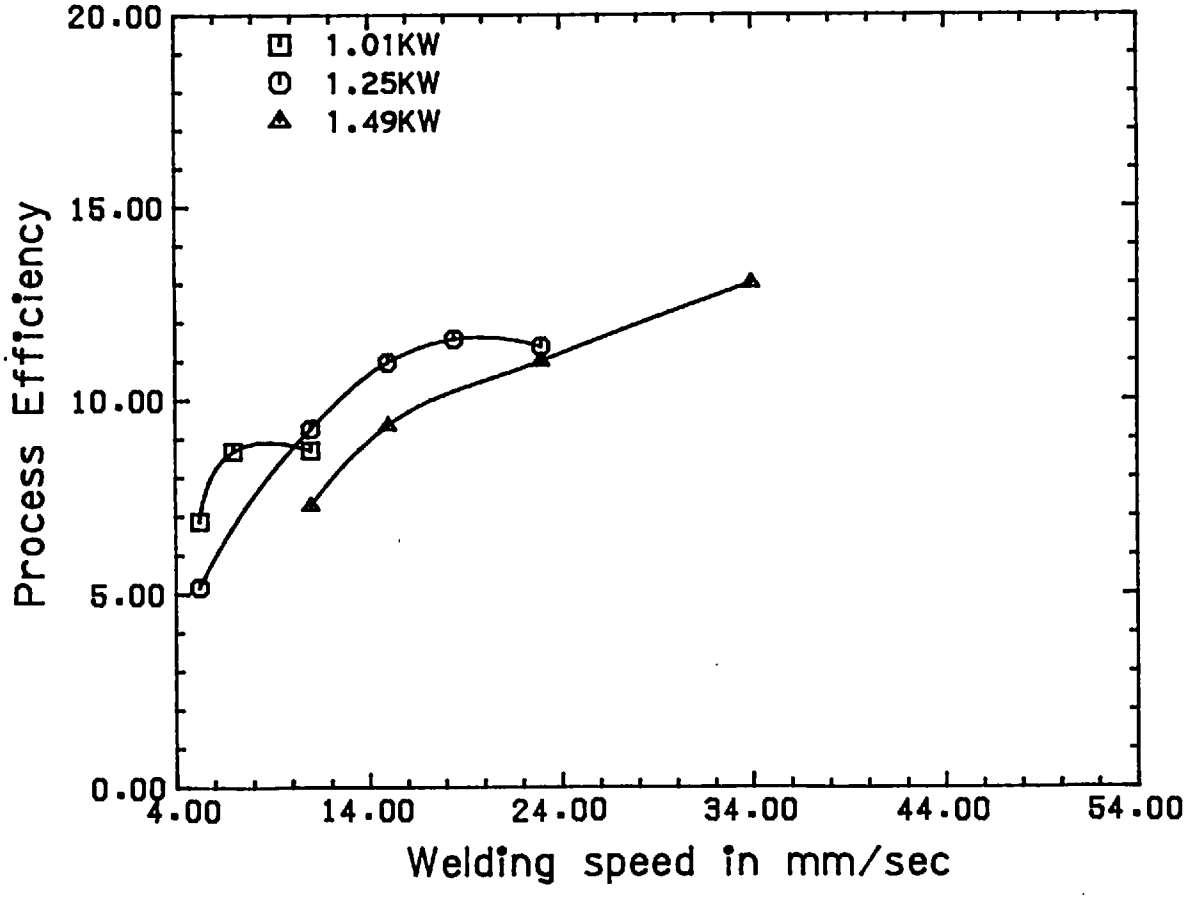

Fig. 7.33 Process efficiency vs. welding speed for tin free steel welds

7.4.6.2 Process efficiency

The process efficiency for tin free steel is calculated using equation 7.2 and the data are given in table 7.20.

When the process efficiency is plotted against welding speed as shown in Figure 7.33 it is noted that the process efficiency increases with the increase of welding speed. It shows that the loss of energy entering the workpiece decreases with an increase of speed. The same phenomenon was observed with both titanium and tin plate welds. This does not agree with the GTAW work of Niles and Jackson[235] on steel. This is probably due to the keyhole phenomena in laser welding.

CHAPTER 8

8.1 Conclusions

Welding by means of a CW CO_2 laser has been shown to be not only possible but one of the better methods.

This is due to (a) the narrow HAZ and rapid quench microstructure associated with laser welding producing favourable fatigue properties with no significant fall in mechanical properties. (b) the cleanliness of the laser beam causing no porosity or chemical contamination and (c) the welding process being conducted at atmospheric pressure resulting in no degassing as is some times found in vacuum welding processes. It is also noted that:-

(i) initially welding speed increase exponentially with power but subsequently tails off near the higher limit of the power available from the laser.

(ii) Welding speed decreases for increase of thickness for a power

(iii) The joining rate tends to start well below average with thin material, to rise as the thickness is increased and optimum welding conditions are established and finally to drop as the thickness becomes too great for the power to handle (Ref. Fig. 7.6).

(iv) Localised heating and rapid self quenching produces narrow HAZ high cooling rate up to 10^4 ^{o}C/sec.

(v) Narrow HAZ leads to almost unaffected mechanical properties

(vi) Unlike EBW undercut and underbead is very small

(vii) Process efficiency decreases with the increase of speed

(viii) Melting efficiency increases with the increase of speed.

For titanium welding it can be concluded that the laser welding provides an opportunity to weld titanium at atmospheric pressure without serious contamination and deterioration of mechanical properties.

For tin plate and tin free steel welding it offers a serious possibility of alternative can making process, of course, more investigation is required to attain higher speeds.

The theoretical model gives good correlation with the experimentally observed

1) Temperature distribution temperature cycle
2) Welding speed
3) Depth of penetration

8.2 Future Work

The present study revealed many interesting areas for further investigation. They are:-

(i) The effect of arc-augmented laser welding on welding speed, mechanical and metallurgical properties etc.

(ii) Extrapolation of tin plate and tin free steel welding with higher power lasers e.g. 5kW, 15kW etc.

(iii) Statistical analysis of fatigue property of laser welded titanium

(iv) Dissimilar metal welding

(v) Direct temperature measurement during welding.

The mathematical model can be made even more accurate by incorporating the following:-

(i) Variation of physical properties with temperature e.g. thermal conductivity, specific heat, reflectivity.

(ii) Latent heat of evaporation

(iii) The convective movement of molten material within the weld pool. But it is obvioulsy very difficult to quantify.

To reduce the computing time different numerical algorithm like line by line method may be tried.

APPENDIX 1

CUTTING RATES FOR METAL SHEETS USING GAS JET ASSIST

Metal	Power	Thickness	Rate	Gas	Reference
2219 Aluminium alloy	3.8 kW	0.25 in	12 IPM	CO_2	Banas (Ref. 151)
Steel	1.2 kW	5 mm	60 cm/min	O_2	Ruffler and Gürs (Ref. 113)
6061 Aluminium	10 kW	0.5 in	40 IPM	He	Locke and Hella (Ref. 83)
Inconel 718	11 kW	0.5 in	50 IPM	He	Locke and Hella (Ref. 83)
Titanium	10 kW	1 in	200 IPM	O_2	Locke and Hella (Ref. 83)
302 Stainless Steel	185 W	10^{-3} in	360 IPM	NONE	Gonsalves and Duley (Ref. 258)
	185 W	$2x10^{-3}$ in	180 IPM	NONE	Gonsalves and Duley (Ref. 258)
	185 W	$3x10^{-3}$ in	120 IPM	NONE	Gonsalves and Duley (Ref. 258)
	200 W	$3x10^{-3}$ in	240 IPM	O_2	Duley and Gonsalves (Ref. 102)
	200 W	$4x10^{-3}$ in	180 IPM	O_2	Duley and Gonsalves (Ref. 102)
	200 W	$8x10^{-3}$ in	120 IPM	O_2	Duley and Gonsalves (Ref. 102)
	200 W	$12x10^{13}$ in	90 IPM	O_2	Duley and Gonsalves (Ref. 102)
Steel	300 W (100 Hz)	0.10 in	40 IPM	O_2	Barber and Linn (Ref. 16, p252)
Aluminium	15 kW	0.5 in	90 IPM	NONE	Locke et al (Ref. 120)
Carbon steel	15 kW	0.25 in	90 IPM	NONE	Locke et al (Ref. 120)
304 Stainless Steel	20 kW	0.187 in	50 IPM	NONE	Locke et al (Ref. 120)
Mild Steel	850 W	2.3 mm	30 mm/sec	O_2	Adams (Ref. 259)
Martensitic-stainless steel	850 W	8 mm	6.4 mm/sec	O_2	Adams (Ref. 259)
Martensitic-stainless steel	850 W	5 mm	12.7 mm/sec	O_2	Adams (Ref. 259)
Austenitic-stainless steel	850 W	3.2 mm	12.7 mm/sec	O_2	Adams (Ref. 259)
Nimonic 90	850 W	1.3 mm	38 mm/sec	O_2	Adams (Ref. 259)
Nimonic 80A	850 W	0.7 mm	76 mm/sec	O_2	Adams (Ref. 259)
Nimonic 75	850 W	0.7 mm	34 mm/sec	O_2	Adams (Ref. 259)

CUTTING RATES FOR NONMETALS USING THE CW CO_2 LASER

Material	Power	Thickness	Rate	Gas	Reference
Corrugated	3.5 kW	0.18 in	350 ft/min	NONE	Banas (Ref. 151)
Borsical tape	3.9 kW	$9x10^{-3}$ in	100 ft/min	NONE	Banas (Ref. 151)
Asbestos (compressed)	180 W	6.4 mm	76.2 cm/min	Air	Harry and Lunau (Ref. 109)
Asbestos (cement)	335 W	6.4 mm	2.5 cm/min	Air	Harry and Lunau (Ref. 109)
Confectionary	250 W	27 mm	100 cm/min	Air	Harry and Lunau (Ref. 109)
	260 W	6 mm	150 cm/min	Air	Harry and Lunau (Ref. 109)
Glass (soda lime)	350 W	2 mm	75 cm/min	Air	Harry and Lunau (Ref. 109)
Paper (matt)	60 W	0.33 mm	2800 cm/min	Air	Harry and Lunau (Ref. 109)
Paper (gloss)	60 W	0.33 mm	4000 cm/min	Air	Harry and Lunau (Ref. 109)

.... CONTINUED

CUTTING RATES FOR NONMETALS USING THE CW CO_2 LASER

Material	Power	Thickness	Rate	Gas	Reference
Plastic (Acrylic)	300 W	3.1 mm	183 cm/min	Air	Harry and Lunau (Ref. 109)
Plastic (PVC)	300 W	3.2 mm	360 cm/min	Air	Harry and Lunau (Ref. 109)
Plastic (expanded polystyrene)	300 W	20 mm	10 cm/min	Air	Harry and Lunau (Ref. 109)
Nylon	180 W	--	360 cm/min	Air	Harry and Lunau (Ref. 109)
Vinyl (36 stack)	330 W	--	2.5 cm/min	Air	Harry and Lunau (Ref. 109)
Leather	225 W	3 mm	305 cm/min	Air	Harry and Lunau (Ref. 109)
Wood (Oak)	300 W	16 mm	27.9 cm/min	Air	Harry and Lunau (Ref. 109)
Wood (deal)	200 W	50 mm	12.5 cm/min	Air	Harry and Lunau (Ref. 109)
Wood (hardboard)	300 W	3.8 mm	91 cm/min	Air	Harry and Lunau (Ref. 109)
Wood (plywood)	350 W	4.8 mm	530 cm/min	Air	Harry and Lunau (Ref. 109)
	225 W	5 mm	110 cm/min	Air	Harry and Lunau (Ref. 109)
	225 W	6.5 mm	65 cm/min	Air	Harry and Lunau (Ref. 109)
	225 W	15.5 mm	30 cm/min	Air	Harry and Lunau (Ref. 109)
	225 W	19 mm	28 cm/min	Air	Harry and Lunau (Ref. 109)
Plastic (perspex)	90 W	10 mm	33 cm/min	Air	Lunau et al (Ref.107)
	200 W	20 mm	20 cm/min	Air	Lunau et al (Ref. 107)
	180 W	30 mm	11 cm/min	Air	Lunau et al (Ref. 107)
Boron epoxy composite	15 kW	0.32 in	65 in/min	Air	Locke et al (Ref. 153)
Fibreglass epoxy composite	20 kW	0.5 in	180 in/min	Air	Locke et al (Ref. 153)
Wood (plywood)	8 kW	1 in	60 in/min	Air	Locke et al (Ref. 153)
Plastic (plexiglass)	8 kW	1 in	60 in/min	Air	Locke et al (Ref. 153)
Glass	20 kW	0.375 in	60 in/min	Air	Locke et al (Ref. 153)
Concrete	8 kW	1.5 in	2 in/min	Air	Locke et al (Ref. 153)
Alumina	40 W	0.635 mm	60 in/min	Air	Conti (Ref. 260)
Perspex	850 W	32 mm	5.0 mm/sec	Argon	Adams (Ref. 259)
Softwood	850 W	14. 0 mm	25 mm/sec	Argon	Adams (Ref. 259)
Hardwood	850 W	5 mm	76 mm/sec	Argon	Adams (Ref. 259)
Plywood	850 W	6.5 mm	89 mm/sec	Argon	Adams (Ref. 259)
Ceramic Tile	850 W	6.5 mm	10.5 mm/sec	Argon	Adams (Ref. 259)
Quartz tubing	600 W	1 mm wall	5 m/min	--	Spalding (Ref. 119)
Quartz	400 W	2	1 m/min	Gas assist	Spalding (Ref. 18)

METAL COMBINATION[a]	REPORTED BY
.003 Tungsten wire .020 Nickel wire	Buddenhagen (1963) (Ref. 261)
20 SiC fibres .005 Nickel wire	Buddenhagen (1963) (Ref. 261)
.0025 Nichrome wire .040 Silver-plated brass	Hice (1963) (Ref 262)
.002-.005 Gold wire Silicon and Al-coated Si	Platte and Smith (1963) (Ref. 263)
.015 Copper wire .015 Tantalum wire	Jackson (1965) (Ref. 264)
.030 Stainless steel wire .025 Tantalum wire	Anderson and Jackson (1965) (Ref. 123)
.005 Tungsten wire .020 Nickel wire	Anderson and Jackson (1965) (Ref. 123)
.020 Nickel wire .025 Tantalum wire	Frick (1966) (Ref. 265)
.015 Copper wire .020 Nickel wire	Frick (1966) (Ref. 265)
.009 Phosph. bronze wire .005 Palladium wire	Orrok (1967) (Ref. 266)
.020 Nichrome wire .140 Monel rod	Orrok (1967) (Ref. 266)
.005-.025 Rene 41 .125 Columbium D36	Orrok (1967) (Ref. 266)
.002-.003 Copper .019 Brass	Barnov and Metashop (1968) (Ref. 138)
.002-.003 Copper .019 Mild steel	Barnov and Metashop (1968) (Ref. 138)
.002-.019 Copper .031 Stainless steel	Barnov and Metashop (1968) (Ref. 138)
.025 Rene 41 .025 Hastalloy X	Kloepper (1970) (Ref. 267)
.031 Titanium wire .016 Gold	Benson (1970) (Ref. 268)
0.1x0.3mm Kovaralloy to 6mm Gold	Velichko et al (1972) (Ref. 140)
Tantalum and Modybdenum	Garashchuk et al (1969) (Ref. 135)
8-1113 steel and 321 stainless steel	Miller and Nunnikhoven (1965) (Ref 129)

(a) decimals indicates thickness in inches unless otherwise mentioned

* after Seretsky and Ryba - Ref. 136

TABLE I - LASER WELDING STUDIES OF DISSIMILAR METALS*

APPENDIX 2

APPENDIX 2

Material	Power (kW)	Thickness (mm)	Width (mm)	Rate (cm/sec)	Remarks	Reference
321 Stainless steel	0.25	0.125 0.250 0.417	0.45 0.70 0.75	3.8 1.48 0.47	Full penetration butt welds in slabs; edge, lap-fillet and corner welds also reported	Webster (Ref. 256)
302 Stainless steel	0.25	0.125 0.203 0.250	0.50 0.50 1.00	2.11 1.27 0.42		
17-7 PH	0.25	0.125	0.45	4.7		
Inconel	0.25	0.100 0.250	0.25 0.45	6.35 1.69		
Nickel	0.25	0.125	0.45	1.48		
Monel	0.25	0.250	0.62	0.64		
Titanium	0.25	0.125 0.250	0.37 0.55	5.90 2.11		
Tin Plated Steel	0.25	0.3	0.64	0.85	Full penetration Lap fillet welds	
1010 Sheet steel	3.9	0.94	--	6.4-5.1	Fillet weld	Banas (Ref. 151)
302 Stainless steel	3.5	12.7	--	2.1	Butt weld	
304 Stainless Steel	17 11.5 9.5 8 20	6 12.5 17 16.5 3.8 5.6 8.9 12.3 8.9 20.3 12.7	1.2 2 4 3.3 2.3	8.4 2.08 1.0 1.26 12.6 8.4 4.2 1.26 1.26 2.11 4.2	Butt weld Butt weld	Locke and Hella (Ref. 83) Locke et al (Ref. 120)
Low carbon steel	4.3	6.4 3.3 1.5		3.6 7.2 11.0	Butt weld, other types of weld reported	Baardsen et al (Ref. 154)
X8 Cr Ni 18 8	1.2	0.5		5	10mm diameter tube wall 5mm thick	Ruffer and Görs (Ref. 113)
Ti-6Al-4V	5.5 5.5 5.5 5.5	6.4 2 1.5 1		2.12 5.93 6.77 6.77	Full penetration Butt weld	Banas (Ref. 164)
Mild steel	2.0	2		2.17	Full penetration butt welds	Regan (Ref. 257)
Stainless steel (18;8)	2.0	3		0.83		
Nimonic 75	2.0 2.0	1.0 2.0		6.0 3.83		

TABLE II

DATA ON PENETRATION WELDING WITH CW CO_2 LASERS

METHOD	SPEED metre/min	ADVANTAGES	DISADVANTAGES
1. Lock seam -solder (L.S.S.)	60-75	a) Fast b) Well tried c) Relatively cheap equipment	a) Uses expensive "Sn" and "Pb" b) Health hazard c) Poor appearance d) Cannot use tin free steel e) Cans cannot be recycled.
2. Draw wall -ironing	comparable to ≈ 70m/min	a) Pleasing appearance b) Thin walls; saves metal for beverage cans c) Recyclable cans d) No filler material required	a) Tool wear b) Cannot make thick wall cans required for food cans. Because food cans have to withstand the pressure due to vacuum sealing c) Cannot use tin free steel
3. Soudronic	25-30 m/min for lap welding 40-50 m/min for H.F. semilap welding	a) Neat b) Fast up to 50 m/min (with frequency tripling) c) Cans can be recycled	a) Electrode problem b) Cannot use tin free steel c) Electrical oscillation problem in the can d) Porosity (Ref. 10, 10)
4. Draw re-draw (DRD)	Comparable to to 70m/min	a) Pleasing appearance b) Thicker walls than DWI c) Can use tin free steel	a) Tool wear
5. Laser weld	7-8 m/min for lap welding of 0.2 mm with 2kW power 10-20 m/min for bead-on-plate welds 0.2mm sheet with 2kW	a) No tool wear b) Pleasing appearance c) No filler materials d) Cans can be recycled e) Can use tin free steel	
6. Laser /arc augmented welds	≈60 m/min bead-on-plate welds	as for laser	a) High special gas shielding problem.

TABLE III

APPENDIX 2

APPENDIX 3

FLOW CHART FOR COMPUTER PROGRAM "LMOD"
SOLVE THREE DIMENSIONAL TEMPERATURE DISTRIBUTION FOR
LASER MATERIALS PROCESSING

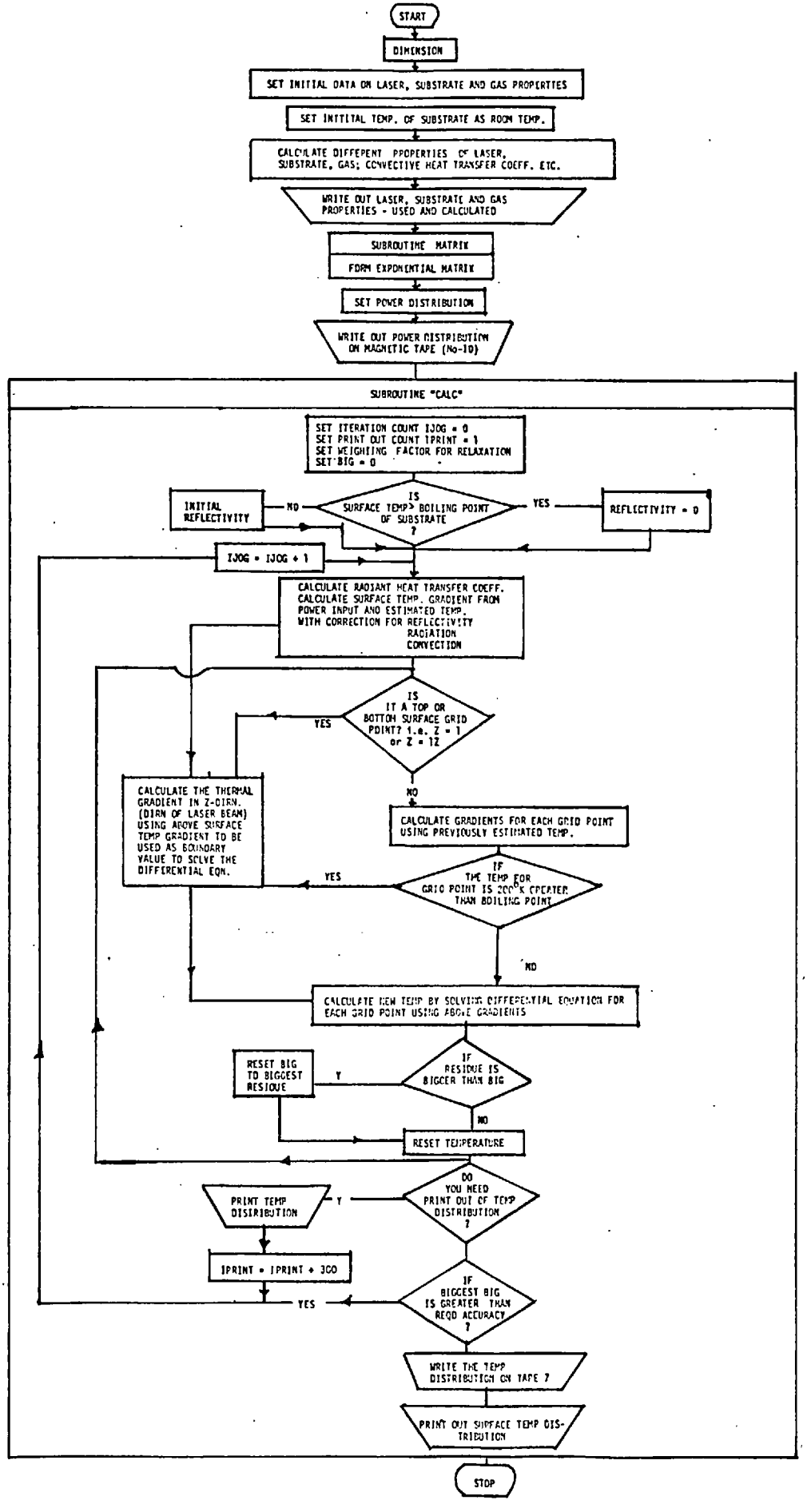

```
0100C ***********************************************************************
0110C * THERMAL CONDUCTION MODEL OF LASER WELDED MATERIAL                    *
0120C   DEVELOPED BY J.MAZUMDER
0130C    LAST MODIFICATION 22ND DEC,1977
0140C    INCORPORATING VELOCITY PREDICTION MODIFICATON
0150C    DATA USED HERE FOR TITANIUM WELD-14
0160C ***********************************************************************
0170C
0180C
0190C
0200C ***********************************************************************
0210C *                                                                     *
0220C *  METHOD OF SOLUTIONOO RELAXATION METHOD                             *
0230C *                                                                     *
0240C *    MATRIX EXPANDING EXPONENTIALLY AND THE LASER BEAM STRIKES*
0250C * THE MATERIAL AT THE TWO THIRD OF THE X- AXIS OF THE MATRIX  *
0260C * AND AT THE MIDLE OF THE Y-AXIS OF THE MATRIX                 *
0270C *                                                                     *
0280C *                                                                     *
0290C *                                                                     *
0300C ***********************************************************************
0310C
0320C
0330C        ***************************************************
0340C        * LIST OF VARIABLE NAMES                          *
0350C
0360C        *                                                 *
0370C        ***************************************************
0380C
0390C
0400C   ALPHA            = THERMAL DIFFUSIVITY----------(M**2)/S
0410C   B                = JET SUBSTRATE DISTANCE -------- M --
0420C   BIG              = LARGEST DIFFERENCE BETWEEN ESTIMATED AND
0430C                      CALCULATED TEMPERATURES ---------- K --
0440C   BPT              = BOILING POINT OF THE SUBSTRATE --- K ---
0450C   COND             = THERMAL CONDUCTIVITY OF SUBSTRATE-- W/M K --
0460C   COUNT            = NUMBER OF ITERATION / STEP
0470C   D                = JET DIAMETER ------ M ---
0480C   DENS             = DENSITY OF SUBSTRATE ---- KG/(M**3) ---
0490C   DR               = RADIAL INCREMENT ---------- M ---------
0500C DLENX = LENGTH OF THE TOTAL MATRIX ------ M ----
0510C DWIDY = WIDTH OF THE TOTAL  MATRIX  ------ M ----
0520C DTHIZ = THICKNESS OF THE TOTAL MATRIX ----M ----
0530C   GCOND            = THERMAL CONDUCTIVITY OF THE GAS ---- W/M K ---
0540C   GCP              = HEAT CAPACITY OF THE GAS ---- J/KG K ----
0550C   GDENS            = DENSITY OF THE GAS AT NTP ---- KG/(M**3) --
0560C   GDIFF            = DIFFUSIVITY OF TITANIUM ---- (M**2)/S
0570C   GRSURF( )        = SURFACE TEMPERATURE GRADIENT
0580C  GRSURFB()         = SURFACE TEMPERATURE GRADIENT AT THE BOTTOM
0590C   GVEL             = VELOCITY OF GAS AT JET EXIT------- M/S ----
0600C   GVISC            = VISCOCITY OF GAS AT NTP ---- N S/(M**2)
0610C   HCONV            = CONVECTIVE HEAT TRANSFER COEFFICIENT-- W/M**2 K
0620C   HRAD             = RADIANT HEAT TRANSFER COEFFICIENT---- W/(M**2)K
0630C   HRADB            = RADIANT HEAT TRANSFER COEFFICIENT AT BOTTOM OF
0640C                      THE PLATE ------ W/(M**2)K
0650C   IBEAM            = NUMBER OF RADIAL MATRIX POINTS OVER WHICH POWER
0660C                      IS INCIDENT
0670C   IOUT             = PRINT ESCAPE
0680C   IPRINT           = NUMBER OF STEPS BETWEEN ANSWER PRINT OUTS
0690C   IX + 1           = NUMBER OF MATRIX POINTS IN X-DIRECTION
0700C   IY + 1           = NUMBER OF MATRIX POINTS IN Y-DIRECTION
0710C   IZ + 1           = NUMBER OF MATRIX POINT IN Z-DIRECTION
0720C   KI,II            = MATRIX POINT OF BEAM CENTER
0730C   LIM              = NUMBER OF PROGRAM STEPS TO BE TAKEN
```

```
0740C     PTOTAL          = TOTAL INCIDENT POWER------ W ------
0750C     RBEAM           = RADIUS OF LASER BEAM ---------- M ------
0760C     REFLEC          = SURFACE REFLECTIVITY
0770C      RHOE           = CONCENTRATION OF VAPOUR AT JET EXIT---- KG/(M**3)
0780C     R(K,I)            = RADIAL DISTANCE FROMC ENTER OF BEAM ---- M ----
0790C     RSTAR()         = DIMENTIONLESS RADIUS
0800C     SIGMA           = STEFFAN - BOLTZMAN CONSTANT
0810C     SPHT            = HEAT CAPACITY OF SUBSTRATE------ J/KG K
0820C     SURFT( )        = SURFACE TEMPERATURE ------- K ----------
0830C     TEMP(K,I,L)     = TEMPERATURE AT LOCATION O- K = X-DIRECTION,
0840C                         I = Y-DIRECTION, L = Z-DIRECTION
0850C     TEMPA           = AMBIENT TEMPERATURE     ------K ------
0860C     TEST            = CONVERGENCY CRITERION
0870C     THETA           = DIMENTIONLESS TIME
0880C     TIMPT      = TITANIUM MELTING POINT IN ---- K----
0890C     STIMPT     = TEMPERATURE OF SUPERHEATED MOLTEN POOL------K------
0900C     TSTAR( )        = DIMENTIONLESS TEMPERATURE
0910C     U               = WELDING SPEED ---------- METERS/SECOND
0920C     W               = WEIGHING FACTOR
0930C     YSTAR( )        = DIMENTIONLESS DEPTH
0940 PROGRAM THECONT(INPUT,OUTPUT,TAPE7,TAPE5=INPUT,TAPE6=OUTPUT,TAPE60,TAPE10)
0950 COMMON/CWSPEED/U
0960 COMMON/CWIDTH/IX,IY,IZ,DLENX,DWIDY,DTHIZ
0970 COMMON/CGEN/SIGMA,PTOTAL,RBEAM,RE
0980 COMMON/CPROP/ALPHA,COND,DENS,SPHT,GVISC,GDENS,GVEL,D,B
0990 COMMON/CSURF/POWER(37,35),REFLEC,HCONV,TEMPA,HRAD(37,35),SURFT(37,35)
1000 COMMON/CGRID/X(37),Y(35),Z(6),R,KI,II
1010 COMMON/CTEMP/TEMP(37,35,6),GRSURF(37,35)
1020 COMMON/CDEP/RHOE,SC,GDIFF
1030 COMMON/COUT/IOUT
1040 COMMON/CREF/REFL(37,35)
1050 DIMENSION HEAD(12)
1060 WRITE(6,110)
1070 110 FORMAT(1H1,10X,*VARIABLE MATRIX*,/5X,*TITANIUM WELD14 VALUES*)
1080C   ***************************************************************
1090C   * SET INITIAL DATA ON * * O LASER BEAM PROPERTIES
1100C   *                       O SUBSTRATE PROPERTIES
1110C   *                       O GAS JET PROPERTIES                  *
1120C   ***************************************************************
1130 IOUT       = 0
1140   DLENX      = 0.15
1150   DWIDY      = 0.10
1160   DTHIZ      = 0.002032
1170 IX     = 32
1180 IY        = 31
1190 IZ        = 4
1200 SIGMA      = 0.0000000567
1210 PTOTAL = 1500.0
1220 REFLEC     = 0.85
1230 RHOE       = 0.000306
1240 RBEAM      =0.000275
1250 GVEL       = 6.2204
1260 GCOND      = 0.148
1270 GCP        = 5191.632
1280 TEMPA      = 300.00
1290 B          = 0.001
1300 BPT = 3500.0
1310 D          = 0.003
1320 SPHT       = 599.96844
1330 DENS       = 4420.0
1340C ..... CONDUCTIVITY VALUE FROM TPRC .........
1350 COND       = 7.3269
1360 GDENS      = 0.1785
1370 GVISC      = 0.00001985
```

```
      U          = 0.0075
      IIX        = IX+1
      IIY        = IY+1
      IIZ        = IZ+1
      DO 100 K=1,IX
      DO 100 I=1,IY
      DO 100 L=1,IZ
      TEMP(K,I,L)  = 300.0
      SURFT(K,I)   = 300.0
      GRSURF(K,I)= 0.0
      X(K)         = 0.0
      Y(I)         = 0.0
      Z(L)         = 0.0
      POWER(K,I)   = 0.0
      HRAD(K,I)    = 0.0
      REFL(K,I)     = REFLEC
  100 CONTINUE
C
C     ***************************************************
C     *   CALCULATION OF PROPERTIES                     *
C     ***************************************************
C
      IBEAM = 5
      ALPHA = COND/(DENS*SPHT)
      WRITE(6,102)DENS,GVISC,GVEL,D,GCP,GCOND,B
  102 FORMAT(10H JET DATA ,/*    GAS DENSITY = *,F10.5,*    GAS VISCOSITY
     +=*,F10.8,*      GAS VELOCITY = *,F10.5,*     JET DIAMETER = *
     +,F10.5,/*    GAS SPECIFIC HEAT = *,F10.6,*  GAS CONDUCTIVITY =*,F10.6,
     +* JET/PLATE DISTANCE =*,F10.4)
      WRITE(6,107) RHOE
  107 FORMAT(* JET EXIT CONCENTRATION = *,F10.8)
      WRITE(6,104)REFLEC,SPHT,DENS,COND,TEMPA,ALPHA
  104 FORMAT (16H SUBSTRATE DATA ,/*   REFLECTIVITY = *,F10.4,*  SUBSTRATE
     + SPHT = *,F10.4,/*  SUBSTRATE DENSITY = *,F10.5,*  SUBSTRATE
     + CONDUCTIVITY=*,F10.4,/*  AMBIENT TEMP =*,F10.5,* THERM DIFFUSIVITY = *,
     +10E9.2)
      WRITE(6,105) PTOTAL,RBEAM
  105 FORMAT (11H LASER DATA,/*    TOTAL POWER =*,F10.4,*   BEAM RADIUS =*,
     + F10.6)
      RE=(GDENS*GVEL*D)/GVISC
      PR=GCP*GVISC/GCONO
      WRITE(6,103) RE,PR,RBEAM
  103 FORMAT (*  RE NO = *,F10.2,*  PR NO = *,F10.4,*  BEAM RADIUS =*,
     +F10.6)
      HCONV = 13.0*(RE**0.5)*(PR**0.33 *GCONO/B
      KI         = ((IX+1)/3)
      II     = ((IY+1)/2)
C     ***************************************************
C     *   SET UP MATRIX POINTS      *********************
C     ***************************************************
C
      CALL MATRIX
C
C     ***************************************************
C     *    SET   UP  GAUSSIAN   POWER   DISTRIBUTION    *
C     ***************************************************
C
      IRBEAM = 2*IBEAM
      DO  101 K=1,IX
      DO  101 I=1,IY
      R        = SQRT((X(K)-X(KI))**2 + (Y(I)-Y(II))**2)
      GK = ((R**2)/(RBEAM**2))
      IF(GK.GT.20.0) GO TO 190
      GAUSK  = 1.0/EXP(GK)
```

```
2020 POWER(K,I)    = (PTOTAL*GAUSK)/(3.142*(RBEAM**2))
2030 GO TO 101
2040 190 CONTINUE
2050 POWER(K,I) = 0.0
2060 101 CONTINUE
2070 WRITE(10) IZ,IX,IY,((POWER(K,I),K=1,IX),I=1,IY)
2080C
2090C   ***********************************************
2100C   *    MAIN    CALCULATION     CYCLE     *******
2110C   ***********************************************
2120C
2130    CALL  CALC
2140    STOP
2150    END
2160C
2170C   ***************************************************************
2180C   *                                                             *
2190C   *     SUBROUTINE  MATRIX  OO  TO  FORM   MATRIX               *
2200C   *                                                             *
2210C   ***************************************************************
2220C
2230 SUBROUTINE MATRIX
2240 COMMON/CWSPEED/U
2250 COMMON/CWIDTH/IX,IY,IZ,OLENX,OWIDY,OTHIZ
2260 COMMON/CGEN/SIGMA,PTOTAL,RBEAM,RE
2270 COMMON/CPROP/ALPHA,CONO,OENS,SPHT,GVISC,GOENS,GVEL,D,B
2280 COMMON/CSURF/POWER(37,35),REFLEC,HCONV,TEMPA,HRAO(37,35),SURFT(37,35)
2290 COMMON/CGRIO/X(37),Y(35),Z(6),R,KI,II
2300 COMMON/CTEMP/TEMP(37,35,6),GRSURF(37,35)
2310 COMMON/COEP/RHOE,SC,GOIFF
2320 COMMON/COUT/IOUT
2330 COMMON/CREF/REFL(37,35)
2340C
2350C     OOOOOOOOOOOOOOOOOOOOOOOOOOOOOOOOOOOOOOOOOOOOOOOOOOOOOOOO
2360C     O   CALCULATION  OF  EXPONENTIAL X-Y-Z   MATRIX      O
2370C     O.....................................................O
2380C
2390 ITP = 9
2400C ITP IS NO OF MATRIX POINT UNOER BEAM IN EACH X - Y OIRECTIN
2410 IBP = ITP/2
2420 KI = ((IX+1)/3)
2430 II = ((IY+1)/2)
2440C WIDTH CO-ORDINATES>>Y-DIRECTION WITH ITP POINTS WITHIN BEAM AND OF
2450C SPECIFIC OVERALL SIZE OWIOY
2460 KW = OWIOY/(2.*RBEAM
2470 MII = II-1
2480 AY = (FLOAT(MII-IBP))/ALOG(FLOAT(KW))
2490 ORY = RBEAM/EXP(FLOAT(IBP)/AY)
2500 Y(II) = 0.0
2510 OO 300 J=1,MII
2520 JP = II+J
2530 JM = II-J
2540 AJ = J
2550 Y(JP) = ORY*EXP(AJ/AY)
2560 Y(JM) = -Y(JP)
2570 300 CONTINUE
2580C
2590C LENGTH CO-ORDINATES>>X-DIRECTION WITH ITP POINTS WITHIN THE BEAM
2600C AND OF SPECIFIED OVERALL SIZE OLENX
2610C
2620 KL = OLENX/(3.*RBEAM
2630 KTL = 2*KL
2640 MIX = KI-1
2650 AX = (FLOAT(MIX-IBP))/ALOG(FLOAT(KL))
```

```
2650 DRX = RBEAM/EXP(FLOAT(IBP)/AX)
2670 X(KI) = 0.0
2680 DO 301 J=1,MIX
2690 AJ = J
2700 MOX = (KI-J)
2710 X(MOX) = -DRX*EXP(AJ/AX)
2720 301 CONTINUE
2730 KII = KI+1
2740 KIX = IX-KI
2750 BX = (FLOAT(KIX-IBP))/ALOG(FLOAT(KTL))
2760 DBX =RBEAM/EXP(FLOAT(IBP)/BX)
2770 DO 302 J = KII,IX
2780 AJ = J-KI
2790 X(J) = DBX*EXP(AJ/BX)
2800 302 CONTINUE
2810C
2820C DEPTH CO-ORDINATES>> Z-DIRECTION WITH SPECIFIED THICKNESS DTHIZ
2830C
2840 KIZ = IZ-1
2850 DRZ = DTHIZ/(EXP(FLOAT(KIZ)))
2860 Z(1) = 0.0
2870 DO 303 J=2,IZ
2880 KT = J-1
2890 Z(J) = DRZ*(EXP(FLOAT(KT)))
2900 303 CONTINUE
2910 WRITE (6,305) ITP
2920 305 FORMAT(2X,*ITP=*,I3,/5X,*X-COORDINATE - METER *)
2930 WRITE(6,306) (X(K),K=1,IX)
2940 306 FORMAT(10G10.3)
2950 WRITE(6,307)
2960 307FORMAT(5X,*Y-COORDINATE - METER *)
2970 WRITE(6,308) (Y(K),K=1,IY)
2980 308 FORMAT (10G10.3)
2990 WRITE(6,309)
3000 309 FORMAT(5X,*Z-COORDINATE - METER* )
3010 WRITE(6,310) (Z(IS),IS=1,IZ)
3020 310 FORMAT (10G10.3)
3030 RETURN
3040 END
3050C
3060C  ************************************************************
3070C  *                                                          *
3080C  * SUBROUTINE CALC == MAIN CALCULATION                      *
3090C  ************************************                       *
3100C  ************************************************************
3110C
3120 SUBROUTINE CALC
3130 COMMON/CWSPEED/U
3140 COMMON/CWIDTH/IX,IY,IZ,DLENX,DWIDY,DTHIZ
3150 COMMON/CGEN/SIGMA,PTOTAL,RBEAM,RE
3160 COMMON/CPROP/ALPHA,COND,DENS,SPHT,GVISC,GDENS,GVEL,D,B
3170 COMMON/CSURF/POWER(37,35),REFLEC,HCONV,TEMPA,HRAD(37,35),SURFT(37,35)
3180 COMMON/CGRID/X(37),Y(35),Z(6),R,KI,II
3190 COMMON/CTEMP/TEMP(37,35,6),GRSURF(37,35)
3200 COMMON/CDEP/RHOE,SC,GDIFF
3210 COMMON/COUT/IOUT
3220 COMMON/CREF/REFL(37,35)
3230 DIMENSION GRSURFB(37,35),HRADB(37,35)
3240 WRITE(6,275)PTOTAL,REFLEC,DLENX,DWIDY,DTHIZ
3250 275 FORMAT(2X,/2X,*PTOTAL=*,F10.4,/2X,*REFLECTIVITY=*,F10.4,/2X,
3260+*LENGTH=*,E12.6,*WIDTH=*,E12.6,*THICKNESS=*,E12.6)
3270C  ************************************************************
3280C  * SET LIMIT ON NUMBER OF CALCULATION  STEPS                 *
3290C  *                                                          *
```

```
3300C   * STATEMENT NUMBER 230 IS STEP LOOP                          *
3310C   * STATEMENT NUMBER 220 IS ITERATION LOOP                     *
3320C   *                                                           *
3330C   ***********************************************************
3340C
3350 IPRINT=1
3360 IJOG = 0
3370 NUJOG = 101
3380 WW = 40.
3390 W = 128.0
3400 220 CONTINUE
3410 BIG1 = 0.0
3420 BIG2 = 0.0
3430 IJOG = IJOG + 1
3440 BPT = 3500.0
3450 BPTK  = BPT + 200.0
3460 TIMPT = 1950.0
3470 STIMPT = 1950.0 + 200.0
3480C
3490C  ***************************************************************
3500C  *   CALCULATION OF SURFACE GRADIENTS                          *
3510C  ***************************************************************
3520C
3530 DO 201 K=1,IX
3540 DO 201 I=1,IY
3550 IF(SURFT(K,I).GT.BPT)REFL(K,I)=0.0
3560 HRAD(K,I) = SIGMA*(1.-REFL(K,I))*((SURFT(K,I))**2+(TEMPA)**2)*((
3570+SURFT(K,I))+(TEMPA))
3580 HRADB(K,I)= SIGMA*(1.-REFL(K,I))*((TEMP(K,I,IZ))**2+(TEMPA**2)
3590+ *(TEMP(K,I,IZ)+TEMPA))
3600 GRSURF(K,I)= -((POWER(K,I)*(1.-REFL(K,I)))-(HCONV+HRAD(K,I))*(SURFT(K,I)
3610+ -TEMPA))/(COND)
3620 GRSURFB(K,I) = -(HCONV+HRADB(K,I))*(TEMPA-TEMP(K,I,IZ))/COND
3630 201 CONTINUE
3640C
3650C    OOOOOOOOOOOOOOOOOOOOOOOOOOOOOOOOOOOOOOOOOOOOOOOOOOOOOOOO
3660C    O  CALCULATION OF FINITE DIFFERENCE  TERMS      OOOOOOOO
3670C    O.....................................................O
3680C
3690C
3700C   DO LOOP FOR MAIN CALCULATION CYCLE FOR FINITE DIFFERENCE TERMS
3710C WITH PROVISION FOR KEYHOLE FORMATION
3720 DO 202 L = 1,IZ
3730 DO 203 I = II,IY
3740 DO 204 K = 1,IX
3750 KJ = K-1
3760 KM = K+1
3770 IJ = I-1
3780 IM = I+1
3790 LJ = L-1
3800 LM = L+1
3810 IF(K.EQ.1) GO TO 205
3820 IF(K.EQ.IX) GOTO 206
3830 DXEF = (2.*ALPHA/(X(KM)-X(KJ)))*((TEMP(KM,I,L)-TEMP(K,I,L))/(X(KM
3840+-X(K)))
3850 DXWF = (2.*ALPHA/(X(KM)-X(KJ)))*((TEMP(K,I,L)-TEMP(KJ,I,L))/(X(K)-
3860+X(KJ)))
3870 XW = ((X(KM)-X(KJ))/2.0)
3880 GO TO 207
3890 205 CONTINUE
3900 DXEF = (ALPHA/(X(KM)-X(K)))*((TEMP(KM,I,L)-TEMP(K,I,L))/(X(KM)-X(K)))
3910 DXWF = (ALPHA/(X(KM)-X(K)))*((TEMP(K,I,L)-TEMPA)/(X(KM)-X(K)))
3920 XW   = (X(KM)-X(K))
3930 GO TO 207
```

```
3940 206 CONTINUE
3950 DXEF = (ALPHA/(X(K)-X(KJ)))*((TEMPA-TEMP(K,I,L))/(X(K)-X(KJ)))
3960 DXWF = (ALPHA/(X(K)-X(KJ)))*((TEMP(K,I,L)-TEMP(KJ,I,L))/(X(K)-X(KJ)))
3970 XW = (X(K)-X(KJ))
3980 207 CONTINUE
3990 IF(I.EQ.1)  GO TO 208
4000 IF(I.EQ.IY) GO TO 209
4010 DYSF = (2.*ALPHA/(Y(IM)-Y(IJ)))*((TEMP(K,IM,L)-TEMP(K,I,L))/(Y(IM)-Y(I)))
4020 DYNF = (2.*ALPHA/(Y(IM)-Y(IJ)))*((TEMP(K,I,L)-TEMP(K,IJ,L))/(Y(I)-Y
4030+(IJ)))
4040  YW = ((Y(IM)-Y(IJ))/2.0)
4050 GO TO 210
4060 208 CONTINUE
4070 DYSF = (ALPHA/(Y(IM)-Y(I)))*((TEMP(K,IM,L)-TEMP(K,I,L))/(Y(IM)-Y(I)))
4080 DYNF = (ALPHA/(Y(IM)-Y(I)))*(TEMP(K,I,L)-TEMPA)/(Y(IM)-Y(I))
4090 YW   = (Y(IM)-Y(I))
4100 GO TO 210
4110 209 CONTINUE
4120 DYSF = (ALPHA/(Y(I)-Y(IJ)))*((TEMPA-TEMP(K,I,L))/(Y(I)-Y(IJ)))
4130 DYNF = (ALPHA/(Y(I)-Y(IJ)))*((TEMP(K,I,L)-TEMP(K,IJ,L))/(Y(I)-Y(IJ)))
4140 YW = (Y(I)-Y(IJ))
4150 210 CONTINUE
4160 IF(L.EQ.1)  GO TO 211
4170 IF(L.EQ.IZ) GO TO 212
4180 DZDF = (2.*ALPHA/(Z(LM)-Z(LJ)))*((TEMP(K,I,L)-TEMP(K,I,LJ))/(Z(L)-Z(LJ)))
4190 DZIF = (2.*ALPHA/(Z(LM)-Z(LJ)))*((TEMP(K,I,LM)-TEMP(K,I,L))/(Z(LM)-Z(L)))
4200 IF(TEMP(K,I,LJ).GT.BPTK)DZDF=(ALPHA*GRSURF(K,I))/(Z(LM)-Z(L))
4210 ZW = ((Z(LM)-Z(LJ))/2.0)
4220 GO TO 213
4230 211 CONTINUE
4240 DZDF = (ALPHA*GRSURF(K,I))/(Z(LM)-Z(L))
4250 DZIF = (ALPHA/(Z(LM)-Z(L)))*((TEMP(K,I,LM)-TEMP(K,I,L))/(Z(LM)-Z(L)))
4260 ZW = (Z(LM)-Z(L))
4270 GO TO 213
4280 212 CONTINUE
4290 DZDF = (ALPHA/(Z(L)-Z(LJ)))*((TEMP(K,I,L)-TEMP(K,I,LJ))/(Z(L)-Z(LJ)))
4300 DZIF = (ALPHA/(Z(L)-Z(LJ)))*GRSURFB(K,I)
4310 IF(TEMP(K,I,LJ).GT.BPTK)DZDF=(ALPHA*GRSURF(K,I))/(Z(L)-Z(LJ))
4320 ZW = (Z(L)-Z(LJ))
4330 213 CONTINUE
4340 IF(K.EQ.1)  GOTO  214
4350 IF(K.EQ.IX) GO TO 215
4360 DXEC = (2.*U/(X(KM)-X(KJ)))*((TEMP(KM,I,L)+TEMP(K,I,L))/2.)
4370 DXWC = (2.*U/(X(KM)-X(KJ)))*((TEMP(K,I,L)+TEMP(KJ,I,L))/2.)
4380 GO TO 216
4390 214 CONTINUE
4400 DXEC = (U/(X(KM)-X(K)))*((TEMP(KM,I,L)+TEMP(K,I,L))/2.)
4410 DXWC = (U/(X(KM)-X(K)))*((TEMP(K,I,L)+TEMPA)/2.0)
4420 GO TO 216
4430 215 CONTINUE
4440 DXEC = (U/((X(K)-X(KJ))))*((TEMPA+TEMP(K,I,L))/2.0)
4450 DXWC = (U/((X(K)-X(KJ))))*((TEMP(K,I,L)+TEMP(KJ,I,L))/2.0)
4460 216 CONTINUE
4470 RESDU = -DXWF-DYNF-DZDF+DXWC+DXEF+DYSF+DZIF-DXEC
4480 RES1 = RESDU/YW
4490 TW = (3.0*ALPHA/(XW**2 + YW**2 + ZW**2))
4500C IF(ABS(RES1).GT.ABS(BIG1)) GO TO 260
4510C GO TO 261
4520C 260 WRITE(6,262)K,I,L,TEMP(K,I,L)
4530C 262 FORMAT(2X,*K,I,AND L=*,3I3,5X,*TEMP=*,G12.6)
4540C 261 CONTINUE
4550 IF(ABS(RES1).GT.BIG1) BIG1=ABS(RES1)
4560 TEMP(K,I,L) = TEMP(K,I,L) + RES1/W
4570 SURFT(K,I) = TEMP(K,I,1)
```

```
4580C IF(I.NE.15.AND.I.NE.30) GO TO 204
4590C  PRINT 5,RES1,GRSURFB(K,I),GRSURF(K,I),TEMP(K,I,L),DZIF,DZOF,DXWF,
4600C+DXEF,DYNF,DYSF,K,I,L,DXWC,DXEC
4610C  5 FORMAT(2X,*RES1*,3G11.4,*TEMP*,7G11.4,3I3,/*DXWC*,G12.4,*DXEC*,G12.4)
4620 204 CONTINUE
4630 203 CONTINUE
4640 202 CONTINUE
4650 DO 502 L=1,IZ
4660 FOR 503 I = II,1
4670 DO 504 K = 1,IX
4680 KJ = K-1
4690 KM = K+1
4700 IJ = I-1
4710 IM = I+1
4720 LJ = L-1
4730 LM = L+1
4740 IF(K.EQ.1) GO TO 505
4750 IF(K.EQ.IX) GOTO 506
4760 DXEF = (2.*ALPHA/(X(KM)-X(KJ)))*((TEMP(KM,I,L)-TEMP(K,I,L))/(X(KM)
4770+-X(K)))
4780 DXWF = (2.*ALPHA/(X(KM)-X(KJ)))*((TEMP(K,I,L)-TEMP(KJ,I,L))/(X(K)-
4790+X(KJ)))
4800 XW = ((X(KM)-X(KJ))/2.0)
4810 GO TO 507
4820 505 CONTINUE
4830 DXEF = (ALPHA/(X(KM)-X(K)))*((TEMP(KM,I,L)-TEMP(K,I,L))/(X(KM)-X(K)))
4840 DXWF = (ALPHA/(X(KM)-X(K)))*((TEMP(K,I,L)-TEMPA)/(X(KM)-X(K)))
4850 XW  = (X(KM)-X(K))
4860 GO TO 507
4870 506 CONTINUE
4880 DXEF = (ALPHA/(X(K)-X(KJ)))*((TEMPA-TEMP(K,I,L))/(X(K)-X(KJ)))
4890 DXWF = (ALPHA/(X(K)-X(KJ)))*((TEMP(K,I,L)-TEMP(KJ,I,L))/(X(K)-X(KJ)))
4900 XW = (X(K)-X(KJ))
4910 507 CONTINUE
4920 IF(I.EQ.1)  GO TO 508
4930 IF(I.EQ.IY) GO TO 509
4940 DYSF = (2.*ALPHA/(Y(IM)-Y(IJ)))*((TEMP(K,IM,L)-TEMP(K,I,L))/(Y(IM)-Y(I)))
4950 DYNF = (2.*ALPHA/(Y(IM)-Y(IJ)))*((TEMP(K,I,L)-TEMP(K,IJ,L))/(Y(I)-Y
4960+(IJ)))
4970  YW = ((Y(IM)-Y(IJ))/2.D)
4980 GO TO 510
4990 508 CONTINUE
5000 DYSF = (ALPHA/(Y(IM)-Y(I)))*((TEMP(K,IM,L)-TEMP(K,I,L))/(Y(IM)-Y(I)))
5010 DYNF = (ALPHA/(Y(IM)-Y(I)))*(TEMP(K,I,L)-TEMPA)/(Y(IM)-Y(I))
5020 YW   = (Y(IM)-Y(I))
5030 GO TO 510
5040 509 CONTINUE
5050 DYSF = (ALPHA/(Y(I)-Y(IJ)))*((TEMPA-TEMP(K,I,L))/(Y(I)-Y(IJ)))
5060 DYNF = (ALPHA/(Y(I)-Y(IJ)))*((TEMP(K,I,L)-TEMP(K,IJ,L))/(Y(I)-Y(IJ)))
5070 YW = (Y(I)-Y(IJ))
5080 510 CONTINUE
5090 IF(L.EQ.1)  GO TO 511
5100 IF(L.EQ.IZ) GO TO 512
5110 DZOF = (2.*ALPHA/(Z(LM)-Z(LJ)))*((TEMP(K,I,L)-TEMP(K,I,LJ))/(Z(L)-Z(LJ)))
5120 DZIF = (2.*ALPHA/(Z(LM)-Z(LJ)))*((TEMP(K,I,LM)-TEMP(K,I,L))/(Z(LM)-Z(L)))
5130 IF(TEMP(K,I,LJ).GT.BPTK)DZOF=(ALPHA*GRSURF(K,I))/(Z(LM)-Z(L))
5140 ZW = ((Z(LM)-Z(LJ))/2.0)
5150 GO TO 513
5160 511 CONTINUE
5170 DZOF = (ALPHA*GRSURF(K,I))/(Z(LM)-Z(L))
5180 DZIF = (ALPHA/(Z(LM)-Z(L)))*((TEMP(K,I,LM)-TEMP(K,I,L))/(Z(LM)-Z(L)))
5190 ZW = (Z(LM)-Z(L))
5200 GO TO 513
5210 512 CONTINUE
```

```
      DZDF = (ALPHA/(Z(L)-Z(LJ)))*((TEMP(K,I,L)-TEMP(K,I,LJ))/(Z(L)-Z(LJ)))
      DZIF = (ALPHA/(Z(L)-Z(LJ)))*GRSURFB(K,I)
      IF(TEMP(K,I,LJ).GT.BPTK) DZDF=(ALPHA*GRSURF(K,I))/(Z(L)-Z(LJ))
      ZW = (Z(L)-Z(LJ))
  513 CONTINUE
      IF(K.EQ.1)  GOTO  514
      IF(K.EQ.IX) GO TO 515
      DXEC = (2.*U/(X(KM)-X(KJ)))*((TEMP(KM,I,L)+TEMP(K,I,L))/2.)
      DXWC = (2.*U/(X(KM)-X(KJ)))*((TEMP(K,I,L)+TEMP(KJ,I,L))/2.)
      GO TO 516
  514 CONTINUE
      DXEC = (L/(X(KM)-X(K)))*((TEMP(KM,I,L)+TEMP(K,I,L))/2.)
      DXWC = (U/(X(KM)-X(K)))*((TEMP(K,I,L)+TEMPA)/2.0)
      GO TO 516
  515 CONTINUE
      DXEC = (U/((X(K)-X(KJ))))*((TEMPA+TEMP(K,I,L))/2.0)
      DXWC = (U/((X(K)-X(KJ))))*((TEMP(K,I,L)+TEMP(KJ,I,L))/2.0)
  516 CONTINUE
      RESDU = -DXWF-DYNF-DZDF+DXWC+DXEF+DYSF+DZIF-DXEC
      RES2 = RESDU/W
      TW = (3.0*ALPHA/(XW**2 + YW**2 + ZW**2))
C     IF(ABS(RES2).GT.ABS(BIG2)) GO TO 520
C     GO TO 521
C 520 WRITE(6,522)  K,I,L,TEMP(K,I,L)
C 522 FORMAT(2X,*K,I AND L=*,3I3,5X,*TEMP=*,G12.6)
C 521 CONTINUE
      IF(ABS(RES2).GT.BIG2)  BIG2=ABS(RES2)
      TEMP(K,I,L) = TEMP(K,I,L) + RES2/W
      SURFT(K,I) = TEMP(K,I,1)
C     IF(I.NE.15.AND.I.NE.30) GO TO 504
C     PRINT 5,RES2,GRSURFB(K,I),GRSURF(K,I),TEMP(K,I,L),DZIF,DZDF,DXWF,
C    +DXEF,DYNF,DYSF,K,I,L,DXWC,DXEC
C   5 FORMAT(2X,*RES2*,3G11.4,*TEMP*,7G11.4,3I3,/*DXWC*,G12.4,*DXEC*,G12.4
  504 CONTINUE
  503 CONTINUE
  502 CONTINUE
      BIG  = AMAX1(ABS(BIG1),ABS(BIG2))
      RES = AMAX1(ABS(RES1),ABS(RES2))
      PRINT 6,IJOG,W,TW,RES,BIG
    6 FORMAT(5X,*IJOG*,I3,* W*,G10.4,* TW*,G10.4,* RES*,G10.4,* BIG*,G10.4)
C     WRITE(60) (((TEMP(K,I,L),K=1,IX),I=1,IY),L=1,IZ)
C     IF(IJOG.EQ.NUJOG.AND.TEMP(KI,II,IZ).GT.STIMPT)U = U + 0.001
      IF(IJOG.NE.NUJOG) GO TO 519
      NUJOG = NUJOG + 20
  519 IF(IJOG.EQ.101) GO TO 517
      IF(IJOG.EQ.IPRINT) GO TO 517
      GO TO 518
  517 WRITE(6,250) IJOG
  250 FORMAT(2X,*TEMPERATURE DISTRIBUTION AT ITERATION LOOP=*,I5,//)
      DO 251 L=1,IZ
      DO 252 I=1,IY
      WRITE(6,253)L,I,(TEMP(K,I,L),K=1,IX)
  253 FORMAT(2X,*L=*,I3,*I=*,I3,8(2X,G10.4))
  252 CONTINUE
  251 CONTINUE
      IPRINT = IPRINT+300
  518 IF(BIG.GT.1200.0) GO TO 220
C
C     ***********************************************************
C     *  STORE  FINAL  ARRAY FOR FURTHER  RUNS        ***********
C     ***********************************************************
C
      WRITE(7) (((TEMP(K,I,L),K=1,IX),I=1,IY),L=1,IZ)
      WRITE(6,280)PTOTAL,U,DTHIZ,RBEAM
```

```
5860 280 FORMAT(2X,//5X,*TOTAL POWER = *,F10.4,/5X,*WELDING SPEED =*,F10.7,/
5870+5X,*SHEET THICKNESS=*,F12.8,/5X,*BEAM RADIUS =*,F12.8,//)
5880 WRITE(6,285) IJOG
5890 285 FORMAT(2X,*TEMPERATURE DISTRIBUTION AT ITERATION LOOP =*,I5,//)
5900 DO 290 L=1,IZ
5910 DO 291 I=1,IY
5920 WRITE(6,292)L,I,(TEMP(K,I,L),K=1,IX)
5930 292 FORMAT(2X,*L=*,I3,*I=*,I3,8(2X,G10.4))
5940 291 CONTINUE
5950 290 CONTINUE
5960 RETURN
5970 END
```

APPENDIX 4

Principal characteristics of commercially available lasers(a)

Laser	Principal output wavelengths (μm)	CW output		Pulsed output*				Beam diameter between $1/e^2$ points (mm)	Beam divergence (half angle) millirad	Efficiency per cent	Comments
		Output power		Pulse energy (J)		Peak pulse power (W)	Pulse width (μs)				
		TEM_{00}	Multimode	TEM_{00}	Multimode						
Ruby	0·6943	0·025	—	1	4×10^2	10^8	3×10^{-3}–10^3	2–20	0·3–5	<0·1	High power pulsed output in visible region. Applications in holography, ophthalmology, fabrication
Nd^{3+} YAG glass	1·06	0·25–25	$1–10^3$	2×10^{-3}–3	1×10^{-3}–6.5×10^2	10^6	1×10^{-2}–7×10^3	1–25	0·15–7·5	>1	High efficiency pulsed and CW outputs. Applications for range-finding and fabrication processes
Helium–neon	0·6328	6×10^{-5}–7.5×10^4	1×10^{-4}–1.5×10^{-1}	—	—	—	—	0·73–10	0·125–3	<0·1	Low cost, visible output. Used for surveying, metrology, holography
	1·152	0.3×10^{-3}–1×10^{-3}	—	—	—	—	—	0·8–1·5	0·5–0·75	<0·1	
	3·391	1.5×10^{-3}	—	—	—	—	—	1·2–2	0·35–1·5	<0·1	
Helium cadmium	0·325–0·4416	2×10^{-2}–5×10^{-2}	5×10^{-2}	—	—	—	—	0·8–2·5	0·25–1	—	
Argon	0·3511–0·5145	1×10^{-3}–10	1.5×10^{-3}–15	2.5×10^{-6}–2.6×10^{-4}	1.5×10^{-5}–10^{-3}	—	2–10^2	0·65–4	0·25–1	<0·1	High power CW output tunable over visible and near UV. Uses include ophthalmology, holography
Krypton	0·3507–0·7993	2×10^{-3}–4	—	2×10^{-5}	6×10^{-3}	—	40	1·4–4	0·25–0·5	<0·1	High power CW output tunable over visible and near UV
Xenon	0·3645–0·5395	—	4×10^{-6}	—	9×10^{-5}–2×10^{-4}	—	0·3–1	2·4–4	1–2·75	<0·1	Pulsed output in visible region used for trimming thick and thin film circuits
Nitrogen	0·3371	—	—	—	3×10^{-6}–6×10^{-2}	—	3×10^{-3}–1×10^{-2}	2·5	0·38–1·5	—	High power pulsed output in near UV. Used for pumping some dye lasers
Carbon monoxide	5·2–5·7	—	—	—	10^{-3}–10^{-1}	—	0·1–0·25	5	1	—	
Carbon dioxide	9·2–10·8	$3–10^3$	$3–10^4$	4×10^{-3}–10^2	$1–2 \times 10^2$	—	0·1–10^7	0·8–25	0·25–4	>10	High power output at high efficiency. Used for cutting and welding
Organic dyes	0·2650–0·9600	2×10^{-1}	—	—	2×10^3	2×10^8	—	2–5	0·2–3	<0·1	Output tunable over broad range. Applications in spectroscopy, pollution detection, etc.
Gallium arsenide	0·85–0·905	—	1	—	5×10^{-6}	24†	0·1–1	$0.2.10^{-3} \times 40.10^{-3}$‡	200	1–40	Small size but high divergence. Uses include range-finding and pollution detection

* Normal operating mode.
† At room temperature.
‡ Dimensions of emitting region

(a) After Harry, Ref. 15, p69

APPENDIX 5

The lasing action of CO_2 laser was first reported by C.K.N. Patel[207-209]. The basic principle is given below.

CO_2 Laser Theory[271]

Only the electronic ground state is of interest for a CO_2 laser Thus, molecular translation, vibration and rotation are the principal forms of energy storage and interchange. The important energy levels of the molecule are shown in illustration A. Carbon dioxide is a linear, symmetric molecule with the carbon atom balanced against the two oxygen atoms, O-C-O. Therefore, characteristic vibrational modes exist; the symmetric mode, where the two oxygen atoms vibrate against each other; the bending mode, where the carbon atom moves out of the molecular axis, thus bending the molecule; and the asymmetric modes, where the two oxygen atoms oscillate against the carbon atom. Each of these vibrating modes is quantised, and the particular vibrational state of the molecule is designated by three integral numbers. The first number is the quantum level or excitation number of the symmetric mode. The second number is the exictation number of the bending mode; and the third number is the excitation number of the asymmetric mode. Only the energy levels of the pure modes are given, but all the mixed vibrational states exist as well (for example 111).

Each and every vibrational state is degenerate or further subdivided into a whole series of levels brought about by gross rotation of the vibrating molecule. These levels are also quantized and designated by J, the rotational quantum number. They are shown in illustration B on an expanded energy scale for the 001 and 100 vibrational level. The lasing transition at 10.6μm a simultaneous change of the vibrational and rotational quantum states. However, this may occur on any one of a number of rotational transitions. The selection rules for the vibrational rotational transition are that J must change by $\pm$ 1. The transitions where J increases 1 are called P-branch transition (e.g. P10) and that where decreases are called R-branch transitions (e.g. R10). The wavelength associated with the dominant transitions are P18-10.57μ , P20-10.59μ , P22-10.61μ etc. When the inversion of the total vibrational level occurs because of the discharge, then P

branch transitions have more gain than their R counterpart. Since P and R transitions compete with each other, the medium lases only on the P branches unless special precuations are taken. Those P branches which have the highest gain are most likely to show lasing action.

Excitation and de-excitation vibrational levels

Experiments show that inversion is not a result of direct electronic excitation but is caused by vibrational energy interchange between N_2 and CO_2. The lowest vibrational level of N_2 is essentially metastable since the molecule is symmetric and cannot vibrate. In a nitrogen discharge, about 20-30 per cent of molecules are vibrationally excited. The energy level of $\nu = 1$ matches the level of the 001 state of CO_2 within 2mV., as illustrated at A (well within the thermal energy spread of about 25mV). When the two gases are mixed effective resonance collisional transfer occurs between the two states. Also, the second level of N_2 matches the 002 mode of CO_2 and on up the ladder. The net result is that the asymmetric ladder 00_n, becomes highly excited, or it has a high vibrational temperature.

The lower laser level and associated symmetric ladder is not excited by N_2 because there are no energy resonances. However, when the laser is operative, the 100 mode and its chain becomes heavily populated. This chain cannot radiate to the ground state and can only radiate weakly to the lower bending modes. However, there is a close Fermi resonance of the 100 mode with the 020 mode, and collisions can cause this transition.

The addition of helium gas helps to increase laser power. Its low mass makes it effective in trading its kinetic energy with the molecule internal energy modes for small energy changes.

As a result, the helium is effective in

(i) Cooling the CO_2 rotational temperature (but not the vibrational temperature).

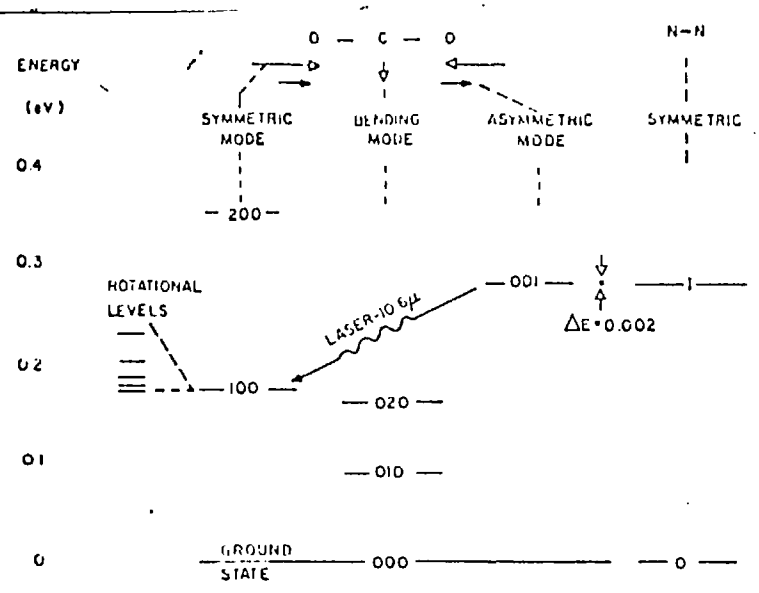

A. CO_2 energy level diagram.

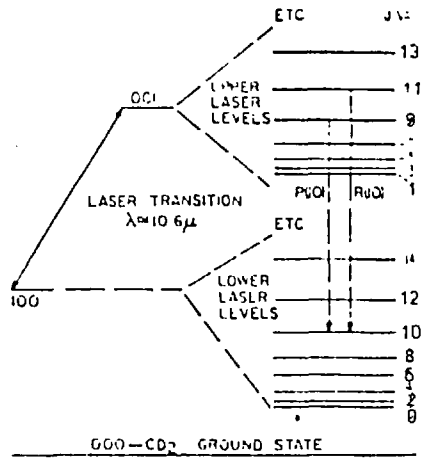

B. Rotational levels of the vibrating molecule, on expanded scale for 001 and 100 vibrational levels.

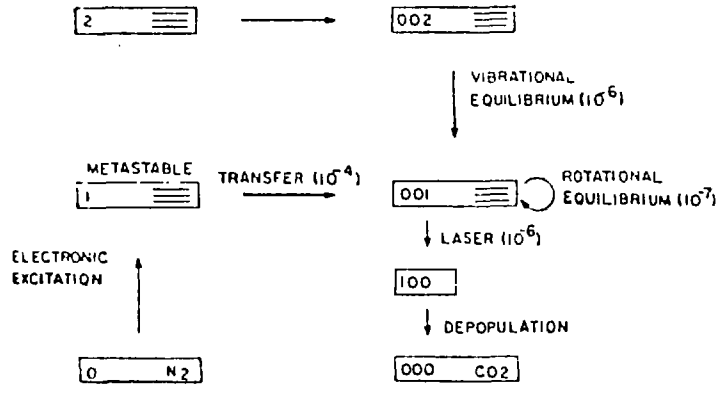

C Important collision lifetimes in a He-N_2-CO_2 system.

(ii) Increasing the thermal conduction to the wall (thus keeping the translational temperature low, the Doppler width small, and the gain high).

(iii) Increasing the depopulation rate of the 010 level of CO_2 which in turn depopulates the 100 lower level. This is because the 010, 020, and 100 levels are all strongly coupled together through resonant collisions.

The important lifetimes in the CO_2 laser are practically all determined by collisional phenomena. The radiative lifetimes vary from a few milliseconds to a few seconds, whereas the mean free time between molecules collision is of the order of 10^{-8} to 10^{-7} sec. These times must then be scaled up by the number of collisions needed to effect a certain energy transfer. The important transfer times are summarised in illustration C, where the partial pressures normally used in the CO_2 lasers are assumed.

APPENDIX 6

ANALYSIS OF PHOTON DRAG CONVOLUTES FOR CO_2 LASER BEAM

Photon drag detector trace of laser beam can be analysed by the Harker method of numerical evaluation of the detector trace function as described by Sanderson[269]. But the main limitation is to analyse the beam basic assumption in that the beam is axisymmetric and gaussian.

An analytical approach for deconvolution of photon drag traces is given below for better understanding of the problem

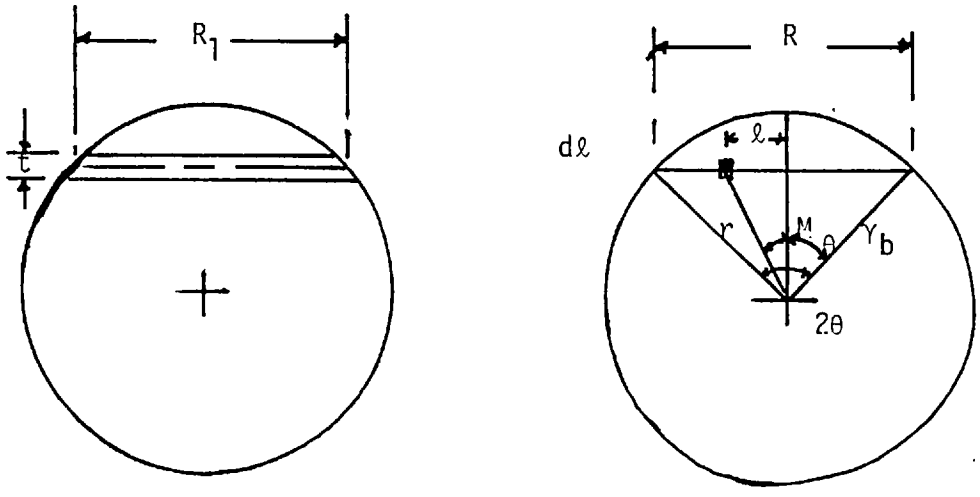

t = thickness of the segment sectioned by chopper

R = length of the segment at any time

γ_b = radius of laser beam

ℓ = distance of the element $d\ell$ from the middle of the segment

2θ = angle subtended by the segment at the centre

$d\ell$ = An element on the segment

r = distance between the centre of the beam and the element "$d\ell$"

Assumptions

1) The laser beam is axisymmetric with a circular cross section
2) The chopper diameter is large compared to the focussed laser beam diameter. Thus the segments scanning the beam are considered parallel to each other.

From the figure it can be written that $\ell = M \tan \phi$

$\therefore \quad d\ell = M \sec^2 \phi \, d\phi$

Now for gaussian power distribution, power at the element $d\ell$ is given by

$$P(r) = P_o \cdot e^{-(r/r_b)^2} \times t \times d\ell$$

$\therefore P(r) = P_o \, e^{-(r/r_b)^2}$ when P_o = power at the centre of the beam

$$= P_o \, e^{-(r/r_b)^2} \times t \times M \sec^2 \phi \, d\phi$$

$\therefore P_s$ = power over the segment

$$= \int_{-\phi}^{+\phi} P_o \, e^{-(r/r_b)^2} \times t \times M \times \sec^2 \phi \, d\phi$$

where $\phi = \cos^{-1}(M/r_b) = \theta$

$$= \int_{-\phi}^{+\phi} P_o \, e^{-(M\sec\phi/r_b)^2} \times t \times M \sec^2\phi \, d\phi$$

$$= \int_{-\phi}^{+\phi} P_o \, e^{-(M^2/r_b^2) \times (\sec^2\phi)} \times t \times M \times \sec^2 \phi \, d\phi$$

$$= P_o \times t \times M \int_{-\phi}^{+\phi} e^{-(M/r_b)^2 (\sec^2\phi)} \times \sec^2\phi \, d\phi$$

N.B. $\phi \equiv \theta$ *for limits*

$$\text{or} \quad P_s = \left[P_o \times t \times M \, e^{-(M/r_b)^2 (\sec^2\phi)} \times \tan\phi \right]_{-\theta}^{+\theta}$$

$$- P_o \times t \times M \int_{-\theta}^{+\theta} \{\frac{d}{d\phi} (e^{-(M/r_b)^2 (\sec^2\phi)}) \int \sec^2\phi \, d\phi\} \, d\phi$$

$$= \left[P_o \times t \times M \, e^{-(M/r_b)^2 (\sec^2\phi)} \times \tan\phi \right]_{-\theta}^{\theta}$$

$$- P_o \times t \times M \int_{-\theta}^{\theta} \{e^{-(M/r_b)^2 (\sec^2\phi)} \times (-M^2/r_b^2) \times 2 \sec\phi \times \sec\phi$$

$$\times \tan\phi \times \tan\phi \times d\phi\}$$

$$= \left[P_o \times t \times M \times e^{-(M/r_b)^2 (\sec^2\phi)} \times \tan\phi \right]_{-\theta}^{\theta}$$

$$+ P_o \times t \times M \times (M/r_b)^2 \int_{-\theta}^{+\theta} e^{-(M/r_b)^2 (\sec^2\phi)} \times 2 \sec^2\phi \times \tan^2\phi \, d\phi$$

....(Eqn. A4.1)

Now, let

$$Y = 2 \int_{-\theta}^{\theta} e^{-(M/r_b)^2 (\sec^2\phi)} \sec^2\phi \times \tan^2\phi \times d\phi$$

$$= 2 \times 2 \int_{o}^{\theta} e^{-(M/r_b)^2 (\sec^2\phi)} \times \sec^2\phi \times \tan^2\phi \times d\phi$$

Now putting $\tan\phi = t \quad \therefore \phi = \tan^{-1} t$

$$\sec^2\phi \, d\phi = dt$$

Again $\sec^2\phi = 1 + \tan^2\phi$

and $A = (M/r_b)^2$

$$\therefore \quad Y = 2 \times 2 \int_0^{\tan\theta} e^{-A(1+t^2)} \times t^2 \, dt$$

$$= 2 \times 2 \; e^{-A} \int_0^{\tan\theta} t^2 \times e^{-At^2} \, dt$$

$$= 4 \, e^{-A} \int_0^{\tan\theta} t^2 \, e^{-At^2} \, dt$$

Now putting

$$V = -\tfrac{1}{2} \, e^{-At^2}$$

$$\therefore \quad dV = -\tfrac{1}{2} \, e^{-At^2} \, (-2At) \, dt$$

$$= At \times e^{-At^2} \times dt$$

and $u = t \quad \therefore du = dt$

So,

$$Y = 4 \, e^{-A} \int_0^{\tan\theta} t \times (At \times e^{-At^2}/A) dt$$

$$= 4/A \; e^{-A} \tan\theta \int_0^{\tan\theta} At \times e^{-At^2} \, dt$$

$$- 4/A \; e^{-A} \int_0^{\tan\theta} 1 \times \int At \, . \, e^{-At^2} \, dt$$

$$= 4/A \; e^{-A} \times \tan\theta \left[-\tfrac{1}{2} e^{-At^2}\right]_0^{\tan\theta} + 2/A \; e^{-A} \int_0^{\tan\theta} e^{-At^2} \, dt$$

$$= - 2\tan\theta/A \;\; e^{-A} \left[e^{-A \tan^2\theta}\right]_0^{\theta} + 2 \, e/A^{-A} \int_0^{\tan\theta} e^{-AU^2} \, du$$

$$= - 2\tan\theta/A \;\; e^{-A} \left[e^{-A \tan^2\theta} - 1\right] + \left[2 \, e^{-A}/A \int_0^{\tan\theta} e^{-(\sqrt{A}\, U)^2} \, du\right]$$

Therefore equation A4.1 becomes

$$P_s = 2\Big[P_o \times t \times M(e^{-(M/r_b)^2} \, (\sec^2\theta) \times \tan\theta - e^{(-M/r_b)^2} \times 0)\Big]$$

$$+ P_o \times t \times M \times (M/r_b)^2 \Big[- 2 \tan\theta/A \;\; e^{-A}(e^{-A \tan^2\theta} - 1)$$

$$+ (2 \, e^{-A}/A \int_0^{\tan\theta} e^{-(\sqrt{A}\, U)^2} \times du)\Big]$$

$$= 2\left[P_o \times t \times M(e^{-(M/r_b)^2} (\sec^2\theta) \times \tan\theta)\right]$$

$$+ P_o \times t \times M (M/r_b)^2 \left[2\tan\theta/M^2 \times r_b^2 \times e^{-(M/r_b)^2} (e^{-(M/r_b)^2\tan^2\theta}-1)\right.$$

$$\left. + (e^{-(M/r_b)^2}/(M/r_b)^2 \times 2 \int_o^{\tan\theta} e^{-(M/r_b \cdot u)^2} \cdot du) \right]$$

(Eqn. A4.2)

Now let $E(u) = 2 \int_o^{\tan\theta} e^{-(\sqrt{A}\, U)^2} \cdot du$

Now putting $\sqrt{A} \cdot U = Z$

$$\sqrt{A} \cdot du = dZ$$

$$\therefore \quad E(U) = 2 \int_o^{\sqrt{A}\tan\theta} e^{-(Z)^2} \times dZ/\sqrt{A}$$

$$= 2/\sqrt{A} \int_o^{\sqrt{A}\tan\theta} e^{-Z^2} \cdot dZ$$

$$= 2/\sqrt{A} \int_o^{x} e^{-Z^2}\, dZ \qquad (\text{where } x = \sqrt{A} \cdot \tan\theta)$$

Now from NAG (SISAAF(x))

$$Erf(x) = \frac{2}{\sqrt{\pi}} \int_o^{x} e^{-t^2}\, dt$$

$$\therefore \quad \frac{\sqrt{\pi}}{\sqrt{A}}\, Erf(x) = \frac{2}{\sqrt{A}} \int_o^{x} e^{-t^2}\, dt$$

Therefore

$$E(U) = \sqrt{\pi/A} \times Erf(x)$$

And $\therefore \quad (M/r_b)^2 \ (\sec^2\theta) = (M/r_b) \ (1/\cos^2\theta)$

$= (M/r_b)^2 \ (1/(M/r_b)^2) = 1$

$$P_s = P_o \times t \times M \times \Big[2(e^{-1} \times \tan\theta) + (M/r_b)^2 \{\tan\theta \ . \ r_b^2/M^2 \times e^{-(M/r_b)^2} \ (e^{-(M/r_b)^2 \ (\tan^2\theta)} - 1) + (r_b/M)^2 \ (e^{-(M/r_b)^2})(\sqrt{\pi/A} \times \mathrm{Erf}(x)\} \Big]$$

(Eqn. A4.3)

when $X = M/r_b \ \tan\theta$

$U = \tan\phi = \ell/M$

N.B. For different values of θ *and* M *a particular* $\phi(\phi < \theta)$ *is to be used*

Weld No.	Material	Power watts	Speed mm/sec	Thickness mm	Joining Rate mm^2/KJ	U.T.S. MN/m^2	0.2% Proof Stress MN/m^2	Elongation %	Remarks
1	CP-Ti (DTD 5063)	1110	8.5-15	2.032	--	--	--	--	Trial run
2	"	1140	9.5	"	16.93	462.49	459.95	4.55	
	"	"	"	"	"	496.745	496.158	5.23	
	"	"	"	"	"	496.549	496.158	5.23	
3	"	"	"	"	"	572.098	502.421	26.82	
	"	"	"	"	"	530.116	462.102	26.14	
4	"	"	13	"	23.17	448.89	448.89	5	
	"	"	"	"	"	548.611	485.589	16.14	
5	"	"	"	"	"	304.3375	304.3375	6.36	
						302.00	302.00	5.45	
6	Ti-6Al-4V (AMS4911)	1140	9.5	2.29	19.08	313.196	313.196	5	Improper penetration
	"	"	"	"	"	293.125	293.125	4.545	
	"	"	"	"	"	334.55	334.55	3.63	
	"	"	"	"	"	321.72	321.72	4.545	
7	"	1110	9.5	2.032	17.39	94.877	94.877	1.818	Not proper penetration
	"	"	"	"	"	201.96	201.96	4.09	
8	"	"	7.5	"	13.73	796.7	781.91	7.27	Not proper penetration
	"	"	"	"	"	802.75	765.92	6.818	
9	"	"	"	"	"	409.452	409.452	3.409	Not proper penetration
	"	"	"	"	"	353.08	353.08	3.63	
10	"	1110	6	2.032	11.00	852.57	852.57	6.36	
	"	"	"	"	"	870.38	833.78	10	
11	"	1110	6	"	11.00	167.93	167.93	2.73	
	"	"	"	"	"	573.08	573.08	4.32	
12	"	1110	5	"	9.15	887.48	830.35	11.36	
	"	"	"	"	"	923.16	860.79	16.82	
13	"	"	"	"	"	890.03	837.75	10	
	"	"	"	"	"	882.6178	815.48	8.64	
14	"	1500	7.5	"	10	942.27	872.94	15.68	
	"	"	"	"	"	905.69	852.96	9.545	
15	Ti-6Al-4V (AMS 4911)	1500	7.5	2.032	10	903.55	838.38	15	
	"	"	"	"	"	905.86	838.38	14.55	
16	"	"	9.5	"	12.67	895.57	865.68	16.36	
	"	"	"	"	"	903.295	873.51	16.14	
17	"	"	"	"	"	754.77	753.142	5.68	
	"	"	"	"	"	879.96	815.48	17.27	
18	"	"	13	"	17.33	851.86	819.199	7.5	
	"	"	"	"	"	863.53	808.297	10.78	
	"	"	"	"	"	858.30	811.96	11.82	
	"	"	"	"	"	909.53	853.254	18.41	
19	"	"	23	1.0	15.33	892.107	847.19	16.59	
	"	"	"	"	"	890.32	831.33	17.27	
	"	"	"	"	"	893.59	847.19	20.23	
20	"	1560	"	"	14.7435	882.52	791.797	17.05	
	"	"	"	"	"	885.68	823.407	17.05	
21	"	1540	50	"	32.468	194.61	Same as	1.36	Imperfect penetration
						229.93	U.T.S.	1.36	focussing trouble
22	"	"	"	"	"	187.65	Same as	1.135	Imperfect penetration
	"	"	"	"	"	570.92	U.T.S.	5.68	focussing trouble

APPENDIX 7

Weld No.	Material	Power Watts	Speed mm/sec	Thickness mm	Joining rate mm^2/KJ	U.T.S. MN/m^2	0.2% Proof Stress MN/m^2	Elongation %	Remarks
23	Ti-6Al-4V (AMS 4911)	1540	50	1.0	32.468	854.83	807.455	17.05	
		"	"	"	"	861.47	831.627	17.61	
24	"	"	60	"	38.955	165.37	Same as	1.36	Non alignment and
	"	"	"	"	"	149.45	U.T.S.	1.36	imperfect penetration
25	"	"	"	"	"	784.88	730.44	13.41	
	"	"	"	"	"	886.38	823.504	15.23	
26	"	"	"	"	"	--	--	--	Non aligned
27	"	1000	23	1.0	23	895.91	830.94	15.22	
	"	"	"	"	"	894.48	830.94	14.55	
28	"	"	"	"	"	547.69	Same as	6.59	Improper penetration
	"	"	"	"	"	584.70	U.T.S.	6.36	due to non-alignment
29	"	970	34	"	35.05	895.91	815.48	17.73	
	"	"	"	"	"	899.03	830.94	17.95	
30	"	1000	"	"	34	232.33	Same as	1.59	Non-alignment
	"	"	"	"	"	235.20	U.T.S.	1.59	
31	"	"	15	"	15	887.15	831.33	17.73	
	"	"	"	"	"	885.57	823.4	17.95	
32	"	"	"	"	"	889.78	839.06	17.27	
	"	"	"	"	"	900.66	831.24	16.82	
33	"	"	11	"	11	899.17	839.06	15.45	
	"	"	"	"	"	902.16	839.06	15.91	
34	Ti-6Al-4V (AMS 4911)	1000	11	1.0	11	815.87	771.83	13.86	
		"	"	"	"	884.91	839.46	15.91	
35	"	"	"	"	"	884.91	839.46	15.91	
	"	"	"	"	"	889.57	847.48	16.82	
36	"	770	15	"	19.48	491.64	Same as	4.09	Non-aligned
	"	"	"	"	"	175.12	U.T.S.	1.59	
37	"	"	7	"	9.09	175.37	Same as U.T.S.	1.36	
	"	"	"	"	"	32.95	" "	2.25	
	"	"	"	"	"	157.34	" "	1.02	
	"	"	"	"	"	659.515	" "	4.87	
38	"	"	11	"	14.29	880.3	823.31	17.61	
	"	"	"	"	"	878.62	815.48	17.27	
39	"	"	"	"	"	334.67	Same as	2.73	Improper
	"	"	"	"	"	438.88	U.T.S.	3.64	penetration
40	"	"	8.5	"	11.04	211.87	Same as	1.86	Improper
						290.57	U.T.S.	1.82	penetration
41	"	1480	60	0.889	36.04	811.76	733.96	8.18	Non aligned and off center focussing
	"	"	"	"	"	661.76	Same as U.T.S.	3.86	
42	"	"	"	"	"	882.07	857.12	15.68	
	"	"	"	"		882.47	857.12	17.84	
43	"	"	50	"	30.03	873.31	815.48	17.05	
	"	"	"	"	"	795.34	742.62	11.82	
44	"	"	"	"	"	914.38	798.16	15.91	
	"	"	"	"	"	912.86	833.44	17.61	
45	"	"	23	"	13.81	901.16	824.19	16.82	
	"	"	"	"	"	904.16	824.19	15.68	
46	"	"	"	"	"	914.94	842.1	15.11	
	"	"	"	"	"	918.49	780.05	15.34	

Weld No.	Material	Power watts	Speed mm/sec	Thickness mm	Joining Rate mm^2/KJ	U.T.S. MN/m^2	0.2% Proof Stress MN/m^2	Elongation %	Remarks
47-50	nickel alloys								
50	Ti-6Al-4V (AMS 4911)	1500	60	0.81	32.4	--	--	--	Not satisfactory
51	"	"	"	"	"	700.48	Same as U.T.S.	4.55	Improper penetration
	"	"	"	"	"	695.36	Same as U.T.S.	5.45	
52	"	"	50	"	27.00	252.75	Same as U.T.S.	1.36	Non aligned and off centering of beam
	"	"	"	"	"	141.08	as U.T.S.	0.91	
53	"	"	"	"	"	633.77	as U.T.S.	4.54	Non aligned
	"	"	"	"	"	608.57	as U.T.S.	5.0	
54	"	"	23	"	12.42	---	---	---	---
55	"	"	"	"	"	855.18	805.69	14.77	
	"	"	"	"	"	870.39	835.15	14.32	
56	"	"	"	"	"	877.94	824.39	14.32	
	"	"	"	"	"	879.41	815.48	16.82	
57	"	1000	7.5-50	"	"	---	---	---	Trial run to judge optimum speed
58	"	"	34	"	27.54	544.82	as U.T.S	4.54	
	"	"	"	"	"	583.46	as U.T.S.	3.64	
59	"	"	23	"	18.63	865.01	805.69	14.55	
	"	"	"	"	"	866.46	805.69	15.57	
60	"	"	15	"	12.15	887.85	825.56	14.09	
	"	"	"	"	"	909.54	855.8	13.98	
61	"	"	"	"	"	904.78	757.25	15.23	
	"	"	"	"	"	807.19	763.42	13.86	
62	"	"	"	"	"	801.71	706.22	10.45	
	"	"	"	"	"	873.16	797.38	15.68	
63	"	"	11	"	8.91	882.97	806.38	12.95	
	"	"	"	"	"	882.97	824.68	13.41	
64	"	"	"	"	"	884.53	844.25	13.86	
	"	"	"	"	"	726.19	678.28	7.5	
65	"	1260	23-60	--	--	---	---	---	Trial bead on plate runs
66	"	"	50	"	32.14	622.84	Same as U.T.S.	4.43	Non aligned
67	"	"	"	"	"	845.00	805.79	15.23	
	"	"	"	"	"	802.02	758.62	6.59	
68	DTD 5047	1500	50	0.711	23.7	618.97	340.85	26.82	
	"	"	"	"	"	643.25	328.62	33.864	
69	"	"	"	"	"	566.30	309.73	35.8	
	"	"	"	"	"	607.76	275.48	35.23	
70	Ti-6Al-4V	1480	50	0.69	23.31	883.49	826.54	18.18	
	(AMS 4911)	"	"	"	"	887.9	815.48	16.25	
71	"	"	"	"	"	895.59	837.89	18.18	
	"	"	"	"	"	894.1	782.01	17.27	
72	"	"	60	"	27.97	906.52	849.54	16.59	
	"	"	"	"	"	743.77	659.78	12.27	
73	"	"	"	"	"	794.11	as U.T.S.	5.45	
74	CP Ti	1490	15	1.6256	16.365	582.69	530.31	15.23	
	DTD 5063	"	"	"	"	539.45	494.69	7.95	

Weld No.	Material	Power watts	Speed mm/sec	Thickness mm	Joining rate mm^2/KJ	U.T.S MN/m^2	0.2% Proof Stress MN/m^2	Elongation %	Remarks
75	CP Ti	1490	15	1.6256	16.365	596.32	530.12	13.41	
	DTD 5063	"	"	"	"	608.73	532.95	18.86	
76	"	"	23	"	25.09	644.25	575.91	32.39	
	"	"	"	"	"	639.33	518.18	24.32	
77	"	"	"	"	"	547.18	as U.T.S.	3.98	
	"	"	"	"	"	571.63	523.95	10.34	
78	DTD 5047	1490	15	"	16.365	609.87	364.04	29.89	
	"	"	"	"	"	612.12	296.52	34.55	
	"	"	"	"	"	531.51	291.63	29.09	
79	"	"	"	"	"	514.84	256.49	33.64	
	"	"	"	"	"	502.86	189.75	29.09	
80	6Al-4V-Ti	1490	60	0.508	20.456	861.80	800.7	10.91	
	AMS 4911	"	"	"	"	608.19	415.13	4.09	
81	"	"	"	"	"	889.87	826.73	15.0	
	"	"	"	"	"	563.91	455.74	4.77	
82	CP Ti	1490	50	0.711	23.86	425.29	312.28	7.95	
	DTD 5063	"	"	"	"	426.00	347.02	7.27	
83	"	1490	60	0.559	22.51	429.47	326.17	21.59	
	"	"	"	"	"	413.97	326.17	21.82	
84	Ti-6Al-4V	2000	50	2	50	--	--	--	
	AMS 4911								
85	"	"	40	"	40	--	--	--	
86	"	"	25	3	37.5	--	--	--	
*C1	6Al-4V-Ti	2000	50-100	1.67	47.75-83.5	--	--	--	Bead on plate weld using 5kW CL5 laser and side blown helium shielding
C2	"	"	60	2	60	--	--	--	
C3	"	"	50-60	2.3	57.30-69.00	--	--	--	
C4	"	"	35-45	3	52.5-67.5	--	--	--	
C5	"	"	120-130	1	60-65	--	--	--	
C6	"	3900	200-235	1	51.28-60.26	--	--	--	
C7	"	"	140-150	1.67	59.95-64.23	--	--	--	
C8	"	"	80-130	2.3	47.18-76.67	--	--	--	
C9	"	"	70-80	3	53.85-61.54	--	--	--	
C10	"	4600	230-260	1	50-56.52	--	--	--	
C11	"	4570	140-160	1.67	51.16-58.47	--	--	--	
C12	"	4600	120-130	2	52.17-56.52	--	--	--	
C13	"	4600	120-130	2.3	60-65	--	--	--	
C14	"	4650	90-100	3	58.06-64.52	--	--	--	
C15	"	3000	160-180	1	53.33-60.0	--	--	--	
C16	"	"	100-110	1.67	55.67-61.23	--	--	--	
C17	"	"	80-90	2.3	61.33-69.00	--	--	--	
C18	"	"	40.50	3	40-50	--	--	--	

*All sample numbers starting with 'C' represent bead on plate welds using the Culham CL-5 5KW CW CO_2 laser.

Weld No.	Material	Power Watts	Speed MM/sec	Thickness mm	Joining Rate mm^2/KJ	U.T.S. MN/m^2	0.2% Proof Stress MN/m^2	Elongation %	Remarks
1	tin coated mild steel	500 "	4.5 "	0.4 "	3.6 "	329.2 329.2	314.96 284.48	17.27 21.36	Lap welded of 0.2mm material
2	" "	500 "	4.5 "	0.4 "	3.6 "	332.59 343.13	301.4 304.37	22.27 22.27	
3	" "	760 "	5.25 "	0.4 "	2.76 "	319.15 312.77	275.36 266.6	21.82 21.36	
4	" "	760 "	5.75 "	0.4 "	3.03 "	322.48 309.83	272.04 267.75	23.18 23.64	
5	" "	760 "	7 "	0.4 "	3.68 "	319.15 329.2	275.36 281.09	24.09 22.73	
6	" "	760 "	8.5 "	0.4 "	4.47 "	339.67 325.8	300.91 278.68	23.64 22.73	
7	" "	760 "	15 "	0.4 "	7.89 "	315.83 322.41	265.41 284.48	24.55 27.27	
8	"	1000	5.75	0.4	2.3	329.0	289.11	20.00	
9	" "	1000 "	7 "	0.4 "	2.8 "	338.02 335.39	295.32 293.77	21.82 21.82	
10	" "	1000 "	11 "	0.4 "	4.4 "	325.80 332.32	267.09 283.38	23.64 24.55	
11	" "	1000 "	15 "	0.4 "	6.0 "	345.75 332.45	299.45 287.45	26.36 26.36	
12	"	1250	11	0.4	3.52	329.13	281.55	23.64	Slow
13	"	1250	15	0.4	4.8	--	--	--	Slow
14	" "	1250 "	50 "	0.4 "	16.0 "	351.36 338.33	307.76 283.94	22.27 22.27	
15	" "	1250 "	50 "	0.4 "	16.0 "	325.8 331.52	250.56 291.93	25.91 25.00	
16	" "	1250 "	60 "	0.4 "	19.2 "	355.72 355.13	278.68 316.23	25.00 23.64	
17	"	1250	60	0.4	19.2	328.13	263.39	27.27	
	Weld numbers 18 - 33 — drum quality steels								
34	"	1700	92	0.4	21.65	--	--	--	Lap weld of 0.2mm
35	"	1700	97	0.4	22.82	--	--	--	
35A	"	1700	90	0.4	21.18	--	--	--	
36	"	1700	114	0.4	26.82	--	--	--	
37	"	1920	170	0.4	--	--	--	--	Too fast
38	"	1920	150	0.4	--	--	--	--	Too fast
39	"	1920	150	0.4	--	--	--	--	Improper penetration (See weld 44)
40	"	1920	130	0.4	27.08	--	--	--	Upper limit of penetration
41	"	1920	130	0.4	27.08	--	--	--	
42	"	1920	130	0.4	27.08	--	--	--	
43	"	1920	114	0.4	26.82	--	--	--	
44	"	1730	142	0.4	32.83	--	--	--	Just makes it but not ideal weld
45	"	1510	90	0.4	23.84	--	--	--	

APPENDIX 8

Weld No	Material	Power Watts	Speed Ml/sec	Thickness mm	Joining Rate mm^2/KJ	U.T.S. MN/m^2	0.2% Proof Stress MN/m^2	Elongation %	Remarks
46	tin coated mild steel	1520	114	0.4	30.00	--	--	--	See also 68-70
47	"	1520	142	0.4	--	--	--	--	Not proper penetration
48	"	1710	114	0.4	26.67	--	--	--	O.K.
49	"	1720	130	0.4	30.23	--	--	--	O.K.
50	"	1720	130	0.4	30.23	--	--	--	
51	"	1920	130	0.4	27.08	--	--	--	O.K.
52	"	1920	130	0.4	27.08	--	--	--	
53	"	1920	130	0.4	27.08	--	--	--	
54	"	1410	234	0.2	--	--	--	--	Bead on plate weld not proper penetration
55	"	1410	200	0.2	--	--	--	--	Not proper penetration
56	"	1410	170	0.2	24.11	--	--	--	Full penetration bead on plate
57	"	1750	234	0.2	26.74	--	--	--	near limit
58	"	1770	170	0.2	19.21	--	--	--	Full penetration
59	"	1770	114	0.2	12.88	--	--	--	Too slow
60	"	1770	142	0.2	16.05	--	--	--	Full penetration
61	"	1750	326	0.2	--	--	--	--	Too fast
62	"	1820	234	0.2	25.71	--	--	--	Full penetration
63	"	1820	326	0.2	--	--	--	--	Not proper penetration
64	"	2000	170	0.2	17.00	--	--	--	Proper penetration
65	"	2000	234	0.2	23.40	--	--	--	Full penetration with fine weld bead
66	"	2000	277	0.2	27.70	--	--	--	Full penetration with very fine weld bead
67	"	2000	326	0.2	32.60	--	--	--	Near limit
68	"	1520 $\pm$ 20	170	0.2	22.37	--	--	--	Slow
69	"	1520 $\pm$ 20	200	0.2	26.32	--	--	--	O.K.
70	"	1520 $\pm$ 20	234	0.2	30.79	--	--	--	Just near limit
71	"	1750 $\pm$ 20	234	0.2	26.74	--	--	--	O.K.
72	"	"	277	0.2	31.66	--	--	--	Near limit
73	"	"	302	0.2	34.51	--	--	--	Near limit
74	"	"	326	0.2	37.26	--	--	--	Just made it
75	"	1240 $\pm$ 20	114	0.2	18.39	--	--	--	O.K.
76	"	"	142	0.2	22.9	--	--	--	O.K.
77	"	"	170	0.2	--	--	--	--	Not satisfactory
78	"	"	162	0.2	26.13	--	--	--	Just made it.

Weld No	Material	Power Watts	Speed MM/sec	Thickness mm	Joining Rate mm^2/KJ	U.T.S. MN/m^2	0.2% Proof Stress MN/m^2	Elongation %	Remarks
79	Tin coated mild steel	1000 ± 20	67	0.2	13.4	--	--	--	too slow
80	"	"	90	0.2	18.00	--	--	--	O.K.
81	"	"	114	0.2	22.8	--	--	--	O.K.
82	"	"	142	0.2	28.4	--	--	--	Just
83	"	1500 ± 10	67	0.4	17.87	--	--	--	Lap weld O.K.
84	"	1750	162	0.4	--	--	--	--	Not proper penetration near limit
85	"	1750	162	0.4	--	--	--	--	
				BUTT WELDS					
101	Tin coated mild steel	1600	215	0.2	--	--	--	--	Not proper penetration diffused beam
102	"	1660	230	0.2	27.71	--	--	--	Just makes it but not satisfactory; overlap in parts
103	"	1660	249.4	0.2	--	--	--	--	Not satisfactory
104A	"	1300	215	0.2	33.08	--	--	--	Overlap in parts not very satisfactory
104B	"	1300	199	0.2	--	--	--	--	Too slow
TCMS1	"	--	--	0.24	--	319.49	266.82	28.18	Unwelded
TCMS2	"	--	--	0.24	--	313.16	267.27	26.636	Unwelded

Weld No.	Material	Power Watts	Speed MM/sec	Thickness mm	Joining Rate mm^2/KJ	U.T.S. MN/m^2	0.2% Proof MN/m^2	Elongation %	Remarks
18	Hi-top drum quality mild steel	1010 ± 10	5.25	0.8	4.158	426.41	380.0	22.27	Lap welding of 0.4mm sheet
		"	"	"	"	416.95	338.27	20.9	
19	"	"	7	0.8	5.54	417.65	329.15	23.18	
	"	"	"	"	"	407.98	377.83	21.82	
20	"	"	11	0.8	8.71	411.36	313.40	23.64	
	"	"	"	"	"	407.26	302.79	23.18	
21	"	"	"	"	"	415.19	381.86	23.64	
	"	"	"	"	"	407.93	368.78	23.64	
22	"	1250 ± 10	7	0.8	4.48	399.22	324.1	24.53	
	"		"	"	"	416.5	326.51	23.64	
23	"	"	"	"	"	420.58	371.67	25.00	
	"	"	"	"	"	433.84	393.56	23.18	
24	"	"	11	"	7.04	411.04	--	--	
	"	"	"	"	"	406.32	373.70	23.64	
25	"	"	15	0.8	9.6	411.73	355.13	23.64	
	"	"	"	"	"	386.7	340.00	23.64	
26A	"	"	18.5	"	11.84	399.88	362.77	23.18	
	"	"	"	"	"	388.74	281.71	24.55	
26B	"	"	"	"	"	403.02	352.34	23.64	
	"	"	"	"	"	398.63	325.39	23.18	
27	"	"	23	0.8	14.72	390.11	336.23	25.45	
	"	"	"	"	"	397.97	354.11	26.36	
28	"	1490 ± 10	11	0.8	5.9	400.70	366.47	21.36	
	"		"	"	"	391.05	351.30	22.73	
29	"	"	15	0.8	8.05	407.54	372.31	23.18	
	"	"	"	"	"	409.45	388.56	22.73	
30	"	"	23	"	12.35	408.52	366.21	24.55	
	"	"	"	"	"	379.47	326.4	24.1	
31	"	"	34	"	18.26	400.91	349.11	24.55	
	"	"	"	"	"	403.71	357.99	26.36	
32	"	1700 ± 10	23	"	10.82	398.45	369.64	23.64	Lap welding of 0.4mm sheets
	"		"	"	"	407.93	379.75	22.73	
33	"	"	50	"	23.53	421.64	347.77	26.36	
	"	"	"	"	"	415.81	331.015	27.27	
MS1	"	--	--	0.41	--	353.16	284.34	31.82	unwelded
MS2	"	--	--	0.42	--	380.01	328.39	30.45	unwelded

APPENDIX 9

MILD STEEL - 1010W 5.25 MM/SEC

Distance mm	Average Indentation	Knoop Hardness
0.2	34.60	1189
0.4	33.20	1291
0.6	33.45	1275
0.8	34.25	1217
1.0	33.50	1267
1.2	32.80	1323
1.4	32.30	1363
1.6	32.65	1339
1.9	31.90	1407
2.0	32.20	1372
2.2	28.90	1703
2.4	29.95	1585
2.6	28.90	1703
2.8	27.00	1951
3.0	27.05	1944
3.2	26.25	2066
3.4	36.60	1520
3.6	27.85	1834
3.8	29.25	1662
4.0	29.95	1585
4.2	31.85	1407
4.4	31.15	1470
4.6	32.53	1347
4.8	33.50	1267

MILD STEEL - 1250W 7MM/SEC

Distance mm	Average Indentation	Knoop Harndess
0.0	33.70	1253
0.2	34.15	1224
0.4	34.50	1196
0.8	33.85	1238
1.0	32.70	1331
1.2	34.85	1168
1.4	32.75	1331
1.6	31.00	1481
1.8	32.90	1315
2.0	32.30	1364
2.2	34.65	1189
2.4	29.75	1607
2.6	30.35	1545
2.8	30.00	1580
3.0	30.30	1550
3.2	30.75	1505
3.4	32.20	1372
3.6	31.60	1425
3.8	32.45	1355
4.0	33.20	1291
4.2	34.90	1168
4.4	33.40	1275
4.6	33.25	1291
4.8	33.35	1283

MILD STEEL - 1010W 11 MM/SEC

Distance mm	Average Indentation	Knoop Hardness
2.4	34.15	1217
2.6	33.15	1291
2.8	31.80	1407
3.0	31.90	1398
3.2	28.30	1776
3.4	29.75	1607
3.6	29.45	1640
3.8	28.50	1751
4.0	30.45	1535
4.2	30.90	1490
4.4	32.15	1380
4.6	34.45	1203
4.8	33.85	1245
5.0	34.80	1175

MILD STEEL - 1250W 26.5 MM/SEC

Distance mm	Average Indentation	Knoop Hardness
0.4	33.85	1245
0.6	33.85	1245
0.8	32.70	1331
1.0	32.30	1364
1.2	32.80	1323
1.4	31.85	1407
1.6	32.30	1364
1.8	30.75	1505
2.0	30.95	1486
2.2	29.40	1646
2.4	27.45	1808
2.6	28.30	1776
2.8	29.05	1685
3.0	28.25	1783
3.2	28.75	1721
3.4	29.35	1652
3.6	31.95	1398
3.8	32.40	1355
4.0	33.40	1275
4.2	33.20	1291
4.4	33.05	1299

APPENDIX 10 MICROHARDNESS RESULTS FOR MILD STEEL AND TIN PLATE LOAD 100 GRAMS

(continued)

MILD STEEL - 1490W 11MM/SEC

Distance mm	Average Indentation	Knoop Harndess
1.2	34.90	1168
1.4	34.60	1189
1.6	36.00	1098
1.8	34.50	1196
2.0	34.55	1196
2.2	33.55	1267
2.4	34.50	1196
2.6	35.15	1154
2.8	32.85	1323
3.0	32.05	1389
3.2	30.20	1560
3.4	31.05	1481
3.6	30.80	1500
3.8	32.35	1363
4.0	34.15	1224
4.2	33.75	1252
4.4	33.53	1267
4.6	33.90	1238
4.8	35.05	1161
5.0	35.50	1128

MILD STEEL - 1490W 34MM/SEC

Distance mm	Average Indentation	Knoop Hardness
2.4	26.20	1148
2.6	33.70	1252
2.8	31.65	1425
3.0	31.60	1425
3.2	28.40	1763
3.4	28.80	1715
3.6	29.00	1691
3.8	29.90	1591
4.0	30.80	1500
4.2	32.45	1355
4.4	32.30	1363
4.6	34.25	1217
4.8	34.45	1203

TIN PLATE - 1000W 5.75 MM/SEC

Distance mm	Average Indentation	Knoop Hardness
0.2	33.45	1275
0.4	32.85	1323
0.6	33.00	1307
0.8	32.90	1315
1.0	32.70	1331
1.2	31.85	1407
1.4	29.85	1602
1.6	30.45	1540
1.8	32.25	1372
2.0	31.05	1481
2.2	26.00	2106
2.4	25.55	2178
2.6	27.75	1848
2.8	26.80	1979
3.0	27.20	1923
3.2	27.55	1875
3.4	30.55	1525
3.6	31.25	1462
3.8	30.25	1555
4.0	28.75	1421

APPENDIX 10

NOMENCLATURE

Symbol	*Description*	*Units*
A	Area	$metre^2$
a	Penetration depth	metre
B	Jet-plate distance	metre
b	Width of the weld ingot	metre
C	Specific heat	
C_p	Specific heat at constant pressure	J/kg^oK
D	Jet diameter	metre
D_b	Unfocussed beam diameter	metre
D_j	Diameter of the jet nozzle	metre
d	Focussed beam diameter	metre
E_m	Energy per unit length required to melt the weld beam	J/metre
E_p	Energy per unit distance entering the workpiece	J/metre
E_t	Total laser energy available per unit length	J/m
F	Focal length of the lens/ unfocussed beam diameter	
F_o	Incident beam power density at the centre	W/m^2
$F_{(t)}$	Incident beam power density	W/m^2
f	Focal length of the lens	m
GDENS	Gas density at NTP	Kg/m^3
GVEL	Gas velocity	m/sec
GVISC	Gas viscosity at NTP	$Nsec/m^2$
g	Plate thickness	metre
h	Increment in difference equation	
h_c	Convective heat transfer coefficient	W/m^oK
h_r	Radiative heat transfer coefficient	W/m^oK
h_{tot}	$(h_c + h_r)$	W/m^oK
IX	Number of points in x-axis of the grid	
IY	Number of points in y-axis of the grid	
I2	Number of points in z-axis of the grid	
i	current	amps
J_1	First minimum of Bessel function = 1.22π	
K	Thermal conductivity	W/m^oK
K_{gas}	Thermal conductivity of gas at boundary layer film temperature	W/m^oK

Symbol	*Description*	*Units*
L	Focal length of the lens	metre
L_c	Length of the cavity of the laser	metre
L_f	Latent heat of fusion	J/kg
M	Normalised power per unit depth	
N	Number of points	
N_A	Nugget area	m^2
N_f	Fresnel number	
Nu_o	Nusselt number at the stagnation point of the jet	
P	Absorbed power	W
P_o	Incident beam power denisty at the centre	Wm^{-2}
$P_{(r)}$	Power density at the radial distance "Y"	W/m^2
Pr	Prandtl number (C_p.GVISC/K)	
P_{TOT}	Total incident power	W
$P_{x,y,z}$	Power density at the point x, y, z	Wm^{-2}
p	Pressure	$Newton/m^2$
Q	Heat input per unit time	W
Q_x	Heat conduction rate in x-direction	W
q	Power over penetration depth (P/a)	W/m
q_o	Uniform intensity of circular source	W/m^2
$q_{r.loss}$	heat loss due to radiation	W
R	Distance to the heat source	m
Re	Reynolds number	
$\overline{R}_i$	Non-dimensional parameter	
$R_\lambda(T)$	Reflectivity for radiation of wavelength "λ" at temperature T°C	
r	Radial distance	m
r_b	Beam radius	m
r_f	Reflectivity	
r_ℓ	Radius of lens	m
r_m	Radius of mirror	m
r_s	Radius of diffraction limited spot size	m
T	Temperature	^oK
T_{EMPA}	Ambient temperature	^oK
T_m	Melting point	^oK
T_o	Original plate temperature	^oK
t	Time	sec
t*	Dimensionless time	
U	Welding speed/thermal diffusivity ($v/2\alpha$)	m^{-1}
u	Gas velocity	$m.sec^{-1}$

Symbol	*Description*	*Units*
V	Welding speed	m/sec
v	Welding speed	m/sec
W	Total melt width	m
w	Heat loss per unit time per unit volume	$Ws^{-1}m^{-3}$
X	Distance along weld centre line	m
x	r cosϕ	m
Y	Distance from weld centre line	m
Y_{max}	Normalised maximum melt width	
y	Half width of the molten pool = r sinϕ	m
Z_m	Melting efficiency	
Z_p	Process efficiency	
Z*	Dimensionless quantity	
z	Depth	m
α	Thermal diffusivity	m^2/sec
β	Dimensionless symbol	
γ	Enter's constant	
ε_a	Otpical absorption coefficient	
$\varepsilon_\lambda(T)$	Emmisivity for radiation having wavelength "λ" at temperature TOK	
θ	KT	W/m
$\overline{\theta}$	θ_i/θ_m = dimensionless quantity	
θ_i	Instantaneous temperature rise	^oK
θ_m	$q_o \cdot r_b/K$	^oK
λ	Wavelength of radiation	m
μ_g	Gas viscosity	$N.sec.m^{-2}$
ρ	Density	$Kg.m^{-3}$
$\rho_r(T)$	Electrical resistivity at temperature T^oK	Ohm-cm
ϕ	Polar angle	
ψ	ierfc = Integrated complementary error function	
σ	Stefan-Boltzman constant = 0.0000000567	

REFERENCES

1) SCHAWLOW Arthur L. "Laser Interactions with materials" p263-266, Conference Proceedings, Laser 77, Opto Electronics, Munich, 20-24 June (1977)

2) WHITEHOUSE D.R. (1967) Laser Technology, PA6-A14

3) CO_2 Laser Theory Laser Technology (July 1967) PA10-A11

4) BROWN C.O. (1970) High power CO_2 electric-discharge mixing laser, Applied Physics Letters, Vol 17 No. 9

5) BROWN C.O. and DAVIS J.W. (1970) Electric discharge convection lasers - paper presented at the I.E.E.E. International Electronic devices meeting, Washington, D.C.

6) Electron Beam Welding: Principles and Practice, pp 95-96, Editor A.H. Meleka, published for Welding Institute by McGraw-Hill, London.

7) BROWN C.O. and BANAS C.M. Deep-penetration Laser Welding. Paper presented at the AWS 52nd Annual Meeting, San Francisco, California, April 26-29 (1971)

8) BANAS C.M. Investigation of Laser Welding at very high Powder Levels. United Technologies Research Center Report R76-912260-1; Final Report under Naval Research Laboratories contract N00173-76-M-0107, August (1976)

9) SWIFTHOOK D.T. and GICK A.E.F. (1973), Welding Research Supplement, p492S-499S

10) WILLIAMS N.T., THOMAS D.E., WOOD K. "High speed seam welding of tinplate cans" Part 1, Metal Construction, Vol 9, Part 4, April (1977), p157-160

11) WILLIAMS N.T., THOMAS D.E., WOOD K. "High Speed seam welding of tinplate cans" Part 2, Metal Construction, Vol 9, Part 5, May (1977), p202-208

12) HOULDCROFT P.T. "Welding Processes", Book published by Cambridge University Press (1973), reprint.

13) CHARSCHAN S.S. editor, "Lasers in Industry", van Nostrand Reinhold Company, New York (1972)

14) READY J.F. "Effects of High Powder Laser Radiation", Academic Press, New York (1971)

15) HARRY J.E. "Industrial Application of Lasers", McGraw Hill Book Company (U.K.), Limited, England (1974).

16) DULEY W.W. "CO_2 Lasers,Effects and Applications" Academic Press, New York (1976)

17) STEEN W.M. "Ph.D. Thesis", London University, (1976)

18) SPALDING I.J. "Lasers - Their applications and operational requirements" - Lecture given at the Von Karman Institute Course on High Powder Gas Lasers, Brussels, 11-15th March 1974

19) SCOTT B.F. and HODGETT D.L. "Pulsed Solid State Lasers for Engineering Fabrication Processes", Proc. Inst. Mech. Eng., Vol 183, Pt 3D, pp75-84, (1969)

20) COHEN M.I. and EPPERSON J.P. "Applications of Lasers to Microelectron fabrication". Advances in Electronics and Electron Physics Supplement, 4, p139-186, (New York, Academic Press Inc., 1968).

21) LETOKHOV, V.S. Chem. Phys. Lett., Vol 15, p221, (1972)

22) BRADLEY MOORE C. Accounts of Chemical Research, Vol 6, p323, (1973)

23) Laser focus, Vol 9, (12), pp18, (1973).

24) LETOKHOV V.S. Science, Vol 180, p451 (1973)

25) AMBARTTZUMIAN R.V. et al Zh. Eksp. Teor, Fiz. Red; Vol 17, p91, (1973)

26) YEUNG E.S., BRADLEY MOORE C.B. Appl. Phys. Letter, Vol 21, p109 (1972)

27) MAYER S.W., KWOK M.A., GROSS R.W.F., and SPENCER D.J. Applied Physics Letter, Vol 17, p516, (1970)

28) PRESSMAN J. U.S. Patent 3558877 (1971)

29) GUERS K. Guer Offen. Vol 2, p232 (Cl. Bold, 13th July, 1972)

30) ASHKIN A. Isotope separation.German Patent 2,065,253 (Cl. B.036), 01 Feb. (1973)

31) LEON S.R. and MOORE C.B. Phys. Rev. Lett. Vol 33, p269, (1974)

32) LIU Y.S. Applied Optics , Vol 13, p2505, (1974)

33) ASHKIN, A. Phys. Rev. Lett. Vol 24, p156, (1970)

34) USIKOV, A. Ya., KONTOROVICH, V.N., KANNER E.A. and BILOCH P.V. Ukri Fiz. Zh, vol 17, p1275 (1972)

35) GELBWACHS J. and HARTWICK T.S. I.E.E.E. J. Quantum Electronics, QE-11, 52 (1975)

36) AMBARTZUMIAN R.V., LETOKHOV V.S., RYABOV E., and CHEKALIN N.V., J.E.T.P. Lett., Vol 20, p273 (1974)

37) FREUND S.M. and RITTER J.J. Chem. Phys. Lett., Vol 32, p255, (1975)

38) LYMAN,J.L. and LOCKWOOD S.D. J. Appl. Phys. Vol. 47, p595 (1976)

39) AMBARTZUMIAN R.V., GOROKHOV Y.A., LETOKHOV U.S., and MARKAROV G.N. J.E.T.P. Lett., Vol 21, p171 (1975)

40) LYMAN J.L., JENSEN R.J., RINK J., ROBINSON C.P., and RACKWOOD S.D. Appl. Phys. Lett., Vol 27, p87 (1975)

41) FARRER R.L. Jr., and SMITH D.F. Nuclear Division of Union Carbide Corp^{n}. Oak Ridge, Rep. 1972, K-L-3054 (Rev. 1) (1972)

42) ALTSCHULER S.J. Possible applications of laser isotope separation to nuclear and conventional technologies. DOW Chemical Co. Rep. RFP 2065 (1973)

43) VANDERLEEDEN J.C. "Laser Separation of Deutarium" Laser Focus, p51-56, June (1977)

44) POWELL C.F., OXLEY J.H., BLOTCHER J.M. "Vapour Deposition" p268, J. Wiley, New York (1966)

45) TOULMIN Jr. H.A., U.S. Patent, 2, 847, 330, (Aug. 12, 1958)

46) DAVIES G.J., "Mass transfer from a turbulent impinging jet with and without chemical reaction", Ph.D. Thesis, London University (1971)

47) ARCHIBALD E., HARPER D.W., and HUGHES T.P., "Spectroscopy of Laser generated micro-plasmas". Brit. J. Appl. Phys. Vol 15, pp1323 (1964)

48) CLARKE J. 3rd Year Project Report, Royal School of Mines, (1975)

49) NICHOLS K.G. Brit. Commun. Electron. Vol 12, p368 (1965)

50) SMITH H.M. and TURNER A.F. Appl. Opt. Vol 4, p147 (1965)

51) GROH G. J. Appl. Phys. Vol 39, p5804, (1968)

52) SAMSON J.A.R., PADUR J.P., and SHARMA A. J. Opt. Soc. Amer., Vol 57, p966, (1967)

53) ZAVITSANOS P.D. and SAUER W.E. J. Electrochem. Soc., Vol 115, p109 (1968)

54) HASS G. and RAMSEY J.B. Appl. Opt. Vol. 8, P1115 (1969)

55) SCHWARZ H. and TOURTELLOTE H.A. J. Vac. Sci. Technol. Vol. 6, p373, (1969)

56) HESS M.S. and MILKOSKY J.F. J. Appl. Phys. Vol 43, p4680, (1972)

57) POLTAVTSER Yu. G., ZAKHAROV V.P., PROTAS I.M. and POZDNYAKOVA, V.M. Izv. Akad. Nauk. SSSR Neorg. Mater. Vol 8, p1535 (1972)

58) MIRKIN L.I. Dokl. Akad. Nauk. SSSR, Vol 206, p1339, (English translation. Sov. Phys. Dokl, Vol 17, p1026), (1973).

59) MIRKIN L.I. Izv. Vyssh. Ucheb. Zaved. Fiz. Vol 11, p106 (1973)

60) MIRKIN L.I. Izv. Akad. Nauk SSSR Neorg. Mater., Vol 9 p125 (English translation: Inorg. mater. vol 9, p109) (1973)

61) MIRKIN L.I. Fiz. Khim. Obrad. Mater. No 1, p143 (1973)

62) MIRKIN L.I. Izv. Vyssh. Ucheb. Zaved. Fiz. No. 2, p106 (1973)

63) BAN, V.S. and KRAMER D.A. J. Mater. Sci. Vol 5, p978 (1970)

64) BALDWIN J.M. Appl. Spectrose. Vol 24, p429,(1970)

65) BALDWIN J.M. J. Appl. Phys. Vol 44, p3362,(1973)

66) Metals and Materials (GB), Vol 1, p159, (1973)

67) LITTLE, V.I., KEY P.Y., WILSHEAR R. and ROWLEY D.M. Nature (London) Phys. Sci. vol. 232, p165 (1971)

68) ALEKSEEVSKII N.E., ZAKESARENKO V.M. and TSEBRO V.I. Pisma Zh. Eksper. Teor Fiz Vol 2 p28 (English translation: J.E.T.P. Lett. Vol 12, p157) (1971)

69) ALEKSEEVSKII N.E., ZAKOSARENKO V.M. and TSEBRO V.I., Ibid, Vol3, p292, (English translation: J.E.T.P. Lett. Vol 13, p412) (1971)

70) KLIWER J.K. J. Appl. Phys. Vol 44, p490, (1973)

71) ADAMS M.D. and TONG S.C. Anal. Chem. Vol 40, p1762, (1968)

72) MADANI N, and NICHOLS K.G. Israel J. Technol. Vol 9, p245 (1971)

73) ENGEL S.L. "Basis of Laser Heat Treating" SME Technical paper no MR76-857, Society of manufacturing engineers, 20501 Ford Road, Dearborn, Michigan, 48128, (1976)

74) GREGSON JR. V.G. and SANDERS B.A. "A Physical Model of Laser Heat Treatment" in Proc. of the 1974 Electro-optical Systems Design Confer. Industrial and Scientific Conference Management, Chicago (1974).

75) SANDERS B.A. and GREGSON JR. V.G. "Optical Reflectivity of Some metals using a Transversely excited CO_2 laser" in Proc. of the 1973 Electro-optical Systems Design Conf., Industrial and Scientific Conference Management, Chicago (1973)

76) ZAVEOZ T.E., SAIFI M.A. and NOTIS M. Appl. Phys. Let. Vol 26, pt. 4, p165 (Feb 15, 1975).

77) SEAMAN F.D. and GNANAMUTHU D.S. Metal Progress, p67-74, (August 1975)

78) WAKEFIELD B.D. Iron Age Metal Working Int. p40-41 (September 1975)

79) COURTNEY C. Third year project, Royal School of Mines (1976)

80) AVCO Everett Research Laboratory Inc., Everett, Mass., Technical Bulletin on HPL Laser System.

81) STEEN W.M. and BENNETT M.G. Under Rolls Royce Research Contract (1976-1977), Imp. Coll. London

82) LOCKE E.V. and HELLA R.A. I.E.E.E. J. Quantum quantum electronics, Vol QE-10, No. 2, p179-185, (Feb. 1974)

83) SCHAFFER G. American Machinist, Vol 118, pt 15, p56-59, (July 1974)

84) RYKALIN N.N. and UGLOV A.A. Teplofiz Vys. Temp. Vol 9, p575 (English translation: High Temperature, Vol 9, p522) (1971)

85) DEMING J.L., WEBER J.H. and TAO L.C., Amer. Inst. of Chem. Eng. J. vol 15 p501 (1969)

86) AKIMOV A.I. and MIRKIN L.I. Sov. Phys. Dokl, Vol 13, p1162 (1969)

87) KLOCKE H. Spectrochim Acta. Vol 24B, p263, (1969)

88) CHUN N.K. and ROSE K. J. Appl. Phys. Vol 41, p614, (1970)

89) SUMINOV V.M. and KUZIN B.G. Russ. Eng. J. Vol 52, p4, (1972)

90) SPITZ H.Y. Record Symp. Electron Laser Beam Technol. 10th Gaithersberg ,Maryland, p223 (1969)

91) GAGLIANO F.P., LUMLEY R.M. and WATKINS L.S. Proc. I.E.E.E. Vol 57, p114 (1969)

92) COHEN M.I. Bell Lab. Rec. Vol 45, pt 8, p247 (1967)

93) EPPERSON J.P., DYER R.W. and GRZYWA J.C. West. Elec. Eng. Vol 10, p2 (1966)

94) PACK U.C. and GAGLIANO F.P. I.E.E.E. J. Quantum Electronics, Vol QE 8, p112 (1972)

95) LONGFELLOW J. Amer. Ceramic. Soc. Bull. Vol 50, p251 (1971)

96) NAKADA Y. and GILES M.A. J. Amer. Ceram. Soc., Vol 54, p354, (1971)

97) DULEY W.W. and GONSALVES J.N. Can. Res. Develop. Jan/Feb 25, (1972)

98) DULFY W.W. and GONSALVES J.N. Can. J. Phys. Vol 50, p215, (1972)

99) DULEY W.W. and YOUNG W.A. J. Appl. Phys., Vol 44, p4236, (1973)

100) BAR-ISAAC C. and KORN U. Applied Physics (Germany) Vol 3, p45-54, (1974)

101) SULLIVAN A.B.J. and HOULDCROFT P.T. Brit. Weld. J. Vol 14, p443, (1967)

102) DULEY W.W. and GONSALVES J.N. Opt. Laser Technol. Vol 6, p78 (1974)

103) ADAMS M.J. Brit. Welding Inst. Res. Bull. Vol 9, p245 (1968)

104) BABENKO V.P. and TYCHINSKII V.P. Sov. J. Quantum Electron, Vol 2, p399, (1973)

105) CLARKE J. and STEEN W.M. Private Communication, Imperial College, London University, (1977)

106) LUNAU F.W. and PAINE E.W. Weld. Met. Fabric. January 3, (1969)

107) LUNAU F.W., PAINE E.W., RICHARDSON M. and WIJETUNGE M.D.S.P. Opt. Technol. Vol 1, p255, (1969)

108) HIGUCHI T., MIYAZAWA T., YOSHIDA E, and OKUDA T. "Mitsubishi Denki lab. Rep." Vol 45, p1298, (1971)

109) HARRY J.E. and LUNAU F.W. I.E.E.E. Trans. Ind. Appl. Vol 1A-8, p418, (1972)

110) TANDLER W.S.W. Laser focus, vol 7, p24, (1971)

111) BOD D., BRAISER R.E. and PARKS J. Laser Focus, p36, (Aug. 1969)

112) SCOTT B.F. and STOVELL J.E. Opt. Technol. vol 1, p15, (1968)

113) RUFFLER C. and GURS K. Opt. Laser Technology, vol 4, p265 (1972)

114) LUNAU F.W. and PAINE E.W. Weld Met. Fab. - Jan. 9, (1969)

115) ADAMS M.J. Adv. in Weld. Proc. Harrogate, Paper No 14, (April 1970)

116) HODGETT D.L. and SCOTT B.F. "Pulsed Laser Machining", Inst. E.E. Conf. Publ. 61, , pp229-38, London (1970).

117) DUTTA Ph.D. Thesis, Birmingham University, Oct. (1974)

118) RUSSEL J.D. "Development of the Laser as a welding and cutting tool" Weld. Inst. Res. Bull., p345-350, December, (1975)

119) SPALDING I.J. "Laser System Developments" - Physics Bulletin, p402, July (1971)

120) LOCKE E., HOAG E. and HELLA R. Welding research supplement, pp245S-249S, May (1972)

121) ARATA Y. and INOUE K. Trans. of JWRI, Vol 2, No. 1, p41-45, (1973)

122) ANDREWS J.G. and ATTHEY D.R. J. Inst. Maths. Applics. Vol 15, p59-72, (1975)

123) ANDERSON J.E. and JACKSON J.E. Weld. J. Vol 44, p1018, (1965)

124) PFLUGER A.R. and MASS P.M. Welding J., Vol 44, p264, (1965)

125) COHEN M.I., MAINWARING F.J., and MELONE T.G. Welding J., Vol 48, p191 (1969)

126) ANDERSON J.E. and JACKSON J.E. Proc. Electron Laser Beam Symp. Penn. State Univ. (Ed. A.B. El-Kareh), p17, (1965)

127) LEBEDEV V.K. and GRANISTA V.T. Automat Weld., Vol 25, p63, (1972)

128) VELICHKO O.A., GARASHCHUK U.P. and MORAVSKII V.E. Auto Weld, Vol 25, pt. 4, p75, (1972)

129) MILLER K.J. and NUMNIKHOVEN J.D. Welding J., Vol 44, p480, (1965)

130) MILLER K.J. Weld. Eng. Vol 51, p46, (1966)

131) EARVOLINO L.P. and KENNEDY J.R. Weld. J. Suppl., Vol 45, p127, (1966)

132) SCHMIDT A.O., HAM. I., and HOSHI T. Welding J. Suppl. p481, Nov. (1965)

133) MOORHEAD A.J. Weld. J., Vol 50, p97, (1971)

134) NICHOLS K.G. Proc. Inst. Elect. Eng., Vol 116, pt 12, p2093-2100, Dec. (1969)

135) GARASHCHUK V.P. and MOLCHAN I.V. Avtomet Svarka, Vol 9, p12, (1969)

136) SERETSKY J. and RYBA E.R. Weld. J. Suppl. p208S-211S, July (1976)

137) BARANOV M.S., METASHOP L.A. nad GEINRIKHS I.N. Svar Proizvod, No 3, p13, (1968)

138) BARANOV M.S., METASHOP L.A. and GEINRIKHS I.N. Weld. Prod. G.B. Vol 15, pt 3, p23-27 (1968)

139) VELICHKO O.A., GARASHCHUK V.P., MORAVSKII V.E. Avtomet. Svarka, Vol 25, No. 3, p71-3 (1972)

140) VELICHKO O.A., GARASHCHUK V.P., MORAVSKII V.E. Avtomet. Svarka, vol 25, No. 8 p48-51, (1972)

141) GARASHCHUK V.P., MORAVSKY V.E., VELICHKO O.A. Automal Weld., Vol 25, No. 3 p64-66 (1972)

142) RYKALIN N.N. and UGLOV A.A. Fizika Khim Obrabot Mat., Pt. 5, p13-22, Sept-Oct. (1969)

143) BARANOV M.S., KONDRATEV V.A., UGLOV A.A. Ibid, pt 5, p11-14, Sept-Oct. (1972)

144) ZHUKOV V.V. Automat Weld. Vol 23, pt. 1, p42-43, Jan. (1970)

145) GAGLIANO F.P. I.E.E.E. Wescon Tech. Pap. Vol 13, pt 7, Session 8/1 Aug. 20-2q, (1969)

146) BODECKER V., SEPOLD G., I.E.E.E./O.S.A. Conf. on Laser Engineering and Applications Digest of Technical papers, Washington, D.C., U.S.A., 30 May -1 June, (1973)

147) BALATSKII A.A., BARANOV M.S. Fiz and Khim Obrab. Mater (USSR), J. paper No. 4, July-Aug, (1973)

148) MAKAROV N.I., RYKALIN N.N., UGLOV A.A. Soviet Physics-Doklady, vol 12, p636-638, Dec. (1967)

149) UGLOV A.A. Airforce systems command, Wright-Paterson AFB, Ohio, Foreign Technol. Div. Transl. from Fiz and Khim. Obrab. Mater. (USSR), No. 5, p133-135, (1967)

150) ARATA Y., MIYAMOTO I., Trans. JWRI, Vol 1, No. 1, p11-16, (1972)

151) BANAS C.M. UARL Rep UAR 125, I.E.E.E. Symp. Electron. Ion, Laser Beam Technol, 11th Boulder, Colorado, San Francisco Press, San Franciso, (June 1971)

152) LOCK E.V., HOAG E. and HELLA R. Weld. J. Welding Research Supplement, Vol 51, p245S-249S (1972)

153) LOCK E.V., HOAG E. and HELLA R. I.E.E.E. J. Quantum. Electron Vol QE 8 p132 (1972)

154) BAARDSEN E.L, SCHMATZ D.J., and BISARO R.E. Welding J., Vol 52, p227-229, April (1973)

155) HOAG E., PEASE H., STAAL J., ZAR J., Appl. Opt. Vol 13, p1959, (1974).

156) BALL W.C. and BANAS C.M. Welding with a high power CO_2 laser. Nat. Aerosp. Eng. and Mfr. Meeting, San Diego, California (1974)

157) BANAS C.M., High power laser welding. ASM/NASA/GWU Symp. on Welding, Bonding and Fastening, Virginia, May 30-June 1, (1972)

158) SICKMAN J.G. and MORIJN R. Phillips Res. Rep. Vol 23, p367, (1968)

159) SICKMAN J.G. and MORIJN R. Phillips Res. Rep. Vol 23 p375, (1968)

160) CRAFER R.C. The Weld. Inst. Res. Bull., vol 17, February (1976)

161) GUREVITCH S.M., KUSHNIRENKO N.A., and ZAMKOV V.N. Titanium Science & Technology Vol 1 p541-551, (1973)

162) MILLER F.R. SME Tech. Paper No. MF73-713, Soc. of Manufacturing Engineers, 20501 Ford Road, Dearborn, Mich. 48128, (Pamphlet), (1973)

163) WEDGE R.H. Titanium Science and Technology, Vol 1, p521-540, Plenum Publishing Corporation, New York, (1973)

164) BANAS C.M. Electron Beam, Laser beam and Plasma Arc Welding Studies. NASA Contractor, report no. NASA CR-132386, March, (1974).

165) FIELDING J. Titanium Science and Technology, Vol 1, p45-56, (1973)

166) ADLER P.N., KENNEDY J. and SATKIEWICZ Welding J., Vol 52, p180S-186S, April (1973)

167) SIMPSON R.P. Welding Res. Supl. Welding J., Vol 56, p67S-77S, March, (1977)

168) "Survey of Lead in Food", Working party on the maintainance of food stuffs for heavy metals. HMSO (1972)

169) Sixteenth Report of FAO/WHO Committee on Food Additives, (1972)

170) WILLIAMS N.T. Problem in the resistance welding of coated steels. Paper presented at a conference on steel sheet and strip welding. Organised by Institute of Sheet Metal Engineering, the Welding Institute, and Sheet Metal Industries, March (1972)

171) BORLAND J.C. and JORDAN M.F. The Institution of Metallurgists - Review Course, Series 2, No. 9, pp95, Oct. (1972)

172) READY J.F. Proc. Indust. Tech. Seminar. Penn. State, Univ. June 27-30, (1965)

173) SEPOLE F., Seminar on Laser Wedling, drilling and cutting, Welding Institute, G.B. June (1975)

174) PERT G.J. Plasma Physics, Vol 116, p1019-1033, and p1035-1049, Nov. (1974)

175) BOBIN J.L. Physics Fluids, Vol 14, p2341, (1971)

176) MYERS P.S., UYEHARA O.A., and BORMAN G.L. Fundamentals of Heat flow in Welding. Welding Research Council Bulletin, No 123, July (1967)

177) CARSLAW H.S. and JAEGER J.C. Conduction of heat in solids. Oxford University Press 2nd Edition (1959)

178) ROSENTHAL D. Welding Journal, Vol 20, p220S-225S, (1941)

179) ROSENTHAL D. Trans. A.S.M.E., Vol 48, p848-866, (1946)

180) RYKALIN N.N. Calculation of heat flow in welding. Moscow (1951)

181) ADAMS C.M. Welding Journal, Vol 37, p210S-215S, (1958)

182) ADAMS C.M. MOFFAT W.G., and IHAVERI P. Welding Journal Vol 41, p12S-18S, (1962)

183) ALWANG W.G., CAVANAUGH L.A. and SAMMARTINO E. Welding Research Supplement, P110S March 1969.

184) CHRISTENSEN N., DAVIES V. de L. and GJERMUNDSEN K. British Welding Journal, pp54-75, February (1965)

185) GUENOT R. and RACINET J. British Welding Journal, pp427-435, August (1967).

186) DENNERY G. and GUENOT R. Pubn. Tech. Ministere de l'Air - NT 112, Paris (1962)

187) GUENOT R., RACINET J. and BOUSQUET A., Soud. Tech. Conn. Vol 20, pp105-128, (1966)

188) LIN TUNG-PO IBM Journal, Vol 11, p527-536, Sept (1967)

189) ANDREWS J.G. and ATTHEY D.R. J. Physics. D: Appl. Physics, Vol 9, (1976)

190) WESTBY OLA, Temperature distribution in the workpiece by welding. Department of Metallurgy and Metals Working, The technical University of Norway (1978).

191) PALEY Z., and HIBBERT P.D., Welding Journal p385S-392S, Vol 54, November (1975)

192) STEEN W.M. Letters in Heat and Mass transfer, Vol 4, No. 3, pp167-178, (1977)

193) RYKALIN N.N. The Calculation of Thermal Processes in Welding. Mashgiz (1951) translated into English by Paley Z. and Adamans C.M. Jr., (1963)

194) CRANK J. Quarterly J. or Mech. and Appl. Maths. Vol X, Pt.2, p220-331, (1957)

195) COHEN M.I. J. Franklin Institute, Vol 283, No. 4, April (1967)

196) DORN V.S. and McCRAKEN D.D. Numerical Methods and Fortran Programming Wiley (1964)

197) DUSINBERRE G.M. Numerical Analysis of Heat Flow, McGraw Hill, New York (1949)

198) SCARBOROUGH J.B. Numerical Mathematical Analysis. Sixth Edition, John Hopkins Press, Baltimore, (1966)

199) LEIBMANN G. Brit. J. Appl. Physics, Vol 6, p129, (1955)

200) CRANK J. and NICHOLSON P. A Practical Method for Numerical Evaulation of Solutions for Partial Differential Equation of the Heat Conduction Type. Proc. Cam. Phil. Soc. Vol 43, p50, (1947)

201) RICHARDSON L.F. Math. Gazette, Vol 12, p415, (1925)

202) RALSTON A. Runge-Kutta methods with minimum error bounds. Mathematics of Computation, Vol 16, p431-437, (1962)

203) KOGELNIK H. and LI T. Laser beams and resonators. Applied Optic., Vol 5, No. 10, p1550, Oct. (1966)

204) GORDON R., COBONPUE J., Int. Heat Trans. Conf. Pt. II, pp454-460, (1961)

205) POLHAUSEN E. Z. Angew Math. U. Mech. I., p115, (1921)

206) BENNET C.O., MYERS J.E. Momentum Heat and Mass transfer. pp379-380, McGraw Hill Book Company Inc., New York (1962)

207) PATEL C.K.N., FAUST W.L., MCFARLANE R.A. Bull. Am. Phys. Soc. vol 9, p500, (1964)

208) PATEL C.K.N. Physics Rev. Letters, Vol 12, p588, (1964)

209) PATEL C.K.N. Physics Rev. Vol 136, A1187, (1964)

210) Handbook for the BOC Model 901 CO_2 gas Laser, BOC Industrial Power Beam, Daventry England.

211) EBOO M. Ph.D. Project (under preparation), London University.

212) GIBSON A.F., KIMMIT M.F. and WALKER A.C. Appl. Phys. Lett. Vol 17, p75-7 (1970)

213) DANISHEVSKII A.M., KASTALSKII A.A., RYVKIN S.M. and YARASHETSKII I.D., Sov. Phys. JETP, Vol 31, p292-5 (1970)

214) GIBSON A.F. and WALKER A.C. J. Phys. C. Solid St. Physics, Vol 4, p2209-2219, (1971)

215) PANYAKEOW S., SHIRAFUJI J., INUISHI Y. J. of Appl. Physics, Vol 46, No. 3, p1245-1251 (1975)

216) CRAFER R.C. Welding Institute, U.K., Private Communication

217) ROFIN I.R. Laser Optics Information Sheet (1975)

218) FOX A.G. and LI T., Proceedings of the I.E.E.E., Vol 51, p80-89, January (1963)

219) CRAFER R.C. The Welding Institute Research Bulletin, Vol 17, April (1976)

220) FOX A.G. and LI. T I.E.E.E. J. of Quant. Electronics, Vol QE2, No. 12, December (1966)

221) KOGELNIK H. Lasers. Vol 1 Edited by Levine A.K. Published by Edward Arnold London, p295, (1966)

222) FOX A.G., LI T. Bell Syst. Tech. J., Vol 40, p453, (1961)

223) GONSALVES J.N. and DULEY W.W. Can J. Phys., Vol 49, pt13 pp1708-1713, (1971)

224) Technical information on Pyroanalyser Model AK-2950AL of Laser Precision Corporation Five West Whitehouse Street, Yorkville, N.Y. 13495 - Rev. Sci. Instrum. Vol 45, No 8 pVI, August, (1974)

225) BOYD G.D. and GORDON J.P. Bell Syst. Tech. J., vol 40, p489, (1961)

226) DICKSON L.D. App. Opts., Vol 9, No. 8, p1854, Aug. (1970)

227) DESCHAMPS G.A. and MAST P.E. Proceedings of the Symp. on Quasi Optics p379, Polytechnic Press, New York (1964)

228) LAURES P. App. Opt., vol 6, p747, (1967)

229) SINCLAIR D.C. and BELL W.E. Gas Laser Technology, Published by Holt, Rinehart and Winston Inc., U.S.A., (1969)

230) WAYNANT R.W., CULLON J.H., BASIL J.T. and BALDWIN G.D., App. Opt. Vol 4, p1648-1651, (1965)

231) Handbook of Materials Science: Vol 1, General Properties. Edited by C.T. Lynch, Published by CRC Press, Ohio, USA, (1974)

232) Kirk-Othmer Encyclopedia of Chemical Technology Published by Interscience Publishers - a division of John Wiley & Sons Inc., New York, 2nd Edition, (1969)

233) Thermophysical Properties of High Temperature Solid Materials. (For titanium Vol 2, part 2 and for mild steel vol 3), Edited by Y.S. Touloukian Published by MacMillan Company, New York, (1967)

234) Metals Handbook: Vol 1, Properties and Selection of Materials Published by American Society for Metals, Metals Park, Ohio, USA, 8th Edition (1967)

235) IMI Titanium 318. Technical Bulletin on Ti-6Al-4V Published by Imperial Metal Industries (Kynoch) Limited, New Metals Division, Birmingham U.K.

236) BRAMSON M.A. Infrared Radiation: A handbook for applications - Plenum Press, New York, (1968)

237) FONTANA M.G. and GREENE N.D. Corrosion Engineering. McGraw-Hill Book Co., London (1967)

238) BOCKRIS J.O'm and REDDY A.K.N. Modern Electrochemistry Vol 2. Published by Macdonald, London (1970)

239) HOCHIED B., KLIMA R., BEAUVAIS C., RAPIN M., ROUX C. Memoires Scientifiques Rev. Metallurge LXVII No 9 (1970)

240) PROKHOROV A.M., BATANOV V.A., BUNKIN F.V., and FEDEROV V.B. I.E.E.E.J. Quantum Electronics QE9, pp503 (1973)

241) COURNTEY C and STEEN W.M. The Surface Heat Treatment of En8 Steel using a 2kW CW CO_2 Laser. Published in Advances in Surface Coating Technology, Feburary (1978)

242) Science Data Book, Edited by R.M. Tennent, Published by Oliver and Boyd, Edinburgh (1976)

243) McQUILLAN A.D. and McQUILLAN M.K. Titanium. Published by Butterworths Scientific Publications, London (1956)

244) ZAIDI M.A. M.Sc. Thesis, London University, Imperial College (1976)

245) SCHWENK W., KAEHLER W.A., KENNEDY J.R., Welding Research Council (Welding Research Supplement), Vol 32, pt 2, p64S-73S, (1967)

246) BARTLO J. Effect of micro-structure on fatigue properties of Ti-6Al-4V bar - fatigue at high temperature. ASTM STP 459, American Society for Testing and Materials, pp144-154, (1969)

247) HICKEY Jr., CHARLES F. Proc. A.S.T.M., Vol 61, P866-878, (1961)

248) NEAL D.F. and BLENKINSOP P.A., Acta Metallurgica, Vol 24, pp59-63, (1976)

249) MARGOLIN H., FARRAR P. and GREENFIELD M.A. The Science Technology and Application of Titanium, Pergamon Press, Oxford, p795, (1970)

250) KORNILOV I.I. and GLAZOVA V.V. Reaction of refractory metals of the transition groups with oxygen (in Russian), Nauka, Moscow, (1967)

251) GLAZOVA V.V., KORNILOV I.I., TOMASKOV N.D. and MODESTOVA, V.N., Dokl. An. SSR, Vol 165 (1965)

252) BRYNZA A.P., KORNILOV I.I., VAVILOVA N.V., MNUSKIN I.P., and MAKSIMOV YU A., Effect of oxygen on the corrosion and electrochemical behaviour of the alloy systems titanium - vanadium and Ti-V-Al in Sulphuric Acid. Proc. Met. USSR, p248-250.

253) HILL D.C. and CHOI C.L. Welding Research Supplement, p152S-158S, USA June (1976)

254) BANAS C.M. United Technologies Research Center Report No. R75-412260-1 Fatigue of laser welded Ti-6Al-4V, July (1975)

255) NILES R.W. and JACKSON C.E. Welding Research Supplement, 25S-32S, January (1975)

256) WEBSTER J.M. Metals Progress, Vol 98, p59, (1970)

257) REGAN A.J. The BOC 2kW CO_2 Laser and its Application. Technical Publication from British Oxygen Company Limited.

258) GONSALVES J.N. and DULEY W.W. J. Appl. Physics, Vol 43, p4684, (1972)

259) ADAMS M.J. Metal Construction and Brit. Weld. J., Vol 2, p1-8, January (1970)

260) CONTI R.J. Welding Journal, Vol 48, p800 (1969)

261) BUDDENHAGEN D.A. Lasers and their metallurgical applications. A.S.T.M.E. Technical paper Sp63-212, (1963).

262) HICE J.H. Lasers - An evaluation of their performance as energy sources for industrial applications, A.S.T.M.E. Technical Paper SP64-91, (1963)

263) PLATTE W.N. and SMITH J.F. Laser techniques for metals joining Welding Journal, vol 42, No 11, Res. Suppl. 481S to 489S, Nov. (1963)

264) JACKSON J.E. Laser promising tool for welding micro-miniature parts. Welding engineer, Vol 50, No. 2, p61-66, (1965)

265) FRICK R.J. Electronic lead welding with the laser. Metals Progress, Vol 90, No. 3, pp91-92, (1966)

266) ORROK N.E. Metals Progress, Vol 91, No 2, pp150-158, (1967)

267) KLOEPPER D. Laser beam welding process development, Grumman Interim Engineering Progress Reports IR822-9-(11) and (111), January and April (1970)

268) BENSON L. Laser welding simplified. American Machinist, Vol 114, No. 8 p81-85, (1970)

269) SANDERSON A. Electron beam monitoring techniques and probe trace analysis. Welding Institute Research report MISC 34/10/75, October (1975)

270) DIETER, GEARE E. Jr. Mechanical metallurgy, International student edition McGraw Hill Book Co. Inc., New York, (1961)

271) CO_2 Laser Theory - Laser technology, PA6-14, July (1967)

LIST OF TABLES

LIST OF FIGURES

LIST OF PLATES

ACKNOWLEDGEMENTS

The author would like to express his sincere appreciation

to:	*for:*
Dr. W.M. Steen	His supervision and guidance and his encouragement and his understanding for various ideas and introduction to the wonderful world of computing and lasers.
His parents, Mr. and Mrs. J.M. Mazumder	Their unending moral support and substantial financial support
British Oxygen Company Limited	Their generous financial support and various experimental facilities
Dr. D.R.F. West	His valuable suggestions on titanium metallurgy
Dr. H.M. Flower	His help for transmission electron miscroscopy of titanium
Mr. A. Neve, his colleagues and all the technical staff of the Department of Metallurgy	Their technical help, equipment design and manufacture, specimen preparation and thesis production.
Mr. C.G.H. Courtney and Miss J. Clarke	Their experimental assistance and stimulating discussions
Mrs. G. Hopkins	Her efficient and accurate typing
British Aircraft Corporation	Their materials support by providing titanium sheets
British Steel Corporation	Their materials support by providing tin plates and drum quality steels.
Miss C. Whiffin and Mr. C.G.H. Courtney	Their help in proof reading
All past and present members of the John Percy Research Group	Their unending co-operation during the preparation of the thesis